Final Report

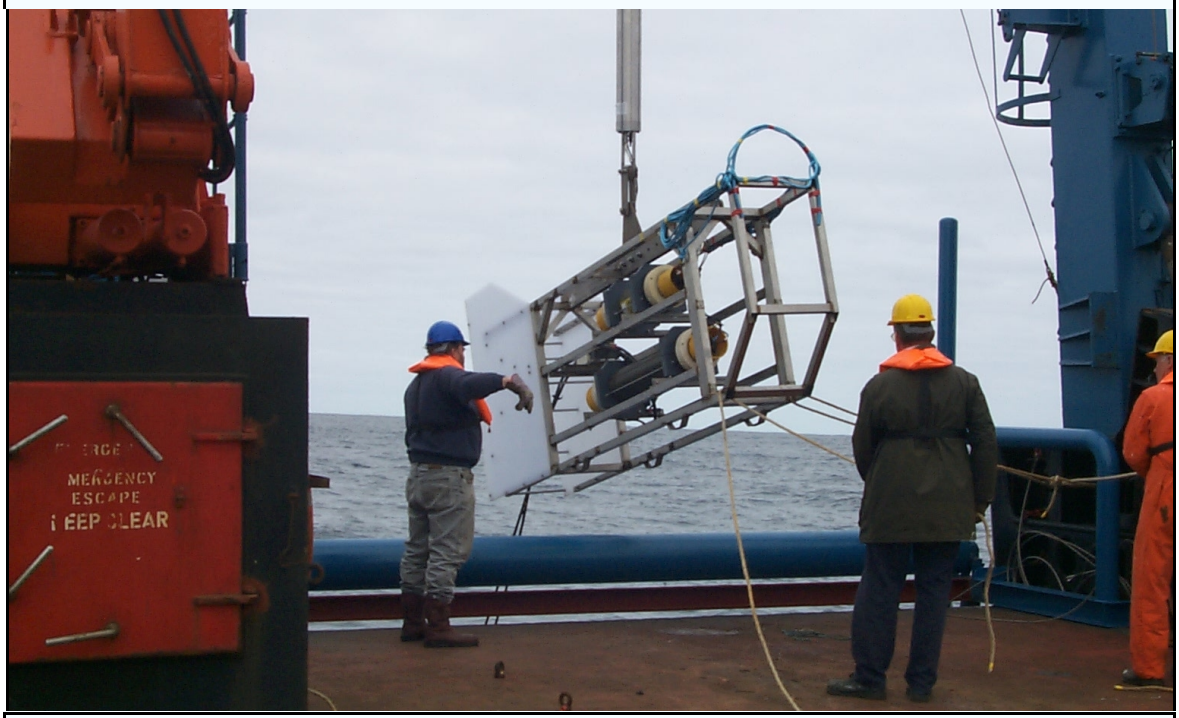

ISO-3D

Applications of 3-Dimensional Electromagnetic Induction by Sources in the Oceans

A MAST-3 Project

Applications of 3-dimensional Electromagnetic Induction in the Oceans

ISO-3D

An RTD project for Mast III under area C:

Marine Technology
Contract Number MAS3-CT97-0120

Final Report

July 2001

Participating Institutions:

Department of Earth Sciences
University of Cambridge, U.K.
(Co-ordinator up to May 2000)

Laboratory of Oceanic and Atmospheric Sciences
Halo ehf.
Reykjavik, Iceland

Institut für Meteorologie und Geophysik
Johann Wolgang Goethe Universität
Frankfurt am Main, Germany

Centro de Geofisica
Instituto de Ciencias da Terra e do Espaço
Universidade de Lisboa, Portugal

Southampton Oceanography Centre

School of Ocean and Earth Science
University of Southampton, U.K.
(Co-ordinator from June 2000)

ISO-3D Working Group

Prof. M.C. Sinha Southampton Oceanography Centre School of Ocean and Earth Science Empress Dock Southampton, SO14 3ZH U.K. sinha@soc.soton.ac.uk (formerly: Department of Earth Sciences, University of Cambridge, U.K.)	Prof. J.M. Miranda Centro da Geofisica Instituto de Ciencias da Terra e do Espaço Universidade de Lisboa, Portugal jmiranda@fc.ul.pt
Prof. Dr. A. Junge Institut für Meteorologie und Geophysik Johann Wolgang Goethe Universität Feldbergstr. 47, D-60323 Frankfurt am Main, Germany junge@geophysik.uni-frankfurt.de	Dr. A.H. Flosadottir Laboratory for Oceanic and Atmospheric Sciences Halo ehf., Sidumuli 31, PO box 8486, Reykjavik Iceland agusta@halo.is
Dr. L. MacGregor Southampton Oceanography Centre School of Ocean and Earth Science Empress Dock Southampton, SO14 3ZH U.K. lucym@soc.soton.ac.uk (formerly: Department of Earth Sciences, University of Cambridge, U.K.)	Dr. F. Santos Centro da Geofisica Instituto de Ciencias da Terra e do Espaço Universidade de Lisboa, Portugal dfams@fc.ul.pt
Dr. J. Luis Universidade do Algarve Campus de Gambelas 8000 Faro Portugal jluis@ualg.pt	N. Lourenço Universidade do Algarve Campus de Gambelas 8000 Faro Portugal nlouren@ualg.pt
A.Soares Centro da Geofisica Instituto de Ciencias da Terra e do Espaço Universidade de Lisboa, Portugal asoares@fc.ul.pt	Dr. S. Dean Southampton Oceanography Centre School of Ocean and Earth Science Empress Dock Southampton, SO14 3ZH U.K. smd9@soc.soton.ac.uk
N. Barker Southampton Oceanography Centre School of Ocean and Earth Science Empress Dock Southampton, SO14 3ZH U.K. ndb@soc.soton.ac.uk	J.L. Rust Southampton Oceanography Centre School of Ocean and Earth Science Empress Dock Southampton, SO14 3ZH U.K. jlr@soc.soton.ac.uk
Z. Cheng *formerly* Department of Earth Sciences University of Cambridge U.K.	S. Riches *formerly* Department of Earth Sciences University of Cambridge U.K.

Contents

Part 1: Introduction

Chapter 1 2

Final Science Report of the ISO-3D Project: Summary

1.1 Summary 3

Chapter 2 6

Induction by Sources in the Ocean: An Introduction to the ISO-3D Project

2.1 Scientific and technological background 7

2.2 Specific Scientific Objectives of the ISO-3D Project 11

2.3 Scientific achievements in relation to original project objectives 13

2.4 References 14

Part 2: Technical developments

Chapter 3 18

Induction Sources In the Sea: A model code for oceanic and controlled sources

3.1 Abstract 19

3.2 Introduction 19

3.3 The code 20

3.4 Intercomparisons for 1-D Earth models 21

3.5 Intercomparison for a 2-D Earth 28

3.6 Considerations of grid resolution, domain size, and convergence 28

3.7 An example of fields in a 3-D Earth 36

3.8 Summary 43

3.9 Acknowledgments 43

3.10 References 45

Chapter 4 48

Controlled Source Electromagnetic Sounding: Methods and Instrumentation

4.1 Introduction 49

4.2 Method 49

4.3 Experimental design considerations 51

4.4 The source 53
4.5 The receivers 55
4.6 References 59
Appendix A: Summary of DASI system specifications 60
Appendix B: LEMUR binary data format 61

Part 3: Scientific results – Natural Sources

Chapter 5 65

Voltage measurements in the CAM-1 submarine cable between the island of Madeira and the Portuguese mainland.

5.1 Abstract 66
5.2 Introduction 66
5.3 Raw Data 68
5.4 Discussion 76
5.5 Acknowledgements 76
5.6 References 76

Chapter 6 78

Studies of the lithosphere using the CAM-1 (Lisbon-Madeira) cable: Preliminary results

6.1 Introduction 79
6.2 MT data 79
6.3 Two-dimensional modelling 79
6.4 Discussion 83
6.5 Conclusions 89
6.6 Acknowledgements 91
6.7 References 91

Chapter 7 92

Magnetotelluric measurements on the Azores Islands

7.1 Summary 93
7.2 Geology 93
7.3 Magnetotellurics - some basics 93
7.4 Experiment 95
7.5 Results 96
7.6 References 96

Chapter 8 101

Oscillations of the on-shore telluric field generated by oceanic tides

8.1 Introduction 102
8.2 Theoretical background 102
8.3 Observations 106
8.4 Modelling 112
8.5 Discussion and future perspectives 112
8.6 Literature 116

Part 4: Scientific Results – Lucky Strike CSEM demonstration experiment

Chapter 9 118

Geological setting of the Lucky Strike segment of the Mid-Atlantic Ridge

9.1 Lucky Strike geological context 119
9.2 Previous baseline data 119
9.3 Photo-interpretation of TOBI and Simrad imagery 122
9.4 Zero age axis 122
9.5 References 125

Chapter 10 126

The MADRIGALS cruise: experimental geometry and data collected.

10.1 Introduction 127
10.2 CSEM experiment 127
10.3 Acoustic navigation 132
10.4 Other data collected 132
10.5 References 134

Chapter 11 135

Magnetic anomaly data from the Lucky Strike seamount.

11.1 Magnetic anomaly data 136
11.2 References 139

Chapter 12 142

The MADRIGALS cruise: CSEM data analysis and preliminary results.

12.1 Introduction 143
12.2 Navigation 143
12.3 Data overview 143

12.4 1-dimensional forward modelling 146
12.5 1-dimensional inversion 146
12.6 Three-dimensional structure at the Lucky Strike Seamount 151
12.7 References 155

Part 5: Conclusions

Chapter 13 157

The digital archive

13.1 Format and structure of the digital archive 158
13.2 Overview of data formats 158
13.3 Accessing the electronic ISO-3D reports and documents 158

Chapter 14 161

Applications of 3-Dimensional Electromagnetic Induction by Sources in the Ocean: Conclusions

14.1 Scientific and technological background 162
14.2 Scientific and technical achievements of the project 162
14.3 Future research and opportunities 163

ISO-3D Final Report

Part 1

Introduction

Chapter 1

Final Science Report of the ISO-3D Project: Summary

M. C. Sinha[1] and the ISO-3D group[2]

1. School of Ocean and Earth Science, Southampton Oceanography Centre, Empress Dock, Southampton, SO14 3ZH
2. Other members of the ISO-3D team: Other members of the ISO-3D group: J.M. Miranda, N. Lourenço, J. Luís, F. Santos, A. Flosadottir, A. Junge, L. MacGregor, A. Soares, S.Dean, N. Barker, S. Riches and Z. Cheng

1.1 Summary

This report presents the scientific results to date of an integrated research project carried out collaboratively by researchers from 6 institutions in four European countries. The ISO-3D project was funded by the European Commission's MAST-III/Framework IV programme from December 1997 until May 2001.

The background to the work is that, in the field of marine geo-electromagnetism, two important emerging technologies have led over recent years to new opportunities for studying the properties of, and processes occurring within, both the ocean itself and the solid earth beneath it. Both of these technologies involve the measurement, for either geophysical or oceanographic purposes, of electric or magnetic fields induced in the ocean and the underlying earth by electromagnetic sources within the water column. The two relevant technologies are controlled source electromagnetic sounding (where the source is introduced artificially by the experimenter); and techniques for measuring naturally induced electromagnetic fields on the seafloor using ocean bottom instruments or telecommunications cables. The two approaches have wide applications both in marine earth science and in physical oceanography. In order to exploit these emerging methods, an important challenge is to be able to model numerically the fields resulting in a 3-dimensional earth and ocean structure from excitation by a localised or distributed 3-dimensional source.

The aims of ISO-3D were firstly to develop an appropriate numerical modelling computer code for this problem, taking as a starting point an existing 3-D electromagnetic code developed for use in geophysical studies on land; and then to carry out a series of studies of both oceanographic and geophysical problems in which 3-dimensional structure is of major importance.

The specific objectives of the project, as summarized in the technical annexe to the research contract, were:

- The development of a numerical computer code for modelling the electromagnetic response of a 3-dimensional earth and ocean structure to induction by an arbitrary 3-dimensional source embedded in the ocean.
- The use of the code in model studies for applications to both physical oceanography and geophysics, including the effects of induction by both natural and artificial sources.
- The completion of a demonstration 3-dimensional controlled-source electromagnetic sounding (CSEM) experiment on the Mid-Atlantic Ridge south of the Azores, within European waters.
- The analysis and interpretation of the results of the demonstration CSEM experiment.

In pursuit of these objectives, the project team have:

- Developed the 'ISIS' (Induction by Sources In the Sea) numerical modelling code, based on a pre-existing 3-D electromagnetic solver; and rigorously tested the ISIS code's stability in a range of applications.
- Carried out an instrument development and construction programme to provide ocean-bottom instrumentation for controlled-source electromagnetic (CSEM) sounding studies.
- Established a monitoring site for logging naturally induced electric fields generated along the abandoned CAM-1 telecommunications cable, which runs from the island of Madeira to the Portuguese mainland.
- Collected and analysed magnetotelluric sounding data from sites in the Atlantic ocean, to determine the geophysical structure of the underlying lithosphere.
- Analysed signals generated by ocean tides in natural source electric and magnetic field data recorded on land in northern Europe.

- Carried out a major geophysical and oceanographic research expedition, MADRIGALS (Mid-Atlantic Deep-towed Resitivity and Induction Geophysics At Lucky Strike - RRS *Charles Darwin* cruise 120), to a segment of the Mid-Atlantic Ridge south of the Azores, during which we carried out a seafloor CSEM survey and simultaneously collected a wide range of supporting oceanographic and geophysical data.
- Analysed the resulting CSEM data in terms of structure and variability in physical properties of the seafloor beneath the Lucky Strike axial volcano and high temperature hydrothermal site.
- Created a digital archive of data and model results.

Scientific and technical results from the project include the following:

We have verified the accuracy of the ISIS code by comparison against other 1-D and 2-D numerical codes.

We have modelled the response to a notional CSEM survey of a simplified 3-D structure such as that which might be encountered at the Lucky Strike axial volcano and hydrothermal site.

We have made substantial improvements in reliability and ease of operation to the DASI transmitter system and to the LEMUR seafloor receiver systems, and provided additional LEMUR instruments for Southampton and Lisbon Universities.

We have analysed a 15 month time series of data from the CAM-1 submarine cable, to assess its stability and to investigate water transport. Data from daily averages of low geomagnetic activity suggest the presence of a long period (several months) variation in the cable voltage, which appears to have its origin in variations in basin-scale water transport.

We have estimated the lithospheric scale (i.e. to depth of at least 200 km) geoelectrical structure of the eastern Atlantic seafloor between Madeira and Lisbon, using data from the CAM-1 cable and the geomagnetic observatory on the Canary Islands. The result indicates that the seafloor sediment layer has an integrated conductance of order 10,000 S; and that this is underlain by a much more resistive crystalline lithosphere, and then by relatively conductive asthenosphere at depths greater than 100 km.

We have made a preliminary analysis of magnetotelluric sounding data from the Azores islands. These suggest a highly conductive shallow structure, influenced by the surrounding ocean, as expected; but also a second highly conducting layer in the mantle, at a depth of approximately 50 km. The structure here, above the Azores mantle hot spot and Mid-Atlantic Ridge, differs significantly from that beneath the mature lithosphere traversed by the CAM-1 cable.

We have analysed data from 6 land MT sites in northern Germany and 8 sites in Scotland, and shown the presence of a strong tidal component at the semidiurnal lunar period. The observed data are matched surprisingly well by simple models based on induction by tidal water movements in the North Sea. Evidently large scale water movements at these periods can be detected by land based geomagnetic observations at some distance from the coast.

We have analysed total field magnetic anomaly data to show that the summit of the Lucky Strike axial volcano on the Mid-Atlantic Ridge is characterized by anomalously weak seafloor magnetization. We attribute this to the effects of hydrothermal fluid circulation, leading to alteration and demagnetisation of shallow crustal rocks in this area.

We have made a preliminary determination of the resistivity structure in the upper 2 km of the crust beneath the Lucky Strike segment of the Mid-Atlantic Ridge, and compared it to that of other spreading ridges. Resistivity at Lucky Strike is less than 1 Ωm immediately beneath the seafloor, increasing to more than 10 Ωm at depths of 800 to 1000 m, and then increasing more slowly (in a logarithmic sense) to

a few tens of Ωm at a depth of 1.5 to 2 km. These resistivity values are substantially higher than those beneath the back-arc, intermediate-spreading-rate Valu Fa Ridge; but similar to, or only slightly higher than, those beneath the Reykjanes Ridge to the north. The upper crust at Lucky Strike is significantly less resistive than that beneath the East Pacific Rise at 13^{o} N, even though both are axial sites of active high temperature hydrothermal venting. It is less resistive by more than an order of magnitude than mature lithosphere in the eastern Pacific. Superimposed on the vertical structure at Lucky Strike are systematic lateral variations in resistivity, with typical wavelengths of 2-3 km or longer. Data from LEMUR instruments deployed close to the summit of the seamount indicate relatively low resistivities in the uppermost crust; while resistivity over the same depth range appears to be higher along the eastern edge of the median valley.

Future research by the ISO-3D working group, after the end of the formal project phase, will be aimed at extending and better constraining these scientific results through further careful modelling of a range of data using the ISIS code.

Chapter 2

Applications of 3-Dimensional Electromagnetic Induction by Sources in the Ocean: An Introduction to the ISO-3D Project

M. C. Sinha[1] and the ISO-3D group[2]

1. School of Ocean and Earth Science, Southampton Oceanography Centre, Empress Dock, Southampton, SO14 3ZH
2. Other members of the ISO-3D team: Other members of the ISO-3D group: J.M. Miranda, N. Lourenço, J. Luís, F. Santos, A. Flosadottir, A. Junge, L. MacGregor, A. Soares, S.Dean, N. Barker, S. Riches and Z. Cheng

2.1 Scientific and technological background

At the outset of this project, new methods for measuring and exploiting electromagnetic fields at the ocean floor were leading to a range of opportunities for advances in their application to problems in both sub-sea-floor geophysics and in studies of water mass movement over various scales. The new approaches have in common that they involve the measurement of electric and/or magnetic fields induced in the ocean and the underlying earth by electromagnetic sources - either natural or artificial - within the water column. Two specific approaches that the ISO-3D project set out to investigate and develop are controlled source electromagnetic sounding; and techniques for measuring naturally induced electromagnetic fields on the seafloor using ocean bottom instruments and telecommunications cables.

Controlled source electromagnetic (CSEM) sounding is a relatively new but rapidly developing geophysical technique which involves the use of an artificial electromagnetic source at or close to the sea floor, and an array of sea bottom recording instruments that measure the resulting fields (see Chapter 4). It has been successfully applied in recent studies of mid-ocean ridges (Evans *et al.*, 1991, 1994; Sinha *et al.*, 1997, 1998; MacGregor *et al.*, 1998, 2001). It has many potential applications in marine geophysics, including studies of environmentally important processes such as hydrothermal circulation, the development of polymetallic sulphide ore bodies and sediment dewatering; and studies of economically important geological targets including hydrocarbons (e.g. MacGregor & Sinha, 2000). Since it provides a means of determining the distribution of electrical resistivity within the crust, it is a particularly attractive geophysical technique for studies of conductive fluid phases within a relatively highly resistive silicate matrix. Seawater resistivity is about 0.3 Ωm throughout most of the ocean. In the oceanic crust the resistivity is generally much higher than this, and can vary through several orders of magnitude. It is largely controlled by the presence of fluids (predominantly seawater, but also high temperature hydrothermal fluids and even magma in the ridge areas), and varies both with the volume and connectedness of the fluid passages and with the properties (composition and temperature) of the pore fluid.

The CSEM method has been shown to be capable of constraining resistivity structure to depths of at least 10 km beneath the ocean floor (Constable & Cox 1996). Use of an artificial source allows both the frequency and the experimental geometry to be chosen to suit the application. As a result, studies of relatively shallow structure (2 km penetration or less) are possible using higher frequencies than are present in the natural source fields used conventionally for seafloor magnetotelluric (MT) sounding, and this combined with the ability to control the source geometry dramatically improves the resolution of CSEM studies over that of the more conventional MT method for certain classes of structure.

Prior to the MADRIGALS study, marine CSEM experiments had been conducted over targets carefully chosen to approximate as closely as possible to either a 1-dimensional or 2-dimensional earth structure. This was partly because the technique was still at a developmental stage, but largely because the interpretational tools for 3-dimensional structures did not exist. However many of the most interesting and significant structures within the ocean floor are undoubtedly 3-dimensional in character. The first stage objective of this project, to develop a 3-D modelling code, was an indispensable first step towards successful CSEM studies of 3-D structures. The second stage objective relating to artificial sources was to use the code in modelling studies to investigate the resolving power of CSEM data, and to optimise experimental design. The third stage objective was to carry out a demonstration CSEM experiment on a suitable, 3-dimensional target of direct and immediate environmental interest - an active, high temperature, hydrothermal site on the Mid-Atlantic Ridge within European waters, close to the Azores.

Induction of electric and magnetic fields in the ocean can occur naturally, both through the movement of water masses and as the result of external disturbances of ionospheric and magnetospheric origin. Motional induction by ocean currents (Figure 2.1) arises when the electrically conducting ocean crosses the

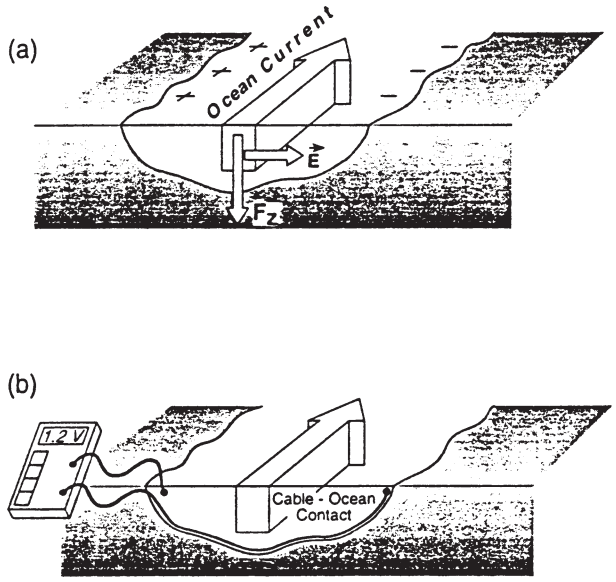

Figure 2.1. (a) Induction of an electric field **E** in the ocean, due to horizontal motion of the conducting water mass through the vertical component of the geomagnetic field, $\mathbf{F}_z$. If we assume that conduction through the solid earth is negligible, and that self induction in the ocean and mutual induction between the ocean and the solid earth are also negligible, then there is a simple relationship between the rate of water movement, the intensity of the vertical magnetic field, and the electrostatic charge build-up across the basin. (b) A seafloor cable can be used to sense motionally-induced voltage differences in the ocean. Insulated cables with endpoints in contact with the local seawater measure the integrated electric field along a path between the end points.

Earth's magnetic field (e.g. Longuet-Higgins, 1954; Sanford, 1971; Robinson 1976; Chave & Luther, 1990; Larsen, 1992).

On the seafloor, ocean bottom electrometers have been routinely used for some years to observe the local electric field (e.g. Filloux, 1987; Petitt, 1994). Voltages across longer distances, up to basin-wide scales, can be monitored using submarine telecommunication cables. As communications companies worldwide update their existing submarine telephone cables, redundant cables have become available for scientific use (e.g. Larsen, 1992; Chave *et al.*, 1992). Voltage measurements are also being made using in-service analogue and fibre optic telecommunication cables (e.g. Larsen, 1991; Rikiishi *et al.*, 1996). Furthermore, discontinued military surveillance cables may become available, and it may be feasible to lay dedicated cables to cover relatively short distances in straits and at circulation choke points. Signals measured by these techniques can be used for geophysical investigations of the deep structure of the crust and upper mantle, for observations of tidal velocities that may lead to improved altimetric tidal corrections, and for naturally integrated ocean transports both locally at points in the ocean and across up to basin-scale distances (Cox *et al.*, 1971; Chave *et al.*, 1991; Constable, 1990; Filloux *et al.*, 1991; Luther *et al.*, 1991; Luther & Chave, 1993; Larsen, 1992; Fujii, 1995; Fujii *et al.*, 1995).

On land, ocean-generated electric fields have been sensed far inland (e.g. Olsson, 1955; Larsen, 1980; Mackie *et al.*, 1988; Junge, 1988). That the origin of these fields is electric current loops generated by water motions is indicated both by these experimental studies and by numerical work (e.g. Flosadottir *et al.*, 1996a; Palshin *et al.*, 1996; see also Figure 2.2 below). An objective of the ISO-3D project was to evaluate the use of these fields for geophysical studies of the continental margin, through which the electric currents must have passed, and for possible information on the ocean flows that generate them.

All models of ocean-generated electromagnetic fields to date have neglected the effects of self-induction within the ocean and of mutual induction with the Earth's mantle. This is a reasonable assumption for ocean currents of sufficiently long periods and moderate spatial scales. However, inductive effects are likely to be important for rapidly varying, large scale motions such as the open-ocean tide, basin-wide sloshing modes, and for rapidly varying, large scale wind-driven motions (e.g. Chave & Luther, 1990). Furthermore, very long cables tend to integrate out voltages due to smaller-scale motions, enhancing the effect of the largest scale motions which are the most likely to be influenced by inductive effects. A modelling code capable of solving for these effects must include a realistic model of the marine sediments and of the solid Earth, since the overall conductivity structure critically limits the electric current loops possible, and these in turn govern the inductive effects. Developing such a code allows us to model the full range of electric field and voltage signals from tidal periods, through the very energetic fluctuations with periods of days to a few hundred days (e.g. Niiler *et al.*, 1993; Fu and Davidson, 1995; Lee *et al.*, 1990; Chave *et al.*, 1996), to the interannual and decadal time scales that are beginning to be achieved with cable voltage monitoring (e.g. Larsen, 1992; Fujii *et al.*, 1995). One of the reasons why this capability is desirable is that the more rapid variations contribute to the aliasing problems of using isolated oceanographic measurements to estimate long-term variability. Putting such measurements accurately in the context of continuous cable or seafloor electric field time series is a highly desirable goal. Another reason is that careful analysis of motional induction at these periods will yield information about the Earth and ocean's electric conductivity structure, and this will contribute to the analysis of oceanographic signals, besides being of intrinsic geophysical interest. Most basically, because the scales of the electric current loops responsible for inductive effects in the ocean are poorly known, numerical modelling is needed to determine in what frequency range it is safe to neglect self-induction for basin-scale cables.

A major limitation of all previous investigative techniques based on induction is that until now we have had no computer codes for fully calculating the induced

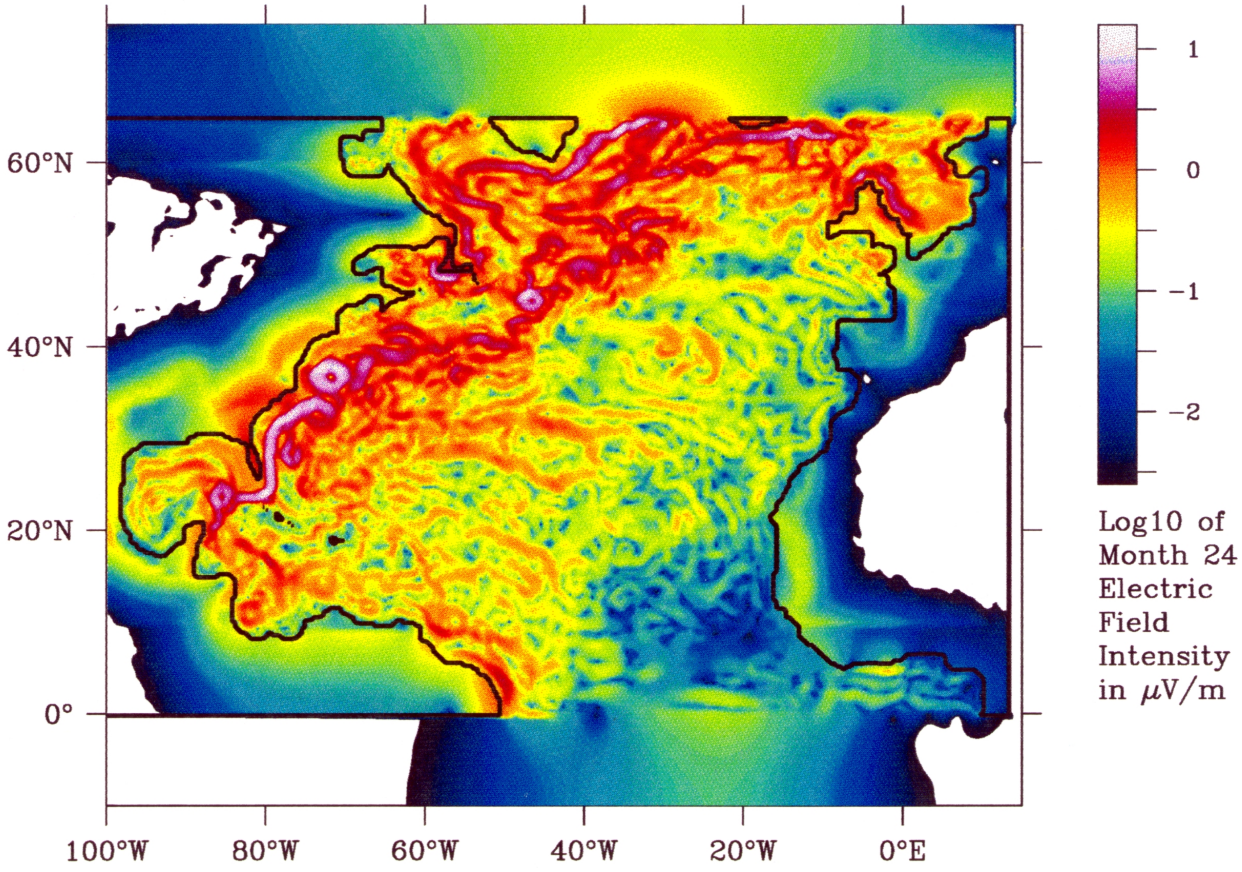

Figure 2.2. The electric field intensity (logarithmic, base 10) in the final month of the North Atlantic simulation of Flosadottir et al. (1996a). The oceanographic variables are obtained from the WOCE Community Modelling Effort's first model (1989), which simulated the wind driven and thermohaline circulation in the North Atlantic using mean monthly winds and realistic topography with resolution permitting mesoscale eddies. Realistic models of seafloor topography, the geomagnetic field and the solid-earth were added, so that the model included the effects of flow meandering, the spatial and temporal variations of seawater temperature and salinity, three dimensional earth models, and the full physics applicable to the large scale, long-period circulation when self-induction may be neglected. Coloured areas within the coastal regions are due to electric currents on land.

fields in a 3 dimensional earth from sources within the ocean, either artificial or natural. As a result, interpretation methods have relied on simplifying assumptions about either the nature of the source field or the structure and influence of the underlying solid earth. Thus the first major deliverable this project - developing a computer code capable of predicting the induced fields in a structure whose electrical resistivity varies in all directions, and which result from an arbitrary source within the ocean - makes significant advances possible in all of the above areas of science and technology.

A key characteristic of electromagnetic induction as it applies to studies of oceanic areas is that a wide range of phenomena spanning both geophysics and physical oceanography, and both natural and artificial sources, are governed by identical physics. Our project has exploited that convergence of disciplines, by carrying out a coherent, phased programme of research aimed at advancing the knowledge base necessary for the improved exploitation of a range of emerging technologies, all of which are likely in the near future to make substantial contributions to marine science. A further benefit of the project has been to bring together a range of researchers from institutions in four European countries, all having widely varying disciplinary backgrounds, in order to concentrate resources and expertise on this important problem; to facilitate the pooling of expertise and experience between countries and disciplines; and so to improve the efficiency of the European research effort in this area of marine science and technology.

2.2 Specific Scientific Objectives of the ISO-3D Project

At the core of the ISO-3D project has been the development of a computer modelling code, acronym ISIS (Induction by Sources In the Sea) able to predict the induced electric and magnetic fields from an arbitrary electromagnetic source, embedded in a structure in which the electrical properties of the ocean and the solid earth are allowed to vary in three dimensions. At the start of the project, such a modelling code did not exist, severely restricting our ability to apply geoelectromagnetic methods to problems in physical oceanography and geophysics. The project then set out to exploit the code, firstly in a series of numerical modelling studies of processes or structures of direct relevance to the MAST III scientific and technological objectives; and secondly in a demonstration experiment in which controlled source electromagnetic sounding was used to investigate the physical properties and state of the deep ocean floor in an area of strong 3-dimensional structural variability. The project's specific scientific objectives as laid out in the original proposal and in the technical annexe to the project contract were:

a) To develop a numerical computer code for modelling the propagation of electromagnetic fields through a 3-dimensional earth and ocean structure, with excitation by an arbitrary 3-dimensional source in the ocean.

b) To apply the code to model studies of the use of basin-scale submarine cables for monitoring climate-related transport of water masses.

c) To apply the code to model studies of controlled source electromagnetic sounding (CSEM) experiments for investigating environmentally and/or economically significant structures and processes at and beneath the ocean floor.

d) To apply the code to model studies of the use of tidally generated electromagnetic (EM) field measurements for :

   (i) assessment of the possibility of using seafloor EM measurements for the improvement of tidal corrections in satellite altimetry,

   (ii) deep induction studies of the earth, using seafloor electric field or submarine cable voltage measurements,

   (iii) structural studies of the continental margin, using fields measured on land,

(iv) possible monitoring of oceanic velocity fields by electromagnetic observing stations on land.

e) To carry out a demonstration CSEM experiment at sea to establish the viability of the technique for imaging 3-dimensional sub-sea-bottom targets associated with structures at the Mid-Atlantic Ridge south of the Azores, within European waters.

f) To analyse and interpret the results of the demonstration experiment and hence to provide

(i) confirmation that the CSEM method can provide constraints on structure in complex 3-dimensional environments,

(ii) an improved understanding of the physical environment of the upper oceanic crust within which hydrothermal circulation takes place at zero age on the Mid-Atlantic Ridge.

These scientific objectives were then organised into a series of tasks and sub-tasks, as indicated in the table below:

Task	Sub-Task	Description	Objective
1	1.1	Modification and development of computer code, and preparation of documentation.	(a)
1	1.2	Assessment of code stability and accuracy (quality control): comparison with other codes; tests against 1-D and 2-D codes for appropriate models; tests for self consistency with varying model parameterisations; tests for accuracy in special/limiting cases.	(a)
2	2.1	Collation of existing, baseline data for use in natural source modelling studies.	(b), (d)
2	2.2	Completion of natural source modelling studies related to basin-wide scales and climate-related movements of water masses.	(b)
2	2.3	Completion of natural source modelling studies for applications to tidally generated fields and land-based observations.	(d)
3	3.1	Collation of existing baseline data for artificial source model studies, including site-specific baseline data for design study of CSEM demonstration experiment.	(c)
3	3.2	Completion of modelling studies for artificial source applications, including final design of CSEM demonstration experiment.	(c)
4	4.1	Logistical and instrumentational preparations for CSEM demonstration experiment.	(e)
4	4.2	Data acquisition at sea: CSEM demonstration experiment on the Lucky Strike segment of the Mid-Atlantic Ridge, SW of the Azores archipelago.	(e)
4	4.3	Analysis, assessment and interpretation of experimental CSEM data set.	(f)

5	5.1	Creation of digital archives of code, modelling results, Experimental data and experimental results.	
5	5.2	Dissemination of results to scientific and user communities.	

2.3 Scientific achievements in relation to original project objectives

In the remainder of this report, we present a series of chapters – each in the form of a discrete paper – which describe the scientific output to date from the ISO-3D project.

In Part 2 of the report, we have included two chapters on technological development. Chapter 3 describes the development and specifications of the ISIS 3-D forward modelling code, together with code testing, verification and stability. The code is based on the pre-existing 3-D electromagnetic induction code of Mackie *et al.* (1993, 1994). In Chapter 4, we document the development and construction programme for seafloor CSEM sounding instrumentation – the DASI (Deep-towed Active Source Instrument) transmitter, and set of LEMUR (Low-frequency Electromagnetic Underwater Recorder) receivers now available for use at Southampton and Lisbon Universities. The work reported in Part 2 relates to our original objectives a) and e) above, and to sub-tasks 1.1, 1.2 and 4.1.

In Part 3, we present a series of four short chapters on studies based around measurements of naturally induced electromagnetic fields. Chapter 5 describes the establishment of a permanent monitoring station for logging naturally induced voltages in the CAM-1 telecommunications cable between Portugal and Madeira. Chapter 6 describes the use of the data from this cable for a geophysical study of the electrical structure of the lithosphere beneath this part of the eastern Atlantic Ocean. Chapter 7 describes preliminary results from a magnetotelluric sounding study, in which natural electric and magnetic fields recorded by temporary stations in the Azores islands have been used to investigate the underlying geophysical structure. Chapter 8 describes a modelling study in which observations made on land in northern Europe of natural electric and magnetic fields have been related to induction by tidal water mass movements in the North Sea. The results in Part 3 of the report relate to objectives b) and d) above, and to sub-tasks 2.1, 2.2 and 2.3 in the table.

A major focus of the ISO-3D work programme was the MADRIGALS cruise – RRS *Charles Darwin* 120 – to the Lucky Strike segment of the Mid-Atlantic Ridge, inside Portugal's Exclusive Economic Zone to the south west of the Azores archipelago. This is documented in Part 4 of the report, which contains four chapters. Chapter 9 presents an overview of the geological setting of the Lucky Strike segment, based on the collation of pre-existing baseline data from previous programmes (including the MAST Marflux-ATJ and AMORES projects). This chapter corresponds to objective c) and sub-task 3.1 above. Chapter 10 is a summary of the cruise programme itself – corresponding to objective e), sub-task 4.2. Chapter 11 presents results from analysing magnetic anomaly data collected during the cruise; while Chapter 12 presents a preliminary analysis of the CSEM data from the cruise (objectives c) and f), sub-tasks 3.2 and 4.3).

Finally, we have brought together all of the output from the ISO-3D project in a single digital archive, which will be distributed with this report. Chapter 13 (Part 5 of the report) provides an overview of the digital archive and its contents, while Chapter 14 presents some overall conclusions from the project. Part 5 of the report corresponds to sub-tasks 5.1 and 5.2 in the table above.

Overall, the project has achieved its primary objectives of creating, testing and documenting a 3-D modelling code; carrying out a demonstration 3-D CSEM study of a target on the Mid-Atlantic Ridge; and carrying out modelling studies of

naturally induced electromagnetic fields related to oceanic structures. All of the objectives a) to f) of our original proposal are addressed at least in part in the scientific results presented in Parts 2, 3 and 4 of this report. The successful creation of the modelling code, and the collation and collection of data achieved during the project, has opened up a number of new scientific opportunities, and the members of the ISO-3D project will continue to exploit these over the next 2 to 3 years. Specifically, in future work, we plan to make substantially more use of our new 3-D modelling capability, both for investigating natural source fields of oceanic origin, and for refining the geophysical analysis and interpretation of the Lucky Strike CSEM data.

2.4 References

Chave, Luther and Filloux, 1996. Observations of the boundary current system at 26.5N in the subtropical North Atlantic Ocean, *J.Phys.Oceanogr.*, submitted.

Chave, A.D., D.S. Luther, L.J. Lanzerotti and L.V. Medford, 1992. Geoelectric field measurements on a planetary scale: oceanographic and geophysical applications, *Geophys. Res. Lett.*, 19, 1411-1414.

Chave, A.D., and D.S Luther, 1990. Low Frequency Motionally-induced Electromagnetic Fields in the Ocean. Part 1: Theory. *J. Geophys. Res.* 95, 7185-7200.

Chave, A.D., S.C. Constable, and R.N. Edwards, 1991, Electrical exploration methods for the seafloor, In *Electromagnetic Methods in Applied Geophysics, vol. 2. , M. Nabighian, Soc. of Explor. Geophys., Tulsa, Okla.*, 931--966.

Constable, S., 1990. Marine electromagnetic induction studies. *Surv. Geophys.*, 11, 303--327.

Constable, S.C. & Cox, C.S., 1996. Marine controlled source electromagnetic sounding II: The PEGASUS experiment. *J. Geophys. Res.*, in press.

Cox, C.S., J.H. Filloux, and J. Larsen. 1971. Electromagnetic studies of ocean currents and electrical conductivity below the ocean floor. *The Sea. A.E. Maxwell.* 4, part I. 637--693. John Wiley, New York.

Evans, R.L., Constable, S.C., Sinha, M.C., Cox, C.S., & Unsworth, M.J., 1991. Upper crustal resistivity structure of the East Pacific Rise near 13^{o}N. *Geophys Res Lett*, 18, 1917-1920.

Evans, R. L., Sinha, M. C., Constable, S. C. & Unsworth, M. J., 1994. On the electrical nature of the axial melt zone at 13^{o}N on the East Pacific Rise. *J. Geophys. Res.*, 99, 577 - 588.

Filloux, J.H., D.S. Luther and A.D. Chave, 1991. Update on seafloor pressure and electric field observations from the North-Central and Northeastern Pacific: tides, infratidal fluctuations, and barotropic flow. *Tidal Hydrodynamics*, Bruce B. Parker, ed., John Wiley and Sons, Inc.

Filloux, 1987, Instrumentation and experimental methods for oceanic studies, *Geomagnetism*, ed. J.Jacobs, Academic Press, London. Chapter 3, p. 143-248.

Flosadottir, A.F. and S.C. Constable, 1996. Marine controlled-source electromagnetic sounding 1. Modeling and experimental design. *J. Geophys. Res.*, 101, 5507-5517.

Flosadottir, A.F., J.C. Larsen and J.T. Smith, 1995. Motional Induction in North Atlantic Circulation Models. *J. Geophys. Res.*, in press.

Flosadottir, A.H., J.C. Larsen and J.T. Smith, 1996b. The Relation of Seafloor Voltages to Ocean Transports in North Atlantic Circulation Models: Model Results and Practical Considerations for Transport Monitoring. *J.Phys.Oc.*, in press.

Fu, L-L and R.A. Davidson, 1995. A note on the barotropic response of sea level to time-dependent wind forcing. *J. Geophys. Res.*, 100, 24,955-24,963.

Fujii, I, 1995, On Geoelectric Potential Variations Over a Planetary Scale, *Ph.D. thesis* , Department of Earth and Planetary Science, University of Tokyo.

Fujii, I., L.J. Lanzerotti, H. Utada, H. Kinoshita, J. Kasahara, L.V. Medford, C.G. Maclennan, 1995, Geoelectric power spectra over oceanic distances. *Geophys.Res.Lett.*, 22, 421-424.

Junge, A, 1988. The telluric field in northern Germany induced by tidal motion in the North Sea. *Geophys. J.*, 95, 523-533.

Larsen, J.C., 1992. Transport and heat flux of the Florida Current at 27^{o}N derived from cross-stream voltages and profiling data: Theory and observations. *Philos. Trans. Roy. Soc London*, 338, 169-236.

Larsen, J. C., 1991, Transport measurements from in-service undersea telephone cables, *IEEE J. Oceanic Engin.*, 16, 313-318.

Larsen, J. C., 1980. Electromagnetic response functions from interrupted and noisy data, *J.Geoelectr. Geomag.*, 32, suppl. I, 89-103.

Lee, T.N., W. Johns, F. Schott and R. Zantopp, 1990. Western boundary current structure and variability east of Abaco, the Bahamas at 26oN. *J. Phys. Oceanogr.*, 20, 446-466.

Longuet-Higgins, M.S., Stern, M.E. and Stommel, H., 1954. The electrical field induced by ocean currents and waves, with applications to the method of towed electrodes. *Pap. phys. Oceanogr. Met.*, 13 (1), 37 pp.

Luther, D.S., A.D. Chave, and J.H. Filloux, 1991. Low Frequency motionally induced electromagnetic fields in the ocean 2, Electric field and Eulerian current comparison. *J.Geophys.Res.*, 96, 12,797-12,814.

Luther, D.S., and A.D. Chave, 1993. Observing ``Integrating" Variables in the Ocean, *Proceedings of the 7th `Aha Huliko'a Winter Hawaiian Workshop on Statistical Methods in Physical Oceanography*.

MacGregor, L.M., Constable, S.C. & Sinha, M.C. The RAMESSES experiment III: Controlled source electromagnetic sounding of the Reykjanes Ridge at 57^{o} 45' N. *Geophysical Journal International*, 135, 1998, 773-789.

MacGregor, L. M. & Sinha, M.C. Use of marine controlled source electromagnetic sounding for sub-basalt exploration. *Geophysical Prospecting*, 48, 2000, 1091-1106.

MacGregor, L., Sinha, M. & Constable, S. Electrical resistivity structure of the Valu Fa Ridge, Lau Basin, from marine controlled source electromagnetic sounding. *Geophys. J. Int.*, 146, 2001, 217-236.

Mackie, R.L., Smith, J.T., and T.R.Madden, 1994. Three-dimensional electromagnetic modeling using finite difference equations: The magnetotelluric example. *Radio Science, 29*, 923-935.

Mackie, R.L., Madden, T.R., and P.E. Wannamaker, 1993. Three-dimensional magnetotelluric modeling using finite difference equations - Theory and comparisons to integral equation solutions. *Geophysics, 58*, 215-226.

Mackie, R.L., B.R. Bennett, and T.R. Madden, 1988. Long-period magnetotelluric measurements near the central California coast: a land-locked view of the conductivity structure under the Pacific Ocean, *Geophysical Journal*, 95, 181--194.

Niiler, P.P., J. Filloux, W.T. Liu, R. M. Samelson, J.D. Paduan, and C.A. Paulson, 1993. Wind-forced variability of the deep Eastern North Pacific: Observations of seafloor pressure and abyssal currents. *J. Geophys. Res.*, 98, 22,589-22,602.

Olsson, B.H., 1955. The electrical effects of tidal streams in Cook Strait, New Zealand, *Deep-Sea Res.*, 2, 204--212.

Palshin, N.A., L.L. Vanyan, and P. Kaikkonen, 1996. On-shore amplification of the electric field induced by a coastal sea current. *Physics of the Earth and planetary interiors*, 94, 269-273.

Petitt, R.A., A.D. Chave, J.H. Filloux and H.H. Moeller, 1994, Electromagnetic field instrument for the continental shelf, *Sea Technology*, 35, 10-13.

Rikiishi, K., M. Michigami, T. Araki, K. Shiwaki, R. Eto, K. Taira, and J. Larsen, 1996. Cross-Stream Voltages Induced by Ocean Currents in the Tsugaru Strait, Northern Japan. *Abstract, 13th Workshop on Electromagnetic Induction in the Earth, Onuma, Japan, 1996*.

Robinson, I.S., 1976. A theoretical analysis of the use of submarine cables as electromagnetic oceanographic flowmeters. *Phil.Trans.Roy.Soc.London*, 280 (1297), 355--396.

Sanford, T.B., 1971. Motionally Induced Electric and Magnetic Fields in the Sea, *J.Geophys.Res.*, 76, 3476-3492.

Sinha, M.C., Navin, D.A., MacGregor, L.M., Constable, S., Peirce, C., White, A., Heinson, G. & Inglis, M.A. Evidence for accumulated melt beneath the slow-spreading Mid-Atlantic Ridge. *Phil. Trans. R. Soc. Lond.* A, 355, 1997, 233-253.

Sinha, M. C., Constable, S.C., Peirce, C., White, A., Heinson, G., MacGregor, L.M. & Navin, D.A. Magmatic processes at slow spreading ridges: implications of the RAMESSES experiment at 57º 45' N on the Mid-Atlantic Ridge. *Geophysical Journal International*, 135, 1998, 731-745.

WOCE Community Modeling Effort, 1989. A high resolution simulation of the wind and thermohaline circulation in the North Atlantic Ocean. *Proceedings of `Aha Huliko'a Hawaiian Workshop*, Jan. 17-20, 1989.

ISO-3D Final Report

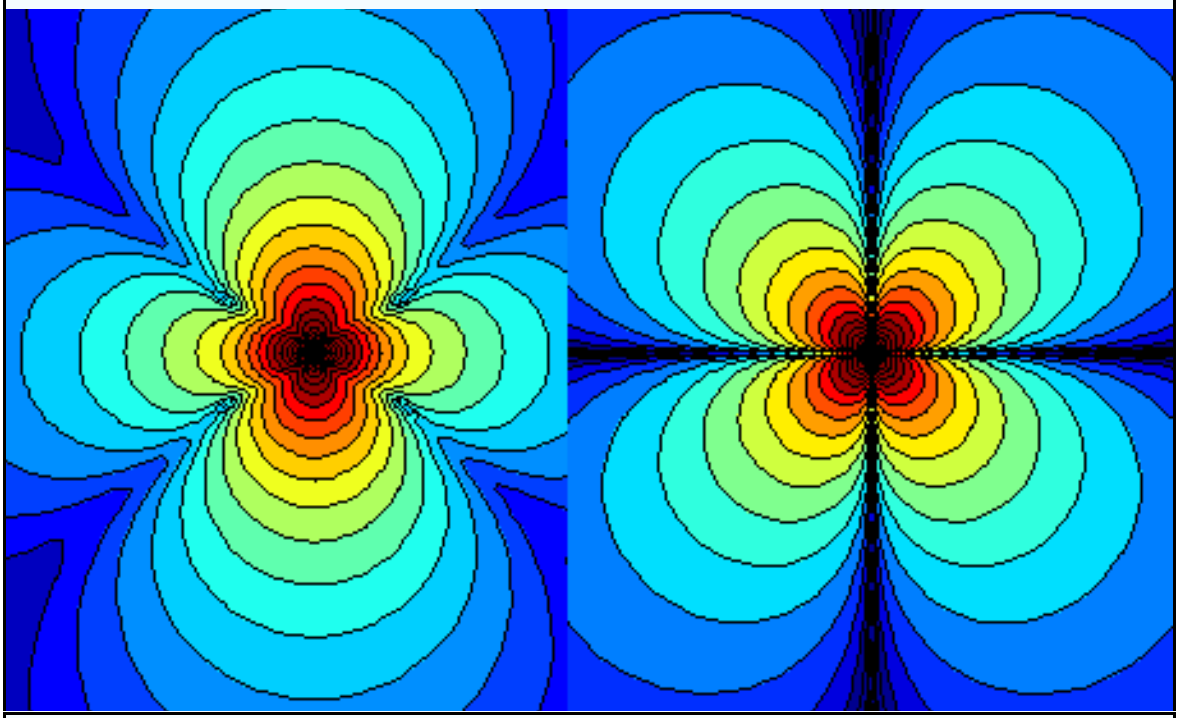

Part 2

Technical Developments

Chapter 3

Induction Sources In the Sea: a model code for oceanic and controlled sources

A.H. Flosadottir[1], L.M. MacGregor[2], and the ISO-3D group[3]

1. Halo Inc., Laboratory for Atmosphere and Ocean Studies, Reykjavik, Iceland, and the Joint Institute for Studies of the Atmosphere and Ocean, University of Washington, Seattle, U.S.A.

2. School of Ocean and Earth Science, Southampton Oceanography Centre, Empress Dock, Southampton, SO14 3ZH, UK

3. Other members of the ISO-3D group: M.C. Sinha, J.M. Miranda, A. Junge, F.M. Santos, A. Soares, J. Luis, N. Lourenco, S. Dean, N. Barker, S. Riches and Z. Cheng.

For submission to Geophysical Journal International

3.1 Abstract

A numerical code for modelling electromagnetic fields generated by arbitrarily distributed induction sources embedded in a 3-dimensional resistivity structure has been developed based on the 3-D magnetotelluric (MT) code of Mackie and Madden. The ISIS code (Induction Sources In the Sea) allows prescribed source currents to be applied anywhere within the model domain. The code is designed to model oceanic or man-made sources within the ocean over a wide range of spatial scales, from basin scale studies of ocean circulation and tides to crustal scale controlled source electromagnetic (CSEM) studies. It permits the use of Cartesian or spherical coordinates, and allows for resistivity models with anisotropy in the principal coordinate directions. The code is described and results are compared with independent models. Tests include intercomparison with analytical results for an electric dipole in a uniform medium, with the quasi-analytical code of Chave and Cox for horizontal electric dipoles in a layered medium, and with the finite-element code of Unsworth, Travis and Chave for a horizontal electric dipole on a seafloor that varies in two dimensions. Considerations of domain size, discretization, and convergence are discussed, and the use of the code for 3-D problems is illustrated for a simplified structure of the type explored by the MADRIGALS CSEM experiment on the hydrothermally active Lucky Strike segment of the Mid-Atlantic Ridge, where electromagnetic signals were transmitted from a deep-towed electric dipole source to an array of seafloor receivers.

3.2 Introduction

A wide variety of both oceanographic and geophysical problems can be addressed using measurements of electromagnetic fields induced in the ocean and the underlying earth by man-made and oceanic sources within the water column. For example, controlled source electromagnetic sounding (CSEM) has been used successfully to study the electrical resistivity structure of the sea floor in a variety of environments (e.g. Nobes *et al.*, 1992; Evans *et al.*, 1994; Webb and Edwards, 1995; Cairns *et al.* 1996; Constable and Cox, 1996; MacGregor *et al.*, 1998, 2001). CSEM sounding involves the use of an artificial electromagnetic source at or close to the sea floor, and an array of sea bottom recording instruments to measure the resulting fields. In oceanography, fields and large scale voltage differences induced by the movement of water masses through the geomagnetic field can be observed by means of ocean bottom instruments and telecommunications cables and used to infer information about temporal variations of ocean currents on spatial scales ranging from a few times the water depth to the scales of ocean basins (e.g. Chave *et al.*, 1997; Baringer and Larsen, 2001; Vanyan *et al.*, 2000; Rikiishi *et al.*, 1996; Lyu and Kim, 2001; Hashimoto *et al.*, 2001; Fujii and Chave, 1999; Flosadottir, 2001).

Great advances have been made in numerical modelling of electromagnetic fields in a three-dimensional earth over the last few years (e.g. Mackie *et al.*, 1994; Druskin and Knizherman, 1994; Smith, 1996a; Wang and Tripp, 1996; Alumbaugh *et al.*, 1996; Avdeev *et al.*, 1997; Zhdanov *et al.*, 2000; Badea *et al.*, 2001).

Practical interpretation methods for observed fields due to CSEM and natural sources in the sea, however, have until now relied on simplifying assumptions about either the nature of the source field or the structure and influence of the underlying solid earth. For the CSEM method, suitable codes have not been available for modelling the electric dipole response when the structure of the medium is allowed to vary in more than two dimensions. For ocean-induced fields, most modelling studies have treated the solid Earth in a highly simplified manner, often as an insulator below a relatively shallow depth; most have furthermore treated the problem electrostatically, so that the effects of self- and mutual induction cannot be quantified (e.g. Robinson, 1976; Stephenson and Bryan, 1992; Flosadottir *et al.*, 1997a; Tyler *et al.*, 1997; Palshin *et al.*, 1999).

The desire to address the computational needs of marine geophysics and oceanography by developing and applying a computer program capable of predicting

the induced field in a structure whose electrical resistivity varies in all directions, and which results from an arbitrary distribution of sources within the ocean, resulted in the ISO-3D project, funded by the European Union and involving scientists from institutions in the U.K, Iceland, Portugal and Germany.

This paper describes the resulting code and its initial application to compute electromagnetic fields in models of the earth and ocean. As part of the ISO-3D project, a CSEM experiment using horizontal electric dipole source and receivers was performed on the Lucky Strike segment of the Mid-Atlantic ridge (Sinha *et al.*, 1999). The Lucky Strike segment is dominated by a 10km wide, 500m tall axial volcano. At the summit of the volcano both diffuse and high temperature venting have been observed (Fouquet *et al.*, 1995). Since the seafloor topography and in all probability the underlying resistivity structure are 3-dimensional in character, one of the first applications of the new code will be to the analysis and interpretation of this dataset. In this paper the primary emphasis is therefore on tests of the code's performance in the context of its application to controlled (i.e. point) sources, with particular application to horizontal electric dipole sources. Subsequent papers will investigate application of the code to other types of controlled sources, and to distributed sources such as ocean currents and the ocean tide.

3.3 The code

One of the most widely used codes for modelling magnetotelluric fields in 3-D models of the Earth in recent years has been the 3-D code of Mackie and Madden (1993; Mackie *et al.*, 1994). This code calculates the fields induced in a 3-dimensional earth by an external, plane-wave source. The problem is discretized on a staggered finite difference grid where the magnetic field components are located along the edges of resistivity grid cells. It is solved in the frequency domain by the method of conjugate gradients with incomplete Cholesky decomposition and an occasional correction for numerically induced divergences of the magnetic field as originally introduced by Smith (1996a, 1996b). The solution is initially obtained for the magnetic induction, B, and the electric field is computed subsequently. The method has been used in extensive intercomparisons with other codes, and has been used in practice on a number of MT datasets collected in the field (e.g. Mackie *et al.*, 1996; Park and Mackie, 1997; Hautot *et al.*, 2000).

The decision to base our work on this code was based on the favorable experience of ISO-3D team members using the code in magnetotelluric data analysis, and on the author's gracious permission. We have named the resulting code ISIS for 'Induction Sources In the Sea'. Originally based on the version described in Mackie *et al.* (1994), we have, in addition to our own modifications and extensions, also implemented a number of the modifications made in the version released by Mackie and J.R. Booker in 1999. We have not, however, had access to the latest, now proprietary, version of the code.

In ISIS, source currents in any direction can be specified wherever that particular electric current component is naturally defined on the staggered grids. Resistivity structures are defined by assigning each cell within the finite element grid a uniform resistivity value. To construct the simple models shown in this paper we have written a program to make resistivity model arrays for a collection of prisms embedded in a uniform background. Fields are output at their natural, staggered grid locations so that the results of the calculation can be viewed directly, and at any location. For applications such as magnetotelluric sounding or CSEM studies, where all the field components are required at a common point (the receiving instrument), interpolation of the field components to common locations can be done at very little computational expense after an ISIS run.

The code can still be used to solve magnetotelluric (MT) problems. If this is requested in the input dialog, the appropriate components of the magnetic field are fixed at the top of a number of air layers and along the sides of the computational domain. For oceanic or CSEM source calculations, by default the program sets the relevant magnetic field values at the side and top boundaries to zero. Handling of the

bottom boundary is unchanged from the Mackie and Madden version. These boundary conditions produce acceptable results when the boundaries are distant enough for the solution in the region of interest to be insensitive to the boundary condition applied. Alternately, the model can be surrounded by a 'buffer' zone around the sides and bottom of the model (using a simple switch in the input dialog). By specifying a high conductivity for this zone, the boundary condition becomes that the component of electric field tangential to the boundary is approximately zero. In a later section, we demonstrate the effect of domain size on the output fields, and give an example of contrasting the two boundary conditions in order to assess over how much of the computational domain the influence of the boundary may safely be ignored.

Convergence of the conjugate gradient iterations was assessed in the original code based on the value of the average change in the model magnetic field from the previous iteration, averaging over all three components of the field, and dividing by the average value of the magnetic field itself. In testing the use of the code for the CSEM problem we found that relatively large errors tended to persist over significant parts of the model domain, despite good convergence by this criterion. By modifying the measure of convergence, we found that we were able to greatly improve the accuracy of CSEM solutions, achieving excellent agreement with independent solutions (see following sections). Convergence is now defined in terms of largest absolute value, over the whole computational domain, of the change in any component of the magnetic field, divided by the vector magnitude of the magnetic field at the same point. Using the vector magnitude is necessary to avoid singularities where particular components go through zero-crossings. At the end of the calculation the convergence measure at every point on the grid is output. We have found this option highly informative in cases where unsatisfactory convergence was achieved, pointing to those parts of the grid where the convergence was particularly poor. These regions can then be re-gridded to improve the success of the calculation.

In this paper, we have restricted the use of the code to Cartesian coordinates and isotropic resistivities. In addition to the extensions already described, however, the ISIS code optionally permits the use of alternate metrics for curvilinear coordinate systems, and resistivity models with anisotropy along the principal coordinate directions. While beyond the scope of the present discussion, these options will be explored in subsequent papers. We have concentrated in this paper on testing the code for the CSEM case with an electric dipole source. The results shown were computed on a single 256 MHz processor of an SG Origin 2000 machine. The parameterisation used for both the layered Earth, 2-dimensional and 3-dimensional structure calculations comprised 117x117x90 cells. This required 2 Gb of RAM and approximately 2 hours of CPU time to converge to an acceptable level. In the present version, our choice to have the code produce a good deal of auxiliary information has been at the cost of greater memory requirements than absolutely necessary for the computation. Memory could be saved, for instance, by not recording convergence information at every point, and by computing the electric field at specified receiver locations only. More nearly absorbing boundary conditions and other future improvements are also likely to reduce the memory requirements. More complex Earth and ocean structures will undoubtedly require a large number of parameters for an accurate solution and fully optimising the code for performance and memory requirements will be the subject of future efforts.

3.4 Intercomparisons for 1-D Earth models

In order to test the accuracy of the ISIS code for CSEM calculations, we begin by comparing the fields with simple analytic or quasi-analytic solutions for 1-dimensional resistivity structures. The range of frequencies and resistivities used in the tests are chosen to be similar to those commonly encountered in marine CSEM experiments. Perhaps the simplest structure to use as a starting point is an isotropic, uniform wholespace. Analytic solutions for the fields of a point electric dipole in this case are well known (e.g. Stratton, 1941; Kraichman, 1970). Figure 3.1

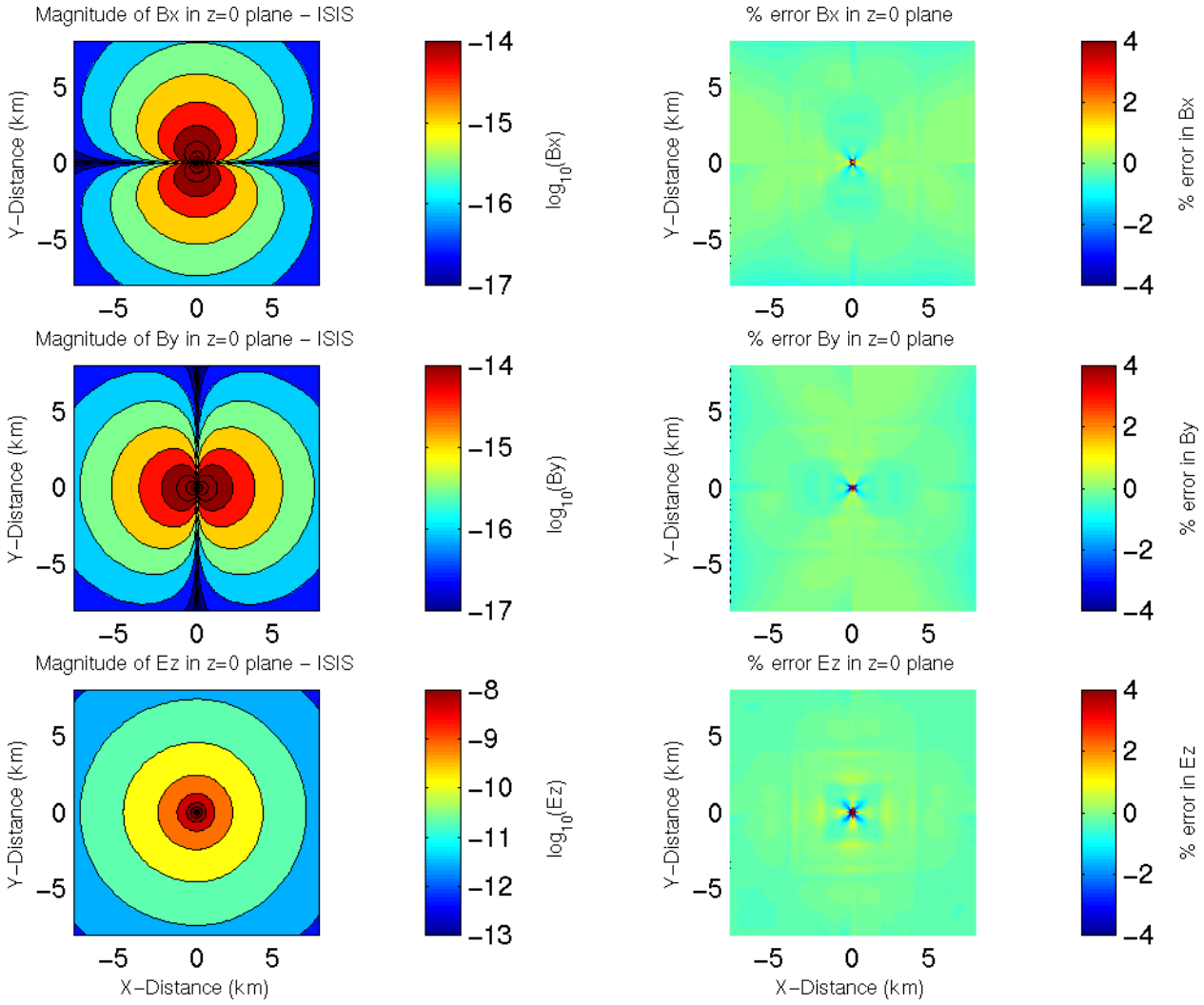

Figure 3.1(a). Comparison between fields calculated analytically and those computed by ISIS for the case of a vertical (parallel to the z-axis) electric dipole of frequency 5 Hz, located at the origin in a uniform 100 Ωm whole space. The left hand panels show the magnitude of the non-zero field components in the source's equatorial plane (the plane z=0, passing through the source dipole and perpendicular to its axis) as calculated by ISIS. The right hand panels show the percentage difference between these fields and those calculated analytically. The full mesh extends from 35 km to 35 km in both horizontal directions, and from 16 km in the ocean to 47 km depth in the seafloor vertically. This region is parameterised into 93 regions in the x and y directions and 105 regions in the z direction. The smallest grid cell, at the source, is 50 m wide horizontally, and 0.5 m tall; the largest, at the corners of the domain, are 8 by 8 by 10 km. The colour scale indicates near-perfect agreement in green, and passes through ±1% error at yellow and turquoise, respectively. The green colours of most of the area indicate agreement to well under 1%.

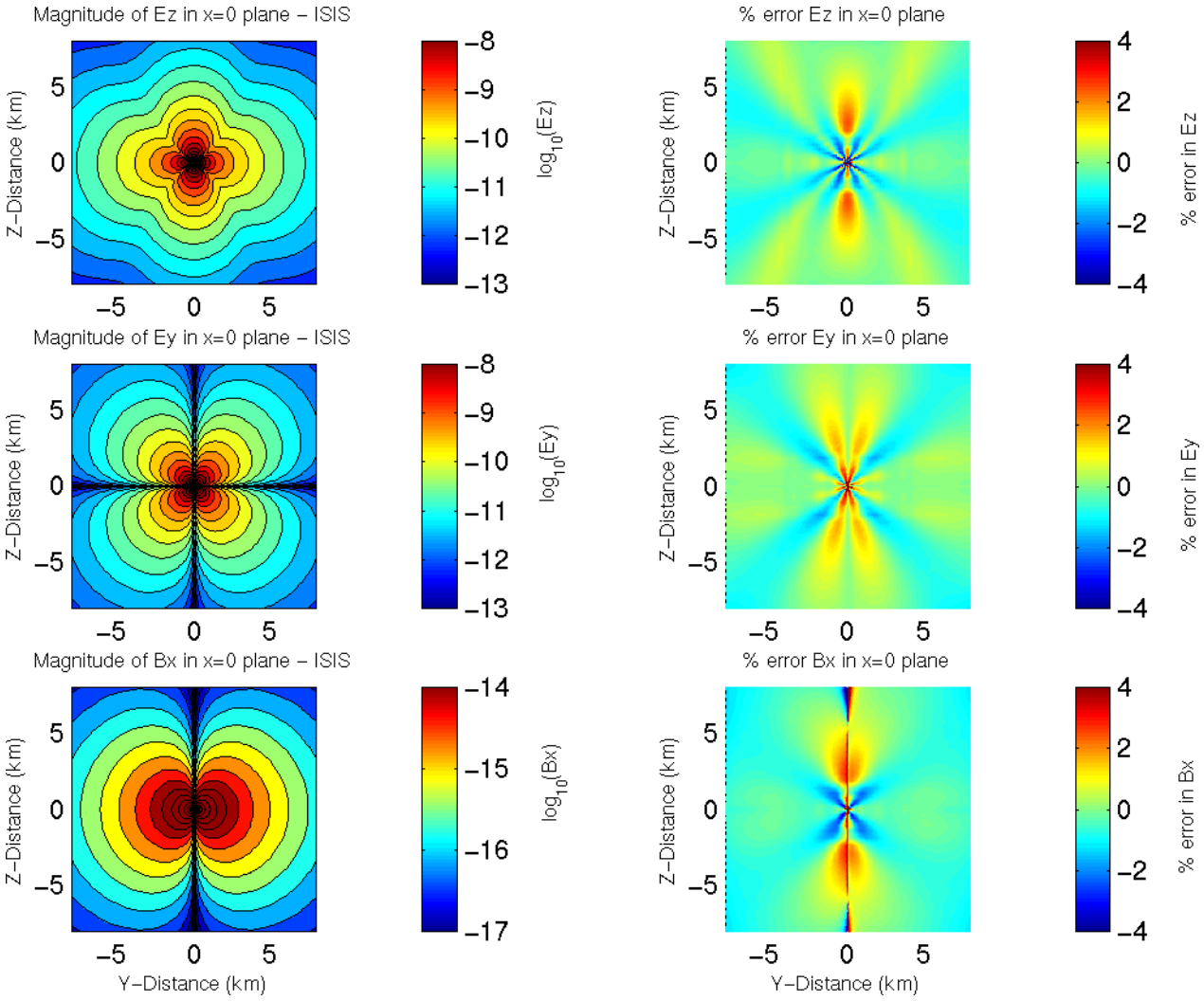

Figure 3.1(b). Field magnitudes in the vertical plane x=0 (passing through the source dipole and parallel to its axis). The left hand panels show the E_z, E_y and B_x fields calculated by ISIS. The right hand panels show the percentage difference between these fields and those calculated analytically. Apart from a 'starburst' pattern around the source, agreement is to 1% or better (yellow through turquoise) over most of the area shown. The starburst pattern of relatively high error fades away at double the grid resolution (cf. the central area of figure 3.9 below).

shows an intercomparison between the fields calculated by ISIS and those calculated analytically for the case of a 5 Hz vertical electric dipole placed at the origin in a uniform space of resistivity 100 Ωm. The agreement in both magnetic and electric fields is excellent.

Although good agreement for the case of a uniform space is gratifying, in order to model real-earth structures the code must be able to model the field accurately in resistivity structures which vary both horizontally and vertically. Comparison with the quasi-analytic solution of Chave and Cox (1982; see also Flosadottir and Constable, 1996, and references therein) for a horizontal electric dipole in a simple layered earth structure tests the ability of the ISIS code to handle vertical variations in resistivity. Since one of our aims is to use the code to interpret CSEM data collected at the Lucky Strike segment of the Mid-Atlantic Ridge, the model resistivities were chosen to be broadly consistent with those observed at other mid-ocean ridge crests (Evans *et al.*, 1994, MacGregor *et al.*, 1998, 2001). The source frequencies were chosen to be consistent with those transmitted during the MADRIGALS cruise. The grid used is described figure 3.2. The intercomparison of the ISIS seabed horizontal field components with the modelling code of Chave and Cox (1982) is shown in figure 3.3. The agreement is very good. Table 3.1 shows the grid-averaged errors in magnitude and phase calculated at the seafloor at three different frequencies calculated on the same finite difference grid. The error increases slightly with increasing frequency since the fixed grid cell size becomes a larger fraction of a skin depth and the exponential decay of the fields are less well resolved. However the errors are satisfactorily small at all three frequencies, and much smaller than errors typically observed in experimental data.

	Frequency		
Field component	0.25Hz	1Hz	4Hz
Ex	0.7%	1.2%	1.2%
Ey	0.6%	1.6%	1.6%
Bx	0.5%	0.5%	0.5%
By	0.5%	0.6%	0.8%

Table 3.1a: The mean absolute value of the relative differences, in percent, between the ISIS and quasi-analytical fields for the layered model described in figure 3.3, and for three different frequencies, spanning the range transmitted during the MADRIGALS cruise. The mean is calculated at the seafloor between -10km and 10km in the x and y directions, and the relative differences are computed as the absolute differences, divided by the vector magnitude of the electric or magnetic field. Errors are largest close to the source.

	Frequency		
Field component	0.25Hz	1Hz	4Hz
Ex	0.5	0.7	1.2
Ey	0.8	1.0	1.7
Bx	0.7	0.8	1.8
By	0.4	0.5	1.3

Table 3.1b: Relative differences of the phase (in degrees), computed as described for Table 3.1a. The means are dominated by large differences close to the points where the phases change rapidly by 180 degrees. Over the majority of the region the difference is less than 1 degree.

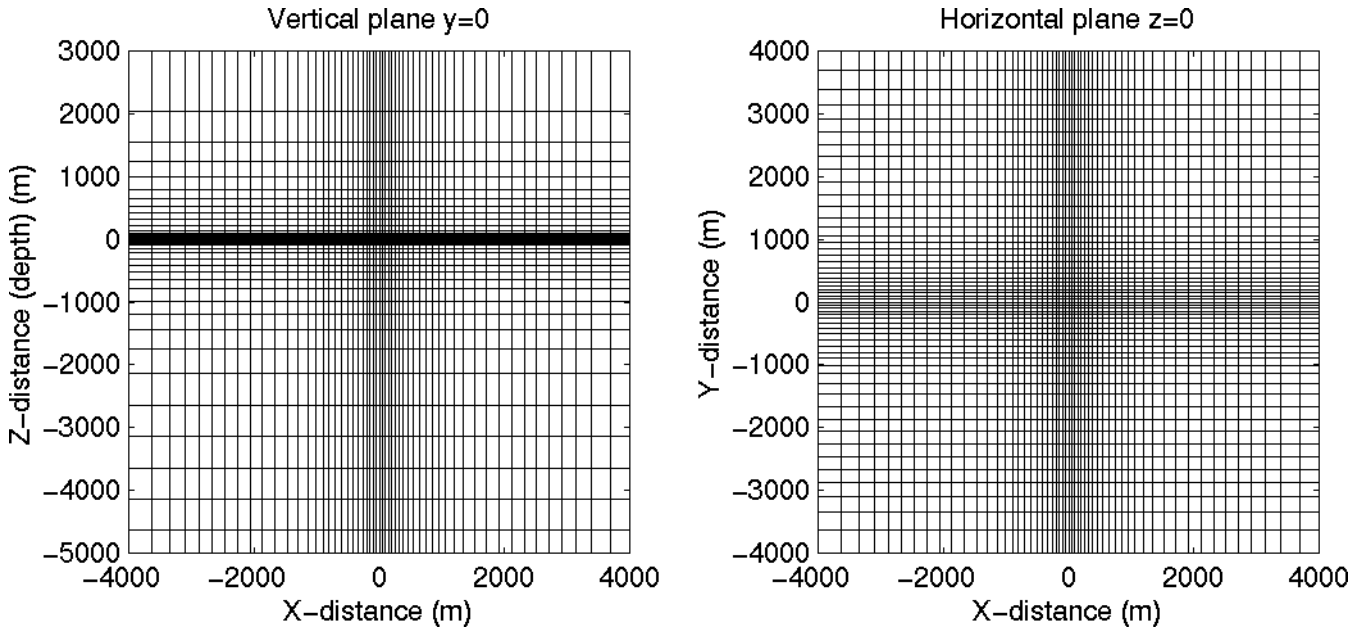

Figure 3.2. The central portion of the finite difference mesh used in the calculation of fields for the intercomparison with the modelling code of Chave and Cox and the modelling code of Unsworth et.al.. The boundary between the seafloor and ocean is at a depth of 0m. The horizontal electric dipole source is located at the origin. The full mesh extends from 75 km to 75 km in both horizontal directions, and from 5 km in the ocean to 68 km in the seafloor vertically (plotted with z negative downwards into the seafloor). This region is parameterised into 117 regions in the x and y directions and 90 regions in the z direction. The parameterisation must be fine round the source to accurately model the rapid variation of the electromagnetic fields close to the source. The parameterisation is also fine at the ocean/seafloor boundary to allow modelling of the sharp resistivity contrast. The left hand panel shows the mesh in the vertical plane y=0, and the right hand panel shows the mesh at the seafloor (z=0 plane). Both panels are plotted without vertical exaggeration. The central part of this grid is very similar to the one used for the intercomparison in figure 3.1a.

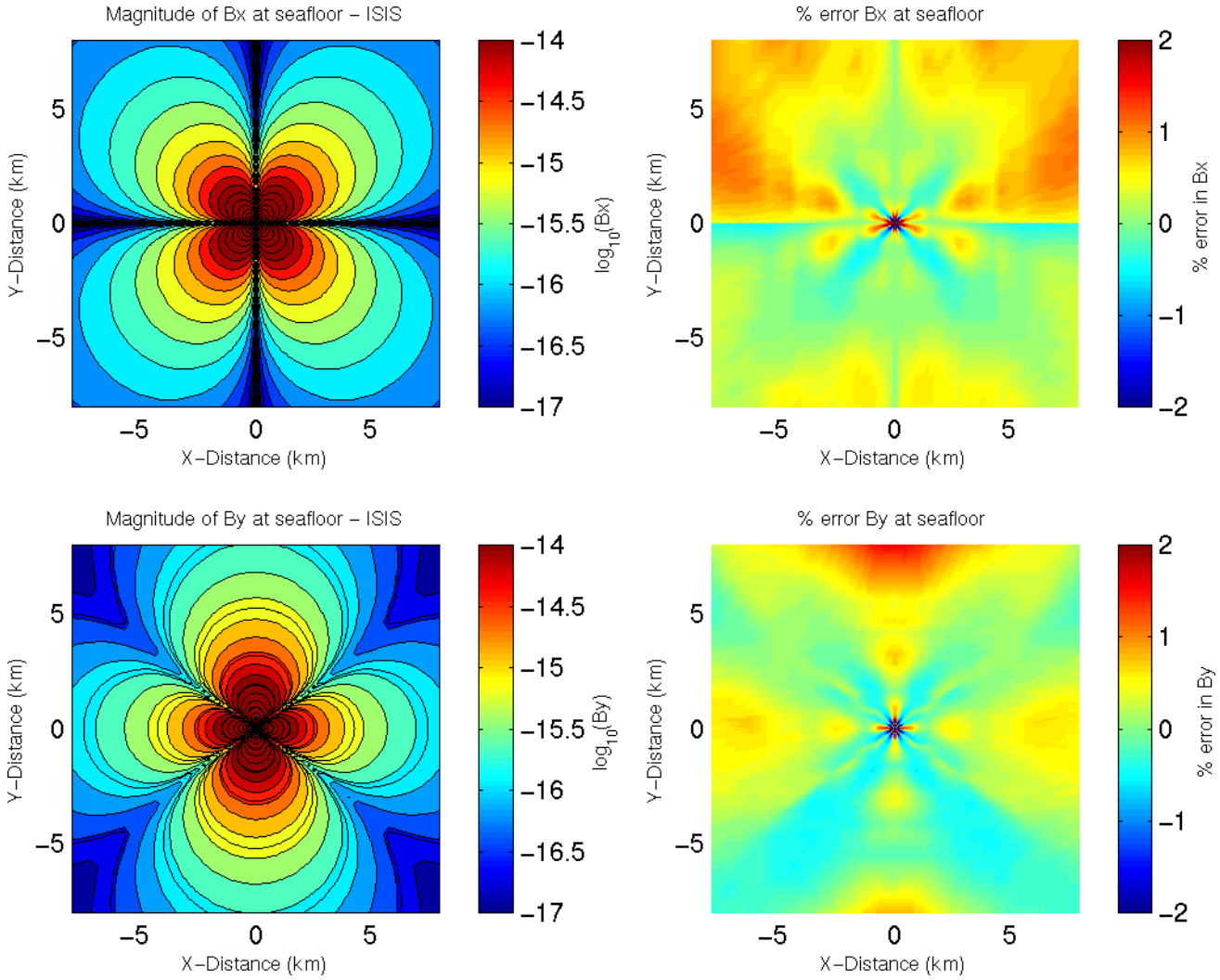

Figure 3.3(a). Comparison of the magnitude of the horizontal electromagnetic fields computed by ISIS with those calculated using the quasi-analytic code of Chave and Cox (1982) for the case of a 1-dimensional layered model, consisting of a 200 m thick, 2 Ωm layer, over a 1000m thick 10 Ωm layer, both overlying a 100 Ωm halfspace. The entire model is overlain by a uniform 0.3Ωm halfspace representing the ocean. The source is an x-directed horizontal electric dipole with a frequency of 0.25Hz, located at the origin, on the model seafloor. The parameterisation for ISIS is described in figure 3.2. The left hand panels show the magnetic fields at the seafloor (z=0 plane) as calculated by ISIS. The right hand panels show the percentage difference between the ISIS and quasi-analytic fields. The colour scale passes through ±0.5% at yellow and turquoise, respectively, and through ±1% at light red and light blue. The agreement is excellent with errors of 0.5% or better over most of the area.

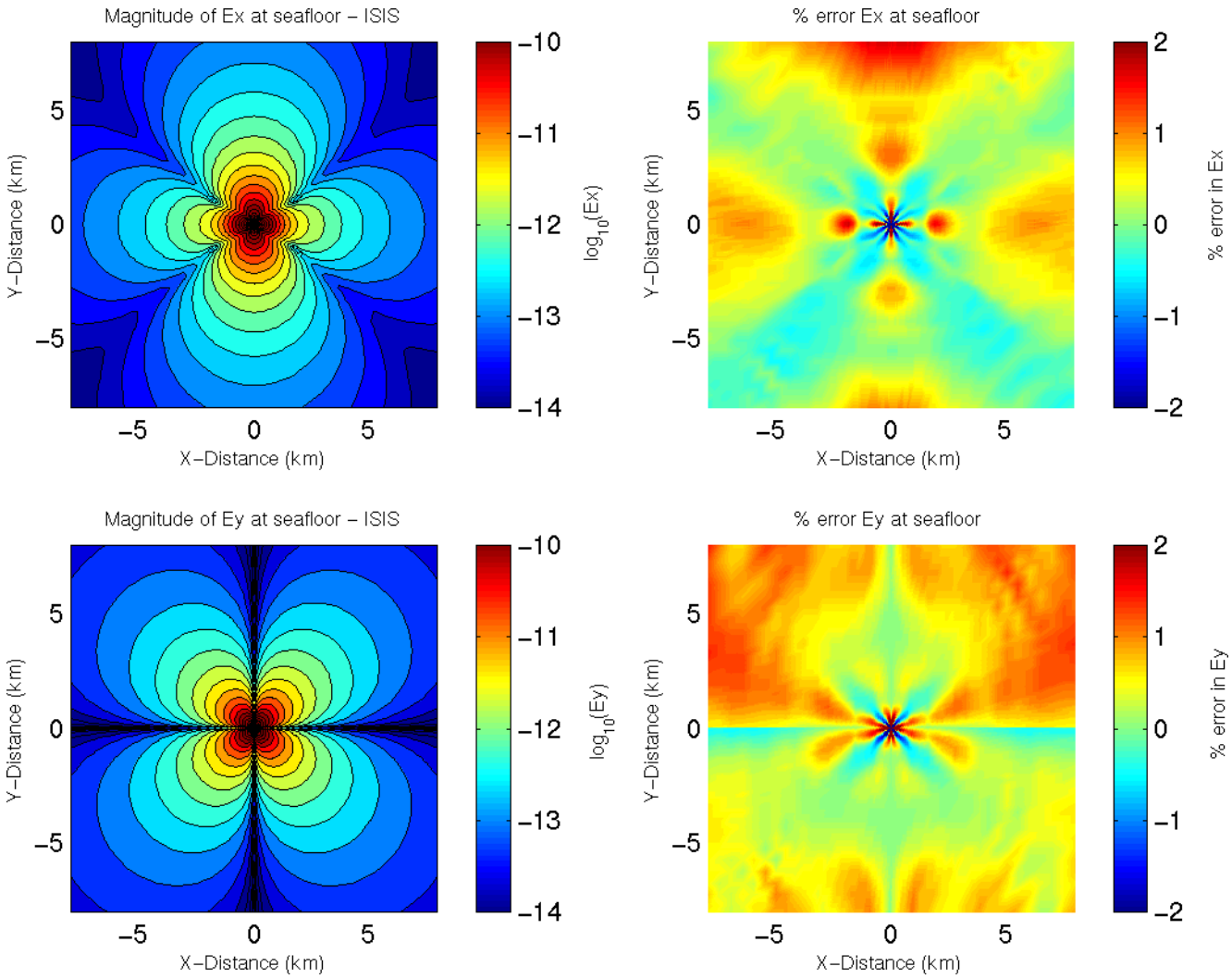

Figure 3.3(b). The corresponding comparison for the horizontal electric field at the seafloor. The agreement between the ISIS and quasi-analytic fields is again very good, though spots of relatively high error appear more prominently than for the magnetic field. Electric field components, inherently more difficult to compute due to the smoother nature of the magnetic field, and subject to additional numerical errors by their calculation from the computed magnetic field by means of the Ampere-Henry law, may require finer resolution for similar accuracy. For spatially averaged errors, see Table 3.1.

3.5 Intercomparison for a 2-D Earth

The effect of lateral variations in resistivity can be tested by examining 2-dimensional resistivity structures - those in which the resistivity varies vertically and in one direction horizontally. The response of a 2-dimensional resistivity structure to the 3-dimensional fields of a point horizontal electric dipole (known as a 2.5-dimensional problem) can be calculated using the finite element code of Unsworth *et al.* (1993), and compared to the fields calculated by ISIS. The finite difference grid is the same as in the previous intercomparison (c.f. figure 3.2). A cross section through the 2-dimensional model used for test purposes is shown in figure 3.4. It consists of a background layer over a halfspace model in which are embedded two long prisms, one more conductive and the other more resistive than the background.

Figure 3.5 compares the horizontal electric fields at the seafloor calculated by the 2.5D finite element code and the ISIS code. The electric fields are shown in preference to other components because these are measured in practice during a CSEM experiment, and because, since they are derived from the calculated magnetic fields, agreement for the electric field implies good agreement for the magnetic field from which it was derived. Results are shown for both a structure-parallel (figure 3.5a) and a structure-perpendicular (figure 3.5b) source dipole, along paths running above the conductive and resistive anomalies at distances of roughly 2 and 4 km away from the axis. In the former case (dipole parallel to structure) electric currents are driven predominantly along the 2D resistivity structure, whereas in the latter case (structure perpendicular dipole) currents across the lateral resistivity boundaries predominate. Apart from close to the source and at the domain edges (where neither code produces a very accurate result), agreement between ISIS and the finite element code is better than 2% in amplitude and phase.

3.6 Considerations of grid resolution, domain size, and convergence

In running the code, a number of choices need to be made. These include determining the numerical grid resolution and laying out the grid, fixing the boundaries of the computational domain, and setting the conjugate gradient convergence target and maximum number of iterations between divergence corrections. In practical use, where exact solutions are not known, it can be difficult to assess whether the numerical parameters are adequate to produce an accurate result. It is therefore important to explore the numerical behaviour of the code as the grid resolution, domain size and level of convergence are varied. The case of a dipole in a uniform wholespace presented earlier is used as an example. By using as simple an Earth structure as possible, inaccuracies inherent to the numerical parameters chosen can be isolated from issues of modelling particular structures.

The effect of varying the grid resolution within the central part of the grid has already been touched on in the context of figure 3.1b. To show the detailed behaviour more clearly, figure 3.6 shows the Ez field at the z=0 level, along the line y=25m, for two grids with same overall domain size, extending horizontally to 10km from the source, but different grid resolutions, one twice as fine in both the horizontal and vertical directions than the other. Over the majority of the domain (figure 3.6a) the agreement with the analytical fields is excellent (the sharp rise at the edge of the domain will be discussed later) demonstrating that both meshes adequately model the fields.

Very close to the source, however, the error in the calculated fields rises sharply. Doubling the near-source grid resolution (figure 3.6b) significantly narrows the zone of high error around the source. Continuing to increase the resolution in the central part of the computational domain does not, however, always result in improved solutions. Refining the central part of the grid too much relative to the outer regions can result in symptoms such as poor convergence and irregular, jagged field contours, particularly on the outer parts of the coordinate axes. This

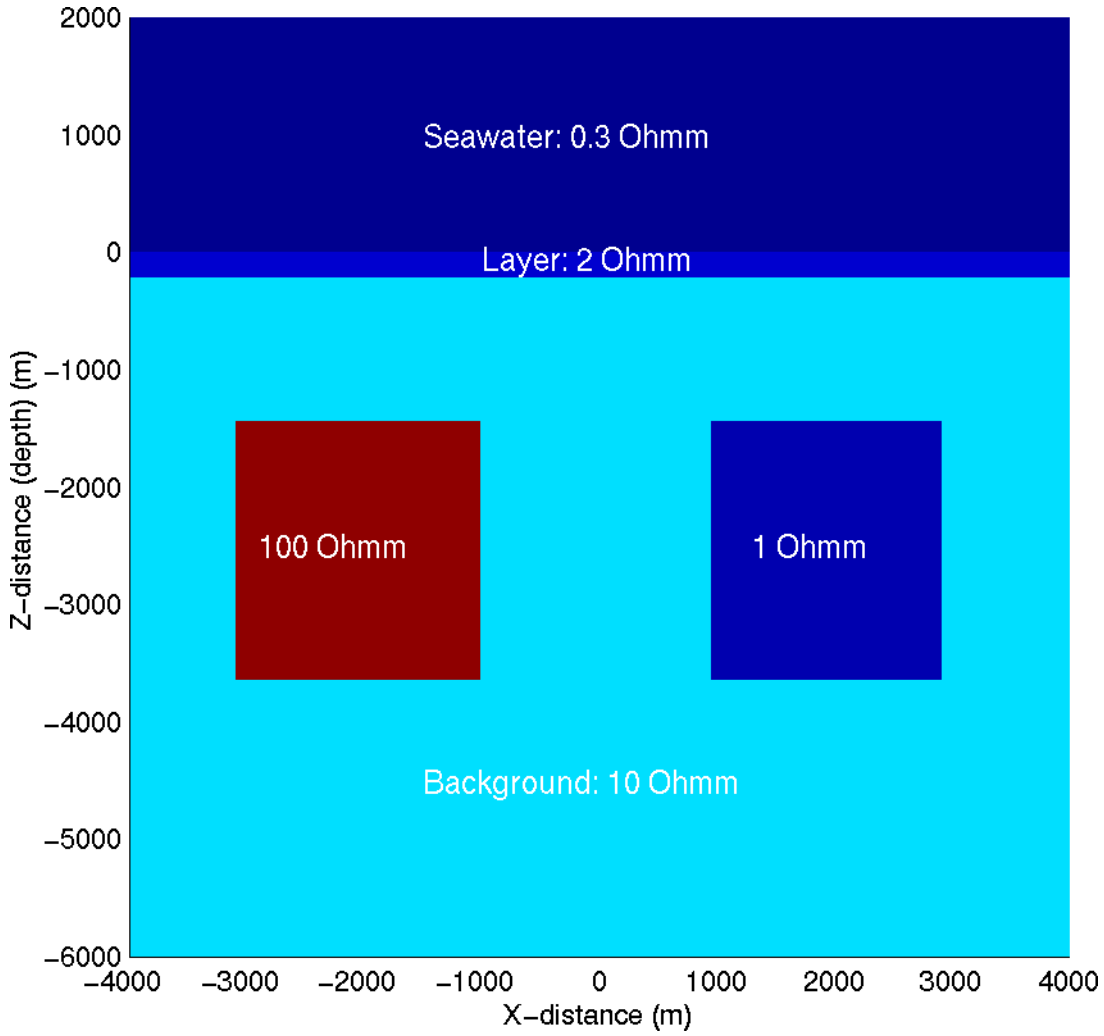

Figure 3.4. The resistivity structure used for inter-comparison of the 2d finite element code and ISIS, plotted with no vertical exaggeration. The structure is invariant perpendicular to the plane of the page. The horizontal electric dipole source is placed at the origin with its axis either along (y-directed) or across (x-directed) the strike of the 2d structure. Resistivities were chosen to be representative of the range found in the upper few km of the oceanic crust.

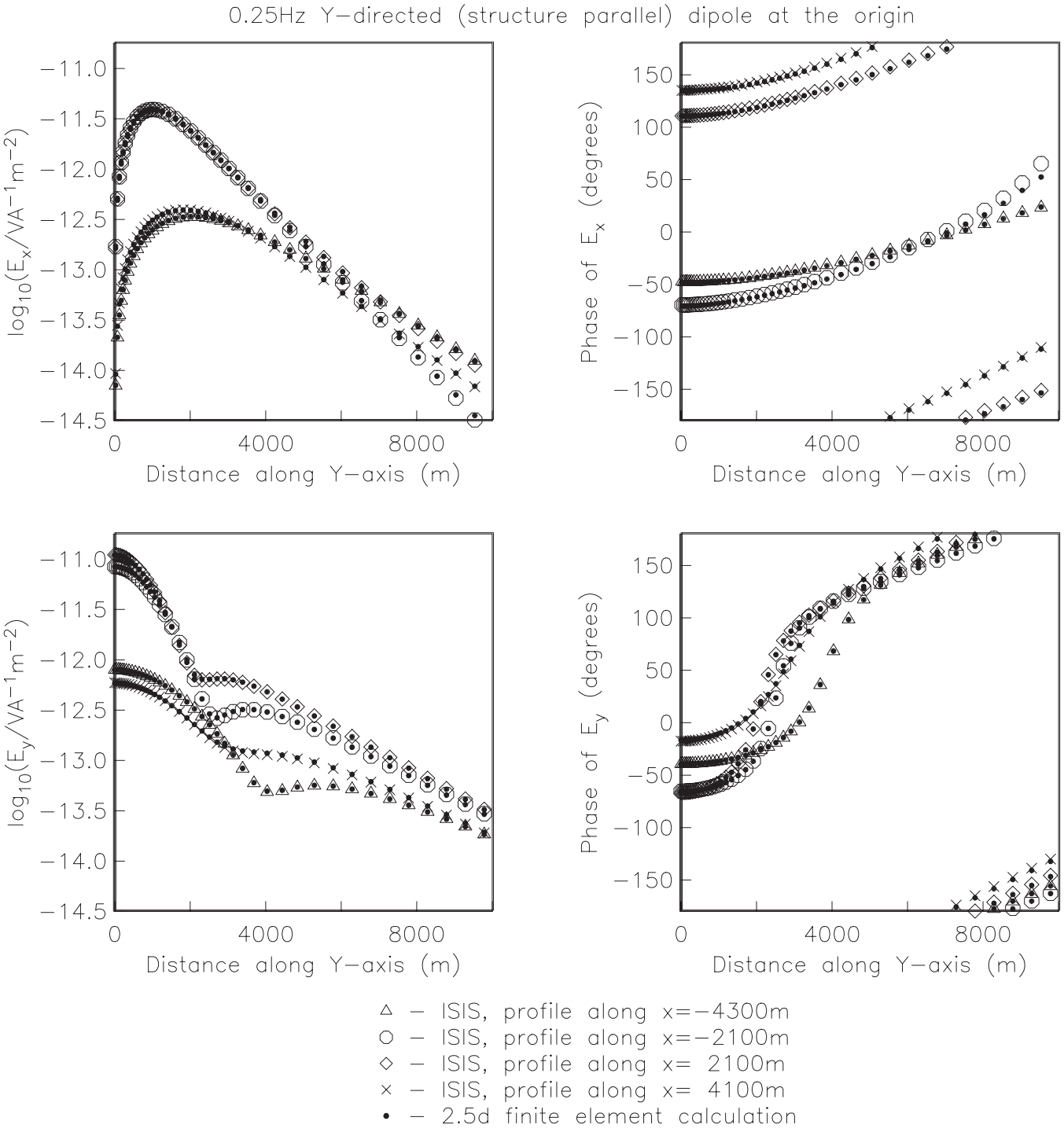

Figure 3.5(a). Comparison of the amplitude and phase of the fields computed by ISIS from the model shown in figure 3.4 (symbols), with those calculated using the 2.5D finite element code of Unsworth et.al. (1993) (solid circles). The case of a y-directed (structure parallel) horizontal electric dipole at the origin, with frequency 0.25 Hz. The amplitude and phase of the E_y (dipole parallel) and E_x (dipole perpendicular) fields are shown in the lower and upper panels respectively, for profiles parallel to the y-axis at x=-4300 m and x=-2100 m (above the resistive anomaly), and x=2100 m and 4100 m (above the conductive anomaly).

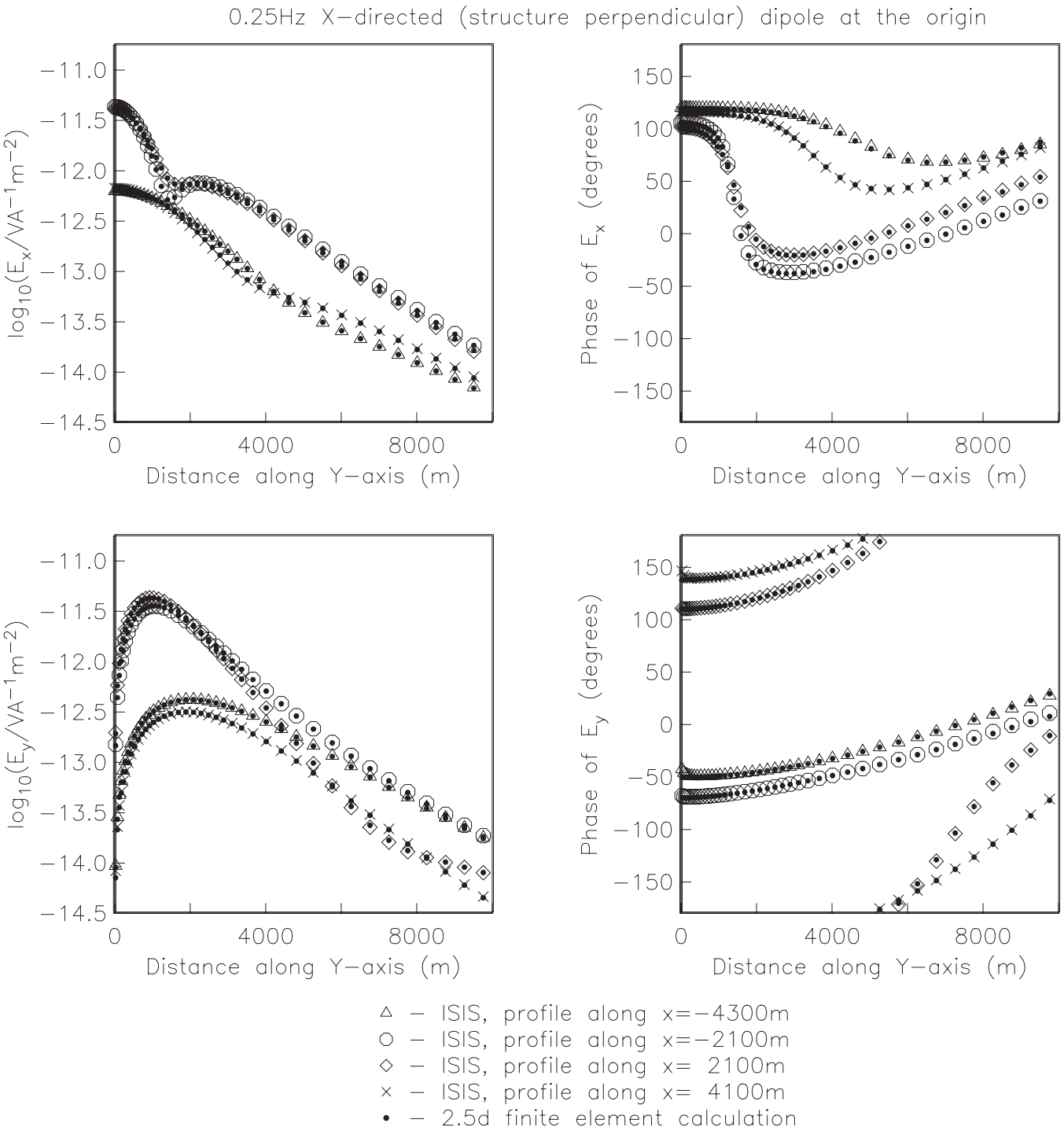

Figure 3.5(b). The corresponding comparison for the case of a x-directed (structure perpendicular) horizontal electric dipole. The amplitude and phase of the E_x (dipole parallel) and E_y (dipole perpendicular) fields are shown in the lower and upper panels respectively. Profiles located as in (a).

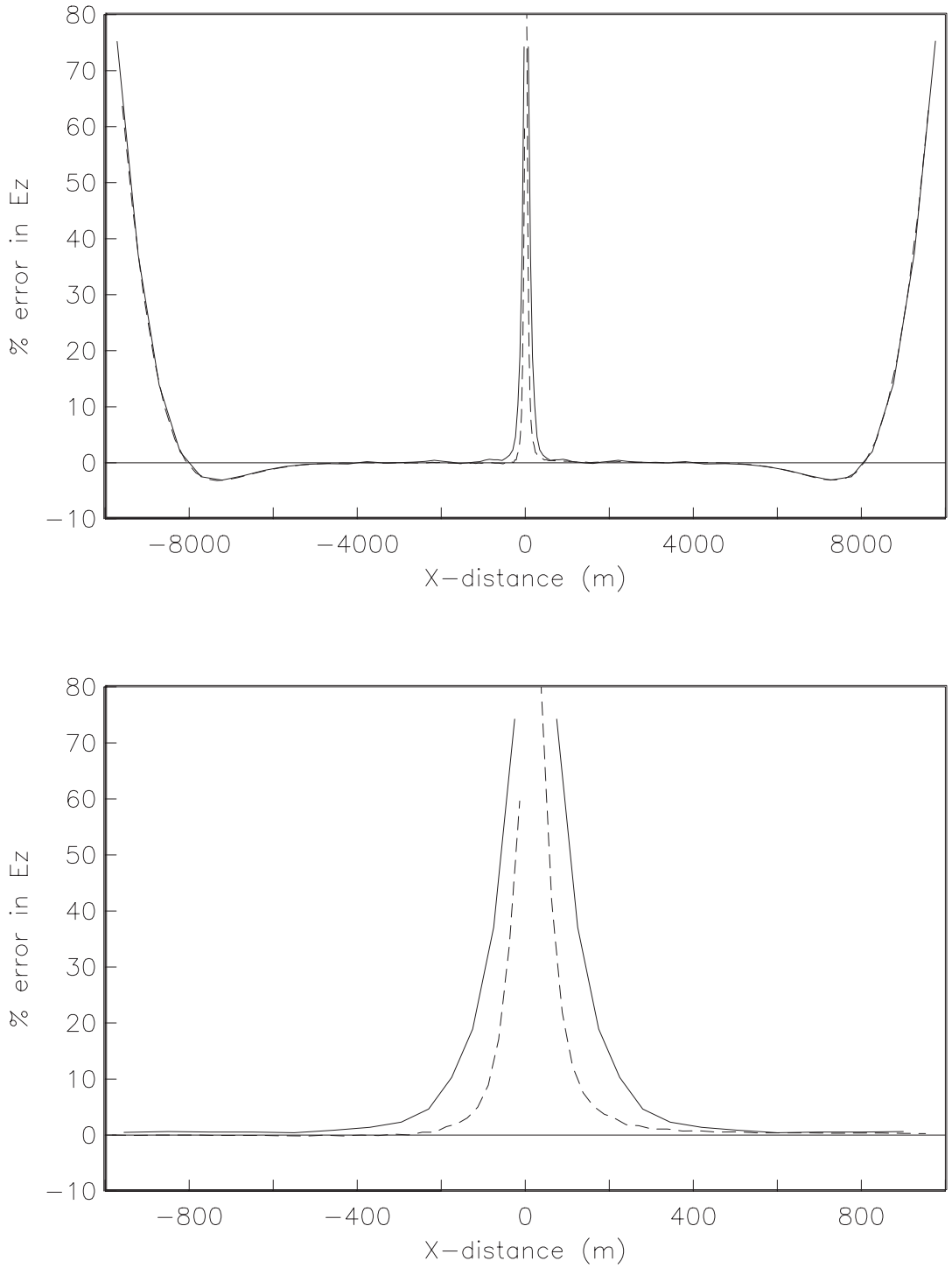

Figure 3.6. Illustration of the effect of grid resolution on the result. Shown is the percentage error in E_z relative to the analytical result for the vertical 5 Hz dipole in a uniform space of resistivity 100 Ωm, along the line y=25 m in the z=0 plane (very nearly through the source). In each case the domain extends 10 km from the source in all directions. Solid - 75x75x75 grid. The central region containing the source has dimensions 50x50x0.5m. Cell dimensions increase gradually to 500x500x500 m over the major part of the domain. Dashed - 149x149x121 grid, with about twice the resolution of the previous one. In this case the central region is 25x25x0.25 m, increasing gradually to 250x250x250 m cells over the majority of the domain. The upper panel illustrates the percentage error in the calculated fields over the full domain. The lower panel shows the central portion around the source in more detail. See text for discussion.

type of behaviour is characteristic of grids where grid cells on the outer reaches of the coordinate axes become extremely elongated, with aspect ratios of 100:1 or more. In fact, any discretised method will have trouble representing the geometric singularity of CSEM fields very near their sources. Many CSEM codes deal with this by splitting the field into a 'primary' field calculated for a simple background model (usually a whole or halfspace), and a 'secondary' field calculated using the difference between the structure of interest and the primary structure. When an appropriate background structure is known, this has the great advantage of reducing the resolution required near the source. With the extensions already implemented in the ISIS code, such a separation would be relatively easy to implement. For CSEM in complicated geography, however, it may not be clear what background model should be used to compute the primary field. Alumbaugh *et al.* (1996), for instance, quote an example of a calculation where use of the wrong background assumption threw off their calculation by an order of magnitude. It is even less clear that such a decomposition would be useful for the distributed fields induced by oceanic motions. For these reasons, and for reasons of simplicity, we have preferred to keep the code as general as possible and avoid a primary/secondary decomposition. In the practical situations where we expect to use the code, the error close to the source does not present too much of problem. Data collected when the source is very close to the receiver are generally affected by amplifier clipping, and are much more affected by errors in the source receiver geometry, meaning that in practical data interpretation, only those data recorded when the source is further than a few hundred metres from the receiver are included in the analysis.

Apart from the absolute resolution, the way grid cell sizes are graduated has a very significant effect on accuracy of the solutions. Figure 3.7 shows the effect of variations in the horizontal gridding gradation. The curve with the lowest errors (solid) illustrates the results when the horizontal size of adjacent cells varies by no more than a factor of 1.25. The curve showing the greatest and most fluctuating errors has piecewise constant grid cell size, with a jump by a factor four at x=+-800m and +-3600m. Also shown are the results for changes of a factor of two and three. Clearly the effect of a jump in cell size is to introduce errors into the calculated fields, and these errors increase the more extreme the change in cell size becomes. Based on this experience, and other models we have run, we believe that gradation in cell size should be kept less than a factor 2 if at all possible. This is a somewhat more restrictive recommendation than the one given in Mackie's discussion of the original code. It is reasonable, however, that care would be needed. For an evenly spaced grid, the model is in effect dealing with central differences, accurate to second order in the grid spacing. As the grid cell size varies more and more sharply, however, the differences become more and more non-central, resulting in greater numerical errors.

Upon approach to the domain boundary, the computed fields begin to disagree strongly with the analytical uniform-space solution. Figure 3.8a shows the percentage error in Ez along the line y=25m through the source for meshes which extend 10 km, 8 km, 6 km and 4 km in the x, y and z directions from the source (the grid resolution is the same in each case). The effect of the boundary is very consistently confined to the region adjacent to the boundary. As the domain is shrunk in steps of 2 km, the point at which the boundary effect begins to be noticeable moves closer to the source. For the case shown the error falls to less than 5% at approximately 2 km from the edge of the mesh. Figure 3.8b shows the effect of domain size at two different frequencies, 5 Hz and 2 Hz. The effect of the boundary extends further into the domain at 2Hz, because at the lower frequency, where the electromagnetic skin depth is longer, fields generated by an imperfect boundary condition do not decay as rapidly as they diffuse from the boundary back into the interior of the domain. The error caused by the boundary falls to below 5% at about 2km from the edge for the 5Hz case, and approximately 3 km in the 2Hz case. The electromagnetic skin depth is 2.2 5km at 5 Hz and 3.6 km at 2Hz. As a practical rule of thumb therefore, the computational domain should be extended at least 1.5 to 2 skin depths beyond the region where the fields need to be computed reliably.

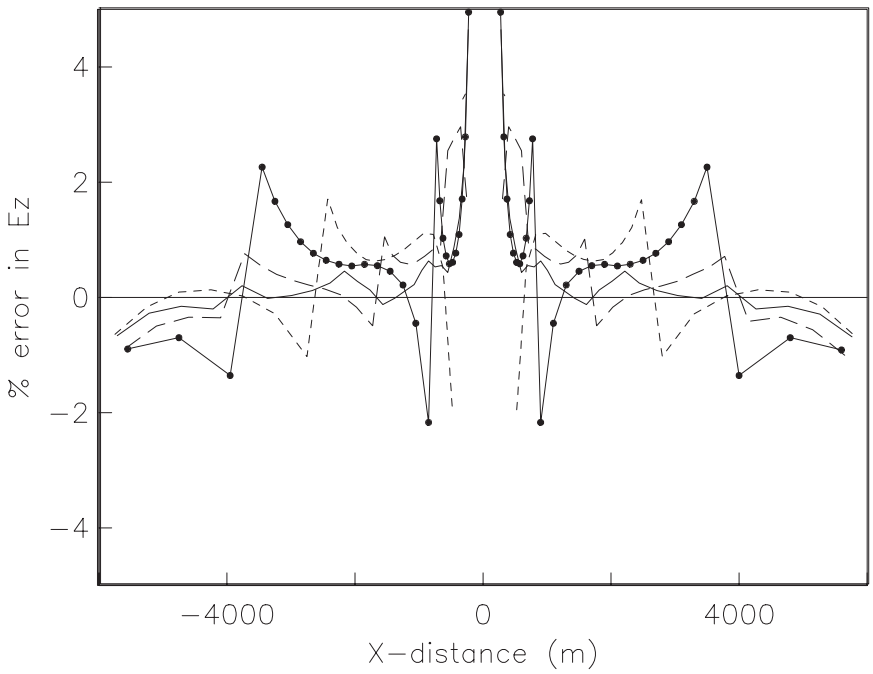

Figure 3.7. Illustration of the effect of grid cell graduation on the accuracy of the solution for the dipole-in-a-uniform-space problem. In all cases the computational domain extends ±10 km from the source in the x, y and z direction, and is parameterised into a 75x75x75 grid of cells. Solid line (smallest errors): results for a mesh where the horizontal size of adjacent cells varies by no more than a factor of 1.25. Long dashed line: A factor of 2 jump in the size of adjacent cells occurs at x=±200 m, ±1600 m and ±3550 m. Short dashed line: A factor of 3 change in grid cell size occurs at x=+-450 m and 2550m. Line with dots: the horizontal cell size is piecewise constant, a factor of 4 change in grid cell size occurring at x=±800 m and ±3600 m. It is clear that a jump in grid cell size produces an error in the calculated field, and that this error increases the larger the change.

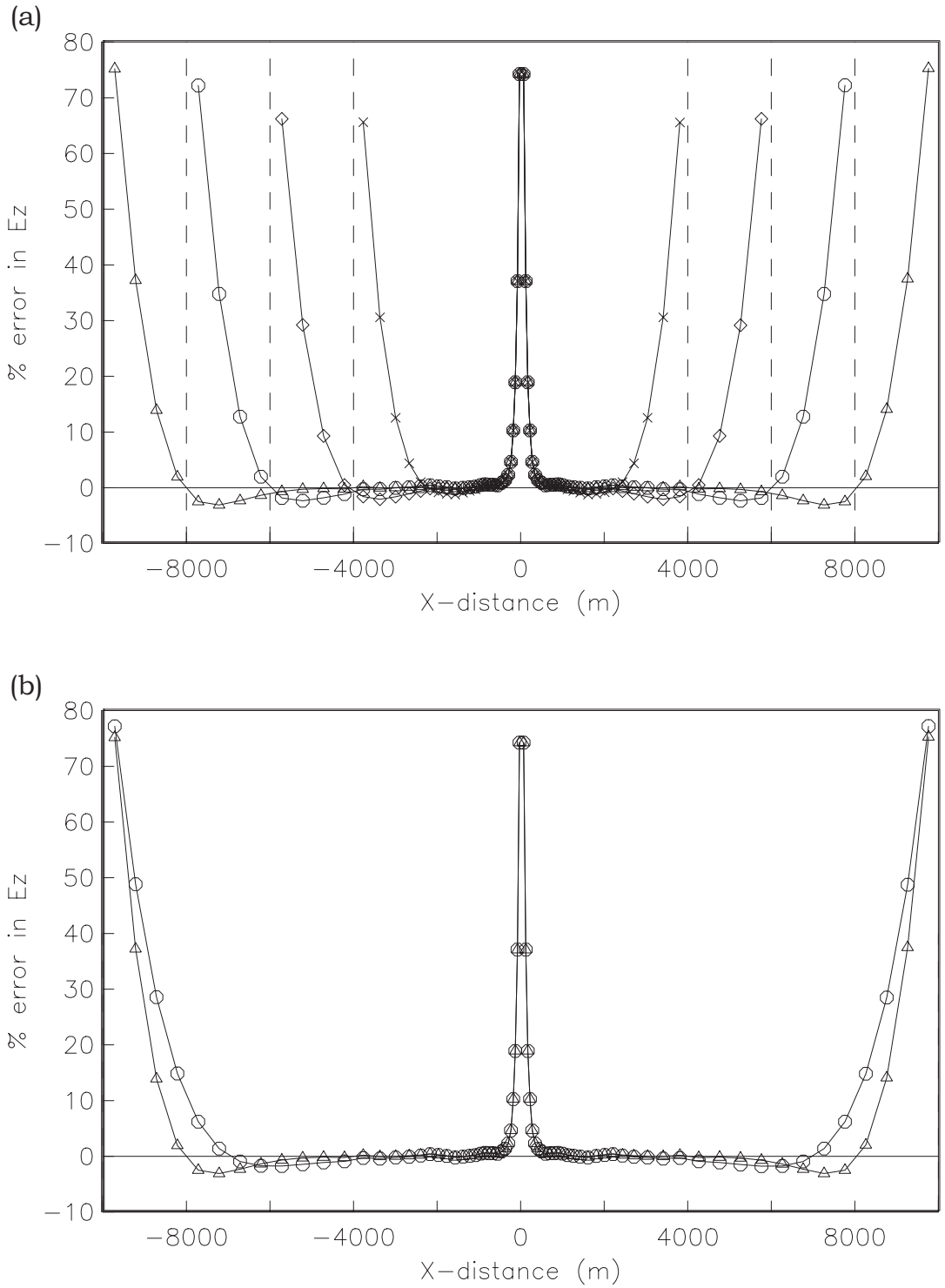

Figure 3.8. (a) The effect of domain size on the computed fields. The percentage error in E_z in the z=0 plane, along the line y=25 m is plotted to highlight the effect of the boundaries. The source is a 5 Hz vertical dipole at the origin of a 100 Ωm wholespace. The domains extend 10 km (triangles), 8 km (circles), 6 km (diamonds) and 4 km (crosses) from the source. In each case the mesh resolution is the same, and equal to the more coarse resolution described in figure 3.6. The boundary condition applied is a Dirichlet condition on the magnetic field, B parallel = 0. See text for discussion. (b) The effect of a domain boundary at 10km for two different frequencies: 5 Hz (triangles) and 2 Hz (circles).

For a different view of where the boundary affects the solution, figure 3.9 shows the non-zero field components in a vertical plane (x=0), for a model where the domain boundaries have been placed at approximately 10 km from the source in the horizontal direction, and at 7 km in the vertical. In the central region the modelled response is unaffected by the boundary condition, the fields agreeing to closer than 1% with the analytical solution. The region affected by the boundary condition is very cleanly confined to the region adjacent to the boundary.

In addition to varying the domain size, figure 3.10 shows the effect of varying the boundary condition itself. Instead of applying B parallel at 8 km, this figure shows the effect of applying a 'boundary buffer' zone between 8 km and 10 km from the source, with a conductivity equal to that of seawater. Although the overall effect on the accuracy of the solution is small, the effect of the two boundary conditions is in opposite directions. Thus, in cases where it is not practicable to increase the domain size until the user is reasonably certain that the boundaries are distant enough not to affect the region of interest, it may be useful to run a similar-sized model twice, with and without a conductive buffer zone. Where the two solutions begin to differ provides a practical indication of the region where the boundary condition may be assumed to be irrelevant.

Whilst it is impossible to provide rules which will cover all the possible situations that might be encountered in modelling the real Earth, the results of the tests performed above can be summarized to provide guidelines for the use of ISIS in the CSEM case. The computation domain should extend at least 1.5 to 2 skin depth beyond the point at which the fields need to be accurately computed to avoid boundary effects contaminating the result. The ratio of adjacent cell sizes should be no greater than two, and approximately 4 cells per skin depth are required over the bulk of the computational domain with a finer parameterisation close to the source to accurately model the rapid variation of the fields in this region. If the cell aspect ratio becomes large (greater than about 100:1) then the code can fail to converge and may produce inaccurate results. The inaccuracies may be more or less confined to the region of extremely elongated cells, or may contaminate the whole of the domain. These guidelines are based on empirical observation of the numerical behaviour of ISIS in a number of circumstances, nevertheless they provide a practical guide to obtaining accurate results.

3.7 An example of fields in a 3-D Earth

For an example of fields in a 3-dimensional earth model, a simple 3-dimensional structure was loosely based on a set of preliminary 1-dimensional analyses of the Lucky Strike data (figure 3.11). The source is a 1 Hz x-directed dipole located at the origin. Figure 3.12 shows (left hand panels) a view from above of the magnitude of Ex (the source parallel field) at the seabed. Over the majority of the region the effect of the 3-dimensional structure is small. Close to the conductive anomaly, however, the field strength is reduced significantly.

For a view of how the code handles the interaction of the CSEM field with the 3-dimensional structure, figure 3.13 shows a view of Ex in two orthogonal vertical planes through the structure (the location of the planes is indicated in figure 3.12). To make it easier to identify the specific effect of the 3D structure, we first show, in figure 3.13a, the corresponding result for a homogeneous halfspace. On the plane that lies closer to the source (the plane x=2915m), the sub-seafloor field has two maxima: the upper hugging the seabed (e.g. discussion of interface waves in Wait, 1981; Flosadottir, 1990), and a broader, deeper maximum. On the orthogonal and more distant plane (y=-4190m), only one maximum is seen. Figure 3.13b shows how the fields are distorted by the presence of the 3D structure. Also illustrated by figure 3.13b is the appropriately discontinuous behaviour of Ex at the vertical conductivity contrasts in the lower panel, where Ex is normal, and continuity of Ex across the contrasts in the upper panels, where it is tangential to the contrasts. Experimentation with varying the grid resolution indicates that where the very fine structure of the source field hits the near corner of the structure, grid resolution

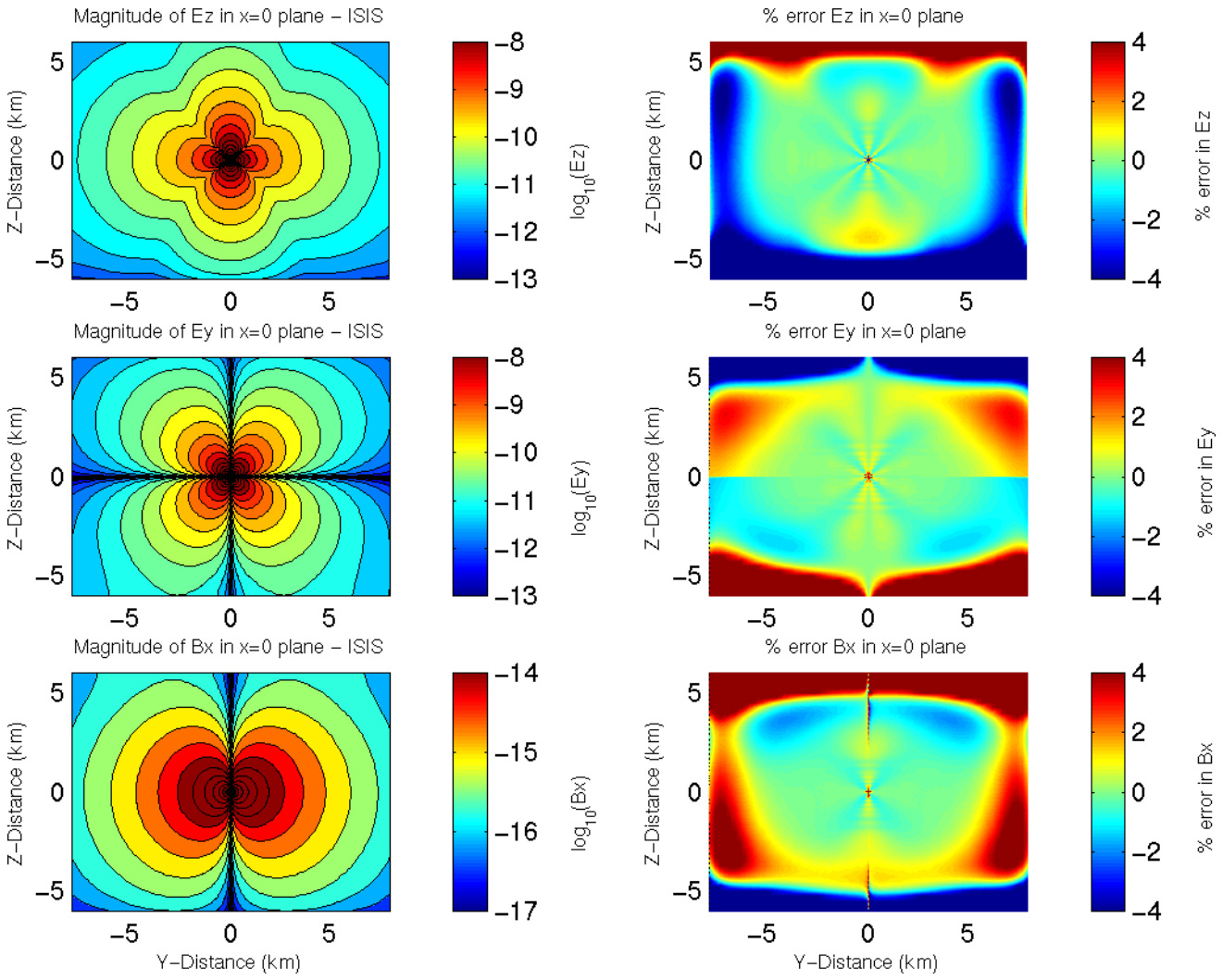

Figure 3.9. Same as figure 3.1b, with double the resolution, and with boundary conditions applied at ±10 km in the horizontal, and 7 km in the vertical. The colour scale saturates at the colour bar extremes, so that the darkest red and blue represent off-scale values (cf. also following figure). The near-source error spike is visible as a central dot (greatly reduced in extent from the coarser-grid calculation of figure 3.1b). The side and top boundary conditions are Dirichlet conditions on the appropriate magnetic field components. The bottom condition is as in the original code.

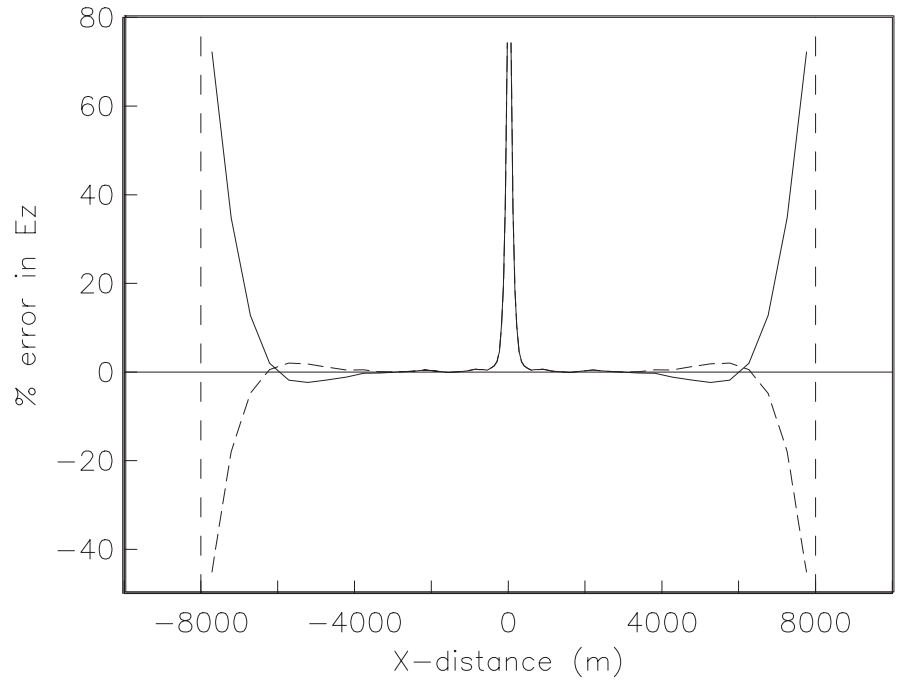

Figure 3.10. The effect of applying a boundary buffer zone. The percentage error in E_z in the z=0 plane, along the line y=25 m is plotted as before, for the mesh extending 8 km from the source in the x, y and z directions described in the caption to figure 3.8. Solid: the boundary condition is a Dirichlet condition on the magnetic field at the boundary as before. Dashed: The mesh is surrounded by a 2km wide buffer zone with the resistivity of seawater. This changes the effective boundary condition at the grid edge to E parallel =0. The error in this case is negative because E_z, tangential to the boundary, is being driven toward zero by the conductive buffer zone. See text for further discussion.

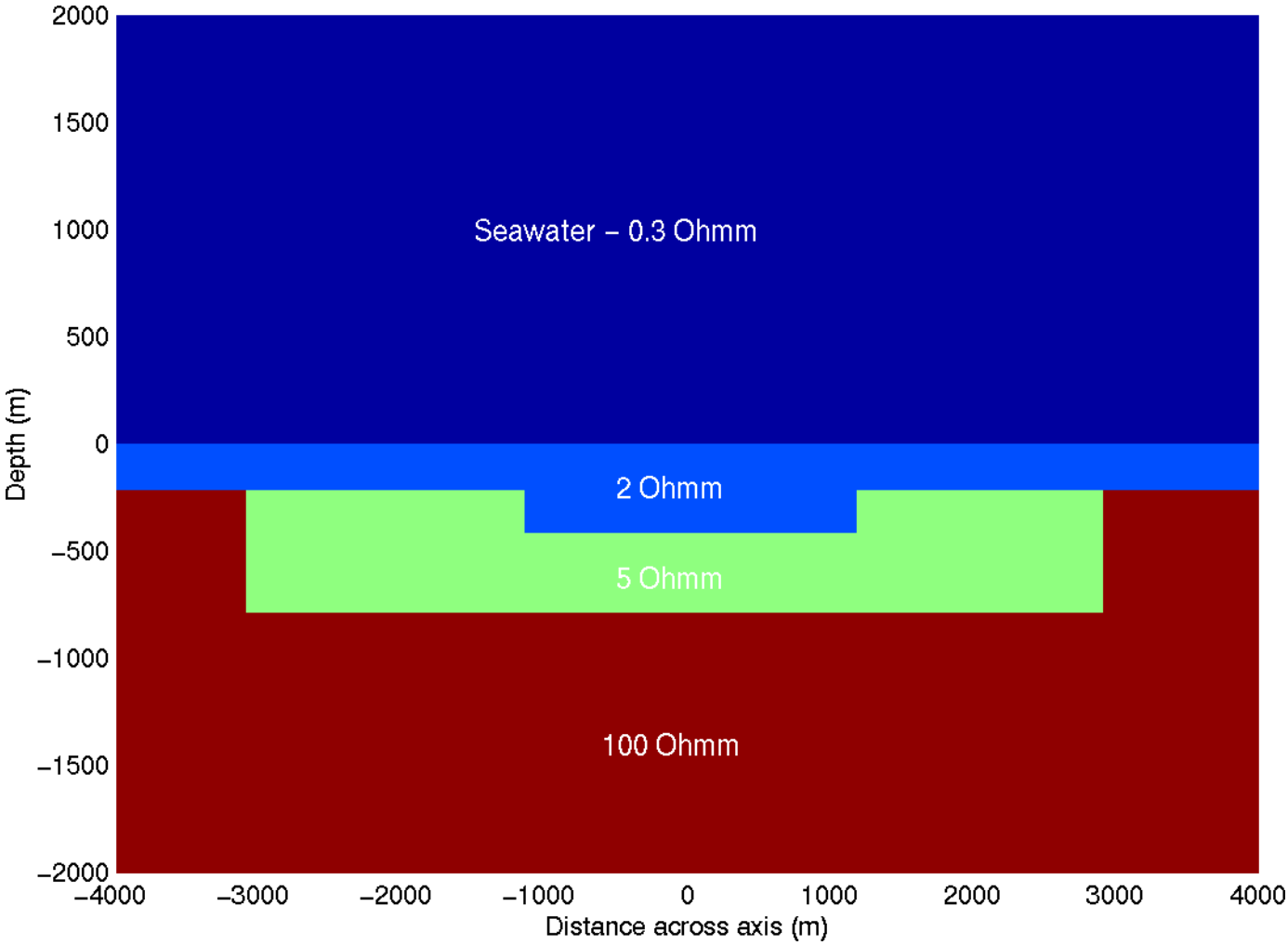

Figure 3.11. A simple 3-dimensional structure. The background model is a 216 m thick, 1 Ωm layer over a 100 Ωm halfspace. Embedded in this is a 5 Ωm zone, surrounding a smaller 2 Ωm zone. A vertical plane through the structure is shown. The structure is the same in the orthogonal plane.

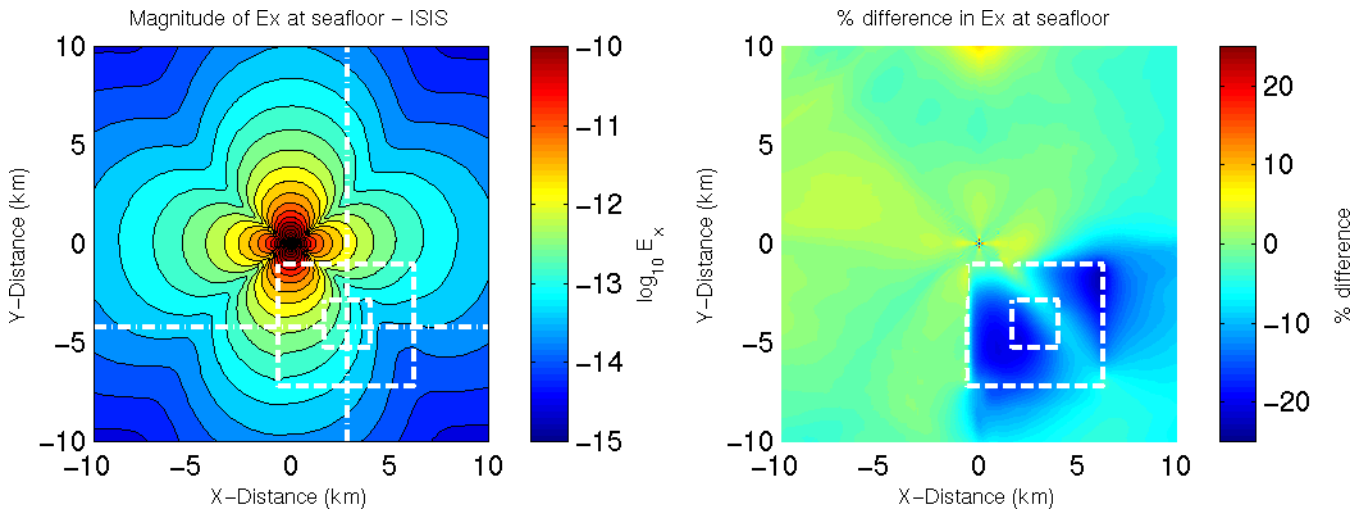

Figure 3.12. Left panel: The magnitude of the source parallel field (E_x) at the seafloor. The source is a 1 Hz horizontal electric dipole at the origin, oriented along the x-axis, and the parameterisation is the same as in figure 3.2. The outline of the 3-dimensional structure (5 Ωm with an interior 2 Ωm zone) is shown by the dashed lines. The dot-dashed lines give the position of the two vertical sections to be shown in figure 3.13. Right panel: The percentage difference in E_x between the response of the 3D model and the background 1D model. Over the majority of the area shown the effect of the 3-dimensional structure is small. In the region of the conductive anomaly, however, the field strength is reduced significantly. The diagonal streak of lighter colour across the anomalous region reflects the zero-crossing of this field component.

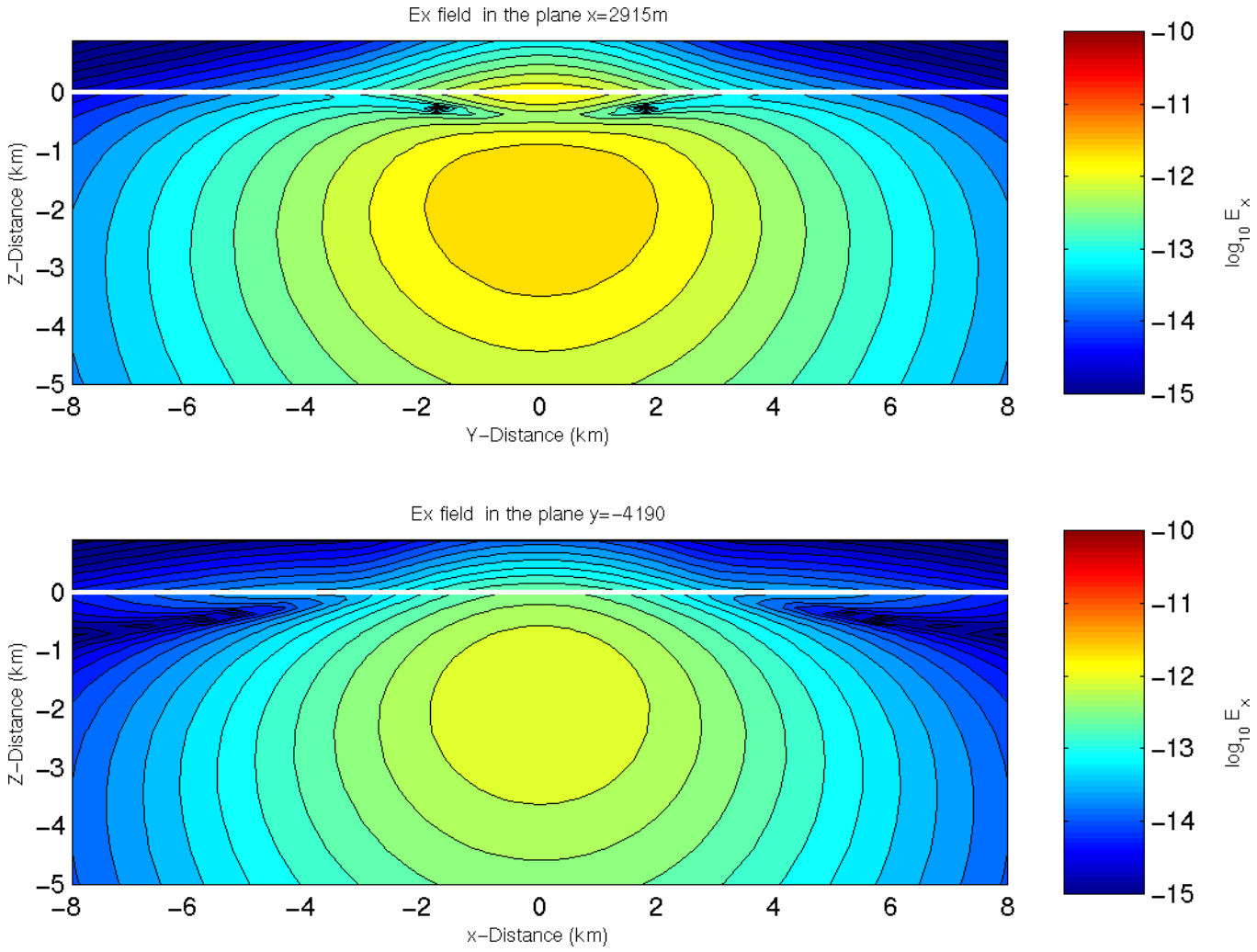

Figure 3.13(a). Magnitude of E_x in orthogonal vertical planes through a homogeneous halfspace model of the background conductivity (100 Ωm). The location of the planes and the colour scale are the same as in figure 3.12. Upper panel: plane x=2915 m, for which the source is perpendicular to the plane of the page. Lower panel: plane y= -4190 m, for which the source is parallel to the plane of the page. The seabed is indicated by a solid white line.

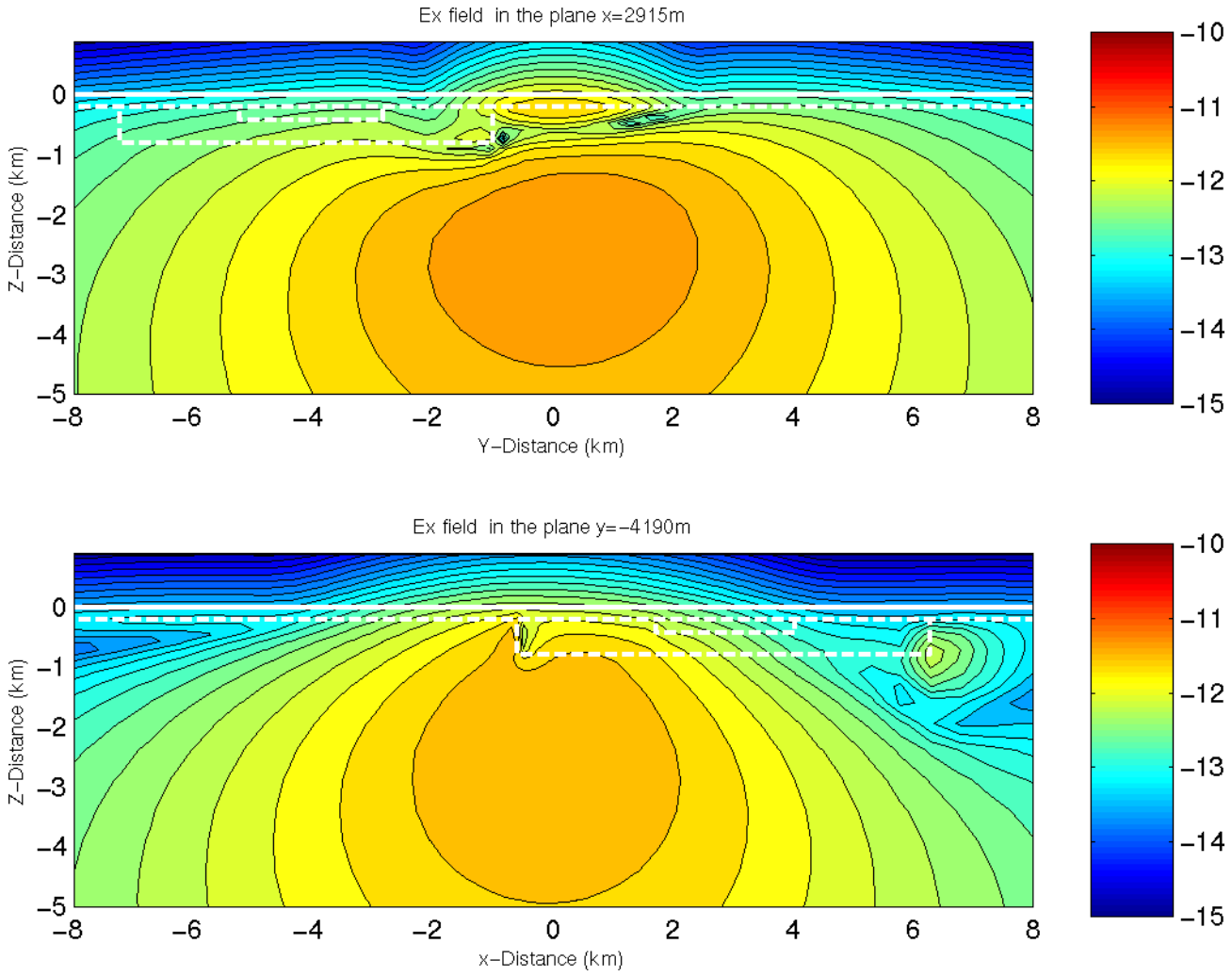

Figure 3.13(b). The same for the 3-dimensional structure. Dashed white lines indicate the outline of the structure.

affects the local detail to some extent, but the features seen in figure 3.13b are reasonably well resolved.

To highlight the effect of the anomalous subsurface structure on the seafloor horizontal electric field, figure 3.14 shows the magnitude of the semi-major axis of the polarization ellipse (PE) at the seafloor, normalized by the corresponding value for the 1D background model. This presentation eliminates some of the complexity of the individual vector component's spatial patterns, and can be a useful way of looking at experimental data since the polarization ellipse is less affected be geometric uncertainties than the separate field components (Constable and Cox, 1996). The effect of the 3-dimensional structure is small over most of the area. It stands out very clearly, however, in the region more or less directly above the conductive anomaly.

3.8 Summary

We have modified and extended the finite difference magnetotelluric modelling code of Mackie *et al.* (1993,1994), so that it can be used to calculate the electric and magnetic fields of an arbitrary distribution of electric current sources embedded in a 3-dimensional resistivity structure. The new ISIS (Induction Sources In the Sea) code will be used in the analysis of electromagnetic data collected using controlled sources in the ocean, to examine oceanographic signals generated by basin scale movements of water masses through the geomagnetic field, and to study tidally generated electromagnetic signals both in the ocean and on land.

In this paper, we have concentrated on tests of the code and illustrations of its performance for the CSEM problem with an electric dipole source. Comparisons with analytical and independent numerical models demonstrate close agreement in both magnitude and phase for earth models that exhibit both horizontal and vertical conductivity contrasts, and where electric currents are driven along and across contrasts. As is the case with any numerical modelling code, the choice of parameters used to describe the model and control the solution is important to ensure an accurate answer is obtained. The influence of the grid resolution, layout, computational domain size and boundary conditions applied at the edges of this domain have been examined to obtain a set of empirical guidelines for the use of the code.

One of the first uses of the ISIS code will be in the analysis of a CSEM dataset collected at the Lucky Strike segment of the Mid-Atlantic Ridge. An illustration of the use of the code for a simplified representation of the type of structure likely to be encountered indicates very promising resolution of underlying 3-dimensional resistivity structure associated with volcanic and hydrothermal processes. The results of the CSEM experiment performed will be presented in future papers.

3.9 Acknowledgments

For permission to build on their codes, and for many helpful discussions, we thank R.L. Mackie, J.R. Booker, J.T. Smith. A.D. Chave and M. Unsworth are thanked for the use of their 1-D and 2D codes, respectively. A.F. thanks Bjorn Erlingsson and Bjorn R. Bjornsson of Halo Inc., Reykjavik, for their encouragement of the initial idea for this work, and for their support during the course of it. She also thanks the University of Washington and NOAA PMEL's Joint Institute for Studies of the Atmosphere and Ocean for support under NOAA Cooperative Agreement #NA67RJO155. This is JISAO contribution #846 and PMEL contribution #2364. LMM was supported by a research Fellowship from Downing College, Cambridge, and a Leverhulme trust Special Research Fellowship. We thank Prof. Adam Schultz for use of the Enigma high performance computing facility in the early phase of our work. The work was supported by the European Union under MAST III project ISO-3D (Contract number MAS3-CT97-0120).

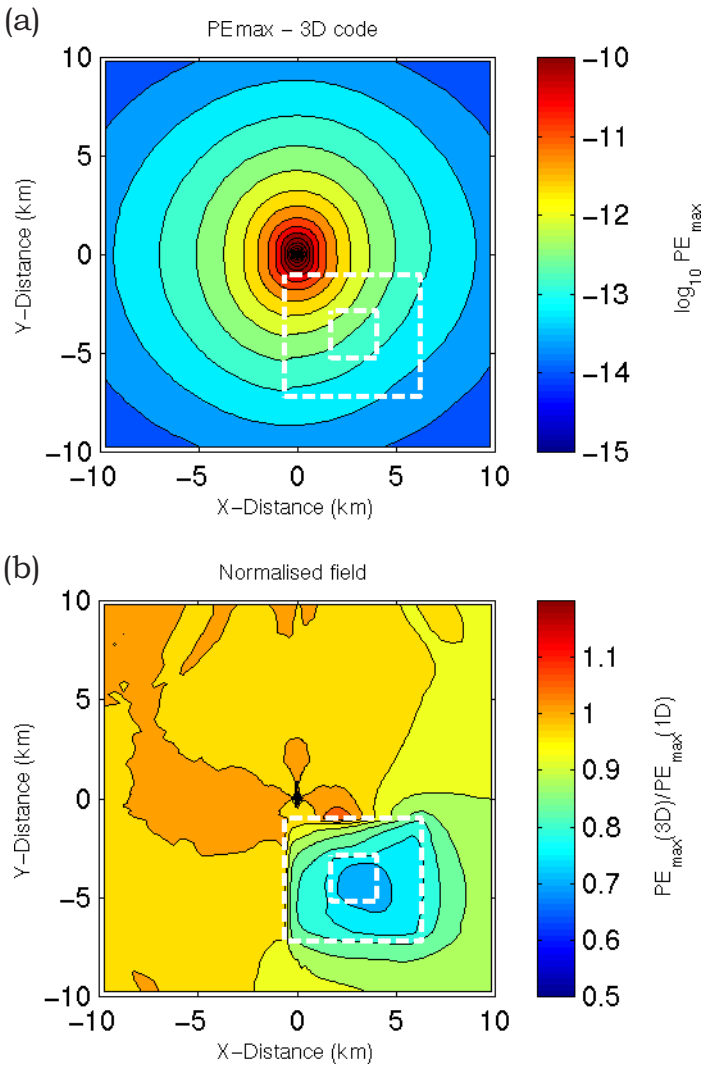

Figure 3.14. (a) The electric field strength at the seafloor, plotted as the semi-major axis of the polarization ellipse (computed after first interpolating the E_x and E_y components from their natural grid positions to a common grid). All parameters as in figures 3.11 and 3.13. The effect of the conductive 3-dimensional structure is to cause a slight 'bowing back' of the contours towards the source. (b) Ratio of the electric field strength at the seafloor (as represented by the semi-major axis of the polarisation ellipse) for the 3D model and the layer-over-a-halfspace background model.

3.10 References

Alumbaugh, D.L., G.A. Newman, L. Prevost, and J.N. Shahid, 1996. Three-dimensional wideband electromagnetic modeling on massively parallel computers, *Radio Science, 31, 1-23*

Avdeev, D.B., A.V. Kuvshinov, O.V. Pankratov, and G.A. Newman, 1997. High-performance three-dimensional electromagnetic modelling using modified Neumann series. Wide-band numerical solution and examples, *J. Geomag. Geoelectr., 49, 1519-1539*

Badea, E.A., M.E. Everett, G.A. Newman, and O. Biro, 2001. Finite-element analysis of controlled-source electromagnetic induction using Coulomb-gauged potentials, *Geophysics, 66, 786-799*

Baringer, M.O. and J.C. Larsen, 2001. Sixteen years of Florida Current Transport, *Geophys. Res. Letts., in press*

Cairns GW, Evans RL and Edwards RN, 1996. A time domain electromagnetic survey of the TAG hydrothermal mound, *Geophys. Res. Lett., 23, 3455-3458*

Chave, A.D., 1983. Numerical integration of Hankel transforms by quadrature and continued fraction expansion, *Geophysics, 48, 1671-1686*

Chave, A.D., D.S. Luther and J.H. Filloux, 1997. Observations of the boundary current system at 26.5 N in the subtropical North Atlantic Ocean, *J. Phys. Oceanogr., 27, 1827-1848*

Chave, A.D., and C.S. Cox, 1982. Controlled electromagnetic sources for measuring electrical conductivity beneath the oceans, 1: Forward problem and model study, *J. Geophys. Res., 87, 5327-5338*

Constable, S.C. and Cox, C.S., 1996. Marine controlled source electromagnetic sounding II: The PEGASUS experiment, *J. Geophys. Res., 101, 5519-5530*

Druskin, V., and L. Knizhnerman, 1994. Spectral approach to solving three-dimensional Maxwell's diffusion equations in the time and frequency domains, *Radio Science, 29, 937-953*

Evans, R.L., Sinha, M.C., Constable, S.C. and Unsworth, M.J., 1994. On the electrical nature of the axial melt zone at 13°N on the East Pacific Rise, *J. Geophys Res., 99, 577-588*

Flosadottir, A.H., J.C. Larsen and J.T. Smith, 1997a. Motional Induction in North Atlantic Circulation Models, *J. Geophys Res (oceans), 102, 10353-10372*

Flosadottir, A.H., J.C. Larsen and J.T. Smith, 1997b. The Relation of Seafloor Voltages to Ocean Transports in North Atlantic Circulation Models: Model Results and Practical Considerations for Transport Monitoring, *J. Phys. Oceanogr., 27, 1547-1565*

Flosadottir, A.H., 2001. Long-term observations of ocean circulation with cables as sensors, *Proceedings of the OHP/ION joint symposium on long-term observations in the oceans, January 21-27*

Flosadottir, A.H., 1990. The Response of the Oceanic Lithosphere to Electromagnetic Controlled Source Transmitters Modeled Using Local Spectral Representation, *SIO Reference Series, 90(23), 228 pp*

Flosadottir, A.F. and S.C. Constable, 1996. Marine controlled-source electromagnetic sounding 1. Modeling and experimental design, *J. Geophys Res., 101, 5507-5517*

Fouquet, Y., Ondreas, H., Charlou, J.L., Donval,J.P., Knoery, J.R., Costa, I., Lourenco, N. and Tivey, M.K, 1995. Atlantic lava lakes and hot vents, *Nature, 377, 201*

Fujii, I., and A.D. Chave, 1999. Motional induction effect on the planetary scale geoelectric potential in the Eastern North Pacific, *J. Geophys. Res., 104, 1343-1359*

Hashimoto, Y., A. Tashiro, T. Shinozaki, H. Ishii, and K. Kawatate, 2001. Monitoring the ocean current in the Tsushima and the Tokara Straits by using submarine cables, *Proceedings of the OHP/ION joint symposium on long-term observations in the oceans, January 21-27, 2001, 232-235*

Hautot, S, P. Tarits, K. Whaler, B. Le Gall, J.J. Tiercelin, C.Le Turdu, 2000. Deep structure of the Baringo Rift Basin (central Kenya) from three-dimensional magnetotelluric imaging: Implications for rift evolution, *J. Geophys. Res., 105, 23493-23518*

Kraichman, M.B., 1970. Handbook of Electromagnetic Propagation in Conducting Media, *U.S. Govt. Prin. Offic., Washington, D.C.*

Lyu, S. J., and K. Kim, 2001. Time-series analysis of the cable voltage across the Korea Strait, *Proceedings of the OHP/ION joint symposium on long-term observations in the oceans, January 21-27, 236-240*

MacGregor, L.M., Constable, S.C. and Sinha, M.C.,1998. The RAMESSES experiment III: Controlled source electromagnetic sounding of the Reykjanes Ridge at 57°45'N, *Geophys. J. Int., 135, 772-789*

MacGregor, L.M., Sinha, M.C. and Constable, S.C., 2001. Electrical resistivity structure of the Valu Fa Ridge, Lau Basin, from marine controlled source electromagnetic sounding, *Geophys. J. Int., 146, 217-236*

Madden and Mackie, 1993. Three-dimensional magnetotelluric modeling and inversion, *Proc. IEEE, 77, 318-333*

Mackie, R.L. and T.R. Madden, 1993. Conjugate direction relaxation solutions for 3-D magnetotelluric modeling, *Geophysics, 58, 1052-1057*

Mackie, R.L., J.T. Smith, and T.R. Madden, 1994. Three-dimensional electromagnetic modelling using finite difference equations: the magneto-telluric example, *Radio Science, 29, 923-935*

Mackie, R.L., Madden, T.R. and Park S.K., 1996. A three-dimensional magnetotelluric investigation of the California Basin and Range, *J. Geophys. Res., 101, 16221-16239*

Nobes, D.C., Law, L.K. and Edwards, R.N., 1992. Results of a sea-floor electromagnetic survey over a sedimented hydrothermal area on the Juan de Fuca ridge, *Geophys. J. Int., 110, 333-346*

Palshin, N.A., L.L. Vanyan, I.V. Yegorov and K.V. Lebedev, 1999. Electric field induced by the global ocean circulation, *Phys. Solid Earth, 35, 1028-1035*

Park, S.K. and Mackie R.L., 1997. Crustal Structure at Nanga Parbat, northern Pakistan, from magnetotelluric soundings, *Geophys. Res. Letts., 24, 2415-2418*

Rikiishi, K., M. Michigami, T. Araki, K. Shiwaki, R. Eto, K. Taira, and J. Larsen, 1996. Cross-Stream Voltages Induced by Ocean Currents in the Tsugaru Strait, Northern Japan, *Proceedings, 13th Workshop on Electromagnetic Induction in the Earth, Onuma, Japan*

Robinson, I.S., 1976. A theoretical analysis of the use of submarine cables as electromagnetic oceanographic flowmeters, Phil.Trans.Roy.Soc.London, 280(1297), 355-396

Sinha, M.C. and the ISO-3D group, 1999. Mid-Atlantic Deep-towed Resistivity and Induction Geophysics at Lucky Strike (MADRIGALS), *RRS Charles Darwin Cruise 120 report, NERC, U.K.*

Smith, J.T., 1996a. Conservative modeling of 3-D electromagnetic fields: I. properties and error analysis, *Geophysics, 61, 1308-1318*

Smith, J.T., 1996b. Conservative modeling of 3-D electromagnetic fields: II. Biconjugate gradient solution and an accelerator, Geophysics, 61, 1319-1324

Stephenson, D., and K. Bryan, 1992. Large Scale Electric and Magnetic Fields Generated by the Oceans, *J. Geophys. Res., 97, 15467-15480*

Stratton, 1941. Electromagnetic Theory, *publ. McGraw-Hill*

Tyler, R.H., L.A. Mysak, and J.M. Oberhuber, 1996. Electromagnetic Fields Generated by a 3-D Global Ocean Circulation, *J. Geophys. Res., 282, 5531-5551*

Unsworth, M., B.J. Travis and A.D. Chave, 1993. Electromagnetic induction by a finite dipole source over a 2-D Earth, *Geophysics, 58, 198-214*

Vanyan, L.L, N.A. Palshin, H. Utada, H. Shimizu, and V.M. Nikiforov, 2000. Study of the Telluric Field Using the Submarine Cable across the Sea of Japan, *Phys. Solid Earth, 37, 539-548*

Wait, J.R., 1981. Wave Propagation Theory, *Pergamon Press, Tarrytown, N.Y.*

Wang, T. and A. C. Tripp, 1996. FDTD simulation of EM wave propagation in 3-D media, *Geophysics, 61, 110-120*

Webb, S.C. and Edwards, R.N., 1995. On the correlation of electrical conductivity and heat flow in Middle Valley, Juan de Fuca Ridge, *J. Geophys. Res., 101, 22523-22532*

Zhdanov, M.S., V.I. Dmitriev, S. Fang, and G. Hursan, 2000. Quasi-analytical approximations and series in electromagnetic modeling, *Geophysics, 65, 1746-1757*

Chapter 4

Controlled Source Electromagnetic Sounding: Methods and Instrumentation

M.C.Sinha[1], J.L.Rust[1], L.M. MacGregor[1], A.Soares[2], Z.Cheng[3], S.Riches[3] and the ISO-3D group[4]

1. School of Ocean and Earth Science, Southampton Oceanography Centre, Empress Dock, Southampton, SO14 3ZH, UK

2. Centro de Geofisica da Unversidade de Lisboa, Campo Grande, Ed. C8, Piso 6, 1749-016 Lisboa, Portugal

3. Formerly at Bullard Laboratories, University of Cambridge, Madingley Road, Cambridge, CB3 0EZ

4. Other members of the ISO-3D group: J.M. Miranda, A. Junge, A.H.Flosadottir, F.M. Santos, J. Luis, N. Lourenco, S. Dean, N. Barker

4.1 Introduction

The DASI (Deep-towed Active Source Instrument) source from Southampton Oceanography Centre (SOC) and the six LEMUR (Low-frequency Electromagnetic Underwater Receiver) instruments (five from SOC and one from the University of Lisbon), provide an integrated source and receiver system for performing controlled source electromagnetic (CSEM) sounding in the frequency domain. The CSEM technique has been successfully applied to the study of mature oceanic lithosphere, volcanically and hydrothermally active spreading centres, and passive continental margins (e.g. Constable & Cox, 1996; Evans *et al.*, 1994; MacGregor *et al.* 1998, 2001). Such studies have driven the continued development of practical methodologies for data acquisition and analysis. Significant up-grading of both the source and receivers was funded through the ISO-3D project, and these developments were tested in the field during the MADRIGALS (Mid-Atlantic Deep-towed Resistivity and Induction Geophysics at Lucky Strike) experiment, a CSEM survey performed on the Lucky Strike segment of the Mid-Atlantic Ridge as part of the ISO-3D project.

Using the controlled source method, the geometry of a survey is under the control of the investigator. The experiment can therefore be optimised to study a variety of sub-surface targets at spatial scales from a few tens of meters to several kilometres. Electromagnetic methods are sensitive to the bulk electrical resistivity of a medium, which is in turn sensitive to the distribution of cracks and pore spaces, their interconnectedness, and the properties (such as temperature and salinity) of the pore fluids. This makes controlled source electromagnetic sounding an extremely powerful tool for the study of sub-surface fluids in a range of oceanic and continental shelf environments. The MADRIGALS experiment, centred on a hydrothermally active segment of the Mid-Atlantic Ridge, was designed to optimise sensitivity to the 3-dimensional resistivity structure of the crust beneath the segment, and hence study the distribution, temperature and composition of the hydrothermal and other fluids circulating there.

4.2 Method

The CSEM method uses a horizontal electric dipole source to transmit a discrete frequency electromagnetic signal to an array of sea bottom receivers which record two orthogonal components of the horizontal electric field at the seafloor (figure 4.1). The resistivity of the seawater is in general less than that of the seafloor, so the signal in the water is rapidly attenuated, with the result that the fields measured by a receiver placed more than a few hundred metres from the source are dominated by signals which have followed crustal diffusion paths, and therefore contain information on sub-seafloor resistivity structure.

During a typical survey the source is towed at a height of around 50 m from the sea bottom, within an array of receiving instruments. By studying the variation in the amplitude and phase of the received electric field as a function of source-receiver separation and geometry, and the frequency of the signal, the resistivity structure of the underlying crust can be determined. Frequencies in the range 0.25-40 Hz are transmitted in a typical survey. Frequencies below this tend to lack resolution of the crustal scale structures that are of interest, and are more likely to be affected by seafloor electromagnetic noise from microseismic and ionospheric sources. At higher frequencies only signals at the very shortest source-receiver separations can be detected above the ambient noise level. Such signals contain little information about the sub-surface resistivity structure. The range of frequencies that in practice can usefully be employed is therefore quite limited. Although transmission at several different frequencies across this band is desirable since it allows resolution of structure on several length scales, both the vertical and horizontal resolution of the technique come primarily from geometric effects which will be explained in the next section. Depths of investigation up to 30 km have been achieved in the past (Constable & Cox, 1996), although the CSEM technique is most effective for probing rather shallower (0-5 km depth) structure.

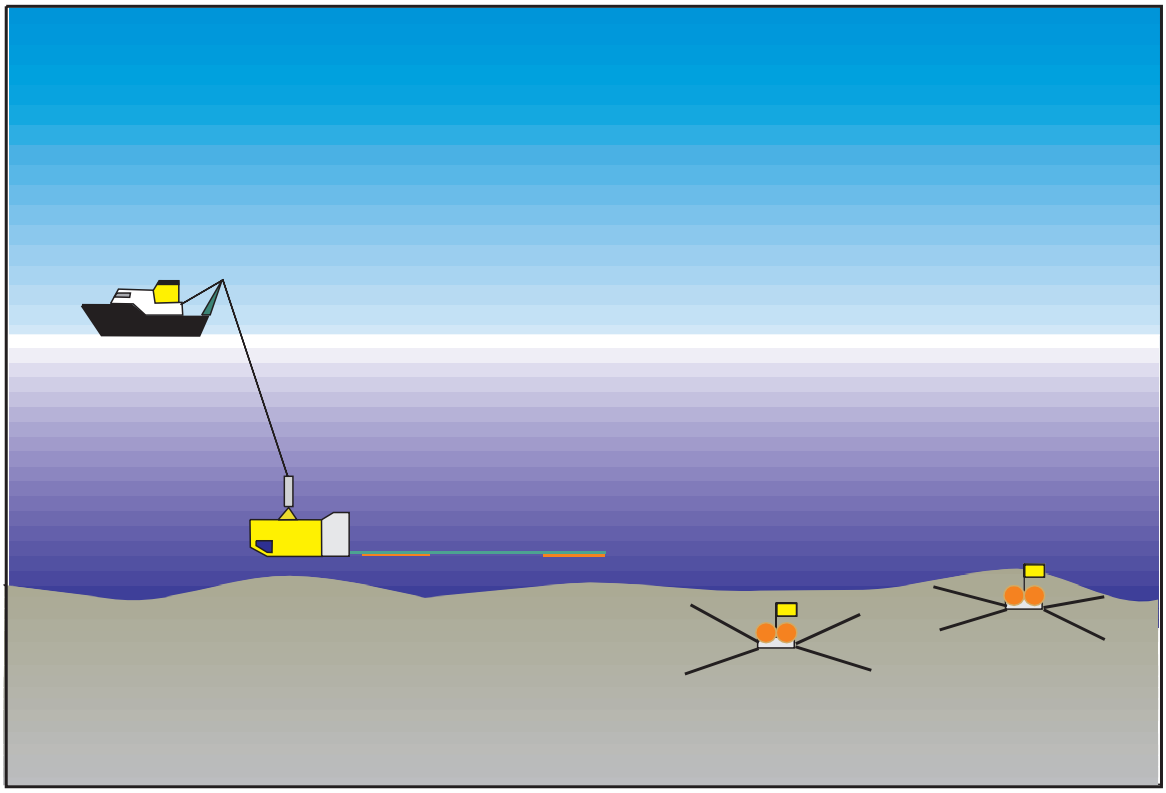

Figure 4.1. Schematic diagram of a controlled source electromagnetic survey. The source, a 100 m long horizontal electric dipole, is towed close to the seafloor within an array of receivers which measure two components of the horizontal electric field. The variation of the electric field with source-receiver separation and geometry and the frequency of the transmitted signal can be used to determine the sub-seafloor resistivity structure. In a typical survey electric fields can be detected to a distance of about 15km from the source, giving sensitivity to resistivity structure in the upper 5-7 km of the crust.

4.3 Experimental design considerations

The attenuation of electromagnetic fields in a medium of resistivity ρ is governed by the electromagnetic skin depth, δ_s.

$$\delta_s = \sqrt{\frac{2}{\omega \mu_0 \rho}}$$

where ω is the angular frequency of the signal and μ_o is the permeability of the medium, assumed to take its free space value. The skin depth is the distance over which the amplitude of the field decays by a factor 1/e and the phase is retarded by 1 radian. Attenuation is lowest for low frequency signals in highly resistive media. The frequency dependence of attenuation means that a structure that significantly perturbs a 10 Hz signal may have little or no effect on a 1Hz signal. Signals at the upper end of the useful (CSEM) frequency band can therefore be used to study small-scale shallow structure. This information can then be used to constrain the interpretation of lower frequency data needed to resolve deeper, larger scale structure.

The attenuative effect is illustrated in figure 4.2(b). The variation of electric field with source-receiver separation is illustrated for two models: one 'Resistive' consisting of a 300 Ωm layer overlying a uniform 1000 Ωm halfspace, the other 'Conductive' consisting of a 300 Ωm layer overlying a uniform 50 Ωm halfspace. The responses were calculated using the quasi-analytic code of Chave & Cox (1982). The fields have been normalised by the corresponding values for a 300 Ωm halfspace to remove the geometric $1/\text{range}^3$ dependence and highlight the component of the response that depends on the underlying resistivity structure. Because the skin depth is longer in the 1000 Ωm medium, and so attenuation is less than in a medium of resistivity 300 Ωm, the amplitude of the electric field is increased above the halfspace value. Similarly in the 'Conductive' model, where skin depths are shorter, a reduction in electric field amplitudes is observed.

To fully optimise a CSEM experiment, the 3-dimensional nature of the source fields must be taken into account. When a body of anomalous resistivity embedded in a medium is excited by an electromagnetic field, two modes of current excitation can occur (Walker & West, 1992). The first mode is inductive and current is confined to circulate within and around the anomaly with no transfer of charge across the surface. In the inductive mode attenuation effects governed by the skin depth dominate the observed response. For this mode, therefore, a conductive anomaly causes an increase in attenuation and hence a decrease in the observed field. Similarly an increase in resistivity decreases attenuation resulting in an increase in the field measured by a seafloor receiver. The second mode is galvanic, with currents crossing the boundaries of regions of different resistivity. In this case the presence of a low resistivity anomaly increases the galvanic current flow and can result in an increase in the measured field elsewhere.

Because a horizontal electric dipole source excites both modes of current flow, the response of a given resistivity structure depends on the interplay between the galvanic and inductive effects, which tend to work in opposition. The magnitude of each mode depends on the properties of the resistivity structure in question. However, because the fields of a horizontal electric dipole are 3-dimensional in nature, the relative magnitude of each mode also depends on the source-receiver geometry. The geometry can be defined in terms of the source-receiver azimuth - the angle between the source dipole axis and the line joining the source and receiver (figure 4.2(a)). At an azimuth of 90°, inductive effects dominate and the observed response can in general be explained in terms of attenuative effects governed by the skin depth. In the orthogonal direction at an azimuth of 0°, the galvanic mode is much stronger.

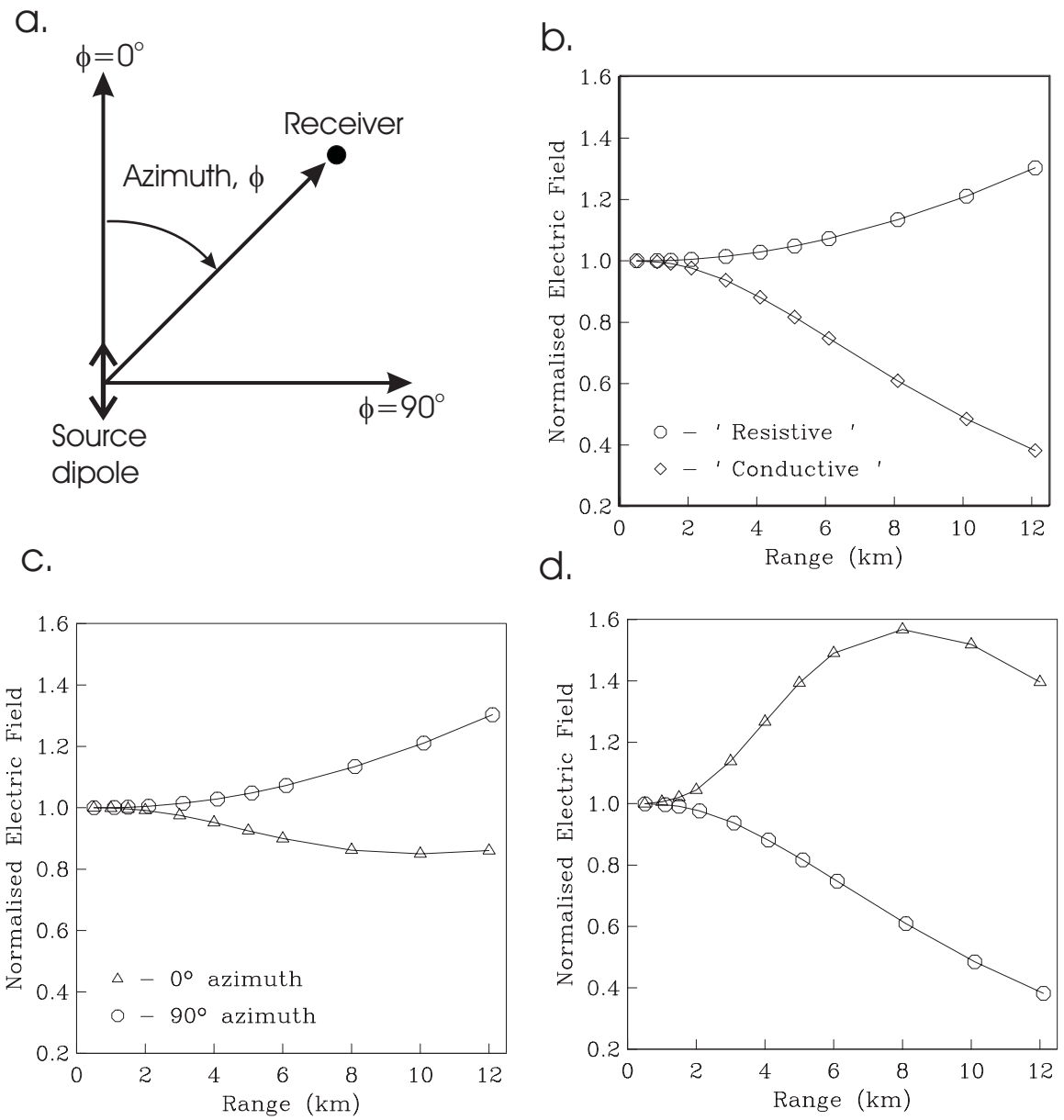

Figure 4.2. (a) Source-receiver geometry can be defined in terms of the azimuth, ϕ, defined as the angle between the axis of the source dipole and the line joining the source and receiver. (b) The response of 1D layered structures. The 'Resistive' model consists of a 1 km thick 300 Ωm layer overlying a uniform 1000 Ωm halfspace. The 'Conductive' model consists of a 300 Ωm layer overlying a 50 Ωm halfspace. The amplitude of the electric field at 90° azimuth as a function of source receiver separation is shown. The signal frequency is 1 Hz. Values have been normalised by the field of a uniform 300 Ωm resistivity structure. The behaviour can be explained in terms of simple attenuation arguments governed by the electromagnetic skin depth. (c) and (d) show the effect of source-receiver geometry. For the purposes of illustration fields at the two extreme azimuths, 0° and 90° are shown. (c) and (d) show the amplitude of the electric field as a function of source receiver separation for the 'Resistive' and 'Conductive' models respectively. Other parameters as in (b). It is clear that the responses in the two orthogonal geometries behave very differently. In particular the buried conductive structure in (d) leads to a characteristic splitting of amplitudes between radial and azimuthal fields.

The geometric effect is also illustrated in figure 4.2. Figure 4.2(c) shows the variation of the electric field at 1 Hz as a function of range for azimuths of 0° and 90°, calculated for the 'Resistive' model discussed above. As before, fields are normalised by the corresponding value for a uniform halfspace of resistivity 300 Ωm. It is clear in figure 4.2 that fields in the two geometries react very differently to even a simple 1-dimensional structure. The 1000 Ωm basement reduces attenuation and therefore increases the magnitude of the fields at an azimuth of 90° that are dominated by the inductive mode. The fields at an azimuth of 0° show a slight reduction in magnitude relative to the halfspace values because the galvanic mode, which has much more influence in this geometry, is being impeded by the 1000 Ωm medium.

Figure 4.2(d) shows the geometric effect for the 'Conductive' model. The 50 Ωm medium causes a reduction in the magnitude of the field at an azimuth of 90°, as expected from simple skin depth arguments. In contrast the magnitude of the fields at 0° azimuth is increased by the enhanced galvanic current flow in the low resistivity basement. The presence of buried conductive structure can therefore cause a characteristic enhancement of field amplitudes measured at small azimuth above those measured at azimuth close to 90°. This amplitude splitting effect can be even larger for more complex 2-dimensional structures, and has been proven to be of use in detecting and quantifying a conductive target (in that case magma) beneath 2-3 km of basalt in a mid-ocean ridge setting using real data (MacGregor *et al.*, 1998). Because of the strong dependence of the response on source-receiver geometry, survey designs that maximise the geometric coverage greatly increase the sensitivity to sub-seafloor resistivity structure.

4.4 The Source

The DASI (Deep-towed Active Source Instrument) electromagnetic deep-tow is a low frequency/high current electromagnetic transmitter for marine controlled source electromagnetic sounding surveys in a variety of environments, ranging from the deep ocean to shallower continental shelf settings. The DASI system was developed initially at the University of Cambridge (Sinha *et al.*, 1990), with further development funded under the ISO-3D project, both in Cambridge and at the Southampton Oceanography Centre.

The system comprises a ship borne power supply unit and the DASI deep towed vehicle. Streamed behind this is a 100 m long horizontal electric dipole formed from two 10 m long copper electrodes supported 100 m apart by a 140 m long neutrally buoyant, oil filled streamer array. This is towed at a speed of 1-1.5 kts and at heights of 30-80 m above the seafloor behind the DASI deep-tow vehicle (figure 4.3). The height above the seafloor is monitored using a 120 kHz Simrad acoustic altimeter mounted on the front of the deep-tow. Source position can be determined in real-time using either long baseline or ultra-short baseline acoustic navigation (or a combination of the two). The design of the deep tow vehicle means that transducers can be mounted on the head of the vehicle for increased navigational accuracy.

The shipboard power supply unit (PSU) is powered from a clean, 360-440 V/50-60 Hz 32 A 3-phase supply from the ship. Within the PSU the 3-phase input is filtered and rectified to 560 V d.c. before being switch-mode inverted and transformed up to a 1-2 kV, 256 Hz output signal. This high voltage waveform is passed via the armoured coaxial towing cable to the deep-tow vehicle. Within the high voltage pressure tube on the DASI vehicle, the waveform is transformed down to 5 V, 200-300 A, and using a silicon controlled bridge rectifier arrangement is switched at binary divisions of the incoming 256 Hz, producing a pseudo square wave output with a frequency in the range 0.25 Hz to 256 Hz. A second transformer provides low voltage AC (100-200V, 256 Hz) that is used to provide power to other electronic circuitry on the DASI system. The output of the DASI system gives a source dipole moment of about 15,000 Am (the exact value depends on the

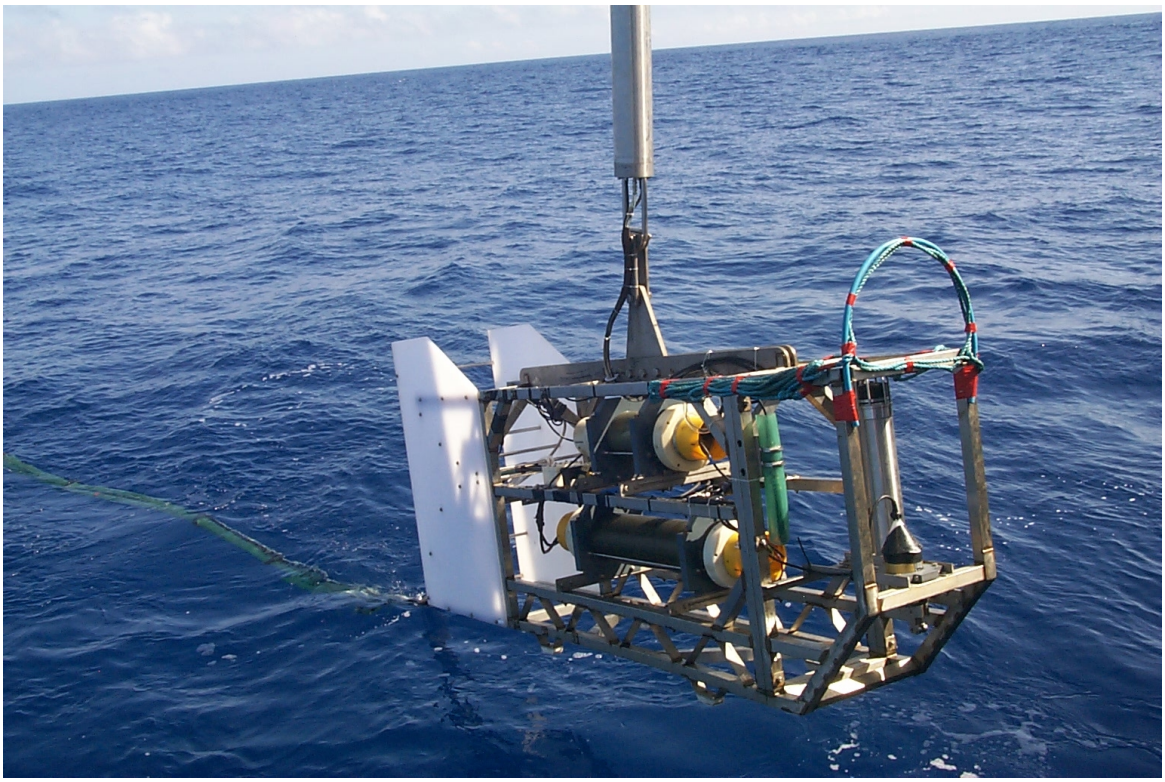

Figure 4.3. Photo of the DASI deep-tow vehicle, taken during deployment on the MADRIGALS cruise. The deep-tow vehicle is connected to the cable using an electro-optical swivel. The 140 m long streamer array, forming the transmitter dipole, is towed from the rear of the vehicle. The acoustic altimeter for monitoring height from the seafloor, and relay transponder for long baseline acoustic navigation of the source are mounted on the front of the deep-tow.

transmission parameters chosen). A summary of the DASI system specifications can be found in appendix A.

Since the output high current waveform is derived from the 256Hz from the PSU, its phase stability is dependant on the stability of the original PSU signal source. Throughout the duration of the ISO-3D project this signal was based on output from a crystal internal to the PSU, which drifted at a rate of a few seconds per hour. To improve the stability, the power supply is currently being upgraded to run from an external clock source. This will allow either a high stability clock source or a GPS derived clock source to be used.

Communications are maintained between the DASI deep tow vehicle and the ship through a single-mode fibre optic link. Transmission parameters (frequency and current) are controlled from the ship, and transmission characteristics are monitored and logged continuously on the ship throughout a survey at 0.5 s sampling interval. Transmission characteristics logged are, temperature in the high voltage pressure tube, depth below sea surface (measured with a pressure gauge), height above the seafloor (from the acoustic altimeter), output voltage, output current and frequency of the transmitted waveform.

During the ISO-3D project an independent 'Piggy-back' logger was installed on the DASI deep-tow to sample and log the transmitted waveform, by means of four ancilliary electrodes spaced along the main streamer array. This data was not piped up the fibre-optic link to the ship, but was stored to a hard disk drive installed on the deep tow vehicle, and was downloaded on recovery of the instrument. This, in principle, meant the phase of the outgoing waveform could be logged with time. In practise clock drift on the logging circuitry made the logging unreliable so this has now been replaced with a circuit that sends the information up the fibre optic link to allow the transmitted waveform to be logged in real time on the ship.

4.5 The receivers

The LEMUR (Low frequency Electromagnetic Underwater Receiver) instruments detect and record time series of two orthogonal components of the electric field at the seafloor (figure 4.4), using two orthogonal horizontal electric dipole receivers. Each dipole is formed from a pair of 6m long plastic arms, supporting low noise silver/silver chloride electrodes at the ends. The arms are mounted at an angle of 47.4^{o} to the long axis of the frame, to give equal length, orthogonal base lines between the electrode pairs, and a dipole length of 13.1m. The ends of the arms are weighted with glass rods to minimise motion due to water currents and keep the ends of the arms in contact with the seafloor.

The LEMUR instruments are deployed with a steel frame base weight with additional sandbags tied underneath for extra weight and stability on the seafloor. Recovery is achieved by using acoustic releases that activate a burn wire release mechanism. This takes approximately 10 mins from activation to the instrument leaving the sea floor, leaving the base weight and sand bags behind. The LEMUR electronics are housed in a glass sphere, with a second sphere providing extra buoyancy. As well as measuring the electric field, supplementary information from a bi-axial tilt meter, a fluxgate magnetic compass, and a temperature sensor is recorded.

The LEMUR data loggers consist of a pre-amplifier, a 24 bit ADC and a TT7 data logger and disk. Data are stored on the disks, which have a capacity of 1 Gb, in the form of up to 512 binary data files. Each data file contains 2097152 bytes (2 Mb), and they are named sequentially from datafile.000 to datafile.511. Since the data come from two orthogonal dipole sensors, each data file is divided into two 1 Mb sections, each containing data from one channel. Each of these sections consists of a header, containing the start time of the file and the supplementary tilt meter, compass and temperature data, followed by the time series of electric field, recorded in 3 byte samples. Details of the data format can be found in appendix B.

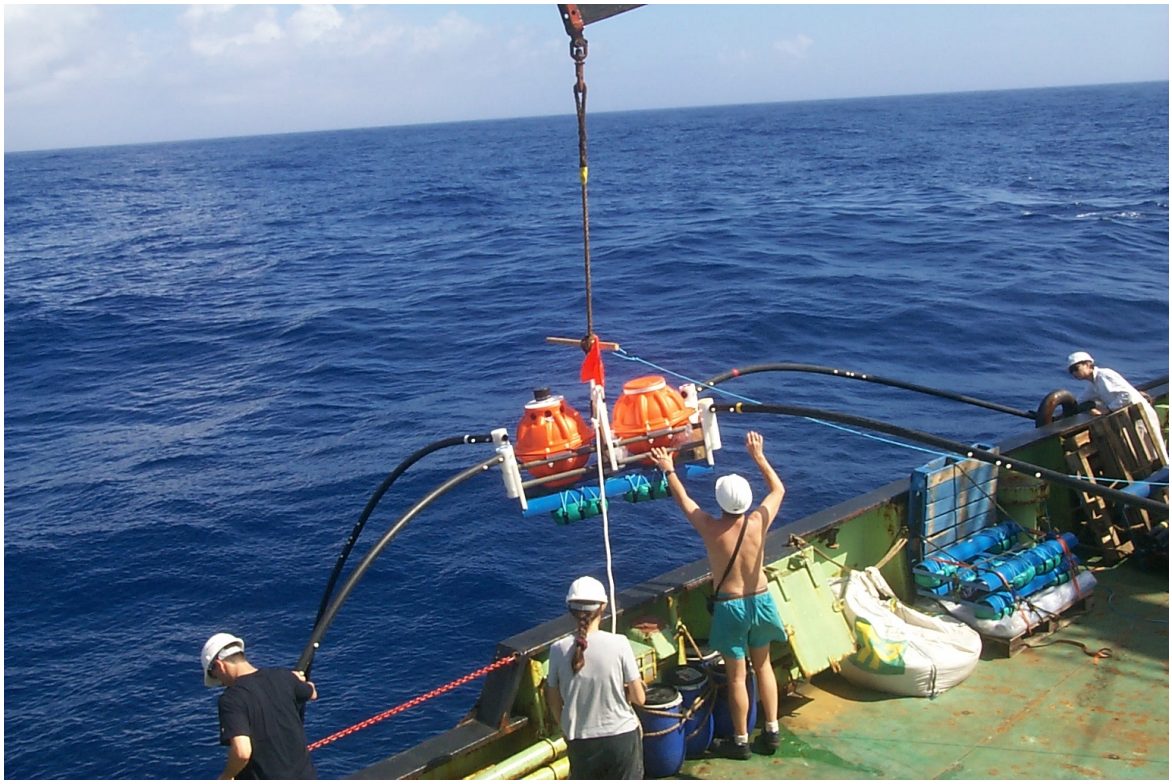

Figure 4.4. Photo of a LEMUR instrument during deployment on the MADRIGALS cruise. The logger and electronics are housed in a glass sphere, with a second glass sphere for flotation. The instrument measures and logs the seafloor electric field for two orthogonal pairs of plastic arms, which form two 13.1 m horizontal electric dipole receivers.

Each block of data contains 340,000 samples, which at a normal sampling frequency of 128 Hz corresponds to 2656.25 s of data (about 45 minutes). After a block of data has been recorded, sampling is suspended, the hard disk is spun up and the 2 Mb block of data written to it. The disk is then shut down and sampling recommences. Although this results in a gap of order 10 seconds in the time series every time the data are written to disk, it prevents noise from the disk spin contaminating the data.

There are currently two models of LEMURs in use: the pre-existing LEMUR 95 (L95) instruments, and LEMUR 99 (L99) instruments, developed from the L95s and built using ISO-3D funding. The L99s are designed to have better clock stability, lower power consumption and hence longer battery life and deployment time than the older L95 instruments. The ADC on the L99s also has a narrower input voltage range and consequently a higher sensitivity than the L95s. Lastly the L99 software has been significantly upgraded to improve ease of use and reliability. Instruments 16 & 18 are L99s, all other's are L95s. It is anticipated that the L95 instruments will be up-graded to L99 standard as soon as is practicable.

Calibration values determined from lab tests of the LEMUR instruments must be used to convert the raw data value in counts to a value of the voltage across the receiver dipole. The calibration values (in volts per count) are given in table 4.1. Also given are values to correct for the low frequency response of the receiver. A digital anti-alias filter that forms part of the ADC system controls the response at high frequency. This filter has a response that is flat up to a frequency of 50 Hz, with an extremely sharp roll off above this.

			Frequency response (multiplier)					
Inst	Ch	Volts/count	0.25 Hz	0.75 Hz	1.25 Hz	1 Hz	3 Hz	5 Hz & above
11	A	3.7e-12	3.1377	1.4304	1.2256	1.2617	1.0210	1.0
11	B	3.83e-12	3.1397	1.4292	1.2252	1.2612	1.0213	1.0
14	A	5.51e-12	2.6961	1.4678	1.2755	1.3137	1.0595	1.0
14	B	10.26e-12	3.2712	1.4669	1.2373	1.2807	1.00	1.0
15	A	3.66e-12	3.1037	1.4186	1.4980	1.2549	1.0201	1.0
15	B	3.65e-12	2.3787	1.2647	1.1449	1.1689	1.0387	1.0
16	A	1.01e-12	1.4518	1.0505	1.0317	1.0291	1.0048	1.0
16	B	1.10e-12	1.4075	1.0434	1.0171	1.0250	1.0040	1.0
18	A	1.05e-12	1.4116	1.0786	1.0295	1.0573	1.0258	1.0
18	B	1.11e-12	1.3749	1.0716	1.0253	1.0517	1.0244	1.0

Table 4.1: Calibration values for the LEMUR receivers, derived from the results of lab tests conducted in January 2001.

Background noise levels on each of the instruments during the MADRIGALS deployment are shown in figure 4.5. These were calculated from electric field time series recorded in a 12 hour period when there was no source transmission, and are therefore representative of the background noise levels during the experiment. The noise levels are comparable to those observed on seafloor electric field receivers in previous experiments (Constable & Cox, 1996; MacGregor *et al.* 1998, 2001). External noise sources include electromagnetic fields generated by ionospheric and cultural sources, and motionally induced fields caused by water currents, microseisms and earthquakes. Noise is also generated internally by the electrodes and instrument electronics.

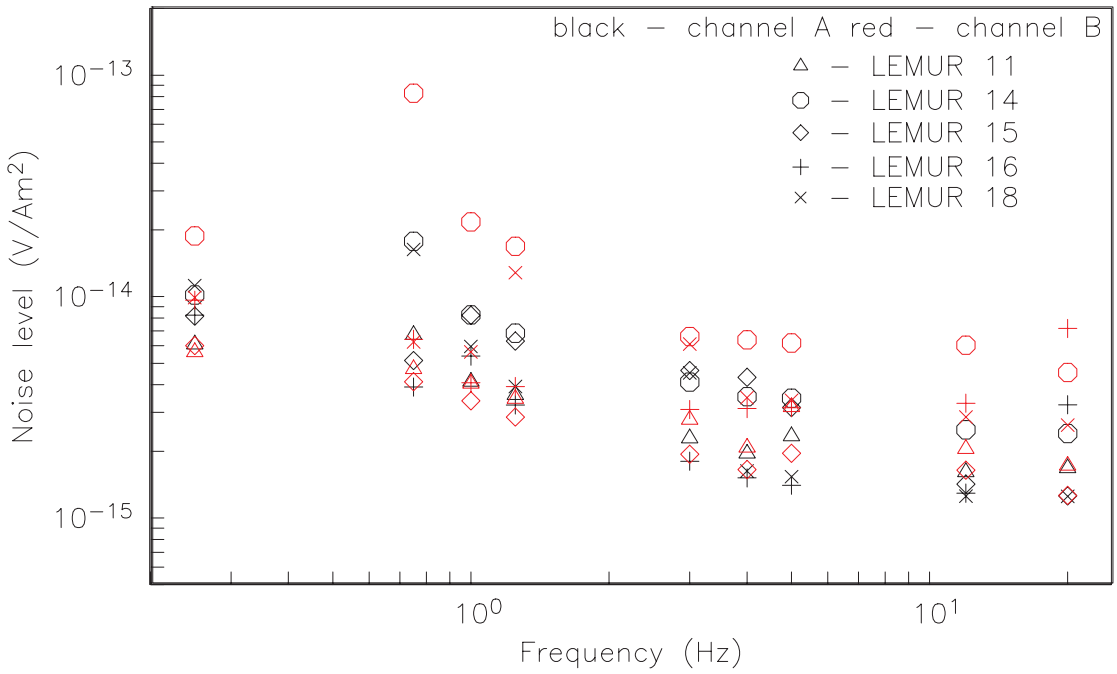

Figure 4.5. The noise levels on the LEMUR instruments during the MADRIGALS cruise in a bandwidth of 0.016 Hz. Frequencies are chosen to cover the range transmitted during the MADRIGALS experiment, and values have been normalised by a source dipole moment of 13700 Am to allow direct comparison with the data.

4.6 References

Chave, A.D. & Cox, C.S., 1982. Controlled electromagnetic sources for measuring electrical conductivity beneath the oceans, 1. Forward Problem and model study, *J. Geophys. Res., 87, 5327—5338*

Constable, S.C. & Cox, C.S., 1996 Marine controlled source electromagnetic sounding II: The PEGASUS experiment, *J. Geophys. Res., 101, 5519--5530*

Evans, R.L., Sinha, M.C., Constable, S.C. & Unsworth, M.J., 1994. On the electrical nature of the axial melt zone at 13°N on the East Pacific Rise, *J. Geophys. Res., 99, 577--588*

MacGregor, L.M., Constable, S.C., Sinha, M.C.,1998. The RAMESSES experiment III: Controlled source electromagnetic sounding of the Reykjanes Ridge at 57°45'N, *Geophys. J. Int., 135, 772-789*

MacGregor, L.M., Sinha, M.C. & Constable, S.C., 2001. The electrical resistivity structure of the Valu Fa Ridge, Lau Basin, from marine controlled source electromagnetic sounding, *Geophys. J. Int., 146, 217-236*

Sinha, M.C., Patel, P.D., Unsworth, M.J., Owen, T.R.E. & MacCormack, M.G.R., 1990. An active source electromagnetic sounding system for marine use, *Marine Geophysical Research, 12, 59--68*

Walker,P.W. & West, G.F., 1992. Parametric estimators for current excitation on a thin plate, *Geophysics, 57, 766--773*

Appendix A: Summary of DASI system specifications.

System components:

1. Shipboard power supply unit (PSU)
2. Shipboard control, monitoring, logging and calibration system
3. DASI (Deep-towed Active Source Instrument) deep-tow vehicle, equipped with acoustic altimeter and depth sensor. Acoustic navigation transponders for source location can be mounted as required.
4. Neutrally buoyant streamer array forming a 100m long horizontal electric dipole transmitter

Input:

Shipboard PSU requires:

1. Clean 360-440 V/50-60 Hz 3-phase supply rated to at least 32A
2. Auxiliary 100-240 V/50-60 Hz supply.

Output:

Output from the DASI transmitter:

1. Pseudo-square waveform
2. Peak-to-peak amplitude of 300 A
3. Source dipole moment of ~15000 Am (exact value depends on transmission chacteristics
4. Transmission frequencies between 0.25 Hz and 256 Hz

System dimensions:

1. Power supply unit:
   Dimensions: 0.5 m x 0.8 m x 1.9 m
   Weight: 300 kg
2. DASI deep-towed vehicle:
   Dimensions: 3.7 m x 0.6 m x 1.5 m
   Weight in air: 850 kg
   Weight in water: 650 kg
3. Streamer array:
   Length: 140 m
   Weight in air: 1000 kg

Additional system requirements:

1. Deep tow cable containing at least two conducting elements and one single mode fibre-optic element, and rated to at least 10 kVA
2. A towing sheave appropriate for the deep-tow cable.
3. An electro-optical swivel to connect the deep-tow to the cable, rated to at least 10 kVA
4. A towing winch fitted with electro-optical slip rings, rated to 10 kVA. This should be equipped with a wire out meter, a tension monitor, and be controllable from a remote station in the lab.
5. A winch for storage and deployment of the towed transmitter array.

Appendix B: LEMUR binary data format.

The SOC LEMUR (Low-frequency ElectroMagnetic Underwater Recorder) instruments record time series data from two orthogonal components of horizontal electric field sensors. Supplementary information is provided by data from a bi-axial tilt meter; a fluxgate magnetic compass; a temperature sensor; and a real-time clock.

The data are stored on disks of 1 Gbyte capacity, in the form of up to 512 data files. Each data file is of 2 Mbytes (=2 097 152 bytes). The files are named sequentially datafile.000 to datafile.511. All data files are binary and have an identical format.

Since the data come from two primary channels, each data block is divided into two 1-Mb sections, each containing the data from one channel. Within each of these sections, data are written in the following order:

- First a header, containing timing and other supplementary data.
- Second, the time series electric field data.
- Lastly, an end-of-data record.

Format of Data Header

The data header is identical for each channel of data. It consists of a sequence of 56 bytes, containing the following information:

Bytes 1-28 The first part of the header defines the time of the first sample in the block, in terms of the instrument's Real Time Clock. Expressed as:

Bytes 1-4	32 bit integer	Number of seconds since midnight, Jan 1st 1904
Bytes 5-8	32 bit integer	The number of clock ticks of 50 microseconds since the last whole second
Bytes 9,10	16 bit integer	Integer second
Bytes 11, 12	16 bit integer	Minute
Bytes 13, 14	16 bit integer	Hour
Bytes 15, 16	16 bit integer	Day of month
Bytes 17, 18	16 bit integer	Month of year (beginning with January = 0)
Bytes 19, 20	16 bit integer	Year (without century)
Bytes 21, 22	16 bit integer	Day of week (0 = Sunday)
Bytes 23, 24	16 bit integer	Day of year
Bytes 25, 26		Defaults to $FF $FF (flag for daylight saving time)
Bytes 27,28	16 bit integer	Year with century

Bytes 29-44 The second part of the header contains information about the instrument set-up, consisting of:

Bytes 29, 30	16 bit integer	Sampling rate, in samples per second
Bytes 31, 32	16 bit integer	Number of bits per sample
Bytes 33-36	32 bit integer	Number of samples per trace
Bytes 37, 38	16 bit integer	Number of traces (channels) in this file
Bytes 39, 40	16 bit integer	Channel recorded in this trace: 0 = channel A 1 = channel B

Bytes 41, 42	16 bit integer	Lemur number
Bytes 43, 44	16 bit integer	Lemur software version number

Bytes 45-52 The third part of the header contains information from supplementary data channels. Recorded once per block, and consisting of:

Bytes 45, 46	16 bit integer	Tilt, x-axis
Bytes 47,48	16 bit integer	Tilt, y-axis
Bytes 49, 50	16 bit integer	Compass orientation
Bytes 51, 52	16 bit integer	Temperature
Bytes 53 to 56		constitute a recognisable 'end of header' string.
Byte 53	$A5	
Byte 54	$A5	
Byte 55	$5A	
Byte 56	$5A	

The header for the first channel in the block begins at the start of the block. The header for the second channel in the block begins at an offset from the start of 1,048,568 bytes.

The tilt, compass and temperature data are digitised using 12 bit A to D converters with 0 to +5 V full scale input ranges. To convert the 16 bit integer value to ADC input voltage, multiply the value by 5/32768.

For both tilt channels,	tilt (degrees)	= (Vadc – 2.5) / 0.035
For temperature,	T (C)	= Vadc / 0.01
For the compass,	Orientation (degrees magnetic)	= (Vadc – 0.1) / 0.005

Note on Dates:

At the time of writing, the modification to the Real Time Clock software to make the instruments Y2K compliant is available but has not been installed or fully tested. For the November 2000 experiment, the instrument Year was set to (19)89. This means that the year fields will be incorrect in the headers. Also, the Julian day number will be wrong by 1 day, since 1989 was not a leap year. However the day of month, month of year and day of week values will be correct.

Format of Electric Field Data

Electric field data are written as sequential samples, each of 24 bits (3 bytes). Each 3-byte sample value takes the form of a signed integer, written with the most significant byte first, in 2's complement format. In order to read these data on most computers, the most convenient method is to assign the three bytes of the 24-bit sample to the three most significant bytes of a 4 byte integer (long integer or I*4); and to set the last (least significant) byte to $00. This will enable automatic handling of the 2's complement sign notation with most compilers. Since the result will be left-justified binary numbers with 8 trailing zeroes, the values can be right-shifted to their original values – still retaining the appropriate sign – by dividing the number by 256.

The first sample from the first channel begins at an offset of 56 bytes from the start of the file (immediately after the first header). The first sample from the second channel begins at an offset of 1,048,624 bytes from the start of the file (immediately after the second header). The first 24-bit sample in the time series was taken at the time specified by Bytes 1 to 28 of the header. Thereafter, each successive sample was taken at sampling intervals specified by Bytes 29 and 30 of the header.

In normal operation, the LEMURs record data with block lengths of 340,000 samples. The time series data field from each channel within a block therefore consists of a string of 1,020,000 bytes. The normal sampling rate is 128 Hz; this data string therefore corresponds to a time series of duration 2,656.25 seconds (about 44 minutes).

Once a block of data has been filled, sampling is suspended. The disk is spun up, and the 2 MByte block of data is written to it. The disk directory is updated with the time at which the file was written. The disk is shut down. Sampling then recommences for the next block. The time gap between the last sample in one block and the first sample in the next block is typically about 10 seconds.

Format of End-of-Data Record

The last byte of the last sample in a time series trace is followed by an end-of-data record, consisting of 4 bytes, $11, $11, $22, $22.

ISO-3D Final Report

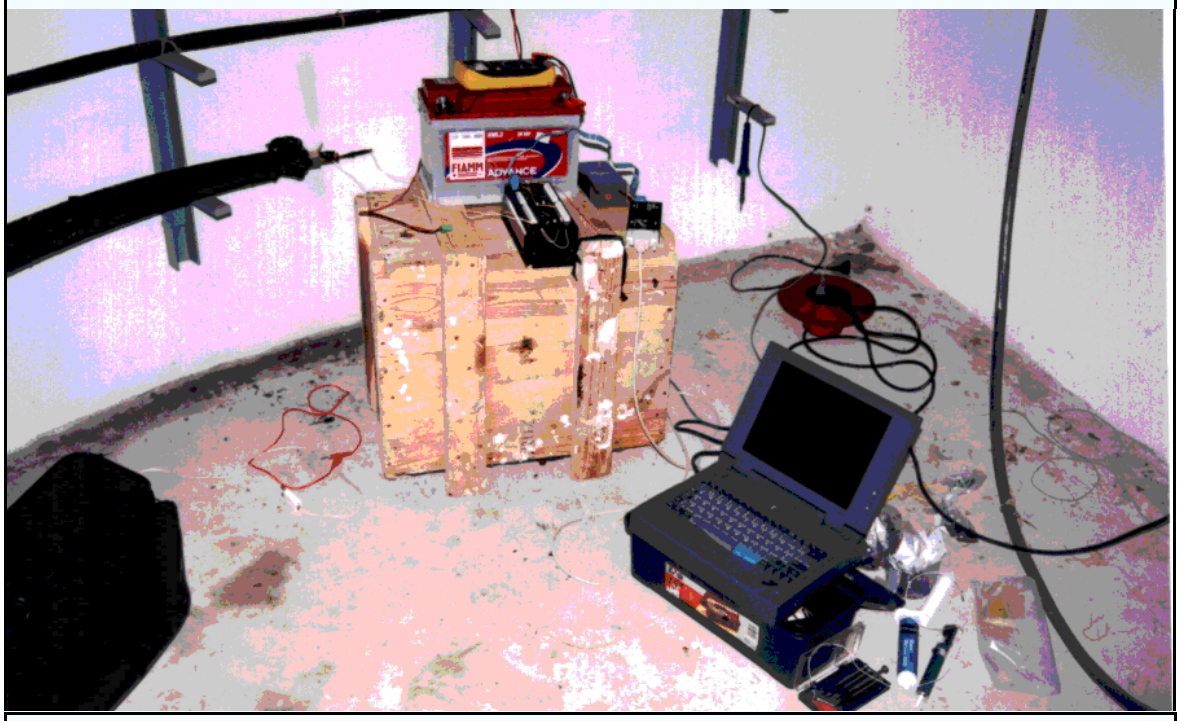

Part 3

Scientific Results:

Natural sources

Chapter 5

Voltage measurements in the CAM-1 submarine cable between the island of Madeira and the Portuguese mainland.

Fernando A. Monteiro Santos[1], António Soares[1], Luís Trindade[1], Rita Nolasco[1], Helena Rodrigues[1] and the ISO-3D team[2]

1. Departamento de Física and Centro de Geofísica da Universidade de Lisboa, Campo Grande, Ed. C8, Piso 6, 1749-016 Lisboa, Portugal

2. Other members of ISO-3D: J.M. Miranda, N. Lourenço and J. Luís, A. Flosadottir, A. Junge, M. Sinha, L. MacGregor, S.Dean, N. Barker, S. Riches and Z. Cheng

Earth, Planets and Space, in press

5.1 Abstract

Electrical voltage data measured between the ends of the CAM-1 cable, over a period of fifteen months, have been analysed in order to determine the electrical stability of the cable and to obtain some preliminary information related to water transport. The monthly average of the potential measured during days with low geomagnetic activity suggests a periodicity of 120 days that was tentatively interpreted as having its origin in water flow. These results show a small trend that is compatible with no drift in the cable. The mean electric field estimated from quiet days is 0.206 ± 0.022 mV/km. If the variations of this potential are attributable to ocean water transport a flow of ± 0.09 cm/s is estimated. This value represents a maximum value for temporal variations of the spatially averaged water-flow velocity.

5.2 Introduction

There are several retired telecommunications cables in use for scientific purposes (see e.g., Sanford, 1982; Larsen and Sanford, 1985; Chave et al., 1992; Vanyan et al., 1998; Flosadottir et al., 19 ; Fujii, et al., 1995; Palshin, 1996; Fujii and Chave, 1999, among several others). The largest numbers of these cables are installed in the Pacific Ocean area. The NOAA-PMEL web page lists 3 cables with measurements in progress in the Atlantic Ocean (TAT-8, CAM-1 and PENCAN2ext). There are also references to some measurements (19 days) in the cable between Tuckerton and Lands End (Lanzerotti et al., 1985) and in the cable TAT-6 (Bell Laboratories), carried out several years ago. The geophysically important sources for large-scale cable voltage have been already mentioned by Sanford (1971; see also Meloni et al., 1983; Chave and Luther, 1990): 1) geomagnetic field variations originating from time variations in the ionosphere and magnetosphere electric current systems, 2) motions of the sea-water through the geomagnetic field, and 3) leakage of telluric currents associated with the toroidal geomagnetic field at the core-mantle boundary.

The decommissioning of the CAM-1 cable between Porto Novo on Madeira Island and Sesimbra on the Portuguese mainland (figure 5.1) in 1995, provides us with an excellent opportunity to contribute to the measurement of earth electrical potentials at a large scale. The geographical coordinates of the cable ends are 38°25'N, 9°50'W (Sesimbra) and 32°39'N, 16°48'W (Porto Novo). The length of the cable is 1150 km, with 35 unpowered repeaters. The impedance of the cable is approximately 5500 Ω. At the Sesimbra terminus the cable is buried in sea sediments and used as ground. In fact, the cable was cut at 2 km distance from the coast and discarded in the ocean, when it was decommissioned. At the Madeira terminus the cable runs into a cellar under the old Marconi office building in Porto Novo. This provides a stable temperature environment. At this end, one of the old telecommunications standard five-foot-long ground rods that is immersed in the sea is used as ground.

The voltage difference between the central conductor of the cable and the sea ground is measured and digitised with a 16-bit ADC (a Campbell datalogger) at 2s intervals, but only the 30s averages are saved. Time is determined by the datalogger clock, which is corrected when data are collected. Experience showed, however, that this process must be improved in order to guarantee more accurate time measurement. A GPS controlled clock system is now in use.

The voltage measuring started in November 1998. However, data acquired during the first 45 days, (considered as an experimental period), were not included in this study (Monteiro Santos et al., 1999, 2000). After some technical improvements the acquisition started on February 19, 1999. This paper deals with the analysis of data acquired between February 1999 and June 2000. The main objectives are: 1) to analyse the long-term (1 year) stability of the cable, 2) to characterise the probable sources of the principal variations and, 3) to obtain preliminary information related to water flow.

Figure 5.1. Location of the CAM-1 cable.

5.3 Raw Data

Figure 5.2a shows the voltage recorded during May 1999. The voltage fluctuates between about –1 and 2 V with a significant semidiurnal period. Examples of data acquired in quiet and disturbed days are shown in figure 5.2b and 5.2c. Plotted in figure 5.3 is the amplitude spectrum of the data collected between December 1999 and March 2000. The spectrum is clearly dominated by peaks at periods of diurnal (1 cpd), semi-diurnal (2 cpd) and 8 hours (3 cpd). All these periods correspond to the combination of tidal, motional and geomagnetic frequencies. The presence of the semi-lunar M2 constituent is also clearly depicted in the spectrum.

Calculation of the average value of all the available data give a value of 230.05 ± 758.17 mV. The high value of the standard deviation arises mainly from tides and the intense geomagnetic activity recorded by the cable. The semi-diurnal tidal component was then filtered by the application of a notch filter. Simple daily mean values were calculated from filtered data (figure 5.4). The average value of the daily series is 225.83 ± 88.33 mV. The standard deviation now has a much lower value. According to Palshin *et al.* (2001), solar daily variations are efficiently suppressed by daily averaging procedure. In our case, due to their importance, tidal signals probably continue to be present in the averaged data and these results are not accurate measures of the integral water transport. A more detailed analysis is needed to reach that objective.

The histogram of the 30 minutes average values, for the interval February 1999, through to June 2000, is shown in figure 5.5. The voltages were binned in 300 mV boxes. From the figure one can conclude that the distribution of the voltage values is not symmetrical around zero potential, being biased towards positive values. In fact, the distribution is close to a normal distribution centred at 0.217 V.

The 30s average values were used to determine averages over seven days and have also been averaged using a twenty day moving window. These results are plotted in figure 5.6. The plot suggests a periodic variation. However, a more useful determination, in the sense that we can correlate it with water-flow, of the average values needs to take into account the levels of geomagnetic activity. In order to decrease the influence of the signal induced by external sources, only the days with low geomagnetic activity must be considered. These are usually estimated from daily geomagnetic indexes. Several indexes are in use, for example K and A*p* among others. Nevertheless, the published indices only consider the lowest ten days in each month. Equivalent information, but not so restrictive, can be obtained by analysing the daily data as follows. The difference $\delta H = H_{\text{maximum value}} - H_{\text{minimum value}}$ of the magnetic component H was determined for each period of 3 hours. The eight values were then used to determine daily averages $\underline{\delta H}$ of those differences. These values are used as rough estimates of the geomagnetic activity. Values less than 10 nT were obtained on several days in January and December, indicating that these were the quietest months in 1999. The highest values (> 60 nT) were obtained on some days in September. In each month of data, those days with $\underline{\delta H}$ < 30 nT and <50 nT were selected and averaged. The results obtained for the $\underline{\delta H}$ < 50 nT condition are shown in figure 5.7. The number of days used in each calculation is shown at the bottom of the figure. The fifteen months data suggests a possible periodicity of around 120 days. There are two maxima: in the transition from winter to spring (March-April) and in summer (August-September) and two minima at the end of the spring (May-June) and in autumn (October-November). There are not enough data to define what happened in December-January.

A semi-annual variation in magnetic activity level has been observed by several investigators according to Lanzerotti et al. (1992 and references therein). To clarify this point we calculated the monthly mean of the magnetic field components from Guimar. Figure 5.8 shows the result for X-component. Note that there is no correlation between the magnetic and the cable voltage signals at these long periods. Therefore, it is unlikely that the approximately 120 day variation seen in figure 5.7 has geomagnetic origin.

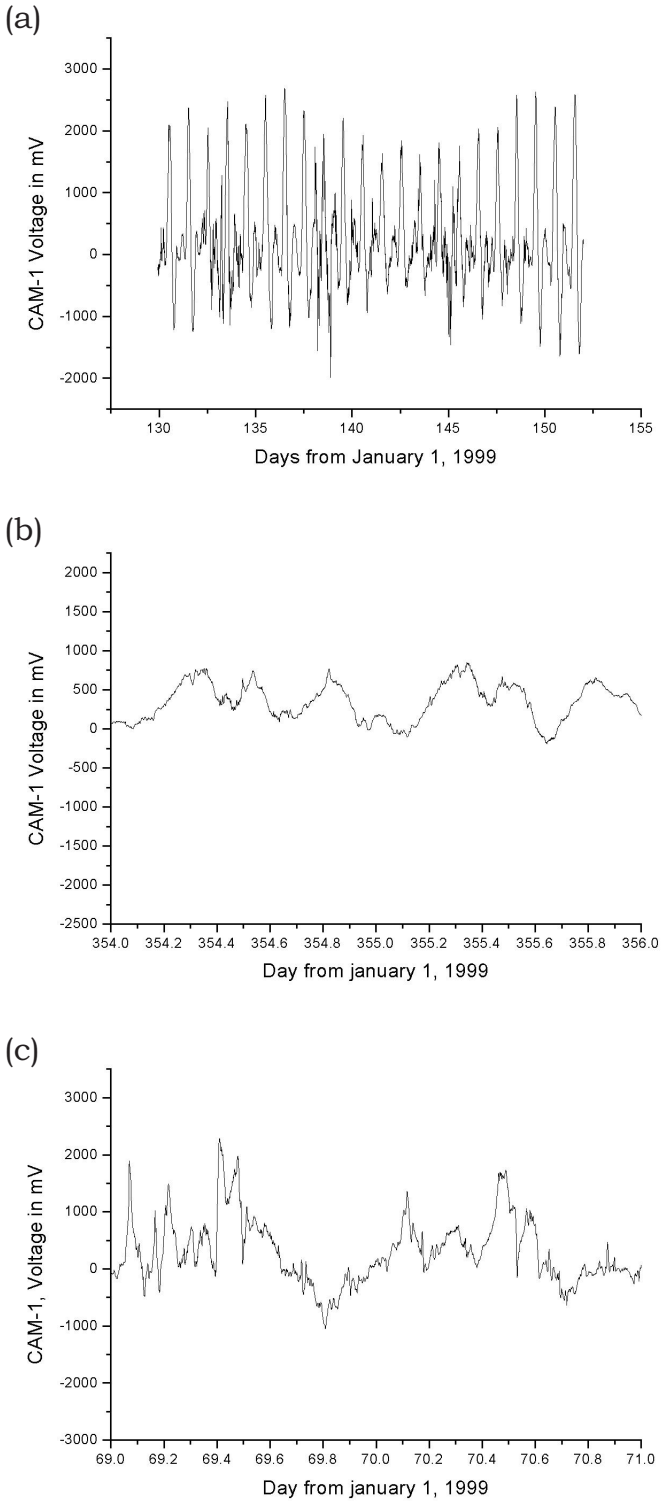

Figure 5.2. Examples of the measured voltage (30 s average), a) during May 1999, b) over two quiet days and c) over two disturbed days.

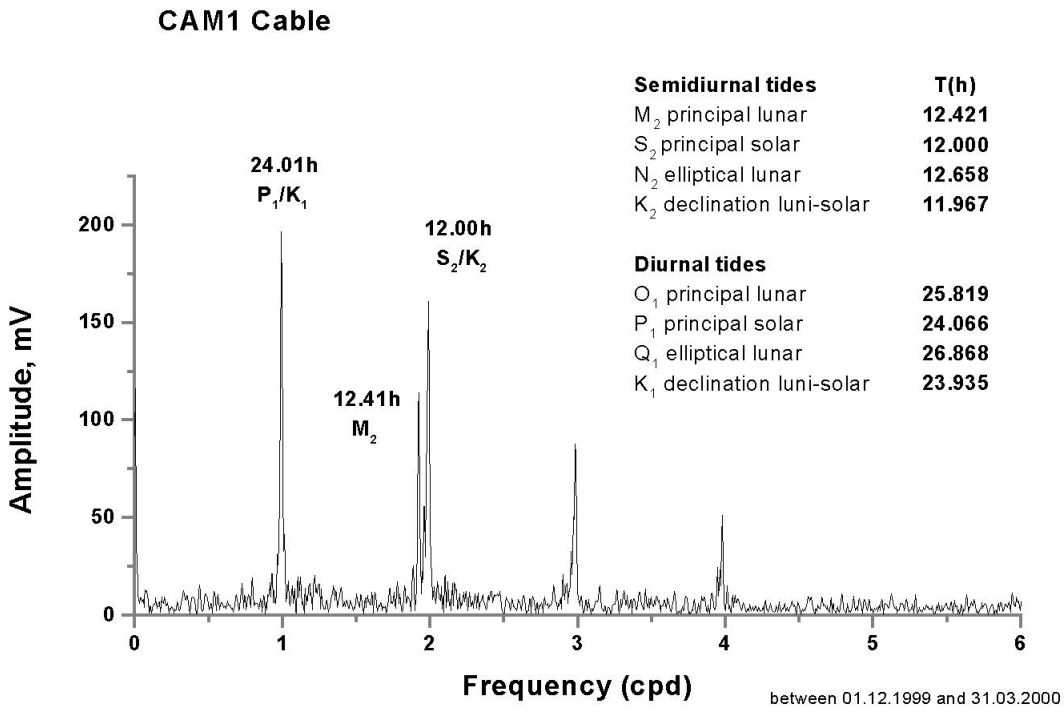

Figure 5.3. Amplitude spectrum obtained from CAM-1 voltages between December 1999 and March 2000.

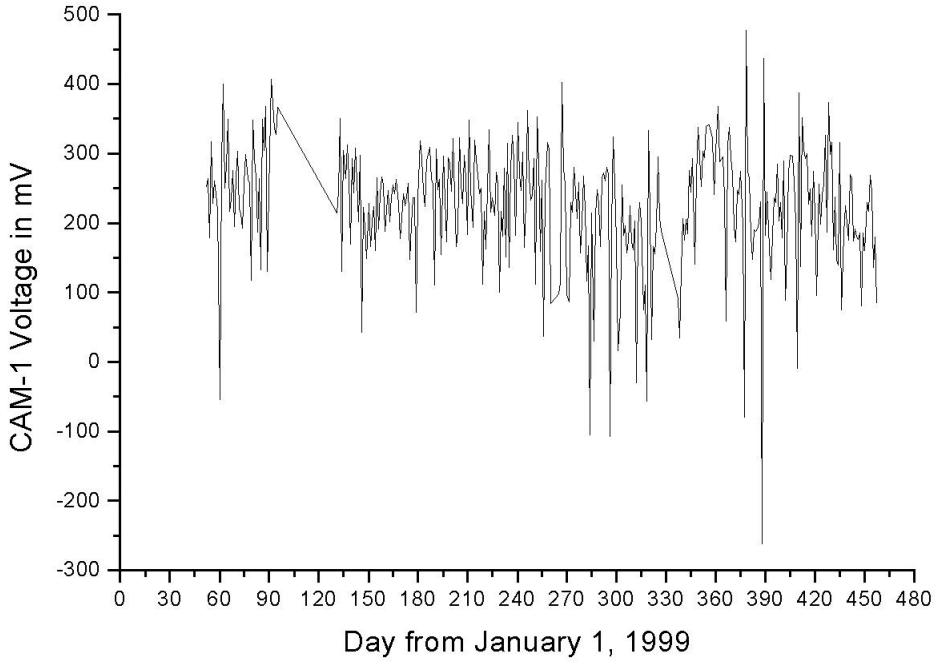

Figure 5.4. Daily mean CAM-1 voltages. Data gaps can be observed in April-May, September and in November.

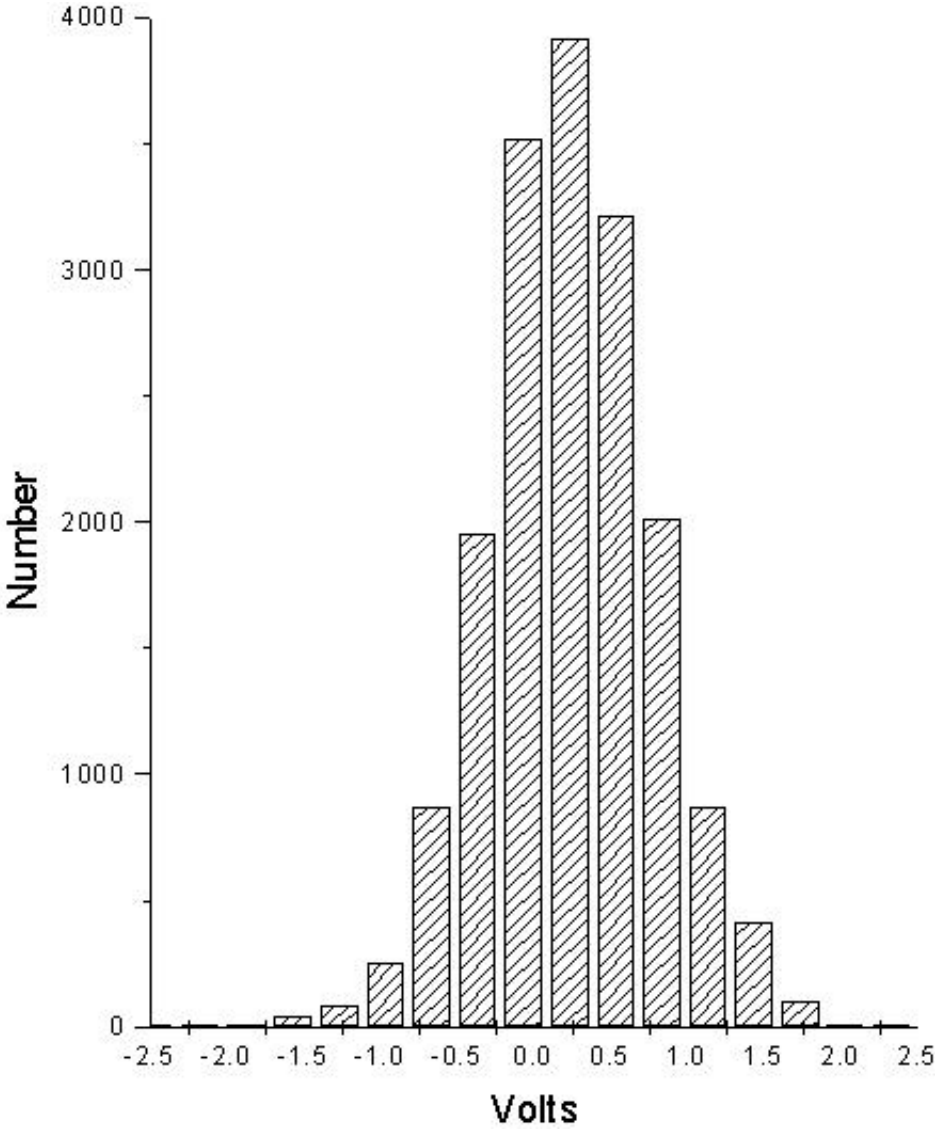

Figure 5.5. Statistical distribution of 30-min mean values of the voltages measured on CAM-1 cable.

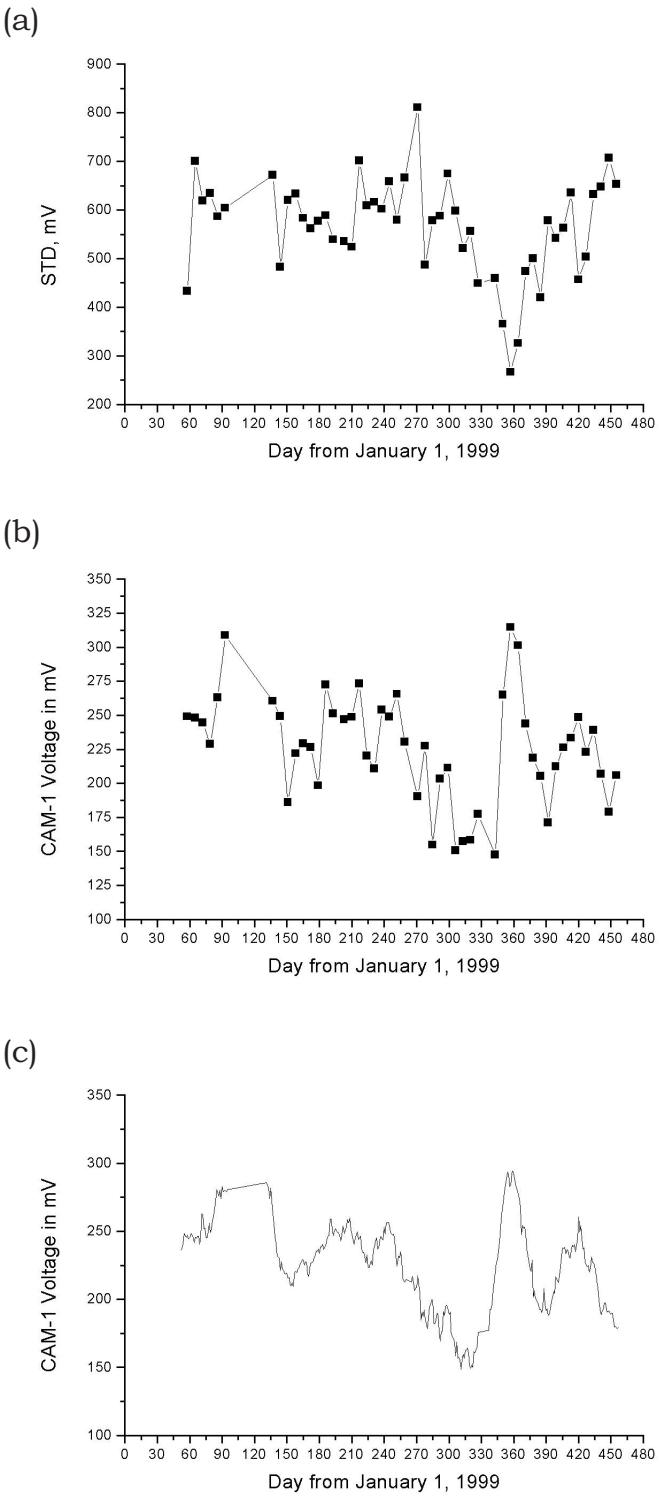

Figure 5.6. Weekly mean of CAM-1 voltages (b) and its standard deviation (a). Smoothed voltages using twenty days adjacent averaging are plotted in (c).

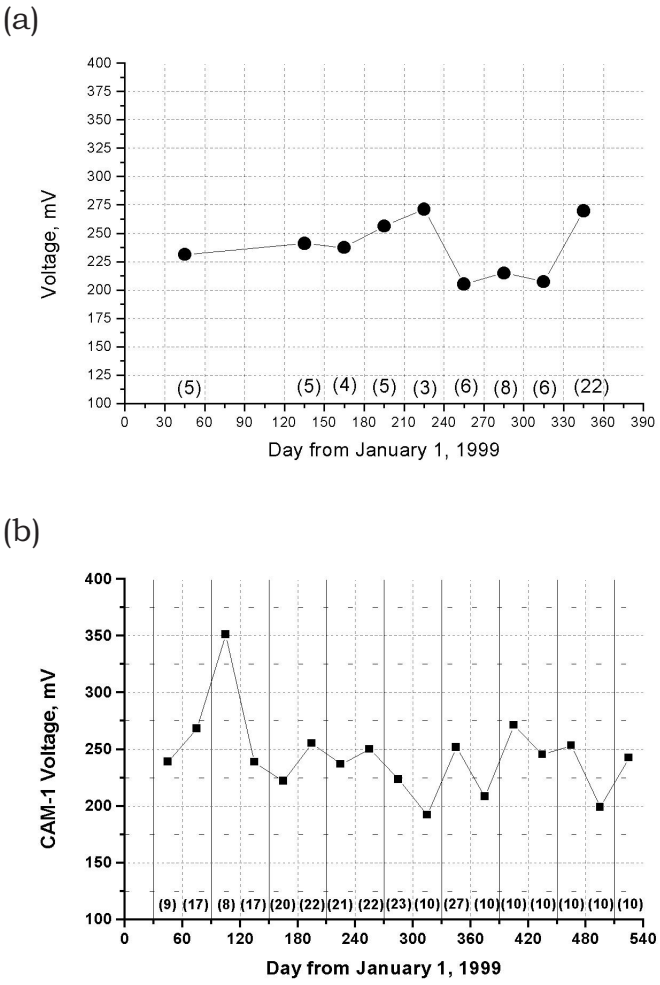

Figure 5.7. (a) Monthly mean voltages estimated using only those days with H<30 nT. (b) as in (a) but including days with H<50 nT. The slope of the best linear fit is -0.080 ±0.057 mV/day.

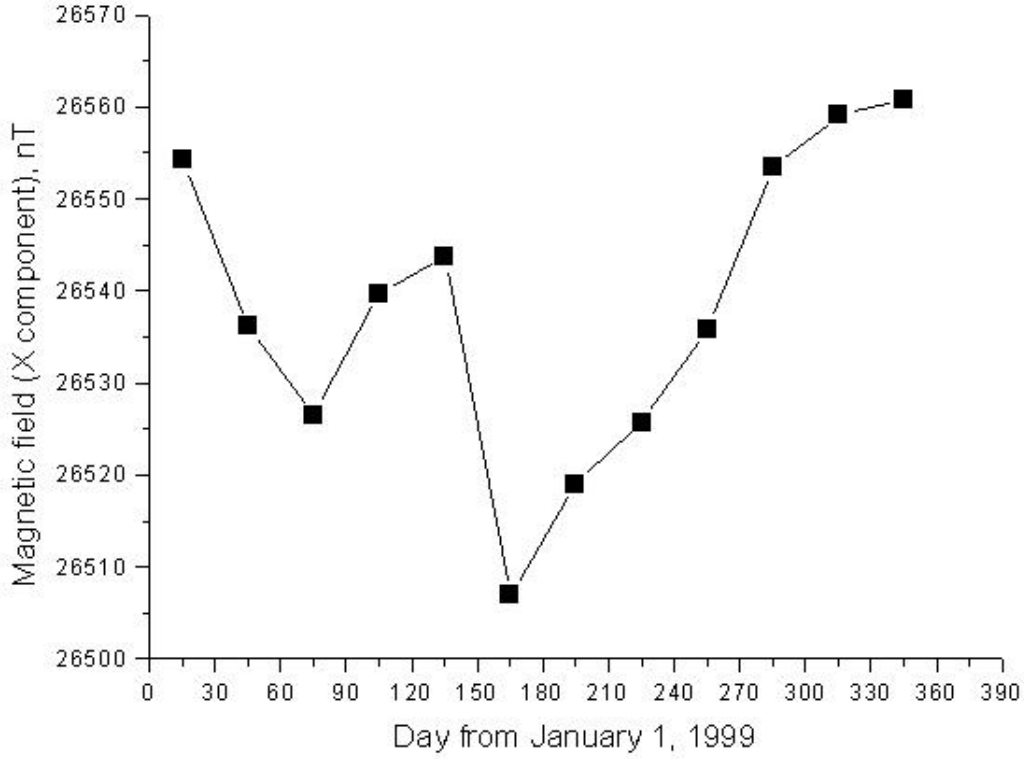

Figure 5.8. Monthly mean of the north magnetic field component measured in Guimar Observatory.

The results presented in figure 5.7 represent the long period variation of the cable voltage and can be used to test for possible systematics in the measurements. A drift in the electrode contact could be expected since the two terminals are made in a different way and are located in different geological (and electrical) environment. The best linear fit obtained from data in figure 5.7 (bottom) with slope of -0.080 ± 0.057 mV/day reveals that no significant drift is observed, at least in the year interval considered.

5.4 Discussion

The average of the mean values estimated from days with $\underline{\delta H}$<30 nT is 237.18 ± 25.19 mV, that is, the mean electric field is about 0.206 ± 0.022 mV/km. This value is higher (three times larger) than that measured by Lanzerotti and his co-authors in North Atlantic (Lanzerotti *et al.,* 1985). Our value is of the same order as the value measured by Lanzerotti in the 4000 km long cable between Hawaii and California (Lanzerotti *et al.*, 1992), and with the same sign. Part of this electric field is due to electrochemical effects associated with the ground connections. The other part can be attributed to possible ocean flows across the cable. It is not possible to determine exactly the contribution of the electrochemical effects to the potential.

An assumption that the value of the mean electric field has electrochemical origin and that the long period oscillations (with amplitude of ± 0.022 mV/ km) can be explained by ocean flows will allow us to estimate a value of the vertical mean of the conductivity- weighted velocity (Sanford, 1971). Neglecting displacement currents, self and mutual induction phenomena, depth integrated electrical currents and large-scale electric currents, the voltage induced by a flow of conductive sea water in the magnetic field of the earth can be expressed approximately by $E=B_z \times v$. E represents the horizontal electric field, B_z the vertical component of the magnetic field and v is the mean conductivity-weighted velocity. The estimated value for the velocity is then ± 0.09 cm/s. A discussion about the origin, oceanographic means and importance of such a flow is out of the scope of this paper. This result was obtained considering B_z=24000 nT.

The information contained in the short period measurements is dominated by induced electromagnetic field and can be used for solid earth investigations (see, e.g., Lizarralde *et al.*, 1995; Vanyan *et al.*, 1998,). More precisely, an estimation of the electrical resistivity with depth can be obtained. These studies, now in progress, are based on the magnetotelluric sounding theory and can be carried out with the help of the geomagnetic data from Guimar Observatory in Canary Islands.

5.5 Acknowledgements

The authors would like to thank many people at Marconi and TRIMAD who provided us the opportunity to use the cable and helped us in several ways. In particular we thank Eng. Vasco Sá, Mr. António Abrantes and Mr. Marçal from Marconi and Dr. Luís Sousa and Mr. Crisóstomo Luís from TRIMAD. Thanks are also due to Luís Matias for his interest in the subject and initial help. Comments and suggestions from the two reviewers (N. Palshin and H. Utada) contributed to improve the paper and are thanked. This work was developed in the scope of the ISO-3D project funded by EC. Thanks to FCT for continuous supporting of the CGUL are also due.

5.6 References

Chave, A.D. and Luther, D.S., 1990. Low-frequency, motionally induced electromagnetic fields in the ocean, 1. Theory. Journal of Geophysical Research, 94, 7185-7200.

Chave, A.D., Luther, D.S., Lanzerotti, L.J. and Medford, L.V., 1992. Geoelectric field measurements on a planetary scale: oceanographic and geophysical applications. Geophysical Research Letters, 19 (13), 1411-1414.

Fujii, I., Lanzerotti, L.J., Utada, H., Kinoshita, H., Kasahara, J., Medford, L.V. and Maclennan, C.G., 1995. Geoelectric power spectra over oceanic distances. Geophysical Research Letters, 22, 421-424.

Fujii, I. And Chave, A.D. Motional induction effect on the planetary scale: geoelectric potential in the eastern North Pacific, J. Geophysical Res., 104, 1343-1359.

Larsen, J.C. and Sanford, T.B., 1985. Florida current volume transports from voltage measurements. Science, 227, 302-304.

Lanzerotti, LJ., Sayres, C.H., Medford, L.V., Kraus, J.S. and Maclennan, C.G., Earth potential over 4000 km between Hawaii and California,Geophysical Research Letters, 19, 11, 1177-1180, 1992.

Lizarralde, D., Chave, A.D., Hirth, G. and Schultz, A., 1995. Long period magnetotelluric study using Hawaii-to-California submarine cable data: implication for mantle conductivity. J. Geophysical Res., 100, 17837-17854.

Meloni, A., Lanzerotti, L.J. and Gregori, G.P., Induction of currents in long submarine cables by natural phenomena. Rev. Geophys. Space Phys., 21, 795-803, 1983.

Monteiro Santos, F.A., Soares, A., Miranda, J.M., Mendes-Victor, L.A. and ISO-3D team, Preliminary electric field observations in the CAM-1 cable between Madeira and Lisboa, Geophysical Research Abstracts, V. 1, nº 1, 180, 1999.

Monteiro Santos, F.A., Soares, A., Flosadottir, A., Junge, A., MacGregor, L., Miranda, J.M., Nolasco, R. and Sinha, M., Measurements of electric potential in CAM-1 cable, 2ª Assembleia Luso Espanhola de Geodesia e Geofísica, Lagos, Portugal, 2000.

Palshin N. A., Vanyan L. L., Medzhitov R. D., Shapiro G. I. , Evdoshenko M. A., Utada H., Shimizu H. and Y. Tanaka, 2001, Use of the Nakhodka-Naoetsu Submarine Cable for Studying the Temporal Variability of the Integral Water Transport in the Sea of Japan, Oceanolgy, Vol. 41, N 3, 447-457.

Palshin, N. A., 1996. Oceanic electromagnetic studies: a review. Surveys in Geophysics, 17, 455-491.

Sanford, T.B., 1982. Temperature transport and motional induction in the Florida Current. Journal of Marine Research, 40, 621-639.

Sanford, T.B., 1971. Motionally-induced electric and magnetic fields in the sea. Jounal Geophysical Research, 76, 3476-3492.

Vanyan, L.L., Utada, H., Shimizu, H., Tanaka, Y., Palshin, N.A., Stepanov, V., Kouznets, 1998. Studies on the lithosphere and the water transport by using the Japan Sea Submarine Cable (JASC); 1, Theoretical considerations. Earth, Planets and Space, 50 (1), 35-42.

Chapter 6

Studies of the lithosphere using the CAM-1 (Lisbon-Madeira) cable: Preliminary results

Fernando A. Monteiro Santos[1], António Soares[1], Rita Nolasco[1], Helena Rodrigues[1], Rafael Luzio[1] and the ISO-3D team[2]

1. Departamento de Física and Centro de Geofísica da Universidade de Lisboa, Campo Grande, Ed. C8, Piso 6, 1749-016 Lisboa, Portugal

2. Other members of ISO-3D: J.M. Miranda, N. Lourenço and J. Luís, A. Flosadottir, A. Junge, M. Sinha, L. MacGregor, S.Dean, N. Barker, S. Riches and Z. Cheng

6.1 Introduction

Studies on spatial characterisation of the electrical conductivity distribution deep in the Earth using potential variations over retired submarine cables have been made in recent years (Lizarralde *et al.*, 1995; Vanyan *et al.*, 1995, 1998).

The CAM-1 cable, connecting Madeira Island and Sesimbra on the Portuguese mainland (Figure 6.1), was decommissioned in 1995 and the scientific use of it started at the end of 1998. The geographical coordinates of the cable ends are 38º25'N, 9º50'W (Sesimbra) and 32º39'N, 16º48'W (Porto Novo in Madeira). The length of the cable is 1150 km, with 35 unpowered repeaters. The voltage difference between the central conductor of the cable and a sea ground is measured and digitised with a 16-bit ADC (a Campbell datalogger) at 2 s intervals, but only the 30 s averages are saved. The main characteristics of the cable, as well as of the data acquired during the first fifteen months can be found in Monteiro Santos *et al.* (2001).

The voltage measured between the ends of a submarine cable has three main sources: 1) geomagnetic field variations originating from time-variations in the magnetosphere-ionosphere current-system, 2) motions of the sea-water through the geomagnetic field, and 3) leakage of telluric currents associated with the toroidal geomagnetic field at the core-mantle boundary. Therefore, voltage measurements carried out in the CAM-1 cable can be used, in combination with magnetic field measurement performed at the nearest observatory, to investigate the conductivity structure beneath the ocean crossed by the cable.

A preliminary discussion of the magnetotelluric (MT) response obtained from data of the geomagnetic Guimar Observatory (Canary Islands) and an average electric field along the CAM-1 cable, is presented in this report.

6.2 MT data

Figure 6.2 shows the electric field recorded for one month and used to estimate the MT responses shown in figure 6.3. After calculating the magnetic field components parallel and normal to the cable direction, the MT responses were calculated using the code of Larsen (1989). The results show very low apparent resistivities with phases increasing from almost 0 to 60º, in the period ranging from 1,000 to 100,000 s. Also shown in figure 6.3 is the model of the electrical resistivity obtained using a one-dimensional regularised inversion approach (Constable *et al.*, 1987). Only the general features of the resistivity distribution suggested by this model can be taken into account, since the geophysical situation is clearly three-dimensional. The model, however, suggests that the upper mantle is resistive, and resistivity decreases with depth, and that the upper crust is much more conductive. This pattern seems to be in accordance with the results obtained by Lizarralde *et al.* (1995) in the Philippine Sea plate, that show a resistive layer between 20 and 100 km depth.

Magnetotelluric (MT) responses calculated from submarine cables are generally significantly distorted by the coast effect (Vanyan *et al.*, 1998). Therefore, the interpretation of those data must be carried out in combination with un-shifted data, like magnetic transfer functions from MT soundings. In this work we used the magnetic transfer functions obtained at two land sites on the Portuguese mainland in order to constrain the model (figure 6.1).

6.3 Two-dimensional modelling

With the aim being to estimate a preliminary electrical resistivity distribution of the oceanic lithosphere, the MT apparent resistivities and phases together with the tipper functions (real and imaginary parts) from two sites carried out on land (figure 6.1), were modelled using a two-dimensional approach.

The ocean was taken to be a homogeneous layer with resistivity 0.3 Ωm. A rough representation of the bathymetry has been included in the model.

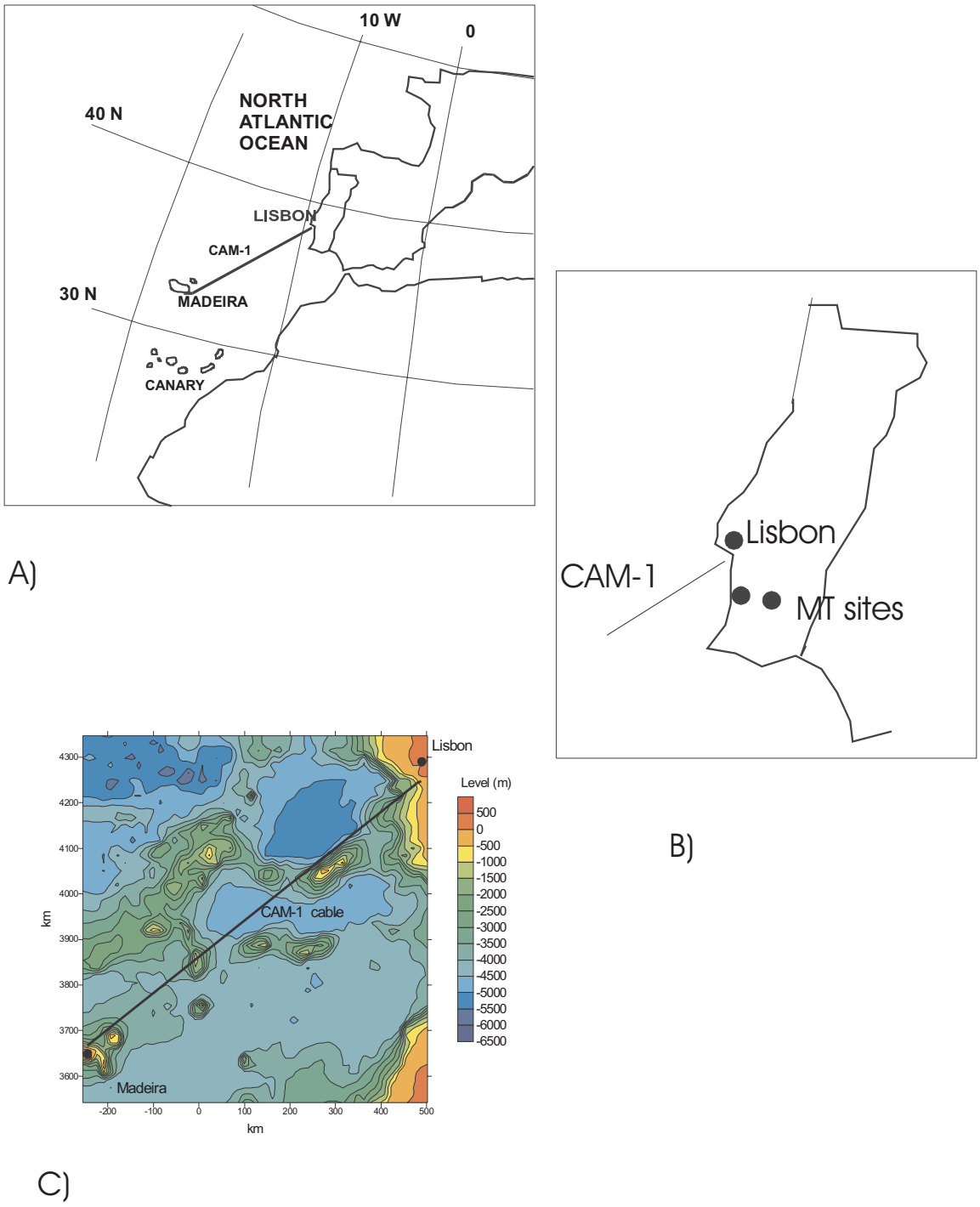

Figure 6.1. A- Location of the CAM-1 cable; B- Location of the MT sites; C- General bathymetry in the cable area.

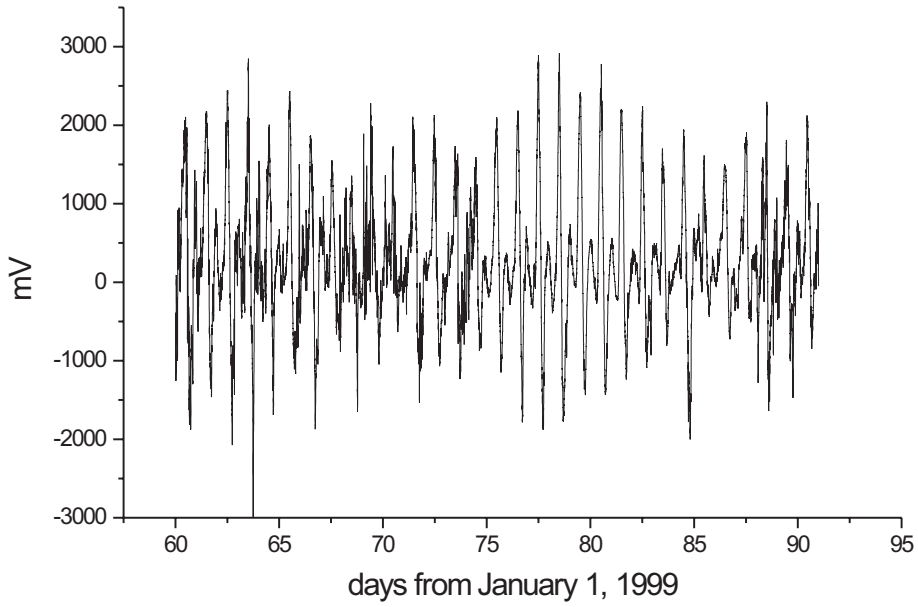

Figure 6.2. Voltage measurements used in the MT response of the CAM-1 calculation.

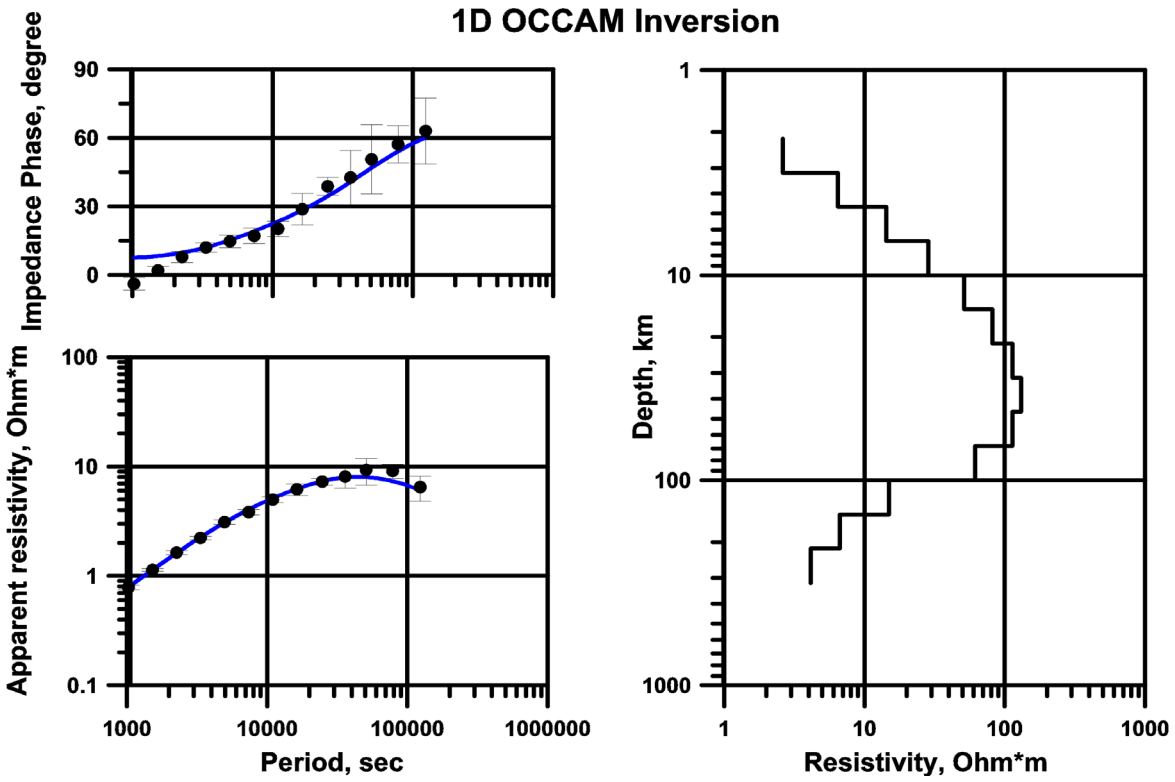

Figure 6.3. Apparent resistivities and phases obtained from cable data (left) and one-dimensional inversion of these curves (right).

Mathematical modelling was performed using finite element software. The model response for the cable was calculated by integrating the transverse component of the electric field along the cable and then dividing by the cable length. The impedance values obtained in this way were used to estimate the apparent resistivities and phases at periods ranging from 1000 to 100000 s.

The two-dimensional model obtained is shown in figure 6.4. Figure 6.5 compares the data with the model response. The agreement between theoretical and field data can be considered quite good.

6.4 Discussion

Only partial information can be obtained from a two-dimensional approach, since it can not represent the influence of all coastlines well (Iberia and Africa are important). It is believed that the effect of the bathymetry is less important due to the length of the cable, which is long enough to smooth out local anomalies caused by bathymetry.

Nevertheless, the modelling result should help to answer some pertinent questions:

1. What is the general pattern of the resistivity distribution in the lithosphere and how well is it resolved?
2. What is the influence of the electric resistivity of the adjacent continent (Iberia)?
3. What is the importance of the uppermost layers beneath the ocean?

The model displays a more resistive structure (100 Ωm) beneath the ocean in the depth range between ~7 and 350 km followed by a conductive deep zone (4 Ωm). The sediments at the seafloor are represented by a conductive layer (0.7 Ωm). The adjacent continental structures are revealed as conductors (10-30 Ωm) in the uppermost part of the lithosphere (whole of the crust) and resistive (500 Ωm) at depths corresponding to the upper mantle.

Due to the galvanic effect, Vanyan *et al.* (1995) argues that the integral resistivity is the most characteristic parameter when studying the oceanic lithosphere from cable data. The integral resistivity is defined as $R=\int \rho dz$ (Berdichevsky and Yakovlev, in Vanyan *et al.*, 1995). The integral resistivity of the resistive lithosphere layer in the model shown in figure 6.4 is of 3.5×10^7 Ω m^2. The conductance (or integral conductivity) of the sea- water and sediments is approximately 9300 S.

In order to investigate the sensitivity of the model to the lithosphere layer we have calculated the model responses for two different values of the resistivity (30 and 300 Ωm). Integrated resistivity is then 1.0×10^7 and 1.0×10^8 Ω m^2, respectively. The corresponding responses are shown in figure 6.6. No significant changes can be noted in the transfer function at sites 1 and 2. Variations of 30% in the apparent resistivity are observed in cable responses at very long periods.

A slightly different behaviour is observed when the thickness of the 100 Ωm layer varies by changing the depth of its deep boundary, from 350 to 100 km (figure 6.7), that is, with the integral resistivity ranging from 3.5×10^7 to 1.0×10^7 Ω m^2. The cable data are quite sensitive to the position of that boundary but the transfer functions measured on land and close to the coast show very small variations.

In order to examine the effect of the deep conductive layer (4 Ωm), model responses were calculated for two values (0.7 and 10 Ωm). In both cases the deep interface of the resistive layer (100 Ωm) was maintained at 350 km. In this case only variations on the apparent resistivity and phase less than 10% have been observed (not shown).

Figure 6.8 shows the results obtained considering variations in the resistivity of the adjacent continental crust (from 10 to 30 Ωm). The response of the submarine

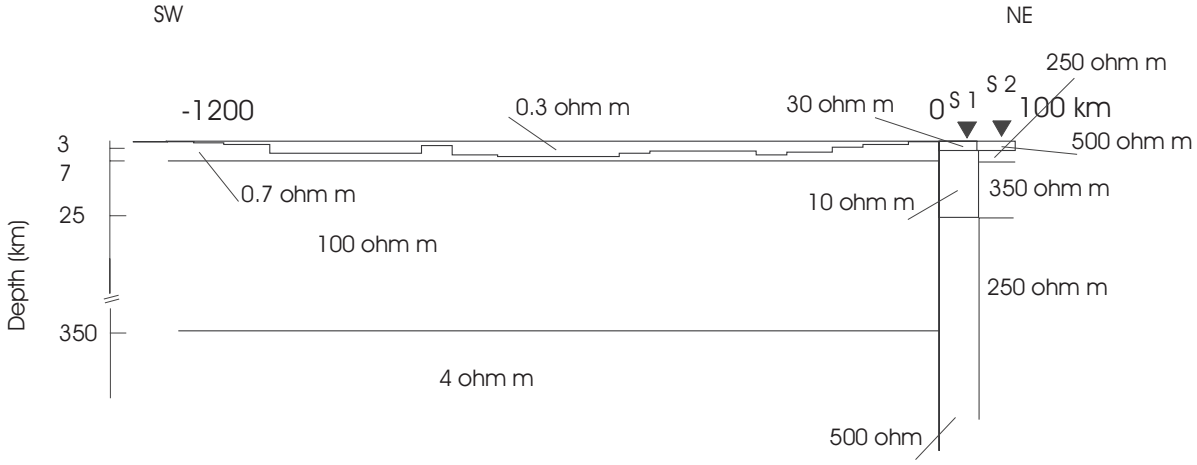

Figure 6.4. Two-dimensional model obtained from cable data (apparent resistivity and phase) and tipper data from MT sites S1 and S2. Note the change in vertical scale.

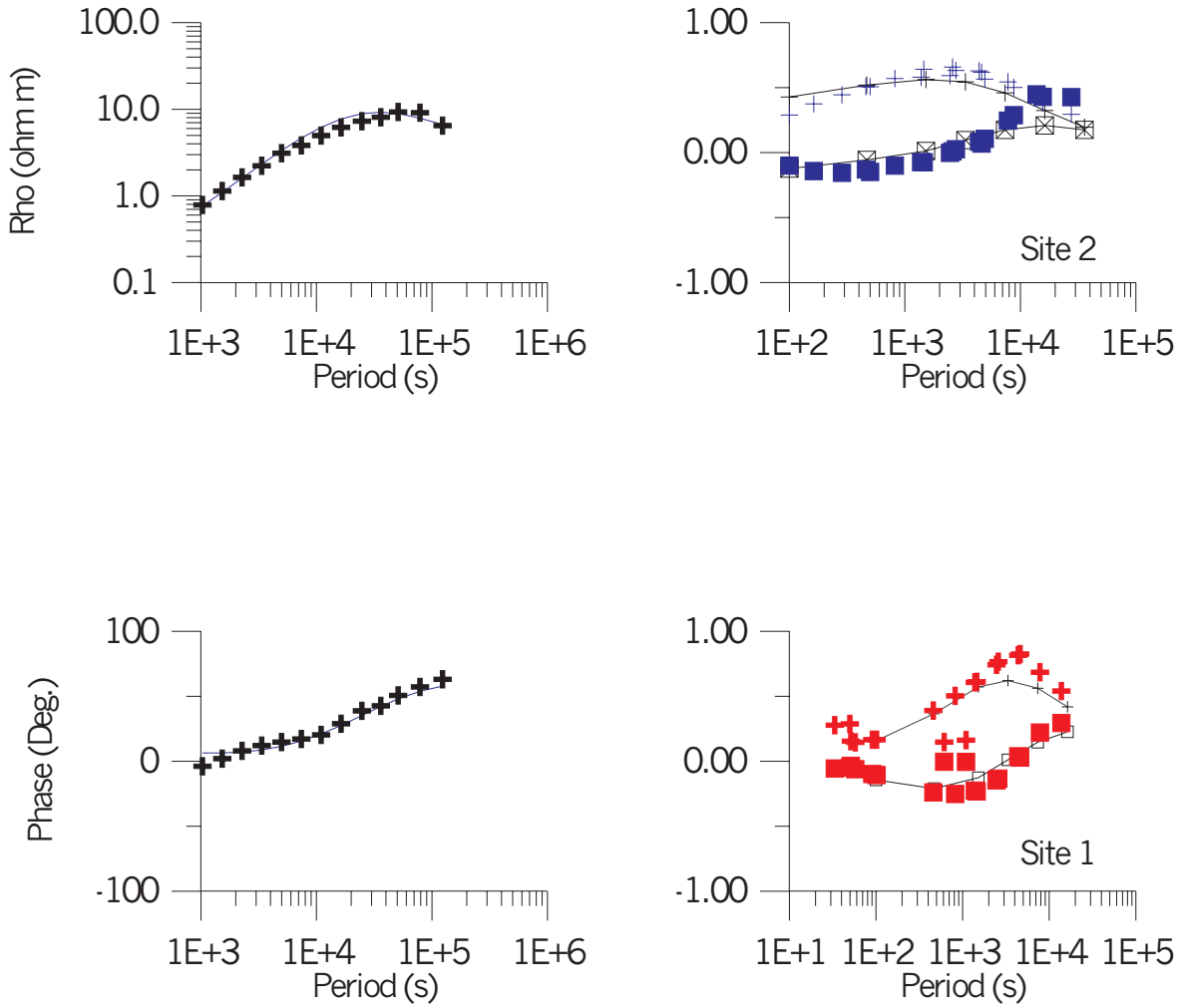

Figure 6.5. Apparent resistivities, phases (left) and tipper (right) from CAM-1 cable and MT sites 1 and 2 compared with the responses of the model shown in figure 6.4. Solid symbols- data; solid lines- model response. Cross real part; squares- imaginary part of the tipper function.

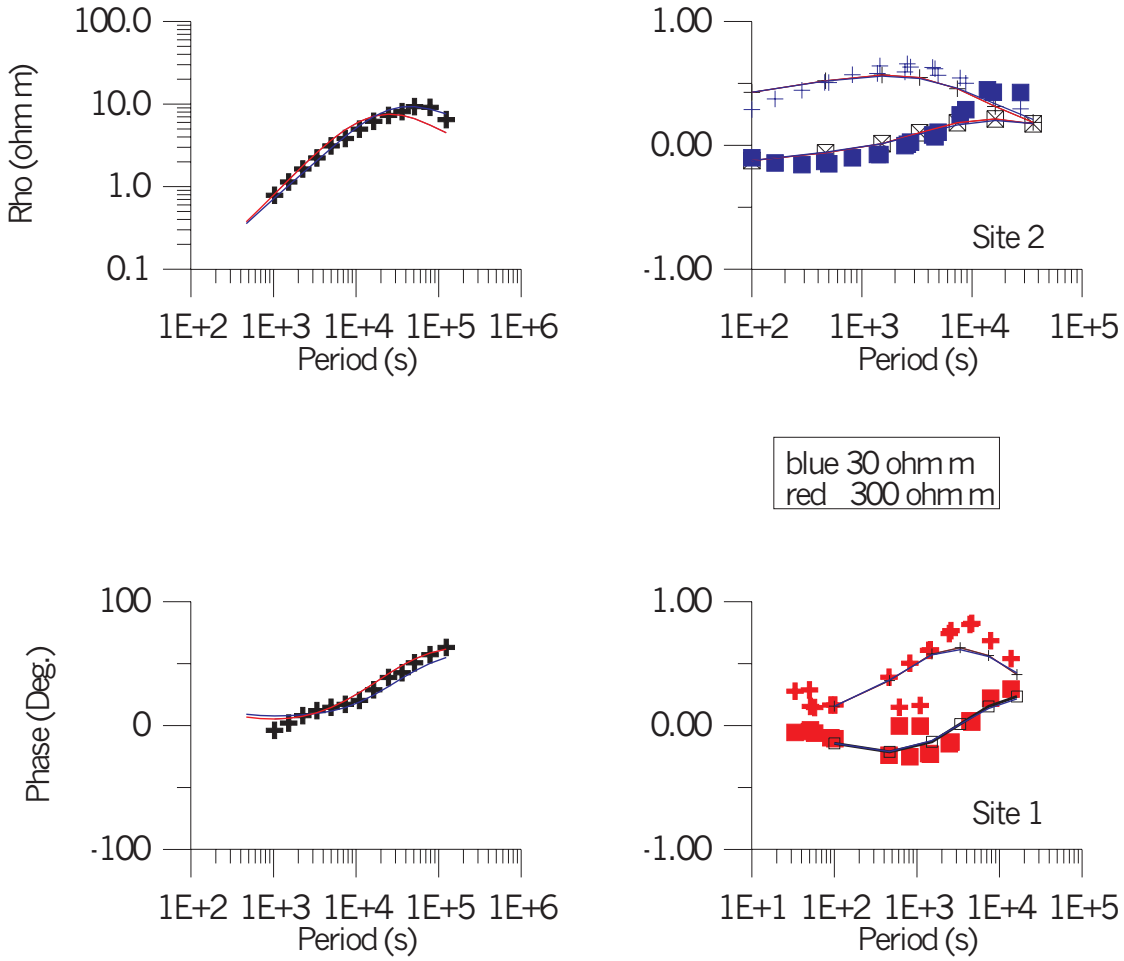

Figure 6.6. Comparison between field data and model responses calculated from model shown in figure 6.4, when the resistivity of the second layer beneath the ocean is 30 and 300 Ωm.

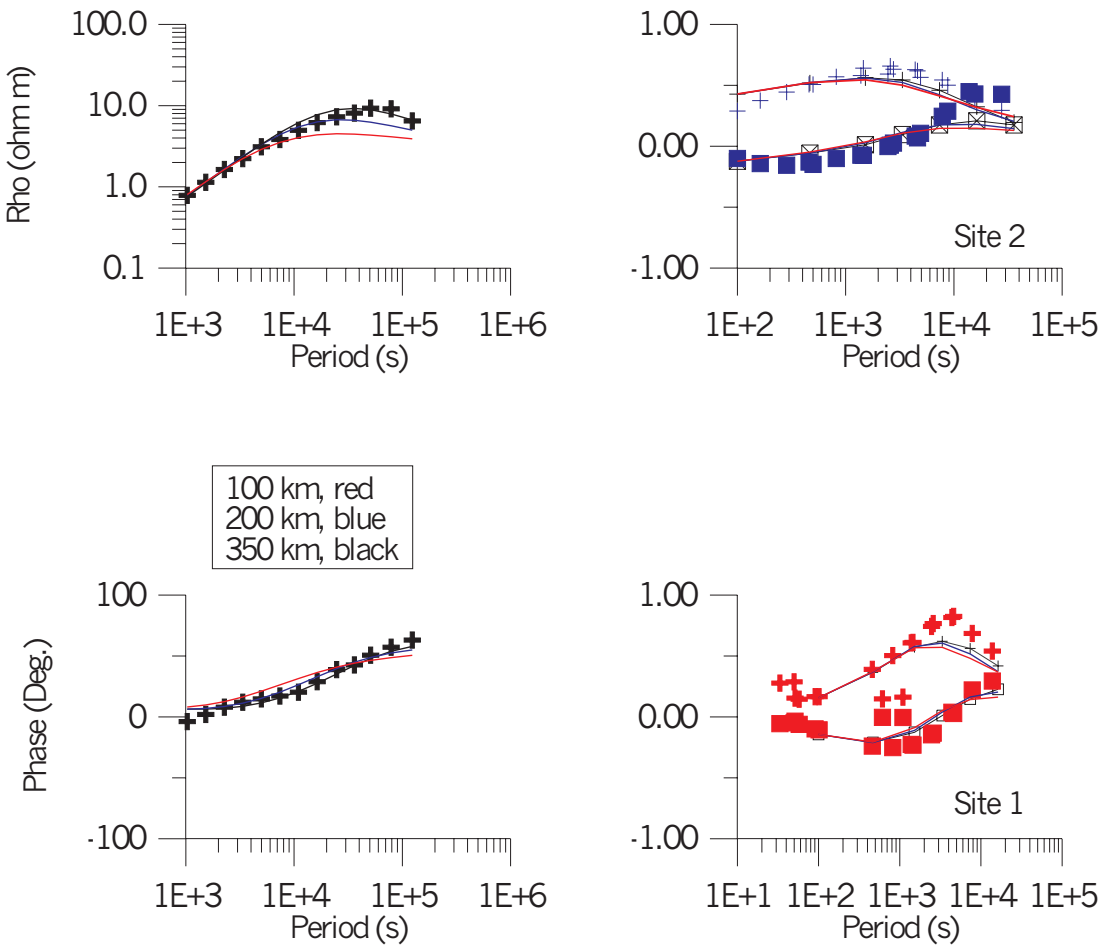

Figure 6.7. Comparison between field data and model responses calculated from model shown in figure 6.4, varying the bottom depth of the second layer beneath the ocean.

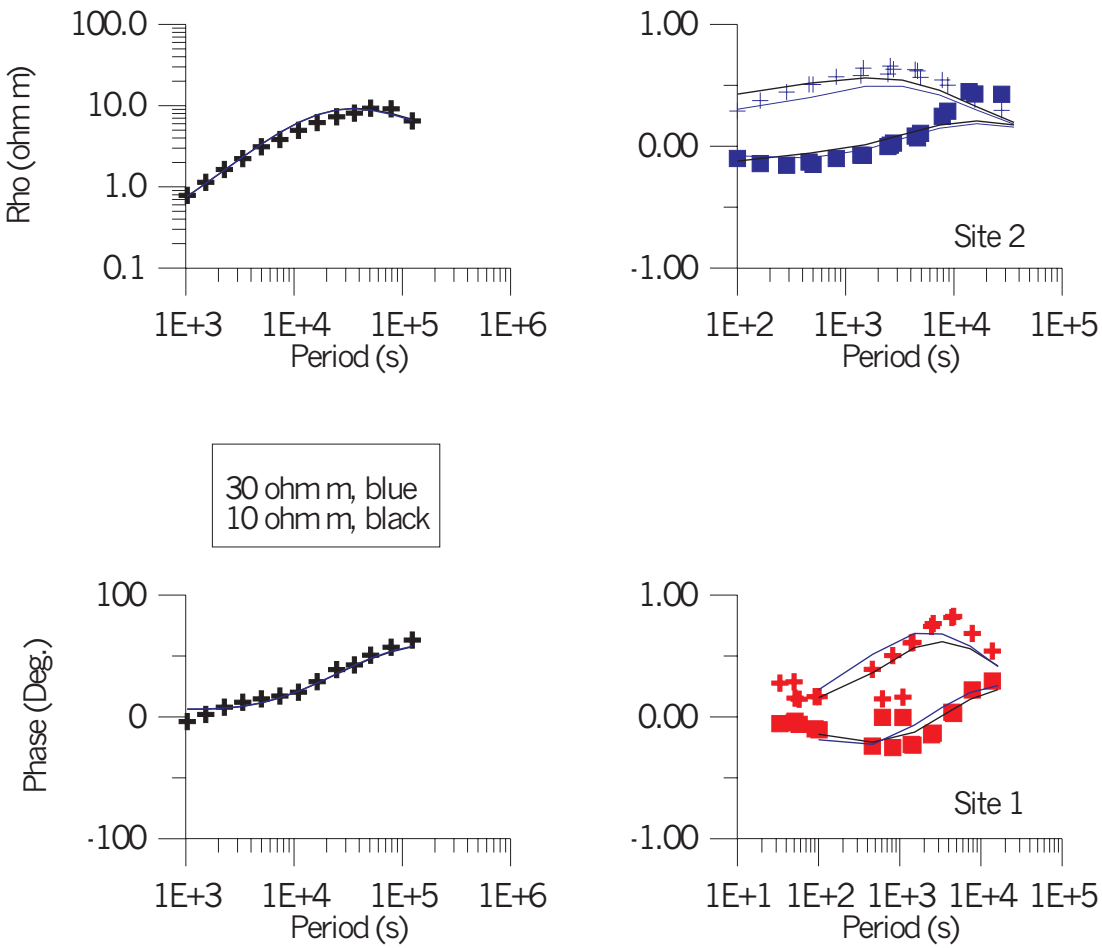

Figure 6.8. Comparison between field data and model responses calculated from model shown in figure 6.4, when the resistivity of the middle crust beneath MT site 1 varies.

cable does not show any sensitivity to this model parameter. In opposition the MT-tipper responses show significant changes, mainly in the real part and at short periods.

The importance of the uppermost layer in the ocean part of the model was investigated by changing the resistivity of the sediments from 0.7 Ωm to 1.7 Ωm, that is, varying the conductance of the sea water-sediments layer from 9300 to 3800 S. The calculated model responses are shown in figure 6.9. As can be noted, both responses are sensitive to the parameter. The cable apparent resistivity is the most affected response, mostly at short periods. The real part of MT-tipper measured on land shows also variations at periods greater than 1000 s.

6.5 Conclusions

Voltage measurements made between the ends of the CAM-1 submarine cable have been used to estimate the geoelectrical structure beneath the ocean between Lisbon and Madeira Island. Using the cable data and the magnetic observations carried out during March 1999 in the geomagnetic observatory of Guimar (Canary Islands), the apparent resistivities and phases were calculated. Magnetic transfer functions (tipper) measured in two long period MT stations located on land but near to the coastline were included in the modelling in order to better constrain some model parameters.

The result obtained by trial-and-error modelling suggests a basic three-layer geoelectrical structure beneath the ocean. The conductance of the uppermost layer, representing marine sediments, might be in the range between 9000 and 10000 S. The must probable order of the integral resistivity of the intermediate layer is 10^7 Ω m^2.

The modelling experiments described above shown that:

1. The apparent resistivities and phases estimated from the submarine cable do not show significant sensitivity to the continental geoelectrical structure;
2. The tipper functions measured on the continent are not significantly affected by the layered structure of the middle lithosphere beneath the ocean;
3. The cable responses and the tipper functions show high sensitivity to the sea-floor conductance at different period ranges. The tipper is significantly affected by the ocean-continental structure at short periods. These results suggest that these type of data can be combined in order to investigate the structure of the shelf;
4. The cable response also exhibits important sensitivity to the integral resistivity of the lower lithosphere-upper asthenosphere structure.

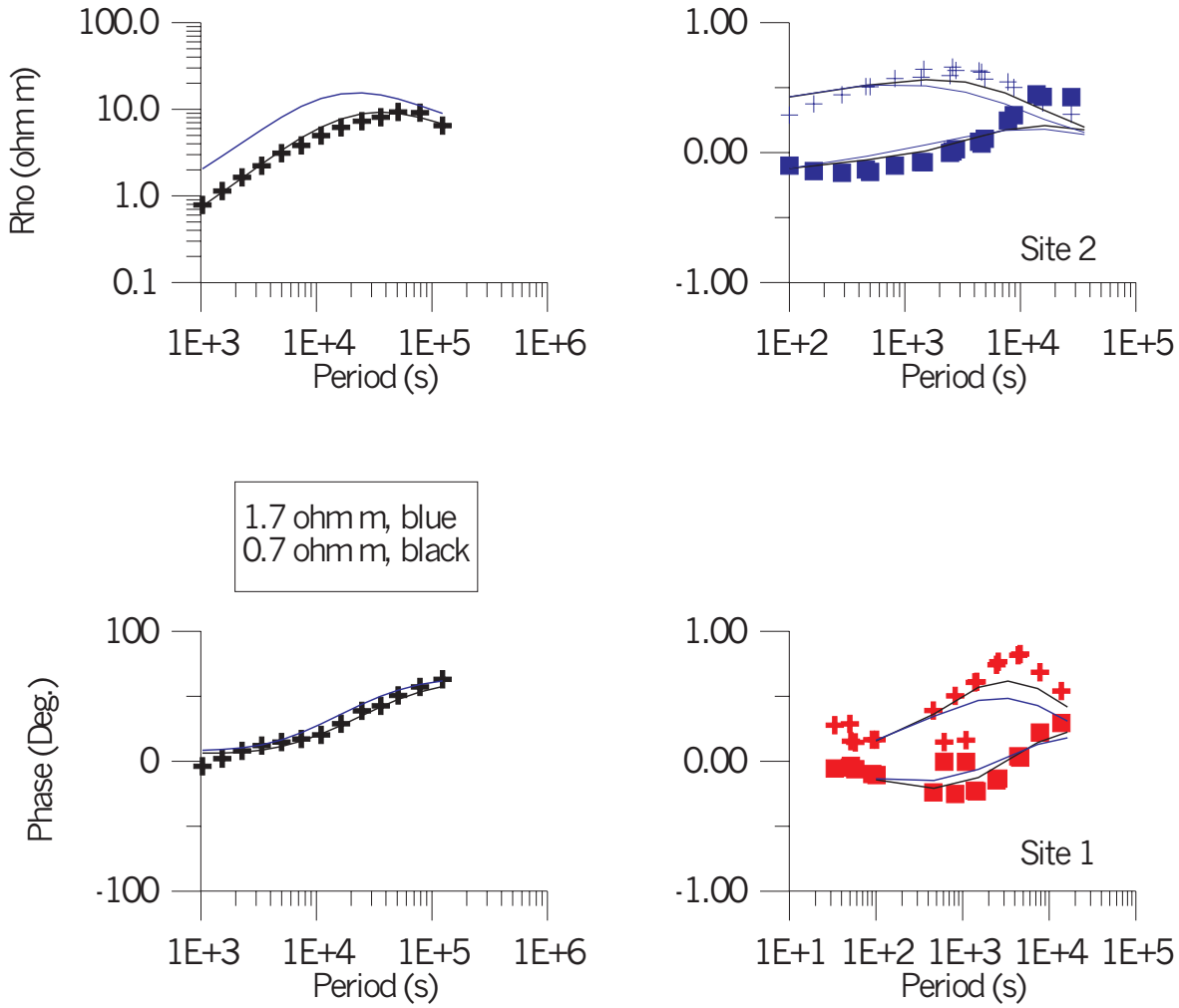

Figure 6.9. Comparison between field data and model responses calculated from model shown in figure 6.4, when the resistivity of the uppermost layer beneath the ocean (sediments) is 0.7 and 1.7 Ωm.

6.6 Acknowledgements

The authors would like to thank many people at Marconi and TRIMAD who provided us the opportunity to use the cable and helped us in several ways. In particular we thank Eng. Vasco Sá, Mr. António Abrantes and Mr. Marçal from Marconi and Dr. Luís Sousa and Mr. Crisóstomo Luís from TRIMAD. Thanks are also due to Luís Matias for his interest in the subject and initial help, as well as, to Nick Palshin for the calculation of the clabe reponse and the Occam's model. This work was developed in the scope of the ISO-3D project funded by EC. Thanks to FCT for continuous supporting of the CGUL are also due.

6.7 References

Constable, S.C., Parker, R.L. and Constable, C.G., Occam's inversion: a practical algorithm for generating smooth models from electromagnetic sounding data, Geophysics,52, 289-300, 1987.

Larsen, J.C., Transfer functions: smooth robust estimates by least squares and remote reference methods, Geophys. J. Int., 99, 645-665, 1989.

Lizarralde, D., Chave, A.D., Hirth, G. and Schultz, A., Long period magnetotelluric study using Hawaii-to-California submarine cable data: implication for mantle conductivity, *Journal of Geophysical Research*, 100, 17837-17854, 1995.

Monteiro Santos, F.A., Soares, A., Trindade, L., Nolasco, R., Rodrigues H., Miranda, J.M, Lourenço, N., Luís, J., Flosadottir, A., Junge, A., Sinha, M., MacGregor, L., Dean, S., Barker, N., Riches S. and Z. Cheng, Voltage measurements in the CAM-1 submarine cable between Madeira Island and Portugal mainland, *Earth, Planets and Space*, 2001 (submitted).

Vanyan, L.L., Utada, H., Shimizu, H., Tanaka, Y., Palshin, N.A., Stepanov, V., Kouznets, Studies on the lithosphere and the water transport by using the Japan Sea Submarine Cable (JASC); 1, Theoretical considerations, *Earth, Planets and Space*, 50 (1), 35-42, 1998.

Vanyan, L.L., Palshin, N.A. and Repin, I.A., Deep magnetotelluric sounding with the use of the Australia-New Zealand cable, 2, Interpretation, Physics of the Solid Earth (English Translation), V. 31, Nº. 5, 417-421, 1995.

Chapter 7

Magnetotelluric measurements on the Azores Islands

A. Junge[1], F. Santos[2], and the ISO-3D team[3]

1. Institut für Meteorologie und Geophysik, Feldbergstr. 47, D-60323 Frankfurt am Main, Germany
2. Departamento de Física and Centro de Geofísica da Universidade de Lisboa, Campo Grande, Ed. C8, Piso 6, 1749-016 Lisboa, Portugal
3. other members of the ISO-3D: J.M. Miranda, N. Lourenço, J. Luís, A. Flosadottir, M. Sinha, L. MacGregor, A. Soares, S.Dean, N. Barker, S. Riches and Z. Cheng

7.1 Summary

Time variations of the Earth's natural magnetic and electric (=telluric) field contain valuable information about the conductivity distribution of the Earth's interior. In the oceans, due to the shielding effect of the highly conducting seawater only fields with periods longer than 1 min will penetrate into the underlying subsurface and resolve the structure of the upper mantle. However, magnetotellric observations along the Mid-Atlantic Ridge can be used to complement marine studies which use active sources and concentrate on the structure of the oceanic crust.

During October 1999 three magnetotelluric field sites were installed on the Azores Islands at Terceira, Faial and Flores. Time variations of the 3 magnetic and 2 horizontal telluric field components were recorded simultaneously for up to 4 weeks in the period range between 1 min to 1 day. The data are of excellent quality. A preliminary analysis reveals a high conductivity layer in the upper mantle aligned parallel to the ridge axis.

7.2 Geology

The Azores archipelago is situated in the Mid-Atlantic Ridge region at the triple junction of the American, European and African plate (Figure 7.1). The rocks are of volcanic origin - active volcanism is still being observed at several islands. The electrical conductivity of the crust and mantle in the Azores area has not been investigated previously. As partial melt is assumed to be beneath the ridge, the electrical conductivity should increase over a certain depth range. Thus conductivity studies might give valuable indications of the vertical and also lateral extent of partial melt occurrence, and can be used as a constraint for rheological and geodynamic modelling of the crust and mantle within the ridge/hotspot/triple junction area.

7.3 Magnetotellurics - some basics

Time varying natural electromagnetic fields induce electric currents in the conductive Earth's interior. The conductivity structure of the subsurface can be derived from continuous and simultaneous observations of the field components B_x, B_y, B_z, E_x, E_y, at the surface. For this purpose frequency dependent and complex valued transfer functions T (= tipper or induction vector) and Z (= impedance tensor) between various field components are statistically estimated in the frequency domain, i.e. the following equations are solved by minimising the residuals.

$$B_z = T_{zx} B_x + T_{zy} B_y + \delta B_z$$

$$E_x = Z_{xx} B_x + Z_{xy} B_y + \delta E_x$$

$$E_y = Z_{yx} B_x + Z_{yy} B_y + \delta E_y$$

The tipper vector is usually plotted as real and imaginary arrows in the x-y plane for different periods. Especially for a 2-dimensional structure, the real arrows point into the direction of the less conducting region.

The complex elements of the impedance tensor Z can be represented by their magnitude $|Z|$ and phase φ, whereby it is more convenient to plot the apparent resistivity $\rho_a = \mu |Z|^2/\omega$ where μ is the magnetic permeability and ω is the angular frequency.

The plot of log ρ_a and φ against log period T gives a first indication of the conductivity structure beneath the site due to the increasing penetration depth of the electromagnetic fields with period (skin effect). In the case of 2-dimensional structures the electric and magnetic field can be described by the sum of two

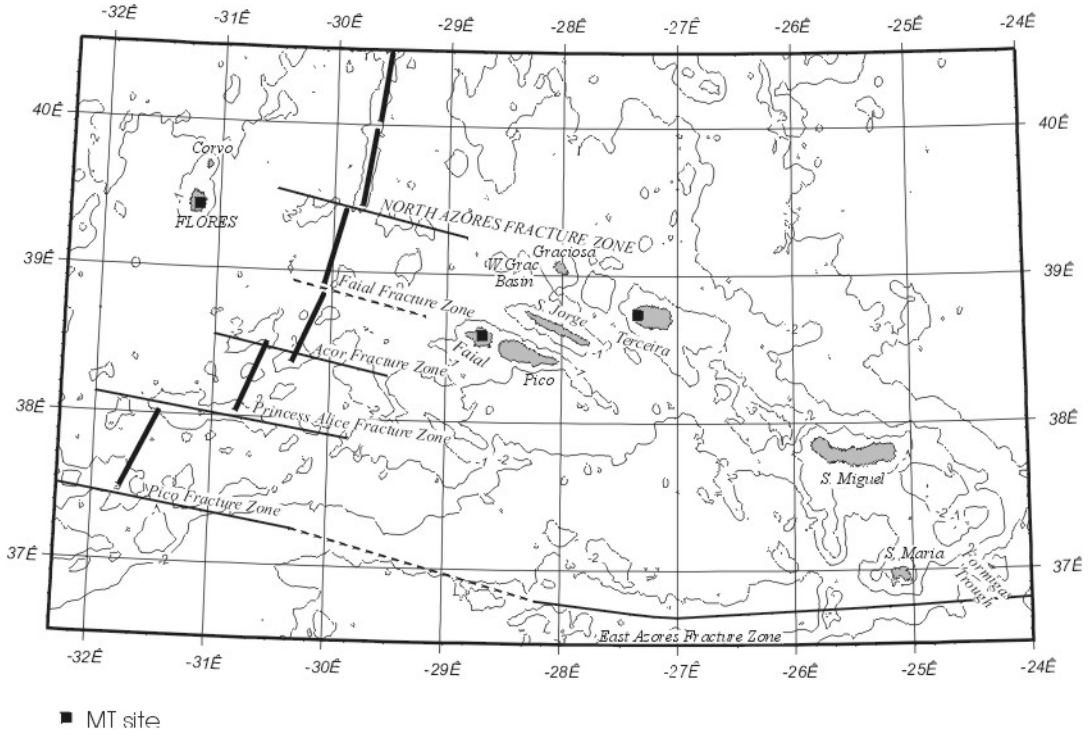

Figure 7.1. The Azores islands: Bathymetry and location of MT sites.

decoupled modes (TE and TM modes). If the x-axis of the instruments' co-ordinate system is parallel to the strike direction, Z_{xy} is related to the TE mode and Z_{yx} to the TM mode, whereas the main diagonal elements Z_{xx} and Z_{yy} vanish.

7.4 Experiment

Beside the Frankfurt Long-Period-Magnetotelluric (= LMT) system, we were able to use two additional LMT systems from the Geophysical Equipment Pool (GEP) of the Geophysical Research Centre (Geoforschungszentrum = GFZ) Potsdam. All systems contain identical parts, i.e. fluxgate magnetometer, data-logger (SRAM) and Ag/AgCl//KCl electrodes (Junge, 1990). The Frankfurt system has an additional low-pass filter for the magnetic channels with cut-off period of either 10 or 240 s. The amplification of the telluric field is site-dependent and may be chosen between 50, 100, 200, 500 and 1000. The low-pass filters for the telluric field are similar to those for the Frankfurt magnetic components.

Site selection was not easy due to intensive cattle farming on all the islands. The locations of the field sites are plotted in Figure 7.1. On Terceira the site is approximately 2 km inland from the coast, on Flores and Faial the sites are close to the centre of each island. The centres were chosen to reduce the influence of the transition between sea-water conductivity (0.25 Ωm) and the conductivity inland (> 100 Ωm) on the measurements (coast-effect). The GFZ-systems were set up on Terceira and Flores, the Frankfurt system on Faial. The length of the telluric lines varied between 40 m and 60 m, the ground was generally humid and thus guaranteed good electrical contact between electrodes and soil.

Each system runs automatically. The logging time is limited by data storage capacity (6.5 MB for the Frankfurt system, 8 MB for the GFZ system, 16 bit word for each sample, 5 channels on each system), sampling rate (2 sec for the GFZ system, 30 sec for the Frankfurt system) and battery power (about 12 days with two 75 Ah lead batteries). The Frankfurt system was run for 48 hours on a 2 sec sampling rate to extend the period range to the shorter period end. In order to achieve maximum recording time, site visits were performed according to the following scheme:

Date	Travel / Stay	Purpose
28-29/09	Travel Junge/Santos to Terceira	Pick up all equipment at Terceira Airport, send 2 systems to Flores and Faial. Look for site on Terceira
30/09-02/10	Stay Junge/Santos on Terceira	Build up site, test run, leave site with 2 batteries
02/10	Travel Junge/Santos to Flores	Pick up equipment, look for field site
02-05/10	Stay Junge/Santos on Flores	Build up site, test run, leave site with 2 batteries, instruct local geologist for battery change
05/10	Travel Junge/Santos to Terceira	Control site on Terceira, change battery against an additionally bought battery
04-05/10	Travel Golden Frankfurt-Lisboa-Faial	Steven Golden is member of the Frankfurt group, picks up equipment at Faial and looks for site
06-07/10	Travel Junge Terceira-Lisboa-Frankfurt	Junge back to Frankfurt
06/10	Travel Santos to Faial	Santos meets Golden, set up site
06-08/10	Stay Santos/Golden on Faial	Test runs

08/10	Travel Santos to Terceira	Control site on Terceira, change batteries
09/10	Travel Santos to Lisboa	Santos back to Lisboa
08-11/10	Stay Golden on Faial	Control site, change batteries
11-12/10	Travel Golden Faial-Lisboa-Frankfurt	Golden back to Frankfurt
21-25/10	Travel Santos to Azores	Collect equipment, send equipment back to Frankfurt/Lisboa

The battery change on Flores had to be performed by a local geologist and unfortunately failed. Thus the Flores time series is limited to 11 days.

7.5 Results

The signal to noise ratio was rather high at all 3 sites. Figure 7.2 shows a 72 hours interval of all 3 magnetic field components at all sites. The data have been filtered numerically with a 10 minute low-pass filter and decimated to a 5 minute sampling rate. There is almost perfect correlation between the horizontal components, whereas differences occur in the vertical magnetic field for short periods. This is certainly due to the well known coast effect but may also give indications of lateral conductivity changes in the subsurface beneath and between the islands.

The induction arrows have been calculated so far for site TERA. They are plotted in figure 7.3 for periods between 70 sec and 60,000 sec. The real arrows point to the west clearly denoting the coast effect as the site is on the eastern side of Terceira. The imaginary arrows are more or less parallel to the real arrows changing sign at 400 sec period where the real arrow reaches a maximum of 0.6. Two-dimensional modelling is needed to show whether the coast effect alone can explain the data.

Figure 7.4 gives a more detailed example of the magnetic and telluric field at all sites. The sampling rate is the same as in the foregoing example, the time section is 12 hours only. For E_y the order has been changed: E_y-Faial is the lower one, the other two are on top of the figure. The vertical magnetic component is small compared to the horizontal components. As the telluric field is much more influenced by local structures than the magnetic field, the different behaviour at the three sites is expected.

For TERA the impedance tensor was calculated for the same period range as for the induction arrows. As the strike direction is orientated towards North-South according to the induction arrows, the Z_{xy} component is interpreted as the TE-mode and subsequently a preliminary one dimensional model was derived (figure 7.5). It shows the highly conducting layer on top due to the seawater around the island but also a second highly conducting layer at about 50 km depth. Although its depth range might still be questionable due to static shift effects, the existence of the conducting layer in the upper mantle seems to be significant. Further studies will concentrate on the data from the other two islands. Comparisons will show possible differences between the conductivity-depth distribution beneath each island. The coast effect will be taken into account and two- or three dimensional models will give a more realistic view of the mantle conductivity.

7.6 References

Junge, A., 1990. A new telluric KCL probe using Filloux's Ag/AgCl electrode, PAGEOPH, 134/4.

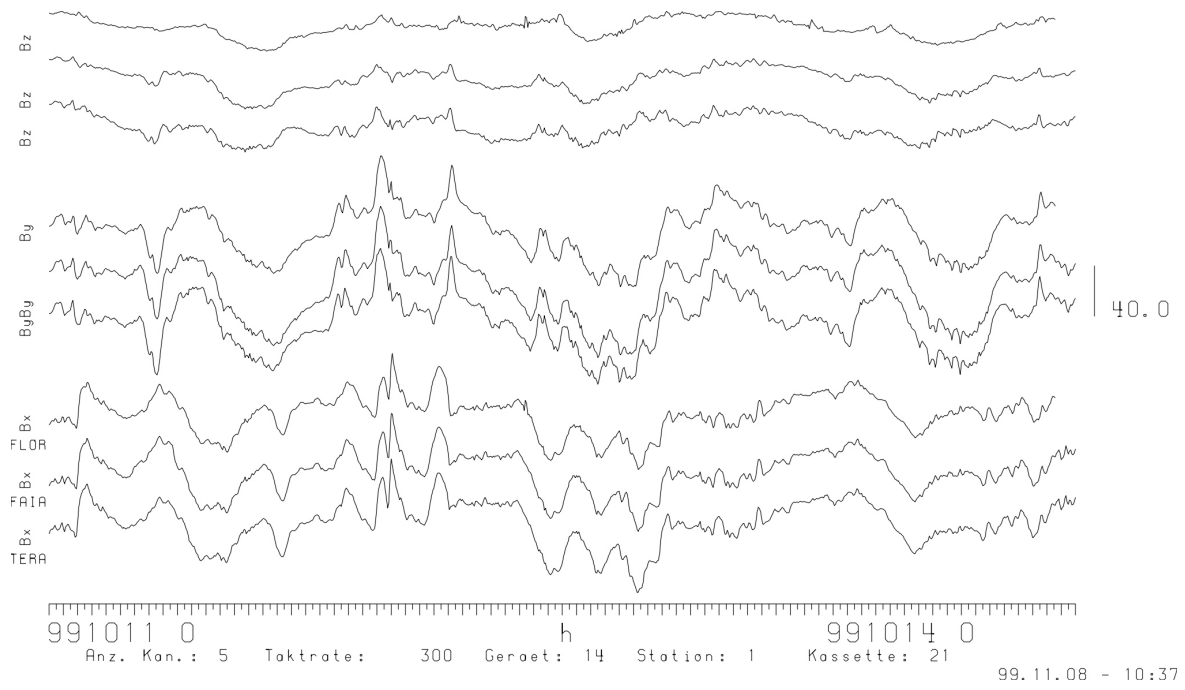

Figure 7.2. 72 hours example of magnetic components measured at Terceira (TERA), Faial (FAIA) and Flores (FLOR) islands between 99-10-11 and 99-10-14. Units are nT.

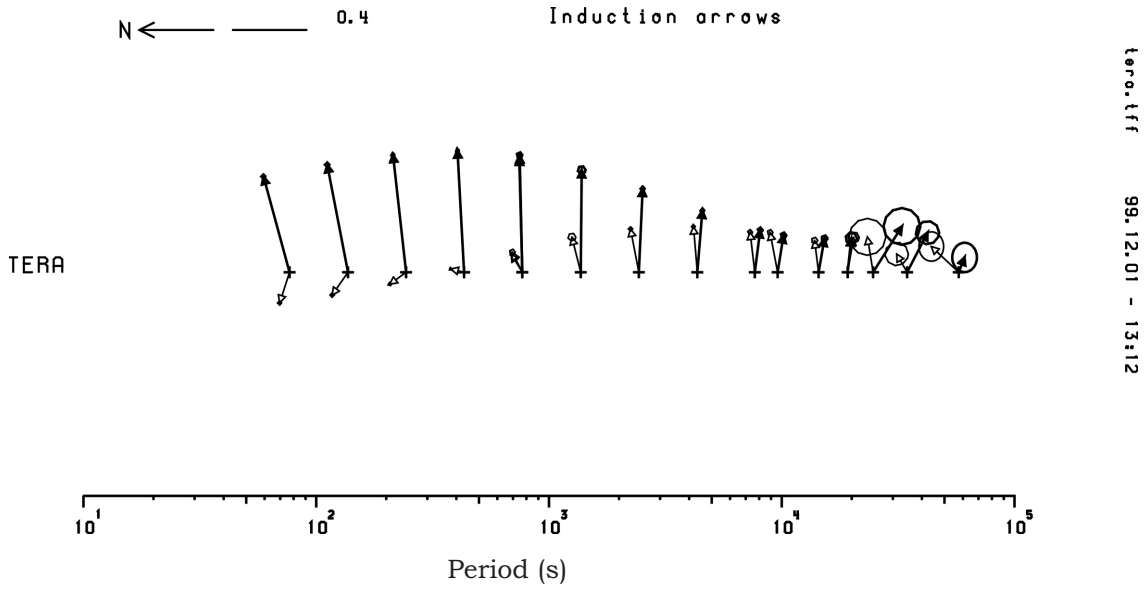

Figure 7.3. Induction arrows for Terceira (TERA) in the period range between 70 sec and 60.000 sec. Full arrows denote the real part, open arrows the imaginary part. Scale on top of Fig., note horizontal arrow on top pointing toward the North.

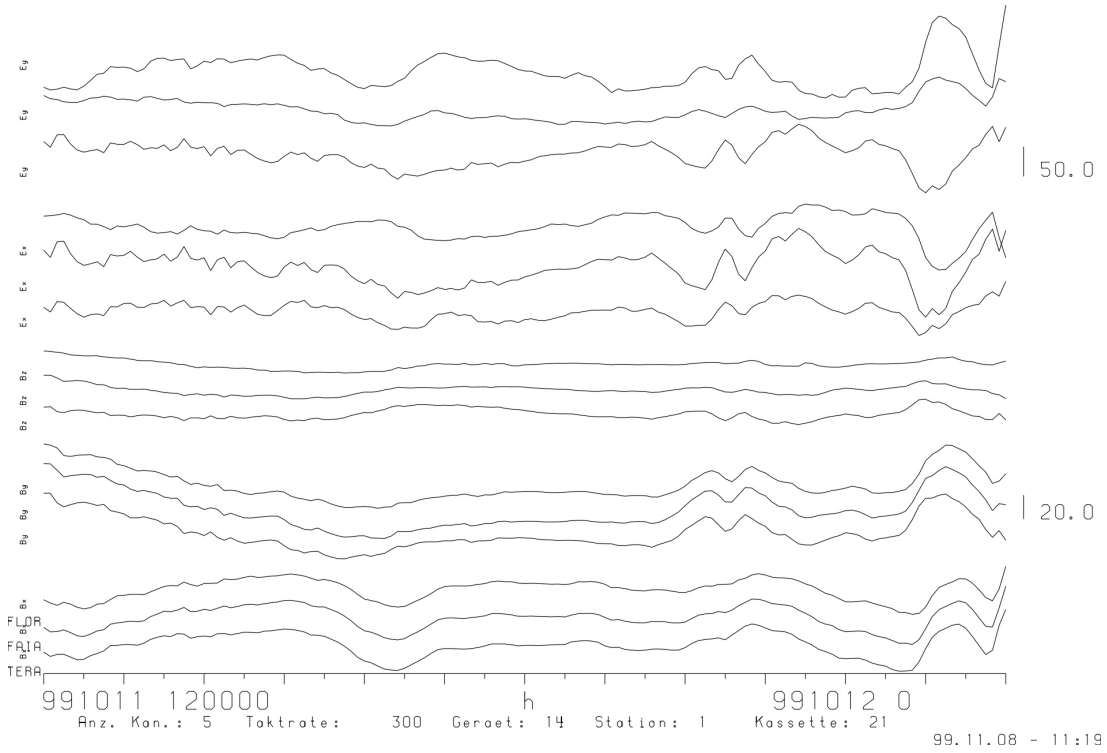

Figure 7.4. 12 hours example of electric and magnetic components measured at Terceira (TERA), Faial (FAIA) and Flores (FLOR) islands between 99-10-11 and 99-10-12. Units are mV/km and nT.

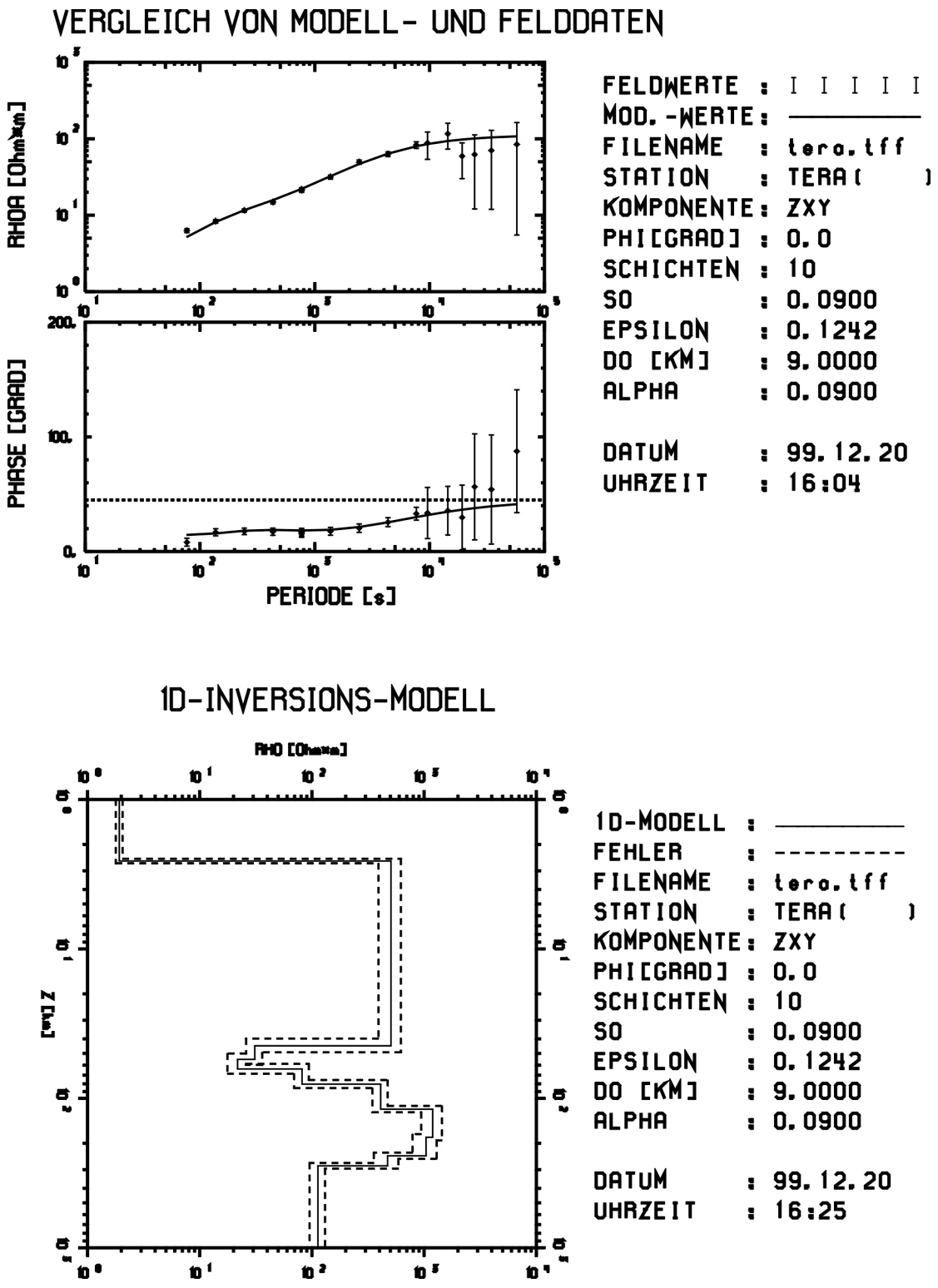

Figure 7.5. One-dimensional model of TE mode magnetotelluric transfer functions of TERA. Top: model fit, 68% error bars. Bottom: inversion model (Schmucker, 1974).

Chapter 8

Oscillations of the on-shore telluric field generated by oceanic tides

A. Junge[1] and the ISO-3D team[2]

1. Institut für Meteorologie und Geophysik, Feldbergstr. 47, D-60323 Frankfurt am Main, Germany
2. Other members of the ISO-3D group: J.M. Miranda, N. Lourenço, J. Luís, F. Santos, A. Flosadottir, M. Sinha, L. MacGregor, A. Soares, S.Dean, N. Barker, S. Riches and Z. Cheng

8.1 Introduction

Tidal oscillations of the telluric field were first predicted theoretically by Faraday more than 150 years ago (Faraday, 1832). They were observed on-shore about 100 years later (Egedal, 1937) and first attempts were made to explain the on-shore observation after another 10 years (Longuet-Higgins, 1949). The physical reason for the oscillation is the tidal movement of water in the ocean. The charged particles in the water are deviated by electromotive forces (Lorentz force) due to the velocity component perpendicular to the Earth's magnetic main field. Thus charges build up at the shore and cause electrical fields spreading far inland. It is obvious that, through the knowledge of the magnetic field and the observation of the electric field, it should be possible to derive the effective water velocity and the mass transport in the water.

However, a general quantitative model is still missing, as calibration is difficult due to the influence of the conductivity distribution in the ground beneath the area under investigation. Efforts have been made by Larsen to model the water transport across the straight of Florida (Larsen, 1992) using a telecommunication cable on the ocean bottom which was no longer in use. Simultaneous land based observations showed good correlation with the cable data and attempts at quantitative calculations were made. As ocean bottom cables are limited in number and location, the idea is to find a suitable method to derive oceanic currents from on-shore telluric fields.

In the second section of this chapter the theoretical background will be given, followed by the presentation of some observations in Germany and Scotland. In the fourth section the results are interpreted by a simple model and finally future perspectives are discussed.

8.2 Theoretical background

The theory of ocean induced electromagnetic fields has been developed continuously over the last decades (Longuet-Higgins, 1949; Sanford, 1971; Chave and Luther, 1990; Larsen, 1992). This chapter shows a model study to explain the ocean induced electric (= telluric) fields (Junge, 1988) in the North-German sedimentary basin.

Figure 8.1 gives a schematic view of the tidal current at the German-Netherland coast in the North Sea for a fixed time t_o. The width of the current is about a = 50 km, its wavelength is λ_y = 660 km, the mean water depth is h_w = 50 m (Hansen, 1952; Sager, 1964). Vertical water flow is negligible compared to v_y ($\approx$ 1 m/s). The y-axis points towards the North-East direction. The conductivity σ_w of seawater is taken as constant to a first order approximation, as well as the water depth h_w, the current width a and current velocity. Then the integrated conductivity of the seawater, $\tau_w = \sigma_w \cdot h_w$, is also constant. The upper crust on land has the integrated conductivity τ_L, and similarly τ_L' beneath the sea, and its thickness is of the order of 10 km. The middle and lower crust and the upper mantle are less conductive and can be regarded as insulating in this model (zero conductivity). The depth dependent conductivity distribution beneath the insulating layer does not influence the following model calculations.

Charge separation will take place as the ions in the seawater move with velocity v_y perpendicularly to the B_z component of the Earth magnetic main field. These charges cause electric currents in vertical planes in and beneath the seawater. As v_y varies along the y-axis, additionally horizontal currents occur at both sides of the current. The scale length of the horizontal currents exceeds the thickness of the conducting crustal layer by more than one order of magnitude. Thus a thin sheet approximation and the vertically integrated current density $\underline{I}^*$ is introduced:

$$\underline{I}^*(x,y,t) = \int_{z_1}^{z_2} \underline{j}(x,y,z,t)\,dz$$

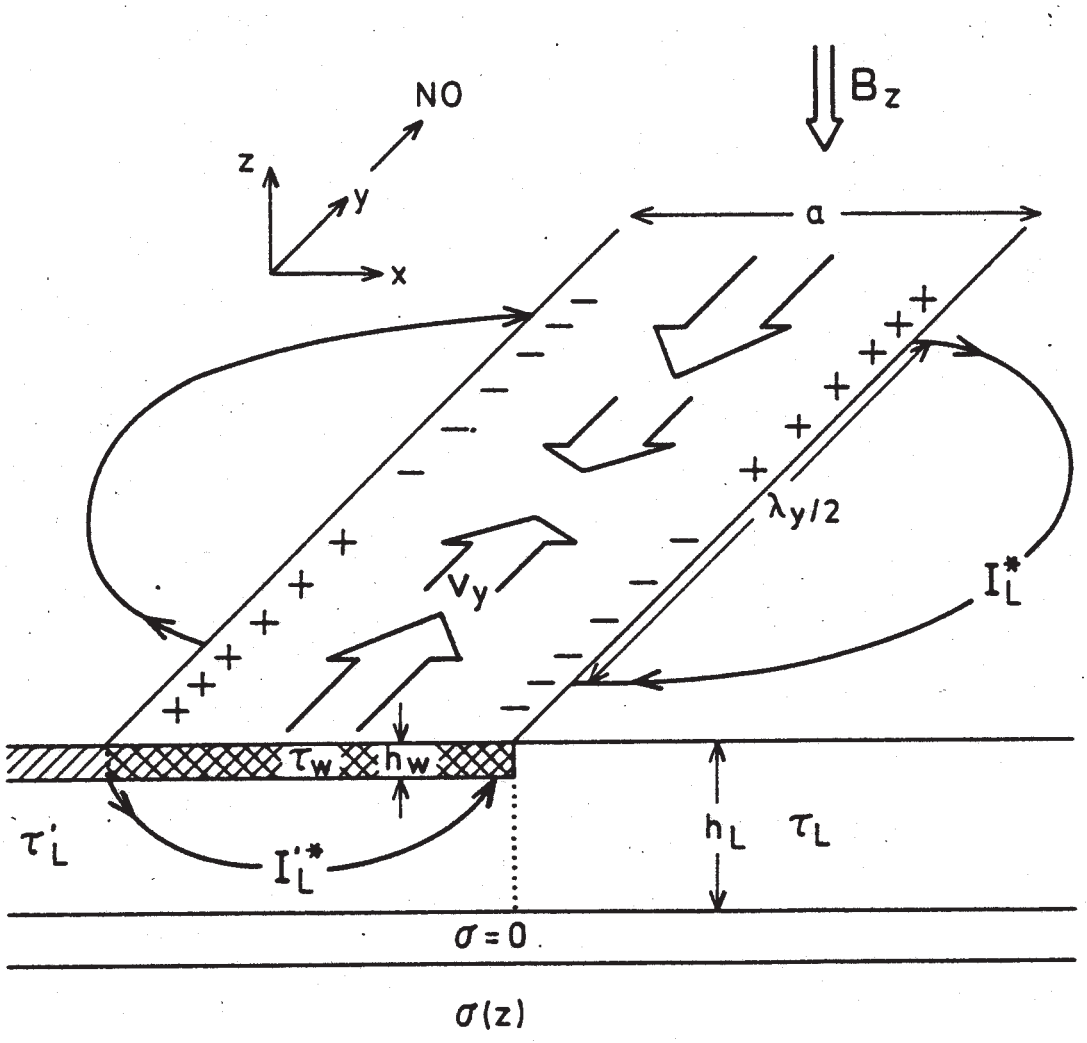

Figure 8.1. Schematic view of the tidal current v_y near the coast and induced telluric currents I* at a fixed time t. The seawater is hatched, the seawater moving with velocity v_y is double-hatched. For further explanations see text.

z_1 and z_2 are the lower and upper boundary of the conducting layer in figure 8.1 and j is the current density. We apply Ohm's law for moving conductors in the oceanic water current for the configuration in figure 8.1 (cf. Larsen, 1992, eq. (2.16)):

$$I_L^* = (\tau_W + \tau_L^{'})E_x - \tau_W B_z v_y$$

and

$$I_L^* - I_W^* - I_L^{'*} = -\tau_W B_z v_y$$

where τ_W and τ'_L are the integrated conductivities of seawater and the conducting sediments beneath. Due to the large scale length of the water current compared to the water depth, the electric field E_x is approximately homogeneous. The right hand side of the last equation is the current source and the left hand side represents the different parts of the resulting currents in the vertical and horizontal planes.

As the time variations are rather slow and the water depth is shallow, the influence of induction can be neglected - contrary to the treatment of the process in the deep ocean. Therefore in the following the electric field of a quasi direct current source in a thin horizontal sheet is considered, i.e. the electrical potential in a thin sheet has to be calculated.

Figure 8.2 shows the current distribution for a current source I_L^* at $(x=0,y_o)$. As we have a 2-dimensional geometry, the potential $V^*(x_p,y_p,t)$ is logarithmic and its value at P in the distance $r_p=[x_p^2 + (y_p-y_o)^2)^{1/2}$ from the current source is

$$V^*(x_p, y_p, t; y_o) = \frac{I_L^*(t)}{\pi\tau_L} \ln\frac{1}{r_p}$$

The distribution of I_L^* along the coast - which is represented by the y-axis - is varying harmonically with the period T_{M2} = 12.4206 h and the phase φ_{M2}, which is the semidiurnal lunar oscillation dominating the southern North Sea:

$$I_L^*(t, y_o) = I_{Lo}^* \sin\left[2\pi\left(\frac{y_o}{\lambda_y} - \frac{t}{T_{M2}}\right) + \varphi_{M2}\right]$$

Then the potential at P is

$$V(x_p, y_p, t) = \int_{y_A}^{y_B} V^*(x_p, y_p, t; y_o)dy_o$$

with fixed integral boundaries y_A and y_B according to the realistic coastal current pattern. The components of the ocean induced electric field, E_x and E_y, are the horizontal derivatives of V:

$$E_x(x_p, y_p, t) = -\partial_x V(x_p, y_p, t) = \frac{I_{Lo}^*}{2\pi\tau_L} c_x(x_p, y_p, t)$$

$$E_y(x_p, y_p, t) = -\partial_y V(x_p, y_p, t) = \frac{I_{Lo}^*}{2\pi\tau_L} c_y(x_p, y_p, t)$$

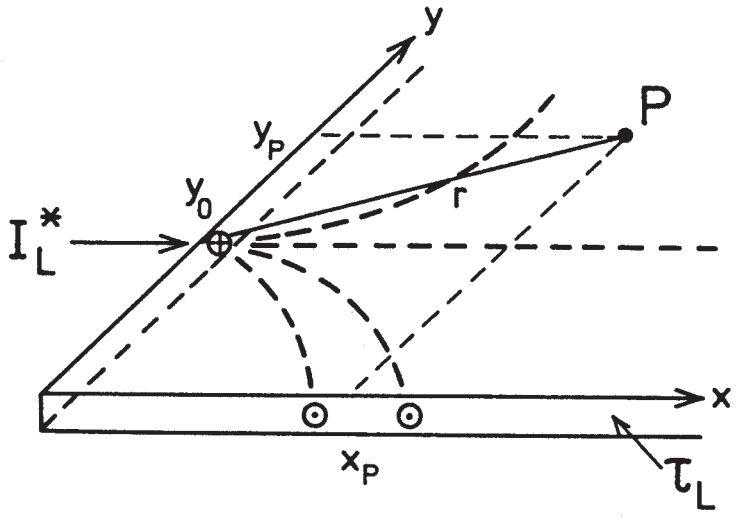

Figure 8.2. Geometry for the calculation of the logarithmic electric potential at P in a thin sheet of integrated conductivity τ_L for a current source I_L^* at y_o.

with

$$c_x(x_p, y_p, t) = x_p \int_{y_A}^{y_B} \frac{1}{x_p^2 + (y_p - y_o)^2} \sin\left[2\pi \left(\frac{y_o}{\lambda_y} - \frac{t}{T_{M2}} \right) + \varphi_{M2} \right] dy_o$$

$$c_y(x_p, y_p, t) = \int_{y_A}^{y_B} \frac{y_p - y_o}{x_p^2 + (y_p - y_o)^2} \sin\left[2\pi \left(\frac{y_o}{\lambda_y} - \frac{t}{T_{M2}} \right) + \varphi_{M2} \right] dy_o$$

as time dependent and location dependent variables.

8.3 Observations

Field measurements were made in Northern Germany (Junge, 1988) and South-East Scotland (Junge, 1995) at locations up to 400 km away from the coast. At each location time variations of the 3 magnetic and 2 horizontal electric field components were observed continuously for at least a 60 days time duration. The field equipment consisted of fluxgate magnetometers and AgAgCl electrodes resp. PbPbCl electrodes. Both electrodes proved to be very reliable. The sampling rate varied between 30 sec and 1 min; the data were reduced to half hourly means for further analysis.

The locations of the Scottish sites are shown in figure 8.3. Eight sites (PILO, BIRN, IMAY, BUDE, BOMU, DAHO, HOUP, LALA) can be used for tidal analysis. The locations of the German sites are given in figure 8.8.

Figure 8.4 gives an example of 30 days of half hourly means of all the field components at site BOMU in Scotland at about 30 km distance from the shore. Both electric field components show typical long period drifts, flattening at the end of the time segment. These drifts are most possibly of electrochemical origin. A semi-daily variation is clearly visible in the electric field, especially in the E_x component, whereas daily variations of ionoshperic origin (Sq) dominate in the magnetic field components.

A 16 hours high pass filter was applied to the time series to remove the trend and the longer periods. Figure 8.5 shows the high pass filtered data for the same time segment as in figure 8.4. It is obvious that the oscillation in E_x and E_y is of other than ionospheric origin as there is no such oscillation in the magnetic field.

The spectra of the time series give more insight into the nature of the oscillation. Figure 8.6 shows the complete raw spectra of the time interval of figure 8.5 for B_x, B_z and E_y. As the sampling rate is 30 min, the Nyquist frequency is 24 cpd (= cycles per day). The length of the time interval is 30 days, thus the frequency resolution is 1/30 cpd. The effect of the high pass filter is obvious but for the shorter period range the spectra are almost white. Significant lines only occur at 2 cpd which is equivalent to a 12 hours period.

The dashed rectangle covers the zoomed area shown in figure 8.7. The positions of the largest peaks is marked by the two vertical dashed lines. The peak at 2 cpd is clearly visible in all the 3 spectra, whereas the peak at 1.93 cpd only dominates the electric field spectrum by mored than one order of magnitude. The different ratio of the two peaks for the magnetic and electric field indicates that the source mechanism is different for the two peaks.

Such spectral lines were observed at all field sites in Germany and Scotland and showed a similar regional pattern. Thus for each region a common source was assumed which - according to the phase and direction of the telluric ellipses - is very likely the tidal motion in the Sea.

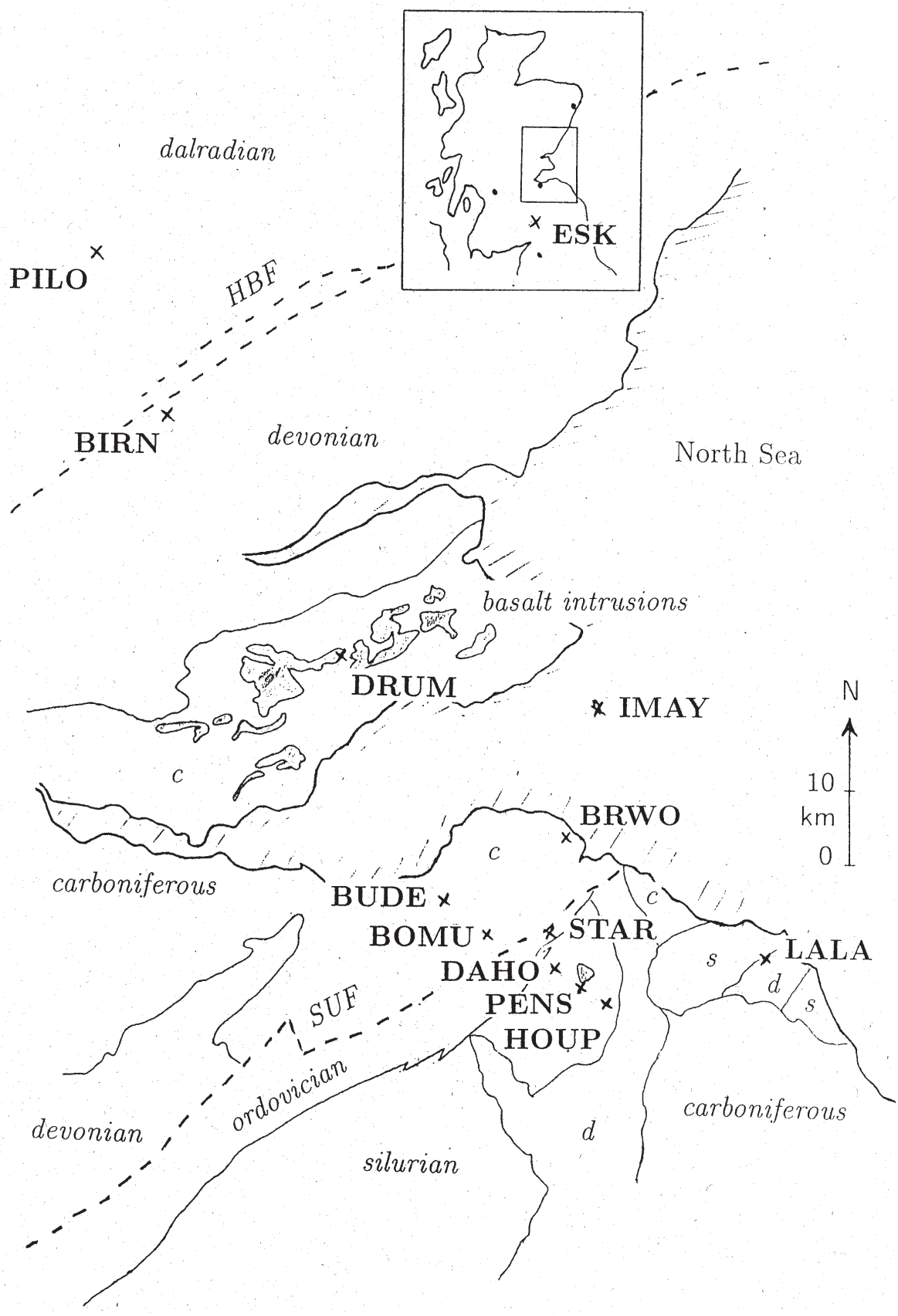

Figure 8.3. Site locations in South-East Scotland. The inlay shows the investigated area within Scotland and the location of the magnetic observatory Eskdalemuir (ESK).

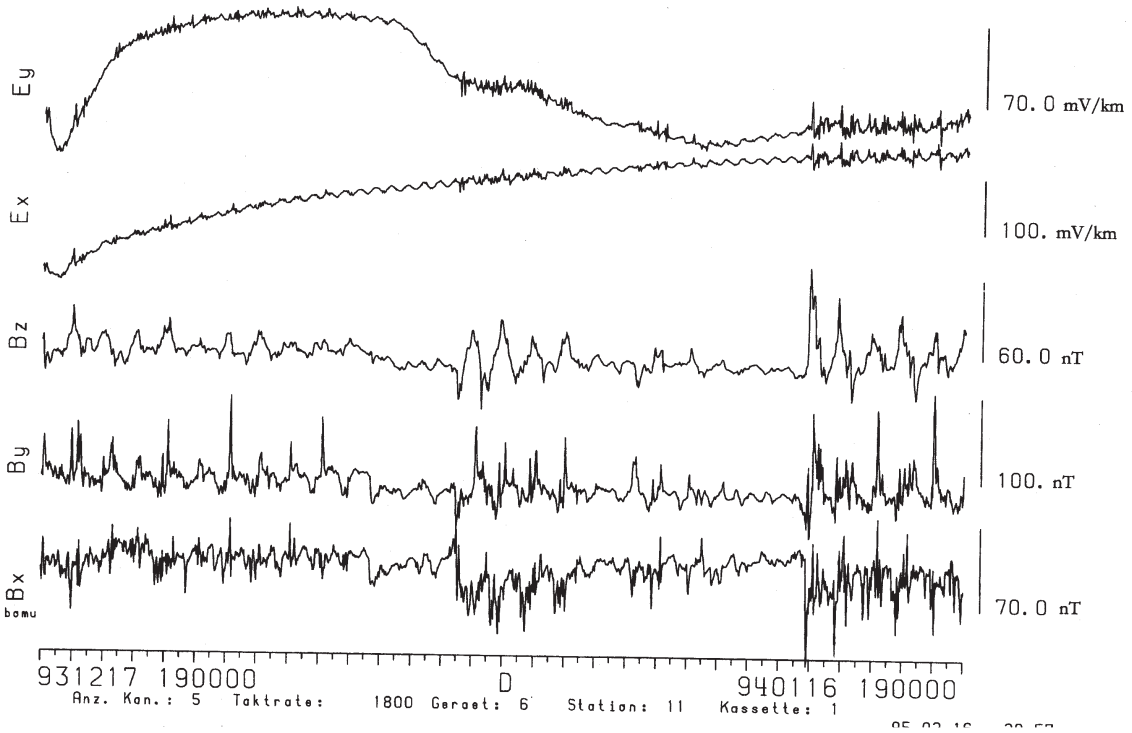

Figure 8.4. Half hourly mean values of a 30 days segment of magnetic and telluric field components. The data are not pre-processed and thus show strong drifts in the telluric components.

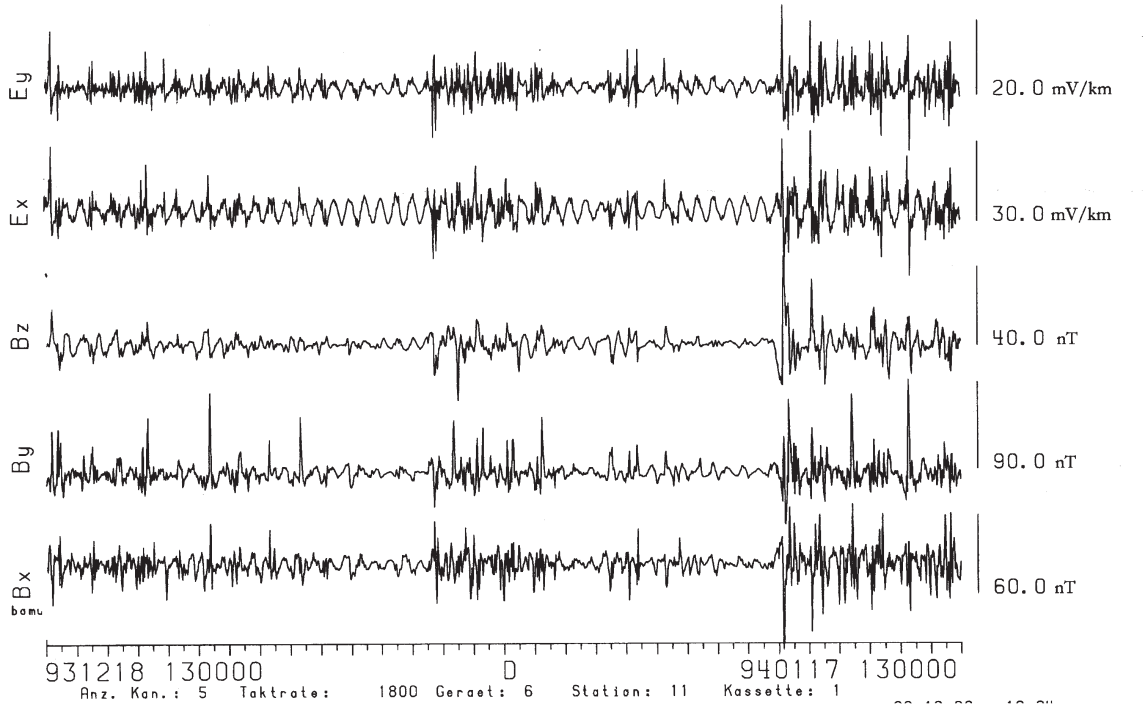

Figure 8.5. Low-pass filtered (cut-off period 16 hours) data of the time segment of figure 8.3. The semi-diurnal lunar oscillation can be seen in both telluric field components especially in E_x.

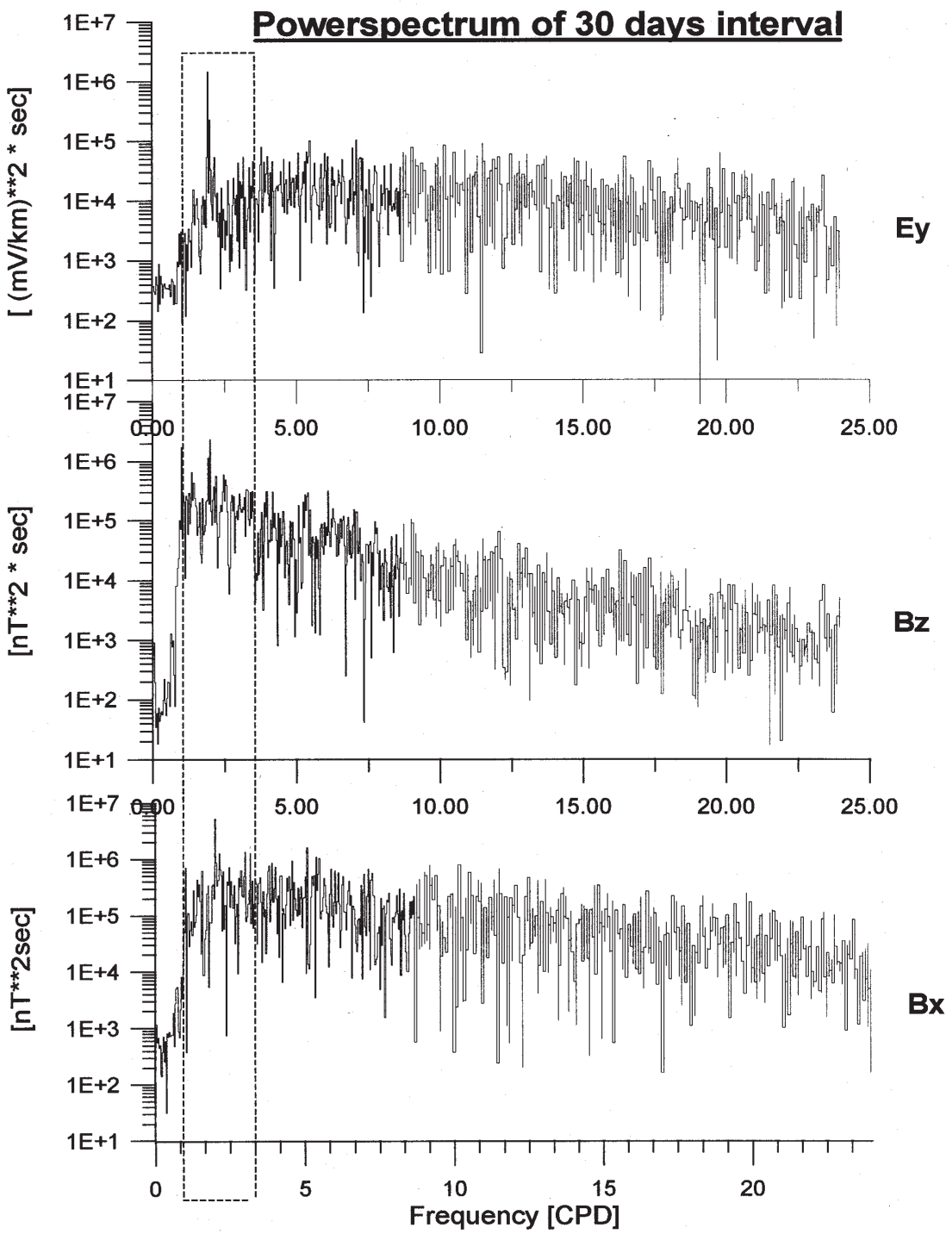

Figure 8.6. Power spectra of the data (B_x, B_z, E_y) from figure 8.4. The only significant lines are at 2 cpd.

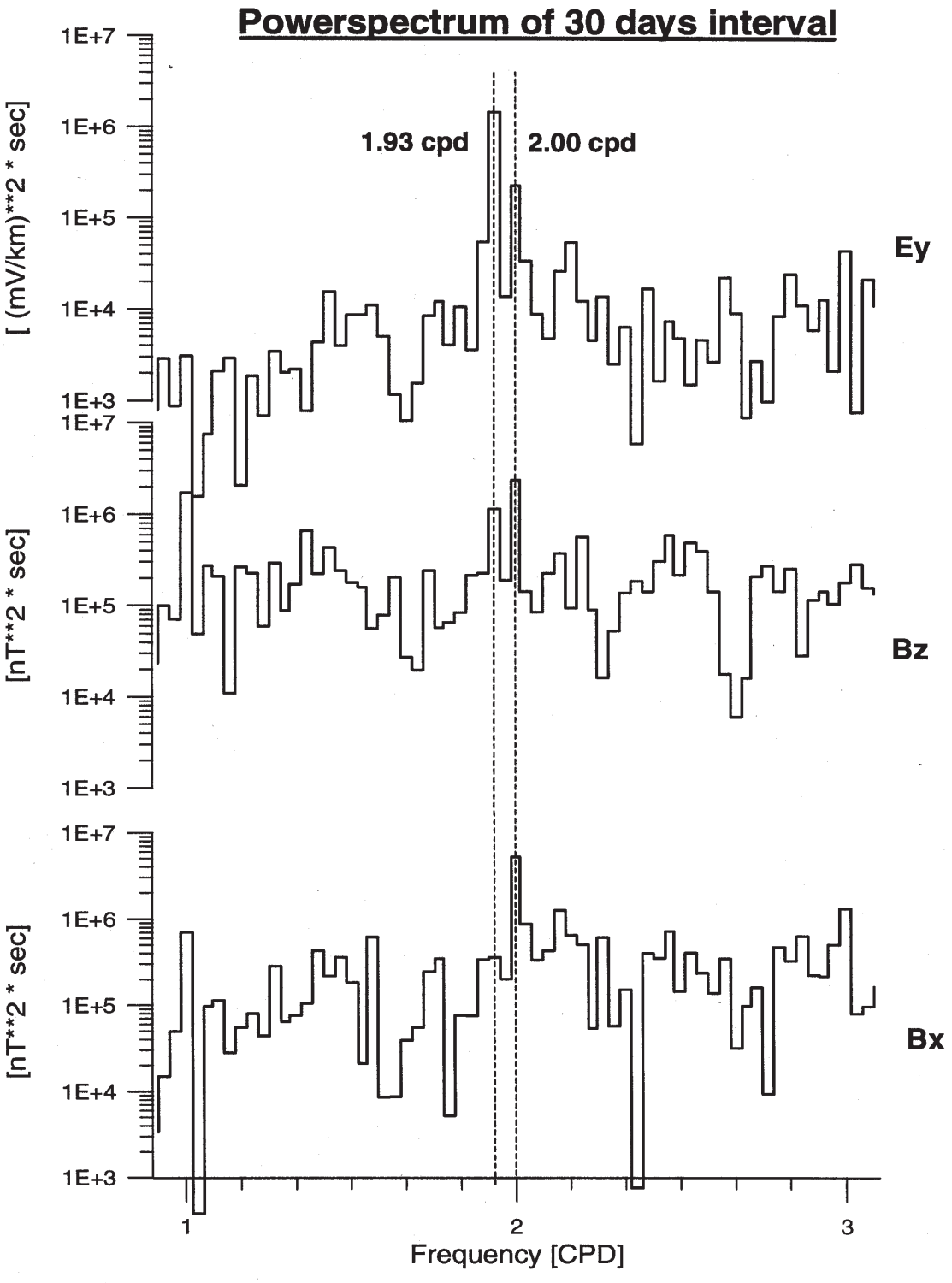

Figure 8.7. Enlarged section of figure 8.5 around the peaks at 2 cpd. The tidal line of E_x (1.93 cpd) is dominating, whereas for the magnetic components the solar lines (2 cpd) are the largest.

8.4 Modelling

Instead of the geological situation in South-East Scotland the North German sedimentary basin can be well approximated by the simple thin sheet model of Sec. 2. Therefore in the following we concentrate on modelling the North German data.

Unfortunately, the lateral conductivity distribution in Northern Germany is not homogeneous due to salt diapirism and thus the observed electric field was locally distorted. As we can neglect inductive contributions to the tidal electric field, just amplitude and field direction are distorted, whereas the phase will remain undistorted. Such a distortion can be expressed by real and frequency independent matrix, which were determined for each location (Junge, 1988) and served to remove the distortion effect on the tidal electric field.

In the following the electric field is always related to the semidiurnal lunar period of 12.4206 hours. Figure 8.8 presents the polarization ellipses of the telluric field at different field sites together with the ellipses of the tidal current in the Southern North Sea. The major axis of the latter are parallel to the coast within the coastal range, therefore the maximum electric current density will be perpendicular to the coast. The dashed lines refer to the location of maximum tidal current at the given lunar time. For example at 2 h lunar time the maximum electric current is orientated towards the coast at the East Frisian islands which corresponds well to the electric field direction on shore at that time.

The distribution of the tidal current along the coast is shown in figure 8.9 and demonstrates that the harmonic formulation of the tidal velocity distribution along the coast is a good approximation for the coastal range between Le Havre and Cuxhaven. Of course local variations of the water depth and velocity may affect the local current density severely, but this is considered to be of minor importance for larger scales.

Therefore the coastline is approximated by the edge of a thin half sheet with N50E strike direction (figure 8.10). According to the theoretical approach (section 2) the integrated electric current distribution I_L^* along the coast is modelled by a harmonic function with wavelength λ = 660 km and y_A and y_B at St. Malo and Husum, i.e. the integration is performed for 1.5 wavelengths. The mean maximum tidal current is taken as v_o = 1 m/s, the mean water depth is h = 50 m. Further constants are the conductivity of the seawater, $\sigma_W \approx 4$ S/m, and the vertical component of the mean magnetic field in Northern Germany at the time of the observation, $B_z \approx 44000$ nT. Then the mean maximum amplitude of the integrated electric current density is $I_{Lo}^* = h\sigma_W v_o B_z = 8.8 \cdot 10^{-3}$ A/m.

With I_{Lo}^* as current source the theoretical telluric ellipses can be calculated at each location according to section 2. In figure 8.10 they are compared to the observed telluric ellipses from figure 8.8, whereby a conductance of τ_L = 4000 S was assumed for the half sheet. The agreement between theoretical and observed ellipses is surprisingly good at the sites GRD, BUR, DEP and EPT. At site EFL large differences occur, but as the site does not lie in the sedimentary basin, the thin sheet assumption is not valid at this site. At BSG theoretical and observed fields point towards the same direction at 2 h lunar time, however, the sense of rotation is opposite, possibly because the integration boundary is very near to that site.

8.5 Discussion and future perspectives

Electromagnetic data have been collated from 6 German and 8 Scottish field sites and have been processed for further tidal analysis. It is shown that the dominant tidal period in the telluric field is the semidiurnal lunar period of 12.4602 hours. Local distortions were removed and polarization ellipses of the telluric field were calculated. It has been proven that ocean induced tidal telluric fields can be observed even far from the coast.

Preliminary theoretical studies have been started already. The knowledge of the conductivity distribution in Northern Germany enabled us to calculate rather

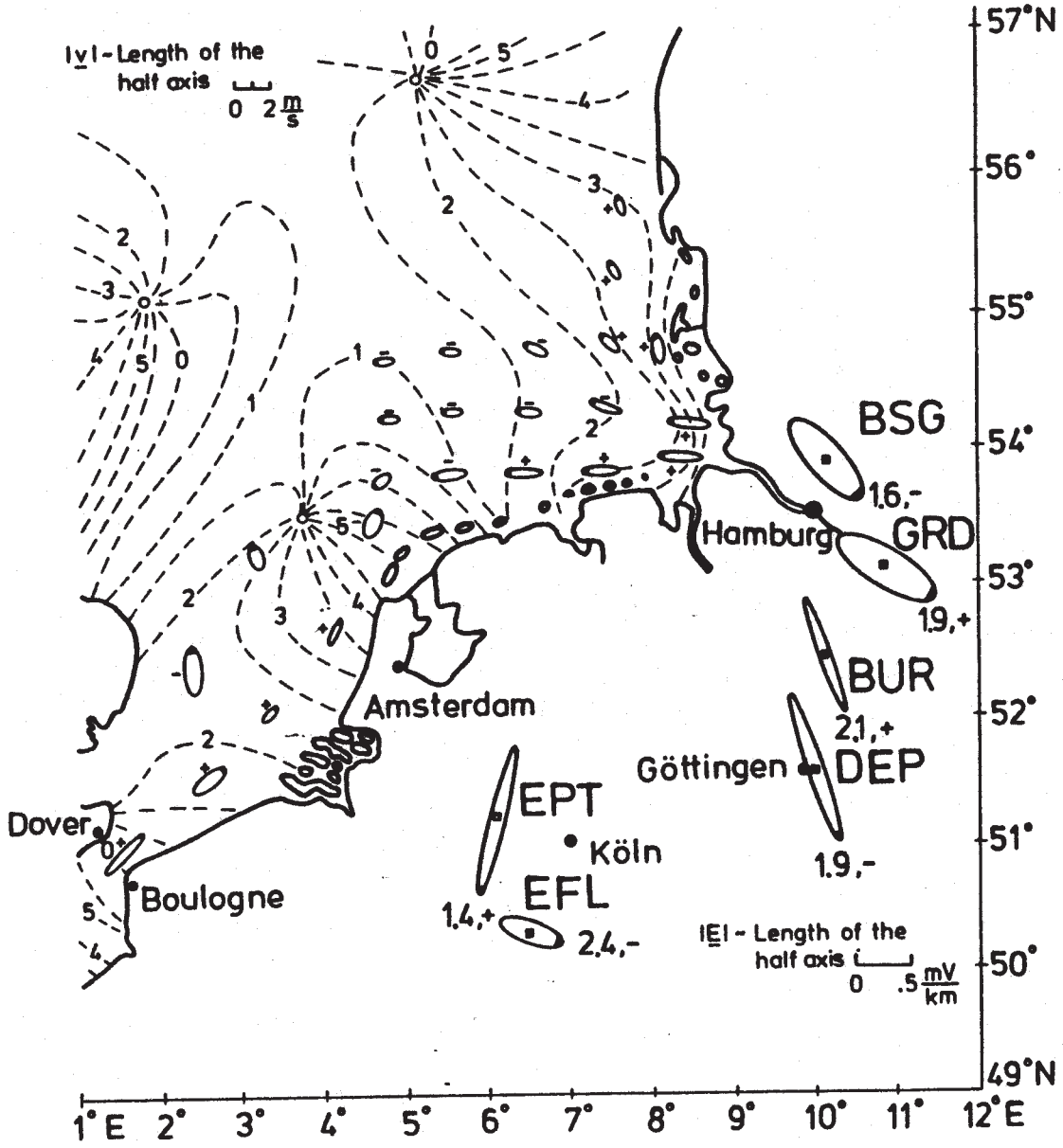

Figure 8.8. Polarization ellipses of the telluric field on shore and of the water current in the North Sea (Hansen, 1952; Sager, 1964) for the semidiurnal lunar period. The numbers denote the lunar time in hours. For the telluric ellipses the sign after each number refers to the sense of rotation of the polarization ellipses (clockwise = positive). The bold end of the ellipses marks the position of the telluric vector at the given lunar time, the length of the half axis is proportional to the magnitude of the electric field on land, and the water velocity in the North Sea.

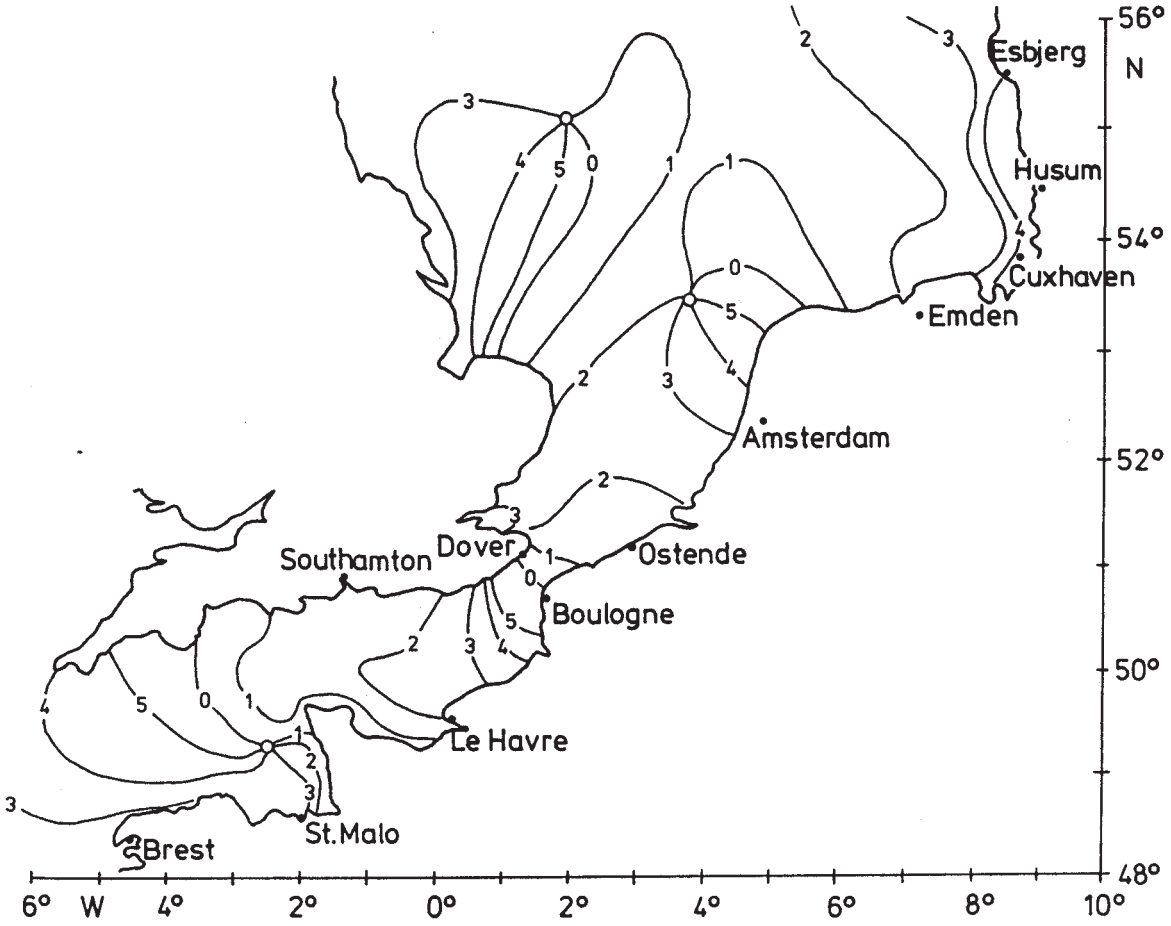

Figure 8.9. Times of maximum tidal current for the Channel and the Southern North Sea (Sager, 1964). The lines give the location and the number the lunar time of the maximum current.

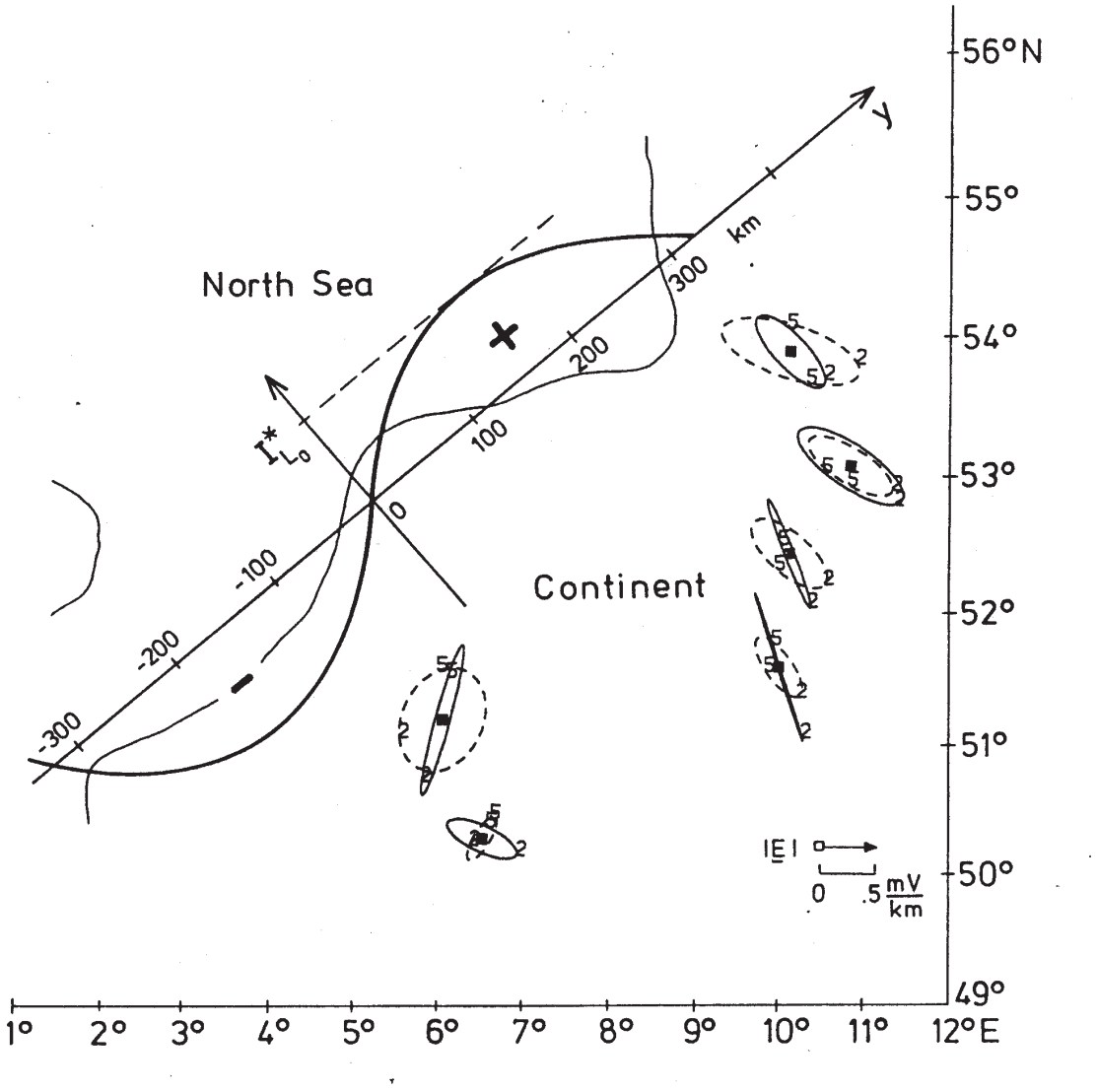

Figure 8.10. Comparison between observed (solid lines) and theoretical (dashed) telluric polarization ellipses. The numbers refer to lunar time and mark the location of the telluric vector at the given time. The y-axis represents the edge of the thin sheet model for the theoretical calculations, whereas its ordinate values denote the form of the integrated current density $I_L^*(y)$ at 2 h lunar time.

realistic theoretical polarization ellipses of the tidal telluric field at the different locations. However, much more sophisticated models are needed to explain the Scottish data as the geology is more complex in that area. Also the influence of the Atlantic Ocean on the Scottish data has to be studied by tidal models and modelling studies of global scale, including the tidal source field in the North Sea.

A very promising further development is the voltage measurements on the CAM-1 cable Madeira-Sesimbra. Telluric fields can be observed simultaneously on shore on Madeira and on the Portugese coast. The comparison and correlation between cable data and land-based measurements may provide a valuable tool for monitoring the total oceanic current flow between Madeira and Portugal.

8.6 Literature

Chave. A. and Luther, D. (1990). Low-frequency, motionally induced electromagnetic fields in the ocean. J. Geophys. Res., 95:7185-7200.

Egedal, J. (1937). On the lunar-diurnal variation in the earth-currents. Terr. Magn. 42, 179-181.

Faraday, M. (1832). Experimental Researches in Electricity - Bakerian Lectures. Phil. trans. Roy. Soc.,London, 122:163-194.

Hansen, W. (1952). Gezeiten und Gezeitenströme der halbtägigen Hauptmondtide M2 in der Nordsee. Dtsche. Hydrogr. Z., Ergänzungsheft 1.

Junge, A. (1988). The telluric field in northern Germany induced by tidal motion in the North Sea. Geophys. J. Int. 95, 523-533

Junge, A. (1995). Magnetotellurics in the Long Period Range, Final Report, EEC Human Capital and Mobility - Individual Fellowship, Prop. Nb. ERB 4001 GT 930152

Larsen, J. (1992). Transport and heat flux of the Florida Current at 27 N derived from cross-stream voltages and profiling data: theory and observations. Phil. Trans. R. Soc. Lond. A, 338: 169-236.

Longuet-Higgins, M. (1949). The electrical and magnetic effects of tidal streams. Mon. Not. Roy. Astr. Soc., Geophys. Suppl., 5:285-307.

Sager, G. (1964). Das Regime der Gezeiten und der Gezeitenströme in der Nordsee, dem Kanal und der Irischen See, Teil II. Habil. math.-nat. Fak. Univ. Leipzig.

Sanford, T. (1971). Motionally-induced electric and magnetic fields in the sea. J.Geophys.Res., 76:3476-3492.

ISO-3D Final Report

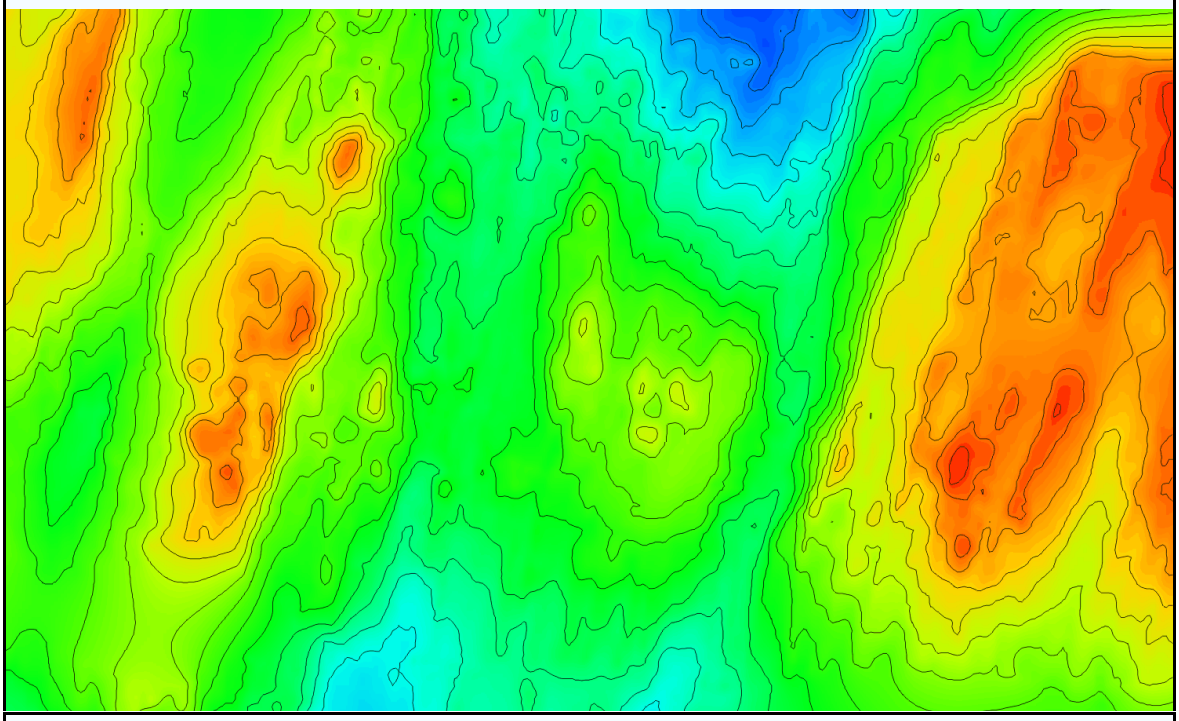

Part 4

Scientific Results:

Lucky Strike CSEM demonstration experiment

Chapter 9

Geological setting of the Lucky Strike segment of the Mid-Atlantic Ridge

J.M.Miranda[1], N.Lourenço[2] and the ISO-3D group[3]

1. Centro de Geofisica da Unversidade de Lisboa, Campo Grande, Ed. C8, Piso 6, 1749-016 Lisboa, Portugal

2. Universidade do Algarve, Campus de Gambelas, 8000 Faro, Portugal.

3. Other members of the ISO-3D group: M.C. Sinha, A. Junge, A.H. Flosadottir, F.M. Santos, A. Soares, J. Luis, L.M. MacGregor, S. Dean, N. Barker, Z. Cheng and S. Riches

9.1 Lucky Strike geological context

The Lucky Strike segment extends between 37º 33´N, 32º 09´W and 37º 06´N, 32º 24´W at the south-western limit of the Azores volcanic Plateau (figure 9.1). Here, the MAR presents transitional morphology. To the north, segments are shorter in length and show less defined axial morphology, whereas south of Lucky Strike, typical slow spreading ridge geometry occurs (Detrick *et al.*, 1995).

The Lucky Strike segment has a length of 50 km, an average orientation of N10ºE and is bounded by two second-order non-transform discontinuities. Its morphology is typical of a slow spreading centre. The axial valley is well defined by the 2000 m isobath, being 10 km wide in the centre of the segment and reaching 15 km wide towards both tips.

One of the characteristics of this segment is the strong asymmetry observed in the axial valley walls. At the northern end of the segment, the inside corner is marked by a steep slope (between -2750 m and –1236 m). In contrast, the outside corner shows a rough relief defining a horst-graben geometry in partial development. This morphology extends from the immediate vicinity of the median-valley to the West, ascending gradually to water depths of 1400 m. The median-valley walls become symmetrical in the central area of the segment, and here it is possible to observe individual scarps reaching 950 m displacement. Towards the South, the asymmetry again becomes more pronounced. The inside corner here is defined by an elliptical seamount, 300 m high, with its major axis orientated N60ºE.

Inside the median-valley, a composite axial volcano 13 km long, 7 km wide and 430 m high, occupies the segment centre. A North-South graben, 200 m deep, splits the top of the volcano in two distinctive parts. To the West a narrow volcanic ridge, 5.4 km long, marks its top. To the East, the volcano summit presents a half-circular shape, where it is possible to identify three small volcanic cones. Between these volcanic constructions, a circular depression with a diameter of 400 m and a relative depth between 3 and 7m (between 1730 m and 1737 m) occurs. During the DIVA1 cruise submersible observations allowed the classification of this depression as a lava lake (Fouquet *et al.*, 1994, 1995). The hydrothermal field of Lucky Strike, which was discovered during dredging on the FAZAR mission (Langmuir *et al.* 1993), is spatially controlled by this structure.

9.2 Previous baseline data

A huge amount of baseline data, comprising observations from the meso to the macro scale (figure 9.2), from the Lucky Strike Segment have been gathered in recent years. The overall segment is densely covered by Simrad EM12 swath bathymetry collected during the SIGMA campaign (Needham *et al*, 1991, Detrick *et al.*, 1995), covering an area of nearly 4110 km^2, up to crustal ages of approximately 3 Ma.

The inner floor of the axial valley was surveyed by two tracks of the high resolution TOBI side scan sonar during the HEAT experiment (German *et al.*, 1996). The TOBI, which operates at a frequency of 30 kHz, was towed at 400 m above the seafloor, providing a coverage width of nearly 9 km (half-swath width across track of 2.2 km). The ground resolution was 1 m, although during processing and post-processing the images were re-sampled to give final 6 m pixel resolution (Blondel, 1996). The resulting images form a panchromatic mosaic with 256 shades of grey, where 0 (black) corresponds to acoustic shadow and 255 (white) represents a highly back scattering surface.

In situ seafloor observations where made over the Lucky Strike hydrothermal field and surrounding areas from the Nautile submersible during the 1994 DIVA1 mission (Fouquet *et al.*, 1994 and Fouquet *et al.*, 1995).

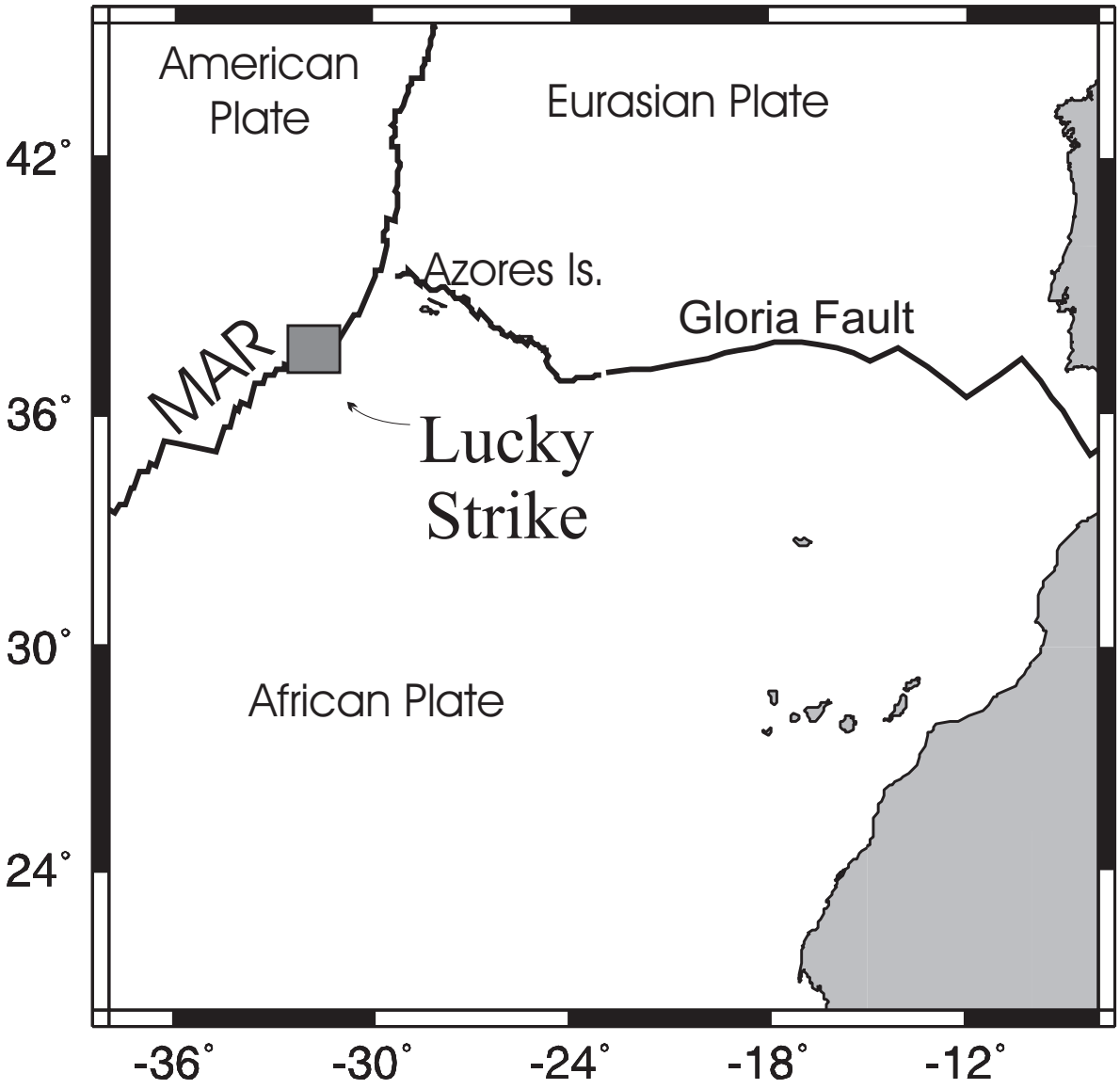

Figure 9.1. Location of the Lucky Strike segment.

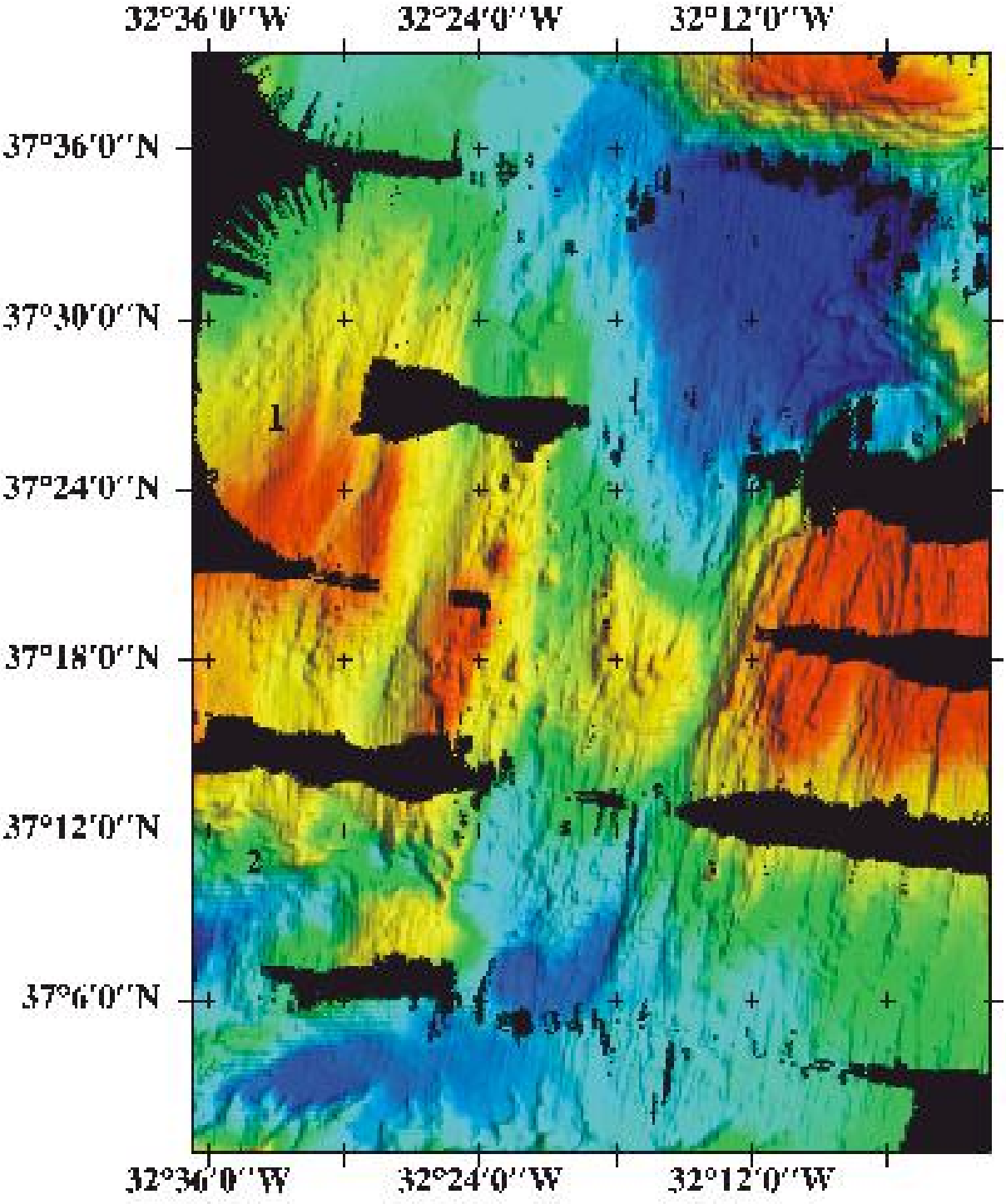

Figure 9.2. Shaded relief of the Lucky Strike bathymetry with the spatial distribution of the data used in this study. The continuous thin line corresponds to the TOBI coverage. The stippled square displays DIVA 1 diving area. Small boxes with letters show the locations of TOBI images presented in figure 9.4. Small stippled lines represent the profiles used to study the fault parameters.

9.3 Photo-interpretation of TOBI and Simrad Imagery

Several different studies have been presented addressing acoustic facies interpretation: Blondel (1996) presented an automatic classification strategy for TOBI imagery; Gracia *et al.* (1998) presented an overview of the main structures and fault geometry in the MAR non transform discontinuities (NTD) across the Azores Plateau. Ondreas *et al.* (1997) made the first classification of the facies distribution along the Lucky Strike segment, using Simrad EM12 backscatter data. These classification methods are very useful for an efficient overall regional classification of the acoustic facies on the ridge axis, allowing an interpretation of the distribution of sedimentary, volcanic and tectonic signatures. However, they neither differentiate between volcanic styles present in the axis, nor do they allow the mapping of fault scarp geometries and interactions.

Figure 9.3 shows the geological map qualitatively retrieved from the TOBI images (figure 9.3a), plus dive information. One striking feature of the sonar imagery, verified during the dives, is the extreme diversity of volcanic facies out-cropping on the median-valley floor, and also the contrasting character observed between the centre and tips of the segment. Both the northern and southern nodal basins (in the intersections between the NTD and the median valley) are covered by pelagic sediment (figure 9.4a). Between the tips of the segment and the segment centre, volcanism is rather discontinuous, forming fault controlled linear volcanic ridges (figure 9.4d), small massive (highly back scattering) seamounts (figure 9.4c) or pillow mounds (figure 9.4g) with a characteristic hummocky texture. These volcanic styles are generally interpreted as resulting from small eruptive volumes connected to small discrete feeding bodies in the crust (Smith & Cann, 1992) both in the initial stages of magmatic activity or as terminal products of a magma pocket re-filling episode.

In contrast, the centre of the segment is occupied by a central composite volcano, which is split by an axial graben 300 m deep. Its western part shows a linear N-S ridge composed mainly of pillows and breccia, whereas on the east side of the graben, three breccia volcanic cones surround a 400 m wide and 6 m deep depression, where a lava lake is located (Fouquet, *et al.*, 1994, 1995). The floor of the graben is covered by very recent lavas, composed mainly of lineated sheet flows (in close association with North-South fissures 15 to 20 m wide), massive sheet flows (outcroping on the western graben wall), and pillow lavas.

9.4 Zero age axis

To study the tectonic signature of the accretion along the Lucky Strike segment, we started by identifying the zero-age axis. Criteria used included fault nucleation patterns, extent and facing direction of fault scarps and fissures retrieved from the TOBI images (figure 9.3c), and correlation with areas of very recent volcanic activity detected by the aerial extent of untectonised lava flows following Malinverno *et al* (1989, 1993). Using this approach, we were able to identify, from North to South, three axes (S1 to S3 in figure 9.3c) striking N14ºE, bounding both inside corners in an en-echelon pattern.

S2 was the target of several DIVA1 dives, providing ground-truth information. An E-W profile, carried out north of the Lucky Strike hydrothermal field by the Nautile submersible, showed that the vast majority of lava is very recent (i.e. little pelagic sediment cover), with the hottest fluid lavas located in the bottom of the graben, where we located S2 (Lourenço, 1997).

S1 and S3 show discontinuous neo-volcanic activity, as expressed by the volcanic facies described above. Again the striking feature is the symmetry present. On the northern tip a massive 'high back scattering' untectonised flow (figure 9.4b) occurs at the base of the inside corner relief. This acoustic signature can also be observed, although in an incomplete way, at the extreme Southwest of the segment, near the southern inside corner.

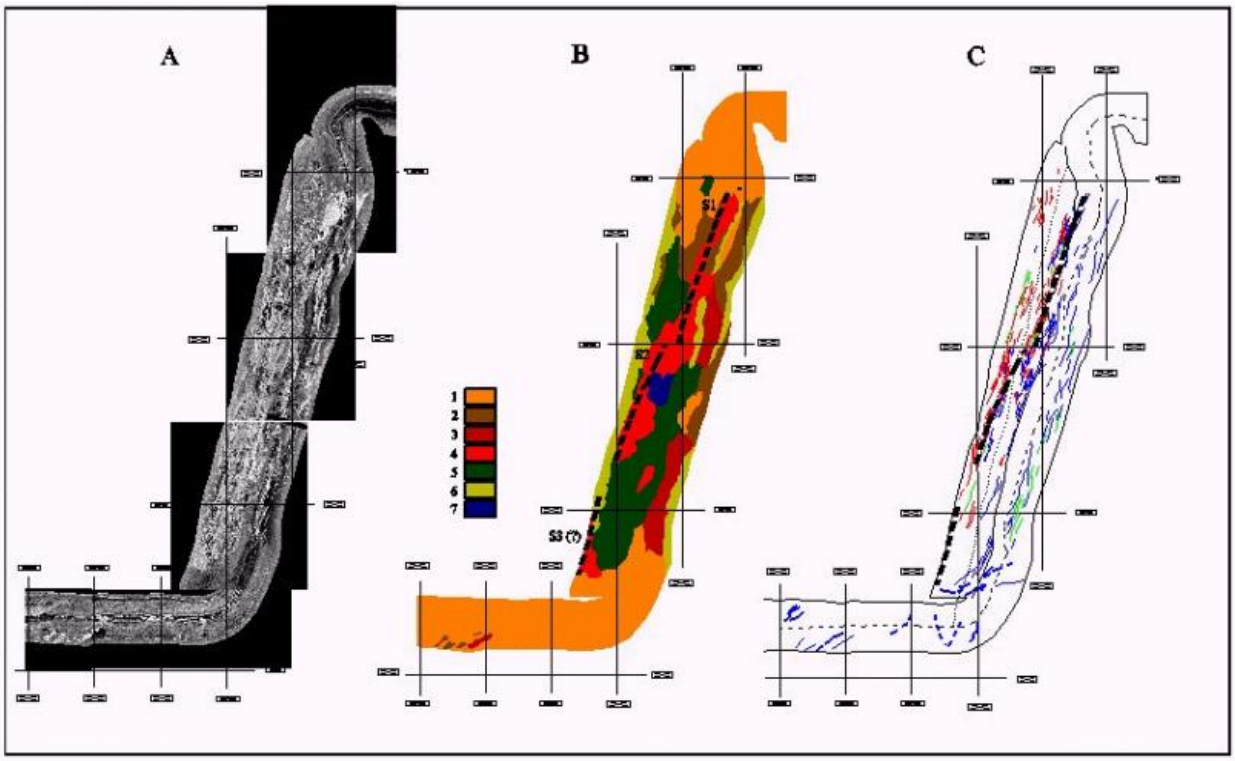

Figure 9.3. A) TOBI sonar mosaic. B) Acoustic facies interpretation. Note the symmetry of the volcanic facies character about the central volcano. Legend: 1. Pelagic sediment; 2.Tectonic relief; 3. AVRs; 4. Undifferentiated seamounts and flows; 5. Pillow mounds; 6. No data; 7.Volcanic breccias. C) tectonic lineations map. Red lineations- Fault scarps facing east. Blue lineations fault scarps facing west. Green lineations AVR axis. Stippled lines (S1 to S3): inferred location of fault nucleation beginning zones. Projection UTM, spheroid WGS 84.

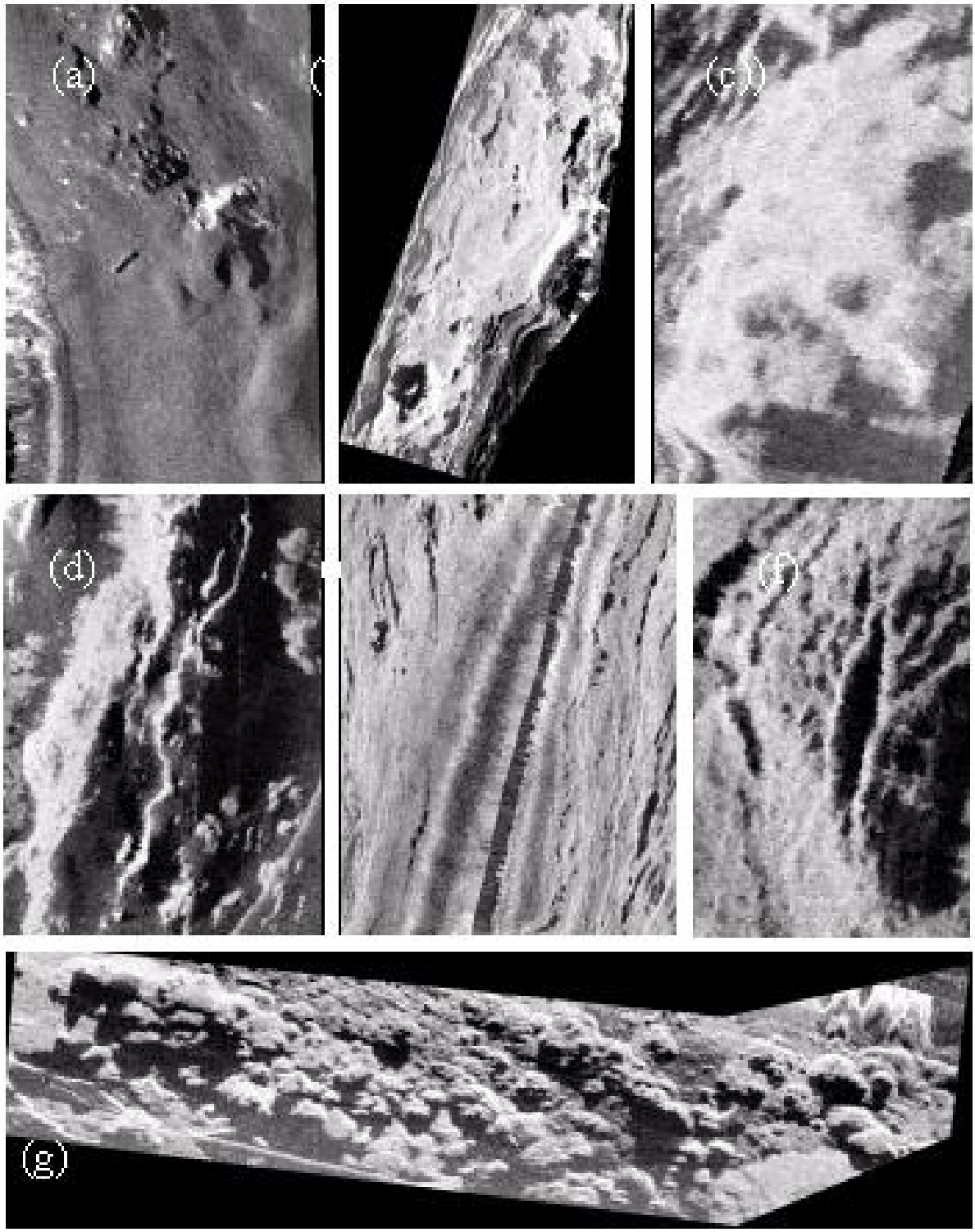

Figure 9.4. Different sonar acoustic signatures for volcanic features present in the interior of the median-valley. Interpretation: a) Pelagic sediment; b) massive flow (see text for discussion) c) Seamount with crater d) Axial volcanic ridge with a crater on the summit e) Lineated volcanic flows (ground truth during dives) f) Volcanic breccia mount (ground truth). g) Pillow mound.

With the available data it is extremely difficult to judge the geological meaning of these 'high back scattering' surfaces. Either they are massive flows resulting from volcanic processes, or they are serpentinites, and their occurrence must in this case be constrained by tectonics associated with pervasive hydrothermal circulation into the upper mantle (Karson & Dick, 1993; Karson & Dick, 1984, 1993; Gracia *et al.*, 1998). Regardless of the interpretation, and despite the absence of any obvious tectonic control, their location seems to be the result of a preferential zone for extension, thus not affecting the assumed position of S1 and S3.

9.5 References

Blondel, P., Segmentation of the Mid-Atlantic Ridge south of the Azores, based on acoustic classification of TOBI data, MacLeod, C. J. (editor), Tyler, P. A. (editor), Walker, C. L. (editor), Tectonic, magmatic, hydrothermal and biological segmentation of mid-ocean ridges, Geological Society Special Publications, 118, p. 17-28, 1996.

Detrick, B.; Needham, H. D., & Renard, V. (1995). Gravity Anomalies And crustal thickness variations along the Mid-Atlantic Ridge between 33ºN and 40ºN. *J. Geophys. Res.*, 100, 3767-3787.

Fouquet, Y *Et Al* (1994). "A Detailed Study Of The Lucky Strike Hydrothermal Site and discovery of a new hydrothermal site: Menez Gwen; Preliminary results of the DIVA1Cruise (5-29May, 1994)". *InterRidge News*, 3, nº2, 14-17.

Fouquet, Y.; Ondréas, H.; Charlou, J.L.; Donval, J.P.; Radford-Knoery, J.; Costa, I; Lourenço, N. & Tivey, M. (1995). "Atlantic Lava Lakes and hot vents". *Nature*, 377, 21-22.

Gracia, E, Parson, L M., Bideau, D, Hekinian, R, "Volcano-tectonic variability along segments of the Mid-Atlantic Ridge between Azores Platform and Hayes fracture zone; evidence from submersible and high-resolution side-scan sonar data", 1998. Mills, R. A. (editor), Harrison, K. (editor), Modern ocean floor processes and the geological record, Geological Society Special Publications, 148, p. 1-15.

Karson, J.& Dick, H. (1993). "Tectonics Of Ridge Transform Intersections At The Kane Fracture Zone". *Mar. Geophys. Res.*, 6, 51-98.

Karson, J.A. & Dick, H.J.B. (1984). Deformed And Metamorphosed Oceanic Crust On The Mid-Atlantic Ridge". *Ofioliti*, 9, 279-302.

Langmuir, C e*t Al* (1993). "Geological Setting and Characteristics Of The Lucky Strike Vent Field At 37º17´N On The Mid-Atlantic Ridge". *Eos, Trans. Am. Geophys. U.*, 74(Suppl.), 99 (Abs.).

Lourenço, N. (1997) "Morfotectónica da Junção Tripla dos Açores: Estudo de Pormenor do Segmento Lucky Strike (37º17,N, 32º16'O) a Partir de Dados de Batimetria Multi-Feixe e Sonar Lateral de Alta Resolução". *Universidade de Lisboa.*

Malinverno, A. & Cowie, P. (1993). "Normal Faulting And Topographic Roughness Of Mid-Ocean Ridge Flanks". *J. Geophys. Res.*, 98, 17921-17939.

Malinverno, A & Gilbert, L. (1989). "A Stochastic Model For The Creation Of Abyssal Hill Topography At A Slow Spreading Center". *J. Geophys. Res.*, 94, 1665-1675.

Needham, H.D. and SIGMA Scientific Team (1991). The crest of the Mid-Atlantic Ridge between 40º and 15º N: very broad swath mapping with EM12 echo-sounding system. *EOS Trans. AGU*, 72, 470.

Ondréas, H., Fouquet, Y., Voisset, M., Radford-Knoery, J., 1997. "Detailed Study Of Three Contiguous Segments Of The Mid-Atlantic Ridge, South Of The Azores (37º N To 38º 30'n) Using Acoustic Imaging Coupled With Submersible Observations", Mar Geophys Res 19 (3) P. 231-255.

Smith, D. & Cann, J. (1992). "The Role Of Seamount Volcanism In Crustal Construction Along The Mid-Atlantic Ridge". J. Geophys. Res., 97, 1645-1658.

Chapter 10

The MADRIGALS cruise: experimental geometry and data collected.

N.D.Barker[1], M.C.Sinha[1], L.M. MacGregor[1], and the ISO-3D group[2]

1. School of Ocean and Earth Science, Southampton Oceanography Centre, Empress Dock, Southampton, SO14 3ZH, UK

2. Other members of the ISO-3D group: J.M. Miranda, A. Junge, A.H.Flosadottir, F.M. Santos, J. Luis, N. Lourenço, A. Soares, S. Dean, Z. Cheng and S. Riches

10.1 Introduction

On Tuesday 21 September 1999, RRS *Charles Darwin* sailed from Southampton, UK on the MADRIGALS (Mid-Atlantic Deep-towed Resistivity and Induction Geophysics At Lucky Strike) research cruise (Sinha, 1999). This cruise was a collaboration between the University of Cambridge, UK; the Universities of Lisbon and Algarve, Portugal; and HALO Ltd, Reykjavik, Iceland. Basic ship time was funded by the UK Natural Environment Research Council (NERC), and all other research costs were funded by the ISO-3D project under the European Union Mast-III programme.

The main objective was to carry out a controlled source electromagnetic (CSEM) sounding study of the upper and middle crust beneath the central volcano of the 'Lucky Strike' segment of the Mid-Atlantic Ridge. Lucky Strike lies to the Southwest of the Azores archipelago, within the EEZ of Portugal (figure 10.1). Its main feature is a large (13 km long, 7 km wide and 430 m high) volcanic seamount, with a drained lava lake at its summit. Around this lava lake, previous investigations have found extensive hydrothermal venting (Fouquet *et al.* 1994, 1995; German *et al.* 1996; Langmuir *et al.* 1993; Wilson *et al.* 1995).

Electromagnetic investigations are ideal for studies of hydrothermal activity. Most other methods (such as dredging, and sampling of venting fluids) only yield information on the geophysical and geochemical characteristics of the system at the seabed, or within the water column. CSEM measures electrical resistivity, which is sensitive to the properties of the pore fluids and their distribution below the sea floor. Unique information can therefore be obtained concerning the nature of the hydrothermal system as a whole.

Specific objectives of this study were to use various techniques (primarily CSEM), along with the known characteristics of the Lucky Strike segment to answer the following questions: -

- Are there systematic variations in resistivity structure within the upper 2 to 3 km of the crust within the segment, that are associated with changes in permeability structure that influence the siting of the hydrothermal system?
- Is the axial volcano underlain by a hydrothermal plumbing system dominated by high temperature fluids, or do fluids at or close to ambient sea water temperatures predominate – and if so, to what depths?
- Is there a deep magmatic heat source still present beneath the centre of the segment, or is the segment magmatically quiescent at the present time?

10.2 CSEM experiment

In a CSEM experiment, an alternating current electromagnetic signal is transmitted through the oceanic crust to an array of electric field receivers placed on the seafloor (figure 10.2). The signal detected by the instruments is dominated by fields that have diffused through the crust, because of the rapid attenuation of fields in the water column. The distribution of electrical resistivity of the rocks below the seabed is determined by measuring the variation of electric field strength and phase as a function of source receiver separation and geometry, as the source is towed through the array of instruments.

During this cruise, the DASI (Deep-tow Active Source Instrument) transmission system (formerly based at Cambridge, now at Southampton), and LEMUR (Low-frequency ElectroMagnetic Underwater Receiver) receivers (formerly Cambridge, now Southampton and Lisbon) were used. Six new LEMUR instruments (three each for Southampton/Cambridge and Lisbon) were constructed specifically for this experiment using ISO-3D resources.

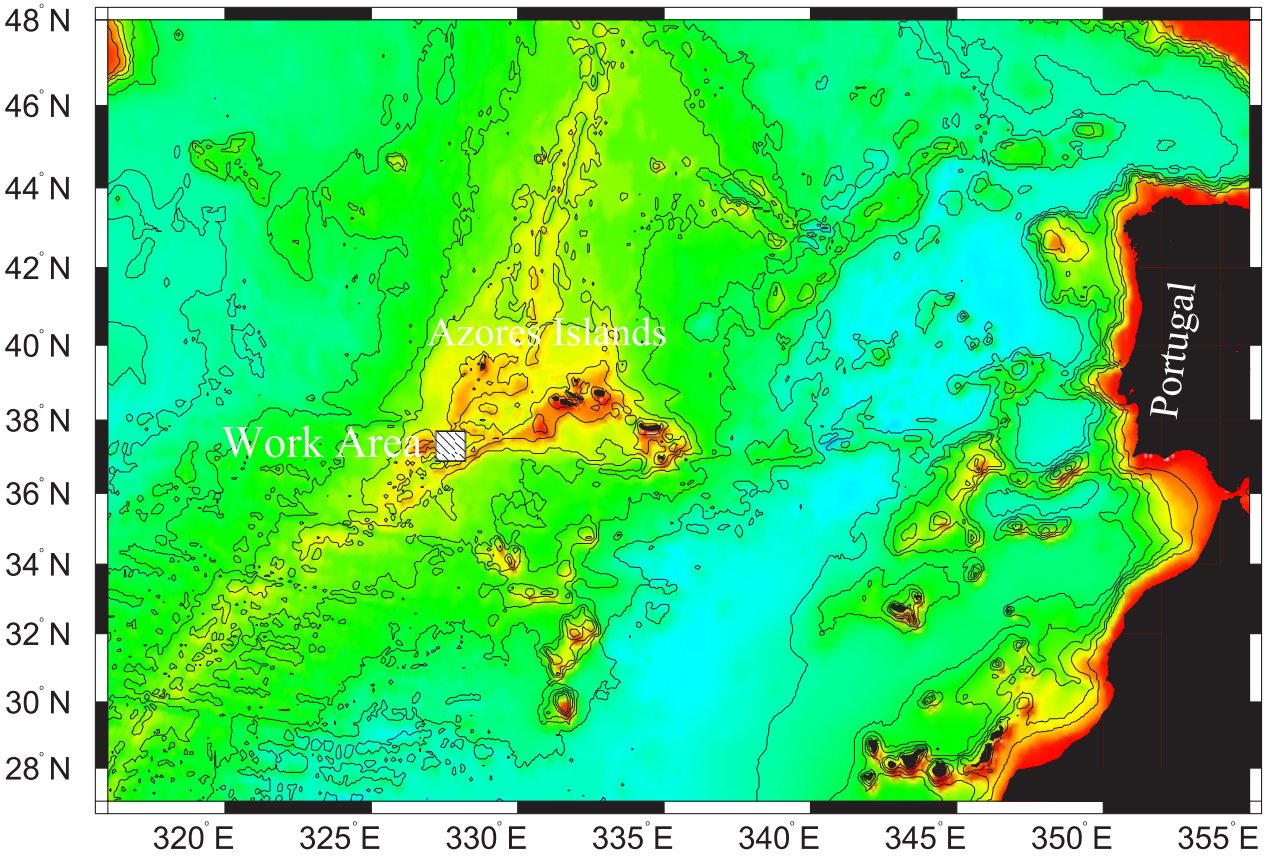

Figure 10.1. Location map of the MADRIGALS work area in the central North Atlantic, on the Mid-Atlantic Ridge axis SW of the Azores archipelago.

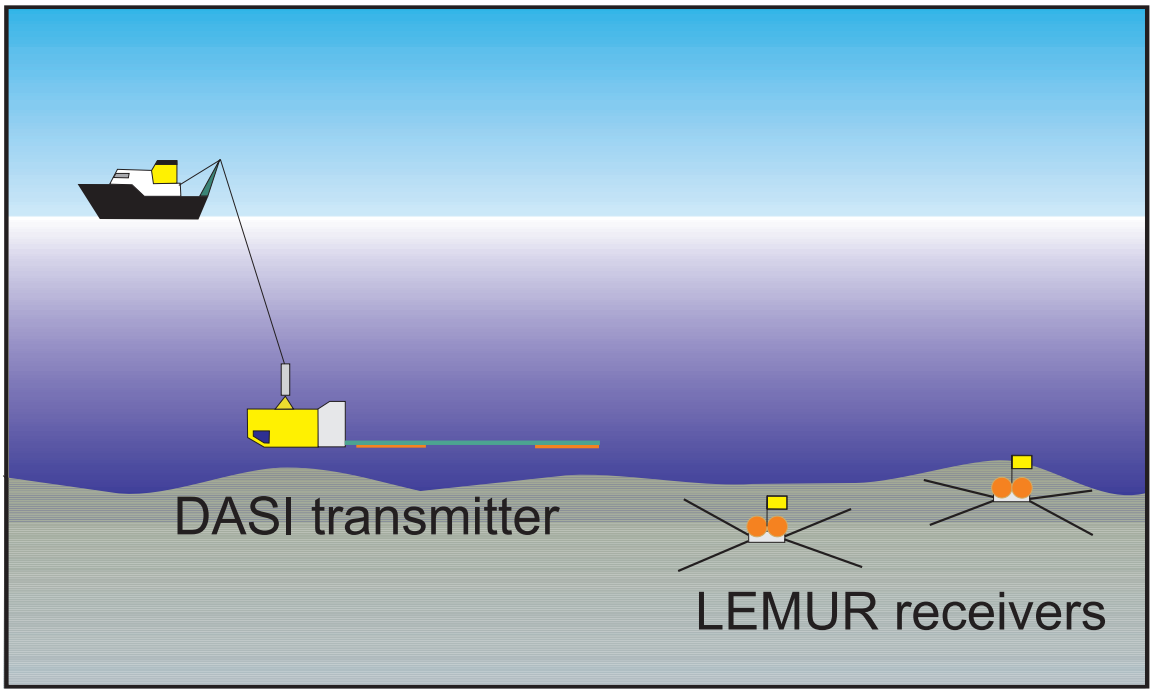

Figure 10.2. A schematic diagram of the CSEM experimental geometry used during the experiment.

The DASI transmitter consists of a 100 m long, neutrally buoyant, horizontal electric dipole (HED) streamed behind a towed vehicle. The height of this vehicle is controlled using the deep-tow winch and monitored acoustically using an altimeter mounted on the towed vehicle. For most of the cruise DASI transmitted at 1 Hz, whilst being flown 70-80 m above the seafloor. It is necessary to tow DASI close to the seafloor in order to reduce the proportion of transmitted energy that is attenuated within the water column, therefore maximising the proportion transmitted through the crust. At higher frequencies, electromagnetic energy is attenuated more rapidly, and it was therefore necessary to fly DASI at a height of approximately 40 m when the transmission frequency was increased to 4 Hz. DASI transmission tows (figure 10.3 and table 10.1) were arranged in order to provide good 3-dimensional coverage over the target area. The HED source was active for nearly 95 hours, over tracks totalling 212 km in length.

Cruise CD 120, 'Madrigals'							
Summary of DASI tow lines							
Line No.	Freq. (Hz)	Start Time	End Time	Hours	km	LEMUR '95s recording ?	Comments
1	1	274/2300	275/1030	11.5	22	No	Whole line
1	1	278/1850	278/2050	2	4	Yes	S end only
2	1	275/1720	276/0250	9.5	21	Yes	Whole line
3	1	276/0810	276/1540	7.5	17	Yes	Whole line
4	1	276/1930	277/0730	12	21	Yes	Whole line
5	1	277/1815	277/2355	5.5	20	Yes	Whole line
6	1	280/1445	280/2344	9	23	Part (18:00)	Whole Line
7	1	280/0220	280/0835	6.2	14	Yes	Whole line
8	1	281/0630	281/11:45	5.25	15	No	Whole Line
9	1	279/0140	279/0500	3.3	8	Yes	SW half only
3	0.25	281/1604	281/2034	4.5	7	No	From I to J
1	4	282/0245	282/0740	5	12	No	Central part
2	4	282/0950	282/1550	6	12	No	Central part
4	4	282/1900	283/0230	7.5	16	No	Almost whole line
Total Transmission Hours:				94.75			
Total DASI Line km:				212			

Table 10.1: A summary of completed DASI tow lines. The older LEMUR 95 instruments, which have a smaller disk capacity than the LEMUR 99s, recorded only part of the experiment.

Ten LEMURs were deployed for this study. These instruments consist of an orthogonal pair of 13.1 m horizontal electric dipole sensors, and a 24-bit recording system. Unfortunately, of the ten instruments deployed (figure 10.3), only five were recovered with data; one was found upon recovery to have failed to record (due to an ADC malfunction); and four were lost, three due to faulty release cards, and one

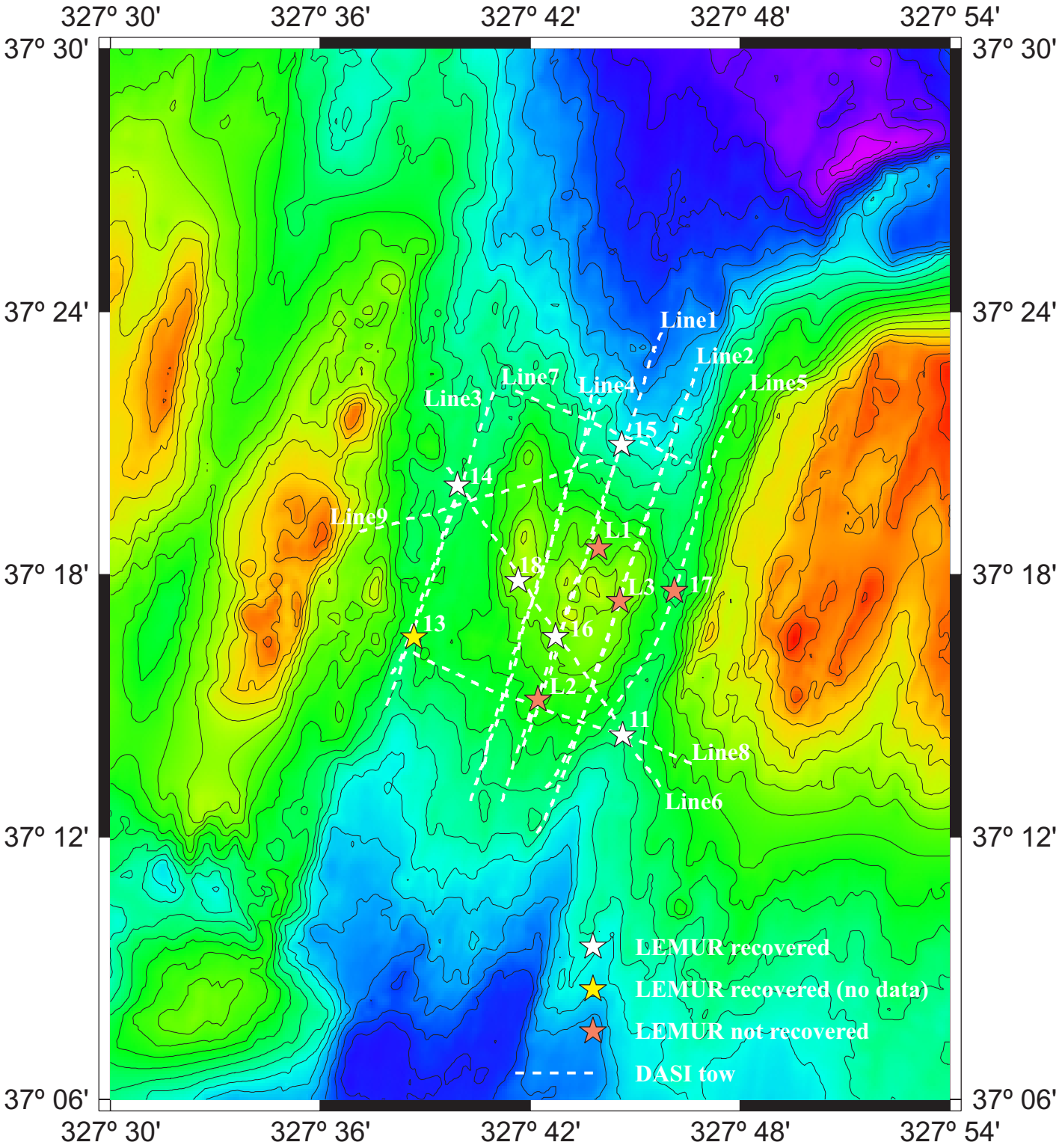

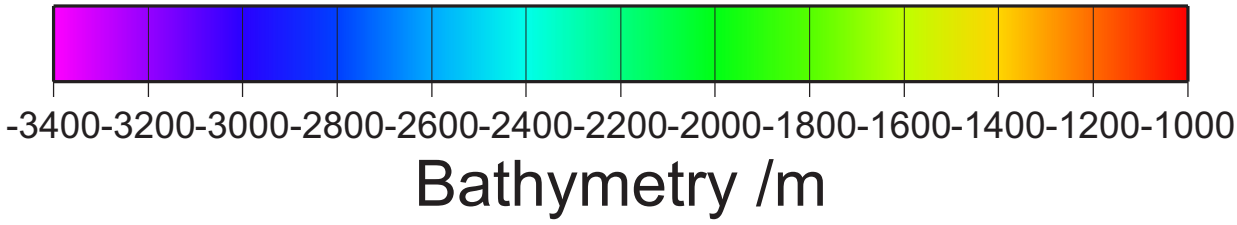

Figure 10.3. Locations of DASI as it was towed along the nine experiment lines, and the deployment positions of the LEMUR ocean bottom instruments, overlaying a swath bathymetric chart of the Lucky Strike segment of the Mid-Atlantic Ridge. Contour interval is 100 m.

when a light failed during a night-time recovery. However, high signal to noise ratio data were collected on the remaining five instruments out to large source-receiver offsets.

10.3 Acoustic navigation

A long baseline acoustic navigation system was used during the experiment to accurately locate both the DASI transmitter and the LEMURs with respect to each other and to the bathymetry base map. For this purpose, an array of six acoustic navigation transponders was deployed within the survey area (figure 10.4). A relay transponder was fitted to the DASI vehicle, allowing the position of the deep tow to be fixed in 3-dimensions relative to the transponder net.

In general, consistent and reliable ranges were obtained from the sea floor transponders to slant distances of 12 to 15 km. However, due to a fault with the relay transponder on the DASI vehicle, the ship-board system received ranges to the deep-tow only on alternate cycles. The navigation software was unable to deal with this situation adequately, and so for much of the time it was not possible to obtain realtime positions for DASI. However, all the data were logged, and as a result it proved possible to edit and post-process the range files to obtain good positions for DASI during all transmitting periods (see chapter 12).

10.4 Other data collected

A number of other data types were collected during the cruise in addition to the CSEM study. An array of 4 current meters was deployed across the narrowest part of the axial valley and the volcano (figure 10.4). These instruments recorded near-bottom water mass velocity, temperature and electrical conductivity. Two of these instruments (C2 and C4) also carried navigation transponders, further improving the acoustic navigation array.

Additional data on water column physical properties were obtained by launching a series of expendable bathythermographs (XBTs) at intervals along the current meter profile (figure 10.4). At the start of the cruise, a sound velocity meter was also lowered through the water column to within 200 m of the seafloor. As well as complementing the XBT and current meter data, the sound velocity profile was essential for accurate calibration and use of the long baseline acoustic navigation system.

Ship positioning was achieved throughout the cruise by differential GPS. A hull mounted acoustic Doppler current profiler (ADCP) was run continuously from the time that the vessel departed from the Azores until its return to the Azores at the end of the cruise. Throughout most of the cruise, 10 kHz precision echo sounder data were collected. The vessel was fitted with both a Lacoste and Romberg sea gravimeter, and a total-field proton precision magnetometer. The gravimeter ran throughout the cruise, with base station ties in Southampton at the start and end. The magnetometer was run throughout the DASI towing period, and at other times when the scientific programme permitted. A summary of the data collected can be found in table 10.2.

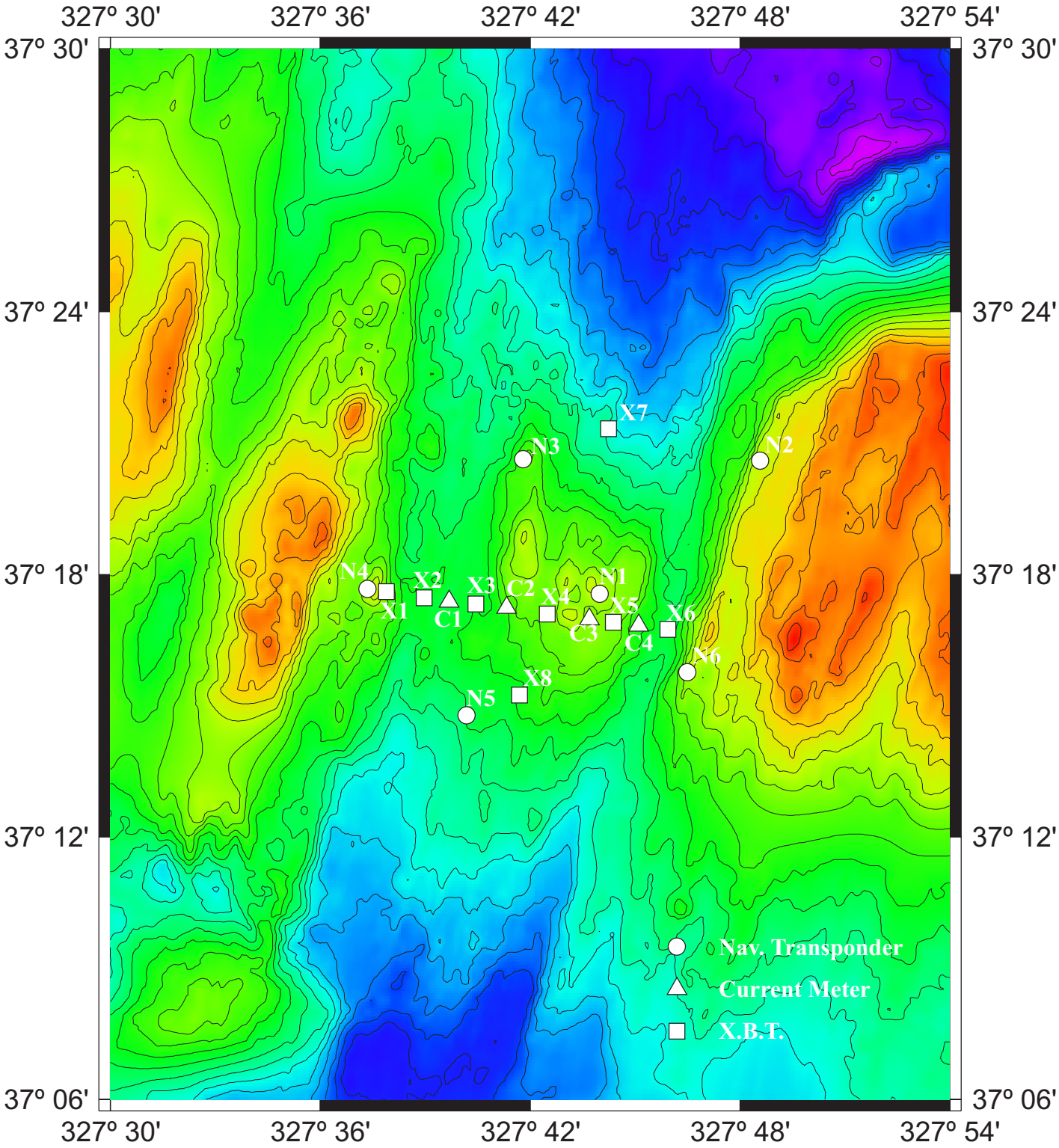

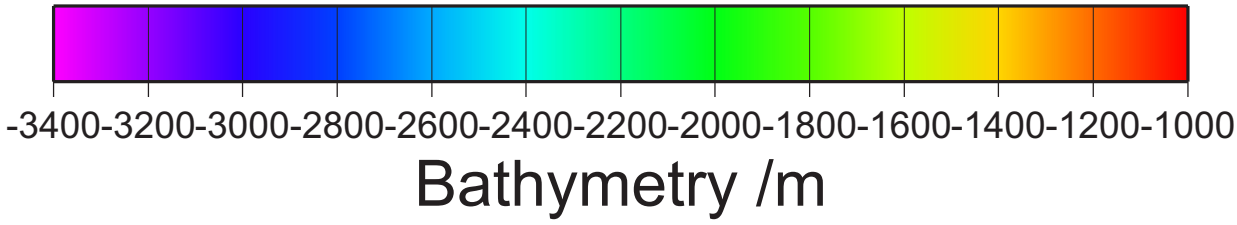

Figure 10.4. The navigation transponders, current meters and XBTs deployed during the experiment.

Data/Instrument Type	Times When Recorded
DGPS	Whole cruise
Gravity	Whole cruise
10kHz Echo Sounding	Most of cruise
ADCP	From leaving Azores until return
XBTs	Eight deployed within the work area (figure 10.4)
Current Meters	Once deployed, until recovery (Figure 10.4)
Magnetic Field	During DASI tows & at some other times
Sound Velocity Profile	Single vertical profile at location of XBT6 (figure 10.4)

Table 10.2: Data collected during the MADRIGALS cruise (other than CSEM data). See text for more detailed information.

10.5 References

Fouquet, Y., H. Ondreas, J. L. Charlou, J. P. Donval, J. R. Knoery, I. Costa, N. Lourenco and M. K. Tivey, 1995. Atlantic lava lakes and hot vents, *Nature*, 377, 201.

Fouquet, Y., J. L. Charlou, I. Costa, J. P. Donval, J. R. Knoery, H. P_lle, H. Ondr_as, N. Louren_o, M. S_gonzac and M. K. Tivey, 1994. A detailed study of the Lucky Srike hydrothermal site and discovery of a new hydrothermal site: Menez Gwen, *Preliminary results of the DIVA1 cruise (5-29 May).*

German, C. R., L. M. Parson and Heat Scientific Team, 1996. Hydrothermal exploration near the Azores Triple Junction: Tectonic control of venting at slow-spreading ridges?, *Earth and Planet. Sci. Lett.*, 138, 93-104.

Langmuir, C. H., J. L. Charlou, D. Colodner, S. Corey, I. Costa, D. Desbruyeres, T. Emerson, D. Fornari, A. Fiala-Medioni, Y. Fouquet, S. Humphris, L. Saldanha, R. Sours-Page, M. Thatcher, M. Tivey, C. V. Dover, K. V. Damm, K. Wiese and C. Wilson, 1993. Lucky Strike - A newly discovered hydrothermal site on the Azores Platform, *Ridge Events*, 3-5, November 1993.

Sinha, M.C., MADRIGALS: Mid-Atlantic Deep-towed Resistivity and Induction Geophysics At Lucky Strike, *RRS Charles Darwin* cruise 120, *NERC Cruise report*, 1999

Wilson, C., Speer, K., Charlou, JL., Bougault, H., and Klinkhammer, G., 1995. Hydrography above the Mid-Atlantic Ridge (33 degrees – 40 degrees North) and within the Lucky Strike segment, *J. Gephys. Res., 100, 20555-20564.*

Chapter 11

Magnetic anomaly data from the Lucky Strike seamount.

J. Luis[1] and the ISO-3D group[2]

1. Universidade do Algarve, Campus de Gambelas, 8000 Faro, Portugal

2. Other members of the ISO-3D group: M.C.Sinha, J.M. Miranda, A. Junge, A.H.Flosadottir, N. Lourenço, F.M. Santos, A. Soares, L.M. MacGregor, S. Dean, N. Barker, Z. Cheng and S. Riches

11.1 Magnetic anomaly data

The total field magnetic data acquired during the MADRIGALS cruise covered only the area inside the median valley of the Lucky Strike segment. In order to characterise the long wavelength geomagnetic field better, we used the data from a previous magnetic field survey carried out during the GEOFAR mission (Sichler *et al*, 1995) in 1992. This survey consists of profiles running parallel to the plate spreading direction, separated by 1 nautical mile and extending off axis as far as anomaly 3. Both data sets were submitted to the standard procedure of removing the IGRF total field in order to obtain a magnetic anomaly map of this ridge segment. Figure 11.1 shows the magnetic anomaly map and the location of data points.

One interesting feature revealed immediately by the magnetic anomaly map is the relative low in the anomaly in the region of the Lucky Strike hydrothermal field vent. Our working hypothesis is that this magnetic low is associated with a rock demagnetisation effect generated by the circulation of hydrothermal fluids. To test this hypothesis the 'Lucky Strike magnetic anomaly' must be isolated from the remaining anomalies, which are mainly due to reversals of the geomagnetic field and crustal demagnetisation with age.

To simulate the creation of new crust, taking into account the spreading rate and the geomagnetic reversals, a new computer code was developed. This code creates the crust not along 2-dimensional profiles but as a surface whose shape is defined by the bathymetry. Inside the stripes of constant polarity, the magnetisation is allowed to vary. In this way, both the effect of demagnetisation with age and a smooth transition of the magnetisation between blocks of different polarity can be simulated. The magnetisation distribution thus obtained can be considered as the 'theoretical regional anomaly' and when solving the direct problem a magnetic anomaly is obtained.

To compute the magnetic anomaly from the magnetisation distribution we developed another computer code based on the method of Okabe (Okabe, 1979). This algorithm computes the magnetic response of a 3-dimensional body constructed as a set of polygonal planar facets. The advantage of using a full 3-dimensional code instead of the 'Parker method' (Parker, 1972) is that the magnetic layer can have a variable thickness and the magnetic effect of bodies with arbitrary shapes can be computed.

The critical parameters in modelling the magnetisation reduction with age are the initial magnetisation, the magnetisation far way from the accretion axis and the time constant decay value. We followed the approach of Tivey & Johnson (1995), which is translated by the following equation:

$$I = (I_0 - I_\infty)e^{-\lambda t} + I_\infty$$

Where I is the magnetisation at time t; I_0 is the magnetisation at the ridge axis; I_∞ is the magnetisation far way from the ridge; and λ is the decay constant.

To estimate these three parameters, a series of model runs were performed. In each run only one parameter was allowed to vary and the other two were set constant. The procedure was repeated for each one of the 3 parameters. The differences between the model and the observed anomalies were used to define an error. The parameter values that gave a minimum error were considered to be the 'best solution'. Figure 11.2 displays the modelled magnetic anomaly and the observed magnetic anomaly. The model anomaly was computed from a magnetic layer of constant thickness of 500 m, with a central magnetisation of 18 A/m (I_0), a level magnetisation of 5 A/m (I_∞) and a decay time of 0.75 Ma.

Differences between the modelled and observed anomalies reflect the deviations from the model assumptions. Namely, the assumption that the magnetic layer has a constant thickness and that the magnetisation varies only along the flow lines of spreading. The effect of the magnetic layer thickness variation was not

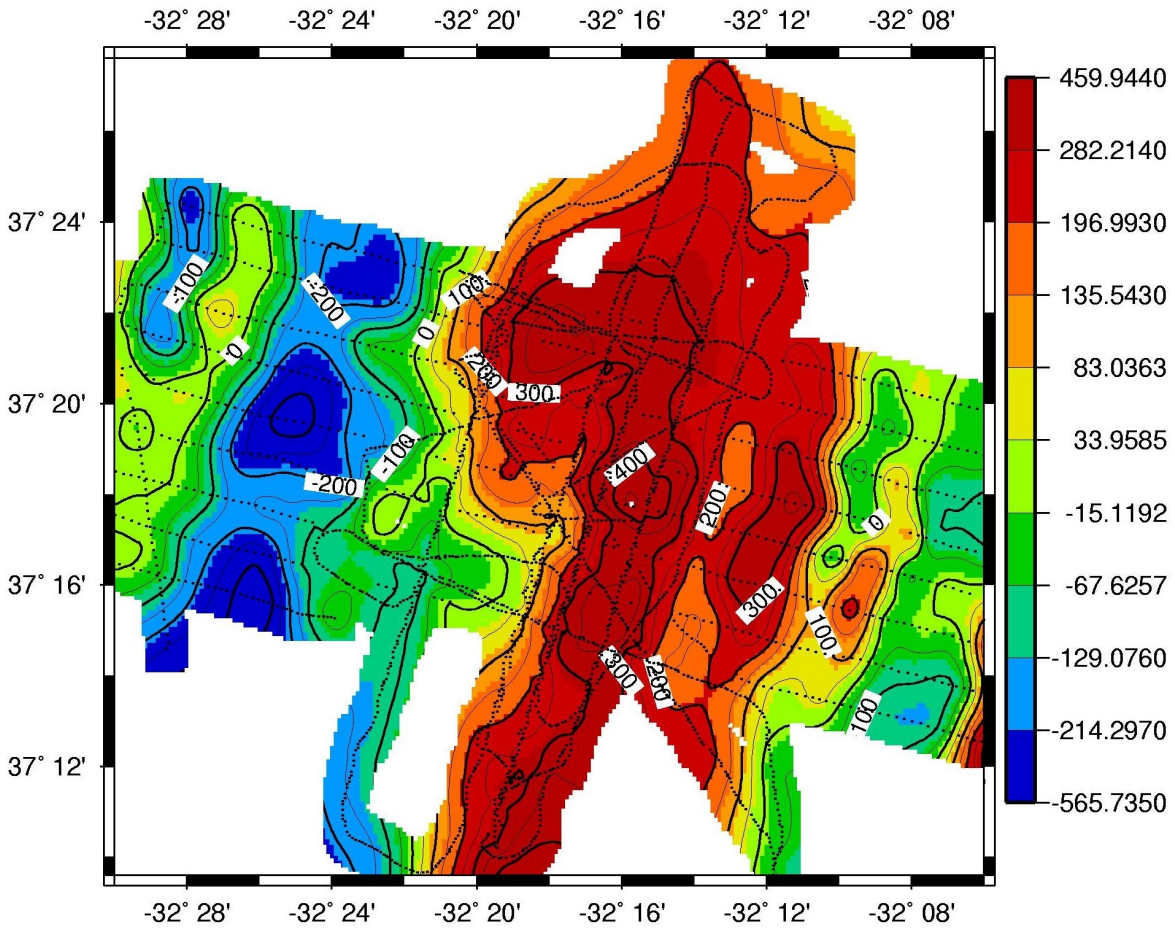

Figure 11.1. Magnetic anomaly map of the Lucky Strike segment. Dotted lines show the locations of the data points.

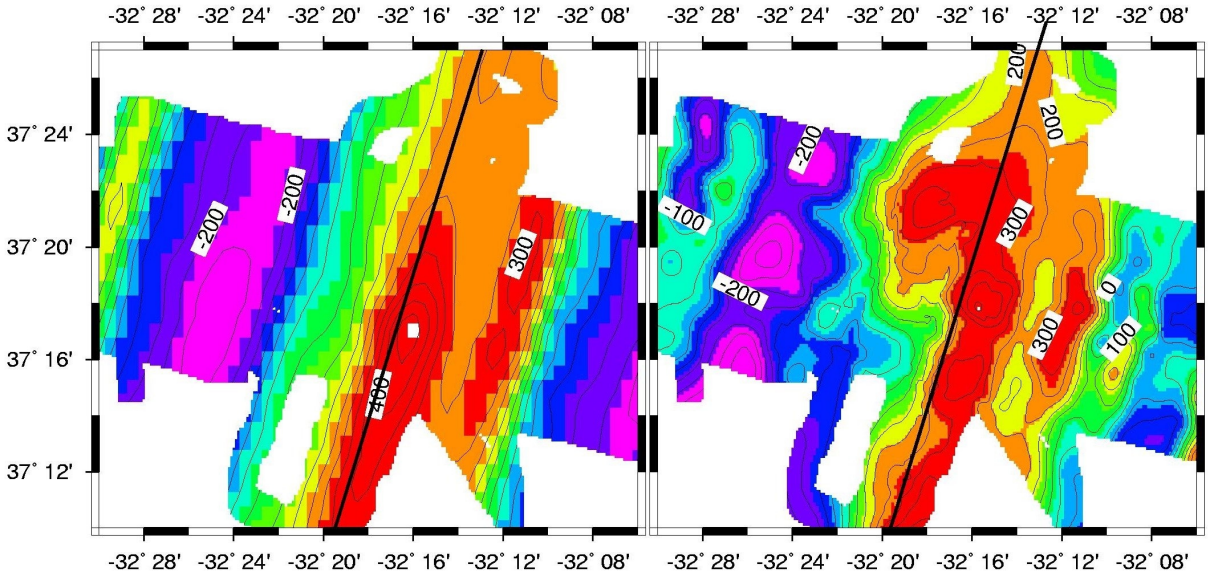

Figure 11.2. Modelled magnetic anomaly (left hand panel) and observed magnetic anomaly (right hand panel). See text for details.

investigated because we were mainly interested in the local anomalies whose source lies in variations of the magnetisation distribution.

Figure 11.3 displays the residual anomaly obtained from subtracting the modelled anomaly from the measured one. In this figure a prominent negative anomaly coinciding with the location of the hydrothermal field is clearly visible. To highlight where the anomaly is located, a figure with the bathymetry of the central volcano where the hydrothermal field sits, is also shown in figure 11.3.

The residual negative anomaly results from a lack of magnetic sources in the altered zone relative to the crustal rocks in the surrounding area. Given that the magnetic anomalous zone corresponds closely to the top of the ridge segment central volcano with known hydrothermal activity, the rock demagnetisation may result from a combination of both of the following effects: the raising of the Curie isothermal surface and chemical demagnetisation due to hydrothermal fluid circulation. From the magnetic point of view, these effects are not easily distinguishable.

Several attempts to model the anomaly using different bodies have shown that a good result is obtained when using a bivariate gaussian body (a bell shaped body) elongated along the segment direction. The shape of this body is defined by its standard deviation lengths along the ridge axis direction (17º) and across it, which are 1700 m and 900 m respectively. The body's height is 500 m, which corresponds to the thickness of the magnetic layer. The body has been assigned a magnetisation of -18 A/m, assumed to be in the direction of the present day field, which corresponds to the magnetisation at the ridge axis (I_0) used when constructing the theoretical regional magnetic anomaly. The negative sign follows from the fact that a negative anomaly is being modelled. Figure 11.4 shows the modelled anomaly produced by the bell shaped body and the residual anomaly after subtracting the effect of this body. The black star indicates the horizontal position of the body's centre. In effect, the new model inserts a localised region of zero net magnetisation into the crust in the area surrounding and underlying the hydrothermal vent field. This model can successfully reproduce the major features in the data.

11.2 References

Okabe, M., Analytical expressions for gravity anomalies due to polyhedral bodies and translation into magnetic anomalies, *Geophysics, 44,. 730-741, 1979.*

Parker, R.L., The rapid calculation of Potential anomalies, *J. R. Astr. Soc, 31, 447-455, 1972*

Sichler, B., M.F. LeQuentrec and J.F. Luis. Magnetism and Hydrothermalism: new Evidence From GEOFAR Magnetic Survey. *Terra Abstracts 7 (1; suppl.), 211, 1995.*

Tivey, M.A. & Johnson, H.P., ALVIN magnetic survey of zero age crust – Coaxial segment eruption, Juan de Fuca Ridge, 1993, *Geophys. Res. Letts., 22, 171-174*

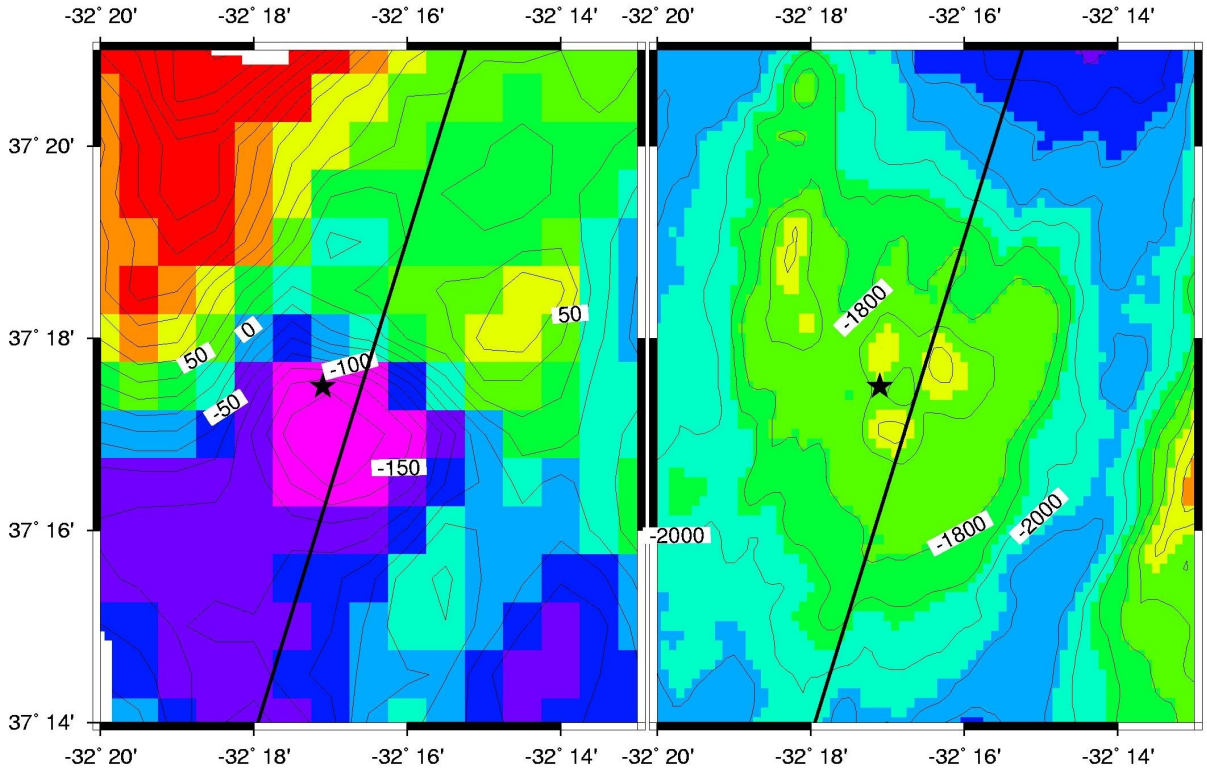

Figure 11.3. Left hand panel the residual magnetic anomaly obtained by subtracting the modelled anomaly from the observed one. The bathymetry of the Lucky Strike segment is shown in the right hand panel for reference.

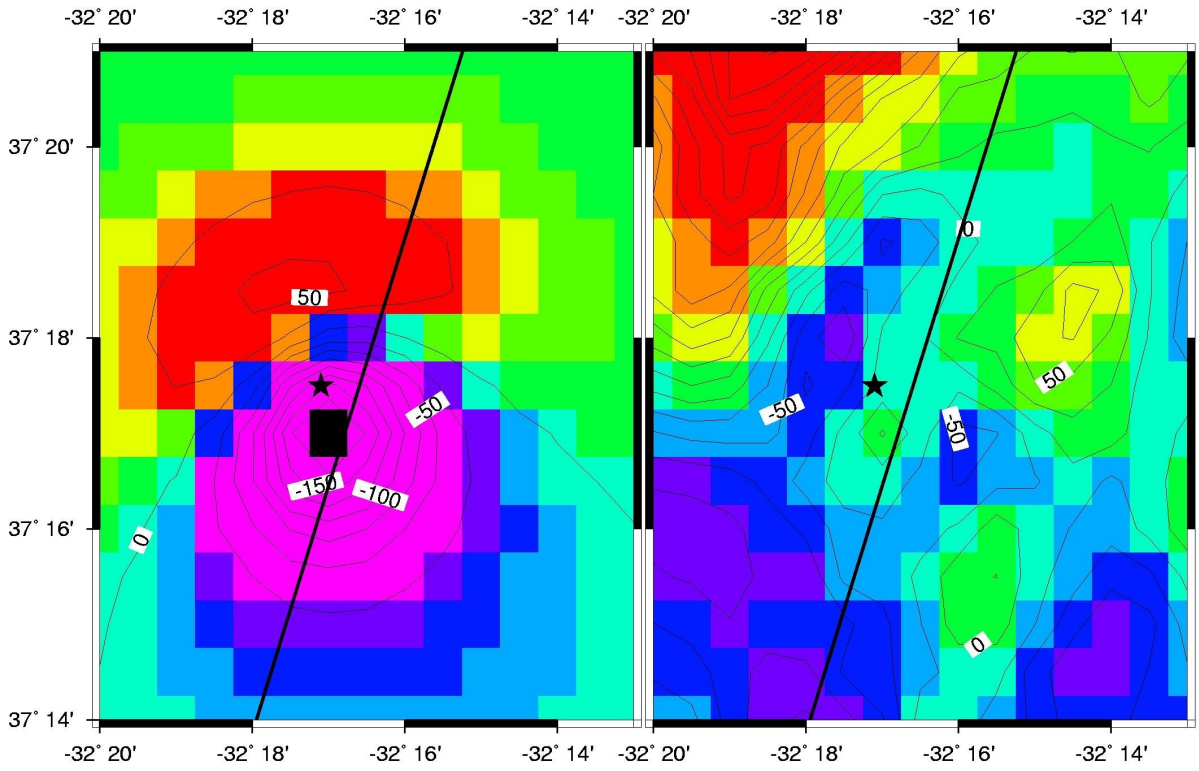

Figure 11.4. Modelled magnetic anomaly produced by a bell shaped body (left hand panel) and the residual anomaly after subtracting the effect of this body from the observed data. See text for discussion.

Chapter 12

The MADRIGALS cruise: CSEM data analysis and preliminary results.

N.D.Barker[1], L.M. MacGregor[1], M.C. Sinha[1] and the ISO-3D group[2]

1. School of Ocean and Earth Science, Southampton Oceanography Centre, Empress Dock, Southampton, SO14 3ZH, UK

2. Other members of the ISO-3D group: J.M. Miranda, A. Junge, A.H. Flosadottir, F.M. Santos, J. Luis, N. Lourenço, A. Soares, S. Dean, Z. Cheng and S. Riches

12.1 Introduction

This chapter outlines the pre-processing steps applied to the navigation and CSEM data; details the 1-dimensional modelling strategy implemented; and describes the results obtained. These results are compared with the results from previous CSEM experiments in various oceanic settings. Finally the response of a simple 3-dimensional structure based on the 1-dimensional results is examined.

12.2 Navigation

Analysis and interpretation of CSEM data relies upon an accurate knowledge of the locations of both the source and receivers. During the MADRIGALS cruise, source locations were determined using long baseline acoustic navigation. This system utilised two cycles. On the direct cycle, ranges were obtained from the ship to all transponders within range (including the relay transponder on DASI). During the second (relay) cycle, a signal was transmitted from the ship to the relay on DASI. This relay transponder sent a response that was received by all seafloor navigation transponders within range, before being returned to the ship. By combining the times obtained from both cycles, it was possible to calculate the ranges of both the ship, and the ocean bottom transponders, to DASI.

The LEMURs and acoustic navigation transponders were located with direct acoustic ranging from the ship. These ranges were modelled in conjunction with the velocity depth profile obtained from the sound velocity meter. A simple simulated annealing inversion process allowed all instruments to be located to within 20 metres.

Once the transponders in the long baseline array had been successfully located, it was possible to locate DASI on average every 4 minutes during transmission tows. Unlike the ocean bottom instruments, where about 15 separate ranges were used to invert for each location, there were usually only four DASI ranges available at any one time. This led to the DASI locations being less accurate, with an uncertainty of up to 100 m. This error level was reduced by smoothing successive inverted locations. It is estimated that this reduced the uncertainty in DASI's location to approximately 30-50 m.

12.3 Data overview

A summary of DASI tow lines completed can be found in table 10.1. Some instruments (LEMURs 11, 14 and 15) could not record all of these tows, as they were equipped with a smaller data storage capacity than the newer LEMURs 16 and 18. Figure 12.1 shows the sections of transmission tows for which viable 1 Hz signal was recorded by each of the five recovered LEMURs. It can be seen that excellent data coverage has been achieved over the target area, with a good signal to noise ratio being maintained up to source-receiver separations of 10 km.

Two channels of electromagnetic data were recorded by each instrument, one channel for each orthogonal HED sensor. This data went through the following stages of processing before modelling could begin:

- As CSEM data analysis occurs in the frequency domain, Fast Fourier transforms (FFTs) of 64 s segments of time series data were carried out in order to extract the signal at the required frequency (figure 12.2).
- The signal was calibrated in order to correct for the frequency response of the instrument.
- The navigation information and EM data were merged.
- The data were normalised by the source dipole moment and height of the source above the seafloor in order to facilitate easier comparison with modelling results.

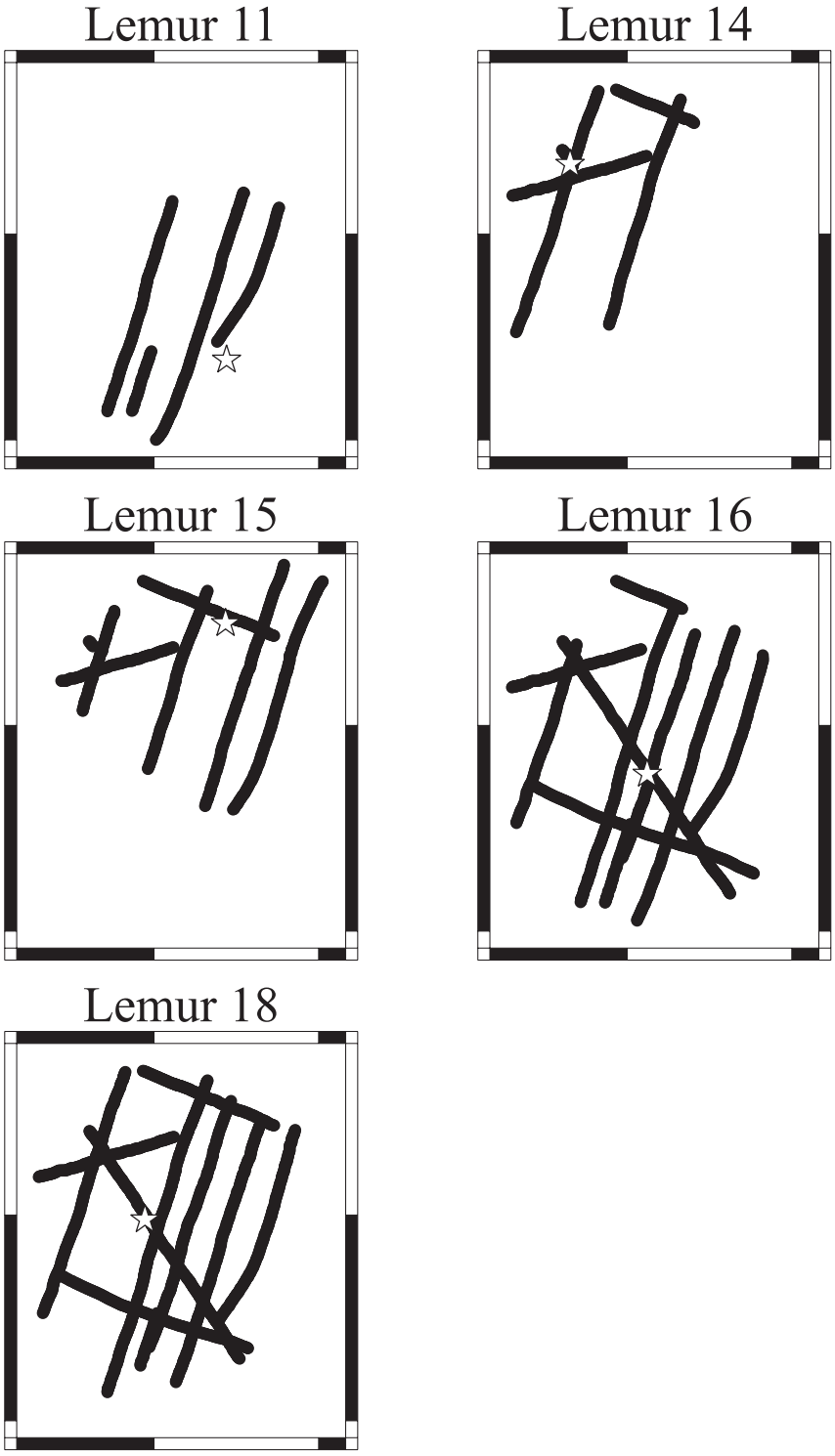

Figure 12.1. Plots of the data coverage obtained by each LEMUR at a frequency of 1 Hz. The LEMUR location is denoted by a star, whilst the black circles correspond to the location of DASI when an acceptable electromagnetic signal was received. The plotted area ranges from 32°23'W to 32°11'W and 37°11.5'N to 37°24'N. Despite instrument losses, full 3-D coverage of the Lucky Strike seamount was achieved.

Channel A

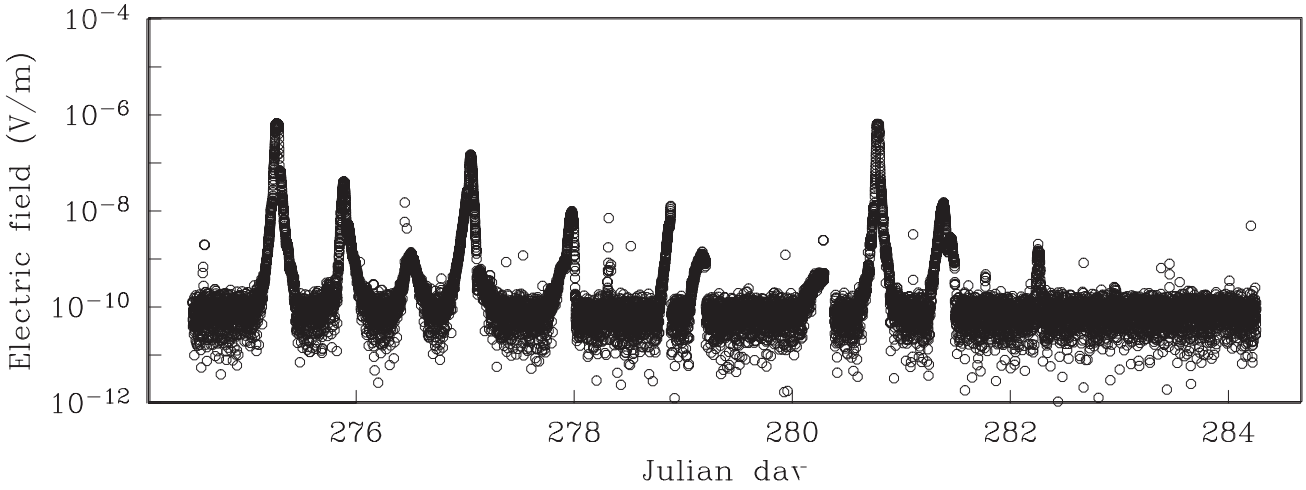

Channel B

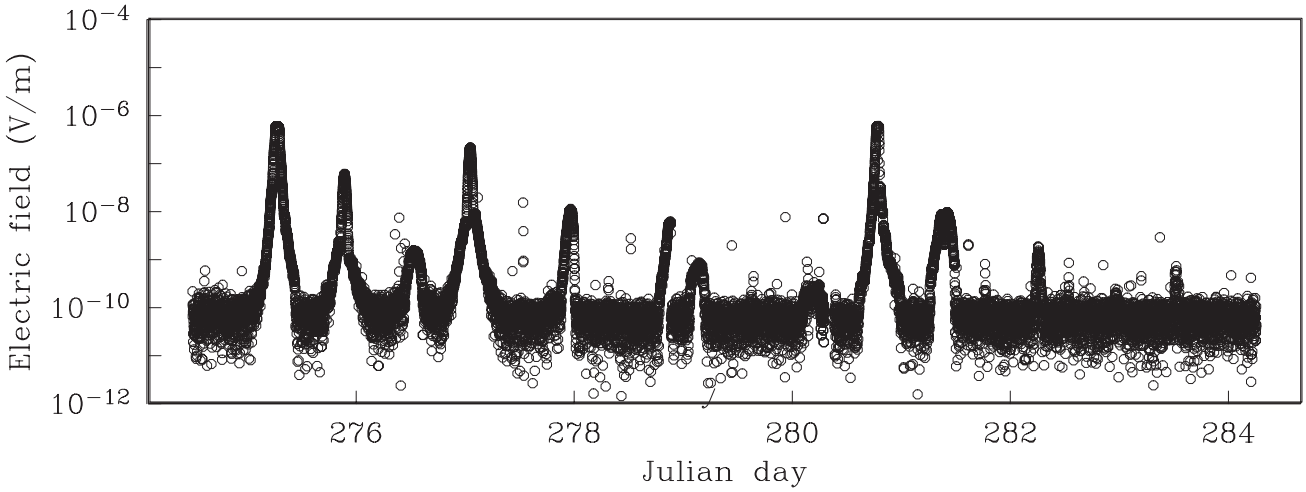

Figure 12.2. Amplitude versus elapsed time plots for each channel of data recorded by LEMUR 16. The graph shows the amplitude of a single frequency component at 1Hz, obtained by Fast Fourier Transforms of 64 s segments of time series data. The peaks in the data correspond to times when DASI is transmitting within range of the instrument. The two highest peaks are formed when DASI tows directly above the instrument (Line numbers 1 and 6 in figure 10.3).

- In several cases, the apparent EM noise levels were significantly different between channels on the same instrument. This was unexpected, and it was therefore decided to re-check the calibration of all the instruments: LEMURs 14 and 18 were found to have incorrect gain applied to one or both EM channels; and most onboard compasses (used to identify the instrument arm orientation on the seafloor) proved to be less accurate than had been hoped. Adequate first order corrections were made by comparing the data with predicted halfspace responses at the shortest ranges observed.

12.4 1-dimensional forward modelling

Figure 12.3 shows a portion of the data recorded by LEMUR 16, plotted against the response predicted by uniform halfspace models. It can be seen that, whilst the recorded data are almost fully bounded by the 1 Ωm and 100 Ωm halfspace lines, it is not adequately predicted by such a simple model.

The next simplest model consists of a resistivity halfspace, overlain by a single layer of a second resistivity. It was possible to obtain best-fit models for all the data transmitted at 1Hz by systematically sampling the 3-dimensional model space of layer resistivity, layer thickness and halfspace resistivity (figure 12.4). The RMS misfits obtained were normalised by the nominal data error, based upon geometric uncertainties. The forward modelling was carried out using code from Chave & Cox (1982). It can be seen that the lowest resistivity of the upper layer occurs at LEMUR 16, the instrument closest to the ridge axis. This upper layer may be equated to layer 2A of the oceanic crust, consisting of heavily fractured volcanic extrusives. The halfspace resistivity was not well constrained from the 1 Hz data alone. However, model misfit functions showed that a lower bound could be placed upon it of between 70 and 100 Ωm.

Slices of the layer-over-halfspace model misfit function (figure 12.5) illustrate the trade-off between upper resistivity and layer thickness. Such a trade-off reflects that this portion of the dataset is more sensitive to the conductance (the product of conductivity and layer thickness) of the uppermost crust, rather than the resistivity. The modelled conductance can be seen to be highest around LEMUR 16, the instrument at the top of the seamount, and lowest at LEMUR 11, the instrument furthest from the ridge axis.

12.5 1-dimensional inversion

The Occam inversion code used (Constable *et al.* 1987) is a regularised 1-dimensional inversion, which finds the smoothest model (defined in terms of spatial derivatives of model parameters) that is compatible with the data. In this case, it was used to minimise the first derivative of log(resistivity) with respect to log(depth) (i.e. to produce a model as close to a halfspace as possible). This modelling technique has already been successfully applied to CSEM data obtained in other oceanic settings (Evans *et al.* 1994; Constable & Cox, 1996; MacGregor *et al.* 1998; MacGregor *et al.* 2001).

The 3-dimensional nature of the resistivity of the target area meant that it proved necessary to subdivide the data before modelling, in order to obtain a 1D inversion that converged satisfactorily. 1-dimensional Occam inversion has now been carried out for subsets of the data from LEMUR 16, the instrument that was located near the seamount summit. The two 1 Hz tows that passed nearly directly over the instrument (Lines 1 and 6 on figure 10.3), were further subdivided into approaching and receding halves before modelling. The results obtained can be seen in figure 12.6.

All four curves show a resistivity increase from less than 1 Ωm near the surface, to between 10 and 100 Ωm at a depth of 2 km. Values at depth are broadly in agreement with the lower bound on halfspace resistivity obtained from the 2-layer

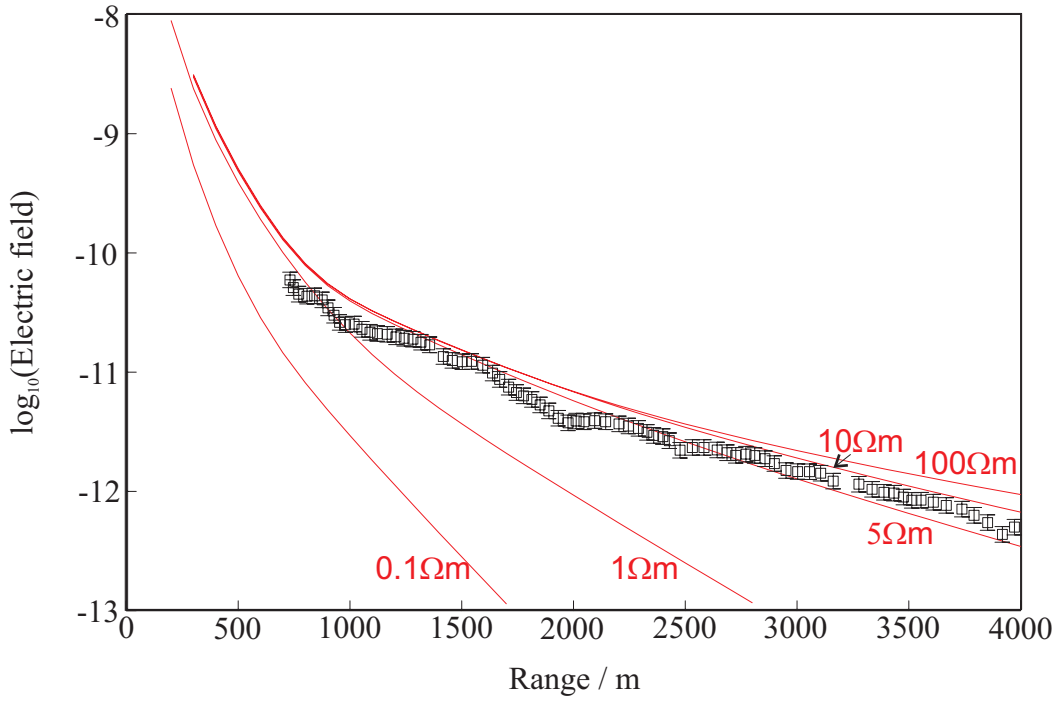

Figure 12.3. Data recorded by LEMUR 16 plotted with modelled halfspace responses. The black squares with error bars are 1 Hz data points recorded during Line 1, when the transmitter was to the north of the LEMUR, up to a source-receiver offset of 4 km. The five red lines correspond to the predicted response of a uniform halfspace, for the resistivities indicated.

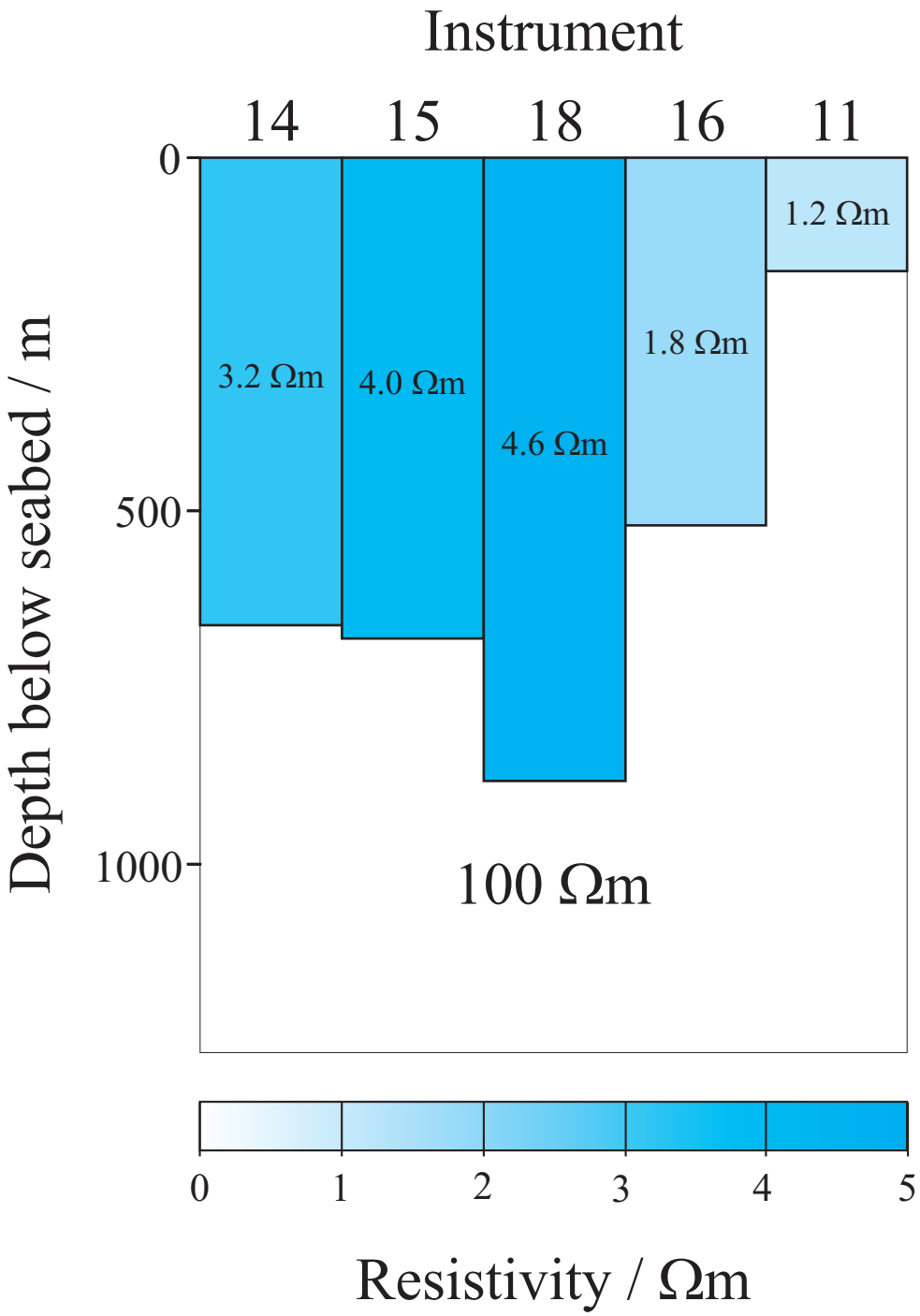

Figure 12.4. Resistivity models consisting of a layer over a uniform halfspace, obtained for each LEMUR at 1 Hz. See text for further discussion.

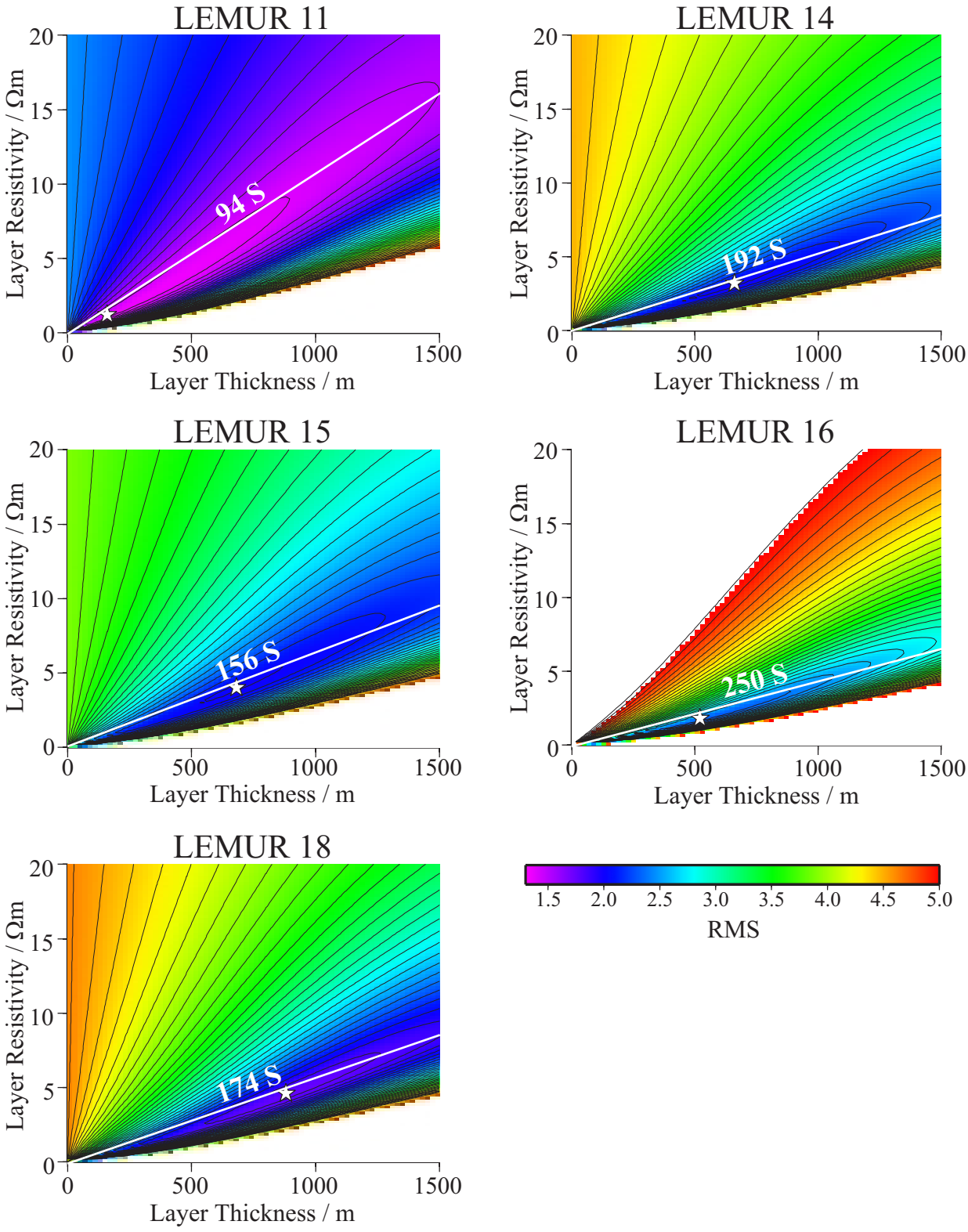

Figure 12.5. Slices through each of the 3-dimensional misfit functions obtained during layer-over-halfspace modelling. In each panel, the halfspace resistivity is 100 Ωm. The stars correspond to the final models obtained (see figure 12.4). The inverse of the gradients of the straight lines plotted through the misfit function correspond to the conductance which best fits the observed trade-off between layer thickness and resistivity.

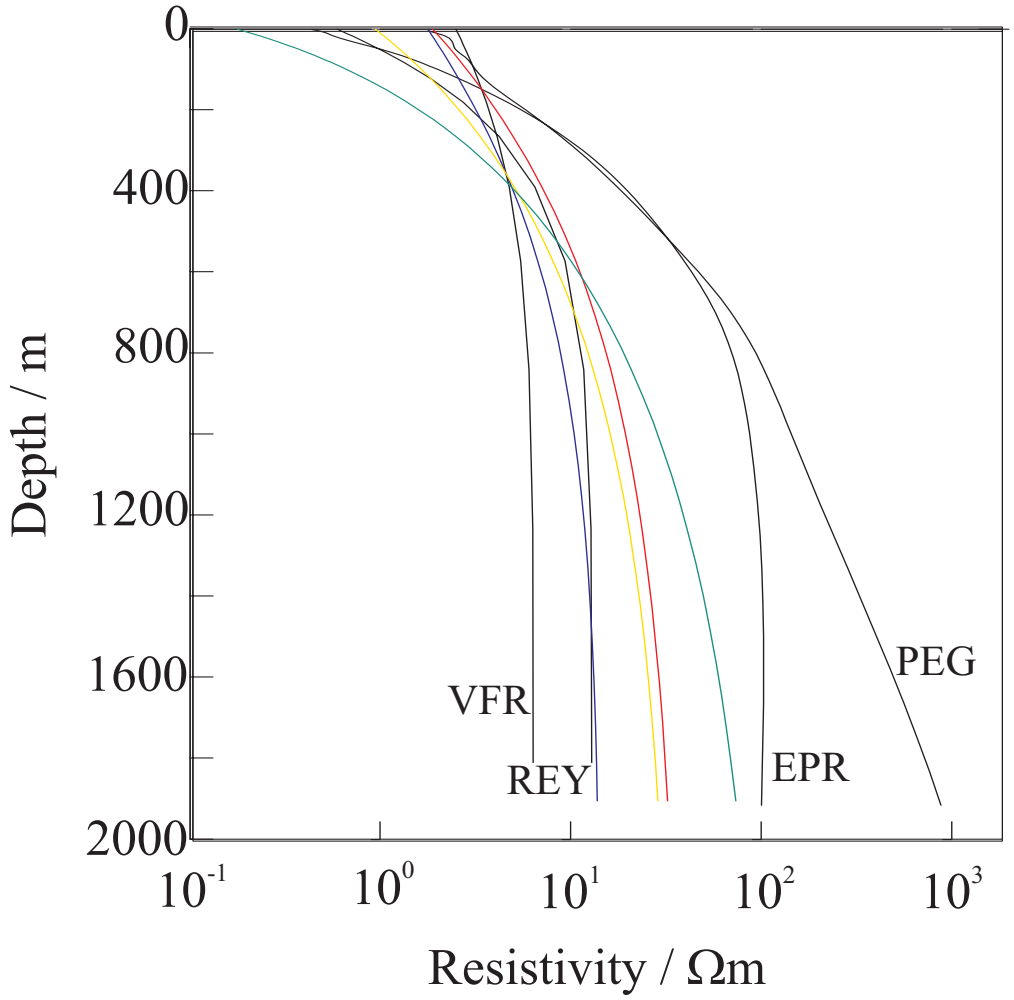

Figure 12.6. A plot of 1-dimensional resistivity-depth profiles obtained by Occam inversion. The four black lines correspond to results from previous experiments (see text for description). The four coloured curves correspond to the following portions of 1 Hz data recorded by LEMUR 16:

Red - Line 1 North of LEMUR 16

Blue - Line 1 South of LEMUR 16

Yellow - Line 6 NW of LEMUR 16

Green - Line 6 SE of LEMUR 16

In all cases the steep resistivity gradient observed in the upper 400-800 m of the crust may be equated to seismic layer 2A, consisting of heavily fractured volcanic extrusives.

modelling above. This is to be expected, as the first derivative smoothing will cause the deeper resistivity to tend to its lowest acceptable value, in order to minimise the vertical gradient. The four 1D profiles obtained so far do, however, show considerable variation, suggesting, as expected, that the resistivity of this area is significantly 3-dimensional in nature.

The results from four previous CSEM studies, also plotted in figure 12.6, originate from the following locations:

- Pegasus (PEG) - The Pegasus experiment was carried out over a 40 Ma old section of the Pacific Plate. This site is a typical example of mature oceanic crust. (Constable & Cox, 1996)
- East Pacific Rise at 13ºN (EPR) - The East Pacific Rise is a fast spreading ridge. However, at 13ºN, the ridge appears to be currently in a state of low magmatic activity (Evans *et al.*, 1994), although it is hydrothermally active.
- Reykjanes (REY) - The Reykjanes Ridge at 57º45'N, a section of the northern Mid-Atlantic Ridge, currently in a state of high magmatic activity, and underlain by a crustal magma chamber. (MacGregor *et al.*, 1998)
- Valu Fa Ridge (VFR) - The experiment carried out on the Valu Fa Ridge in the Lau Basin, was centred over the central segment of the spreading ridge. This ridge is in a back-arc environment, forming andesitic rocks, and is both magmatically and hydrothermally active. (MacGregor *et al.*, 2001)

It can be seen, even at this early stage of data processing, that Lucky Strike appears most like the Reykjanes Ridge in its shallow resistivity. This should not be surprising, as both form part of the Mid-Atlantic Ridge.

12.6 Three-dimensional structure at the Lucky Strike Seamount.

The results of the 1-dimensional modelling and inversion demonstrate that the structure of the Lucky Strike seamount is 3-dimensional in nature. In order to demonstrate the effect of 3-dimensional structure on the fields of a horizontal electric dipole, a simple 3-dimensional model was constructed, again based on the results of the 1-dimensional modelling. A vertical section through the model is shown in figure 12.7 (the structure is the same in the orthogonal plane). The model can be described as a 3-dimensional conductive anomaly embedded in a simple 1-dimensional background model (a 200 m thick, 2 Ωm layer overlying a 100 Ωm halfspace, the same 1-dimensional model used to normalise the data in figure 12.8). The dimensions of the conductive anomaly are chosen to be broadly consistent with the horizontal dimensions of the Lucky Strike Seamount.

Figure 12.8 shows the response of this model for the case of a 1Hz, x-directed dipole at the seafloor. The effect of the conductive 3-dimensional structure is to retard the diffusion of the electromagnetic fields through it, causing the contours of electric field strength shown in the upper panel to be bowed back towards the source when they meet the anomaly. This effect is seen more clearly in the lower panel of figure 12.8, which shows the response of the 3-dimensional model normalised by the response of the background 1-dimensional model. Away from the anomalous 3-dimensional structure the response is close to that of the background structure. However local to the 3-dimensional conductive structure, the field strength is significantly reduced relative to the response of the background structure. This result illustrates the sensitivity of the type of CSEM experiment performed to underlying 3-dimensional structure associated with hydrothermal or volcanic processes at the Lucky Strike seamount.

This 3-dimensionality in the data can also be highlighted by looking at the normalised electric field, that is the electric field strength recorded by the instrument divided by the corresponding electric field calculated from a 1-dimensional background model for the same source-receiver geometry. The normalised 1Hz data are shown in figure 12.9 for a background model chosen on the

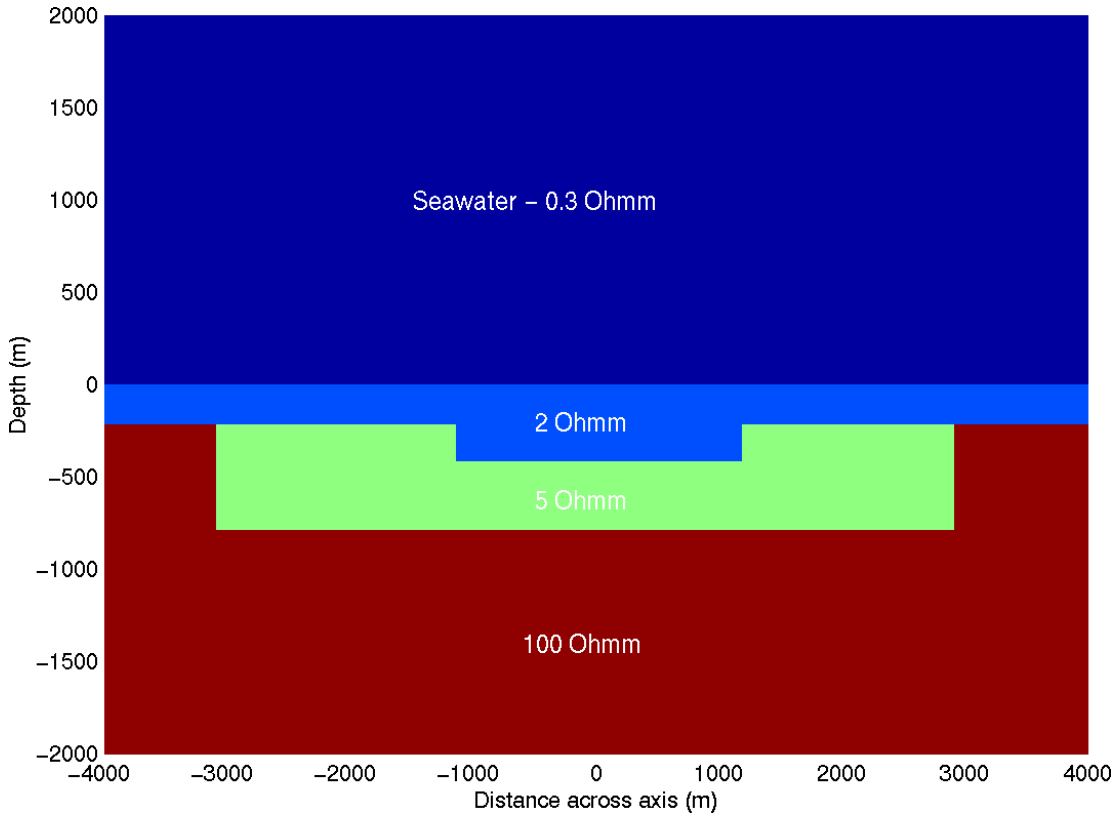

Figure 12.7. Three-dimensional structure, based on the results of 1-dimensional modelling data from each instrument. The background model is a 200 m thick, 2 Ωm layer over a 100 Ωm halfspace. Embedded in this is a conductive region comprising a 2 Ωm zone surrounded by a 5 Ωm zone, representing the Lucky Strike seamount. The lateral extent of the 5 Ωm zone was chosen to be consistent with the horizontal scale of the seamount above the 1900 m depth contour. The 2 Ωm zone was chosen to be approximately the area of the three summit volcanic cones and drained lava lake, the region where hydrothermal activity has been observed. The figure shows a vertical section thorough the 3-dimensional structure. The structure is the same in the orthogonal plane.

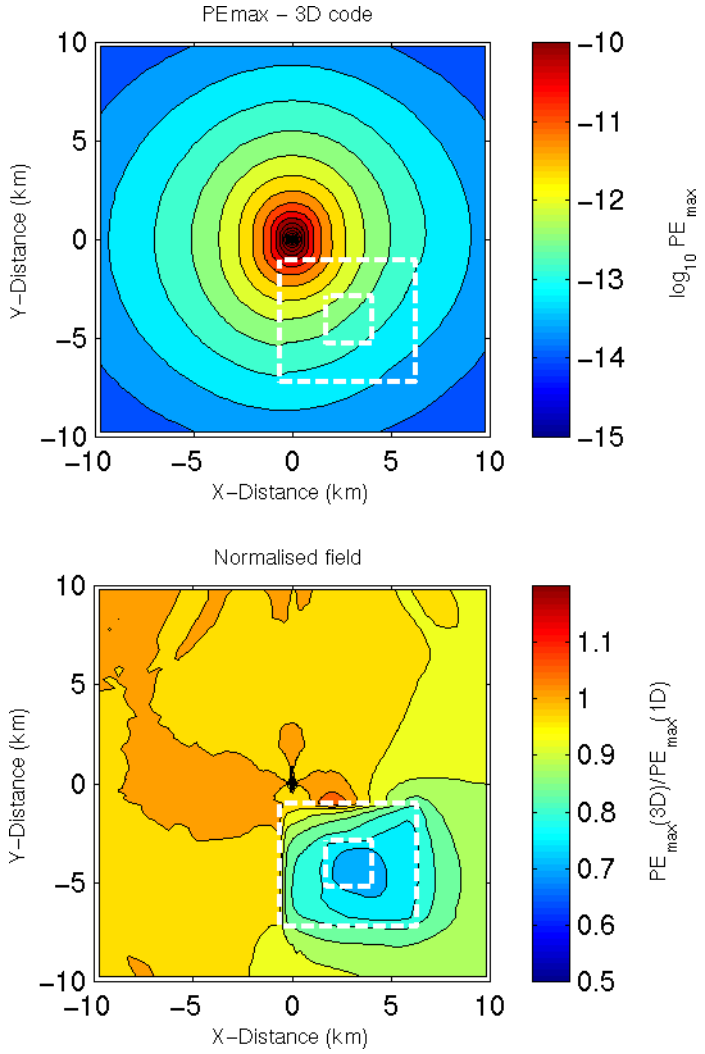

Figure 12.8. Upper panel: semi-major axis of the polarisation ellipse, contoured at the seafloor for structure shown in figure 12.7. The source is a 1 Hz HED at the seafloor oriented long the x-direction, and is offset from the 3-dimensional structure. The outline of the 5 Ωm zone and 2 Ωm zone inside it are shown by the white lines. The lower panel shows the normalised electric field strength at the seafloor. Fields were normalised by the response of a 1-dimensional model consisting of a 200 m/ 2 Ωm layer over a 100 Ωm halfspace. See text for discussion.

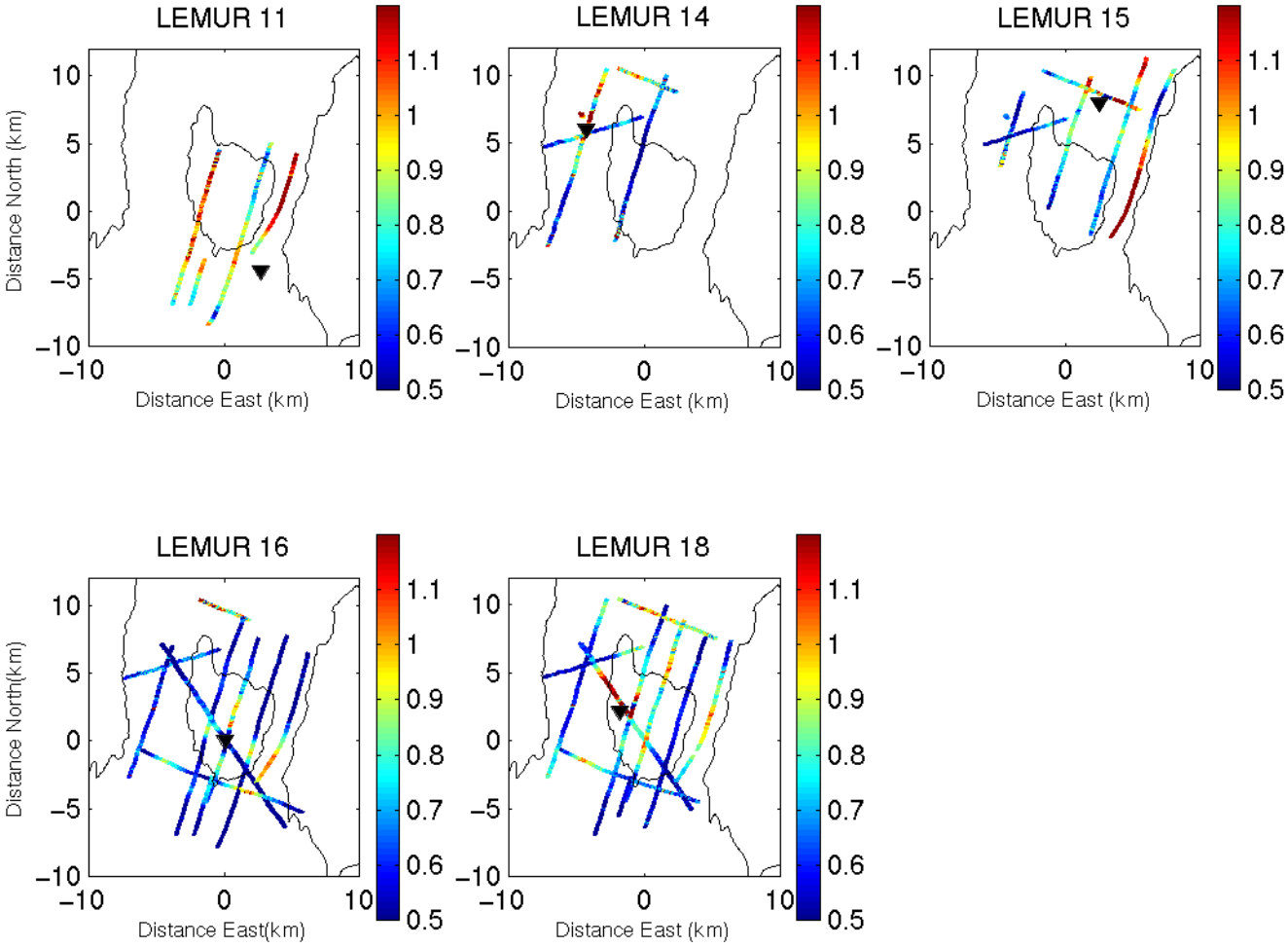

Figure 12.9. Normalised electric field data, derived from the 1 Hz data collected on the LEMURs during the MAGRIGALS experiment. The colour scale corresponds to the normalised electric field strength (data value divided by the corresponding result for a 200 m thick/2 Ωm layer over a 100 Ωm halfspace). Normalised data are plotted at the appropriate source location, in km East and North of LEMUR 16, which was located at the centre of the array. Receiver locations are shown by black triangles. The Lucky Strike Seamount and median valley walls are outlined by the 1900 m depth contour.

basis of the 1-dimensional modelling results, and consisting of a 200 m thick, 2 Ωm layer overlying a 100 Ωm halfspace. The normalised data are plotted at the appropriate source location for each of the receivers. A value of one corresponds to a data value of the same magnitude as the response of the background model. Values less than one (blue) indicate a data value of lower magnitude, and values greater than one (orange) indicate a data value of greater magnitude than the response of the 1-dimensional background model.

There are clear systematic trends in the normalised data. For instance, data collected by LEMUR 16 and LEMUR 18 give normalised values which are predominantly less than one, indicating structure around the instrument which is less resistive than the assumed 1-dimensional background model. This is as expected since both these instruments are located on the Lucky Strike seamount, where the bulk resistivity is likely to be lower because of the presence of hydrothermal fluids in the crust. The eastern flank of the seamount appears to be consistently more resistive than the background model (indicated by consistently high values of normalised data along the eastern tow, and high normalised data values from LEMUR 11, located to the East of the seamount).

As well as the large scale trends in the normalised data, there are smaller systematic variations with wavelengths of order 2-5 km throughout the dataset. These are caused by the presence of 3-dimensional variations in resistivity structure at scales less than 10 km. Some of this variation is likely to be the result of the rugged seafloor topography of the Lucky Strike segment, however previous work on the Mid-Atlantic Ridge (MacGregor *et al.* 1998) suggests that the response is primarily governed by sub-seafloor structure with topography as a second order effect. Determining the exact structural cause of the variations in the received electric field will require careful modelling of the data, which will be the subject of future work.

12.7 References

Chave, A. D., and C. S. Cox, 1982. Controlled electromagnetic sources for measuring electrical conductivity beneath the oceans, 1. Forward problem and model study, *J. Geophys. Res.*, 87, 5327-5338.

Constable, S. C., Parker R. L. and Constable, C. G., 1987. Occam's inversion: a practical algorithm for generating smooth models from electromagnetic data, *Geophysics*, 52, 289-300.

Constable, S. C., and C. S. Cox, 1996. Marine controlled source electromagnetic sounding II: The PEGASUS experiment, *J. Geophys. Res.*, 101, 5519-5530.

Evans, R. L., M. C. Sinha, S. C. Constable and M. J. Unsworth, 1994. On the electrical nature of the axial melt zone at 13°N on the East Pacific Rise, *J. Geophys. Res.*, 99, 577-588.

MacGregor, L.M., S. C. Constable and M. C. Sinha, 1998. The RAMESSES experiment III: Controlled source electromagnetic sounding of the Reykjanes Ridge at 57°45'N, *Geophys. J. Int.*, 135, 773-789.

MacGregor, L.M., Sinha, M.C. & Constable, S.C., 2001. Electrical resistivity structure of the Valu Fa Ridge, Lau Basin, from controlled source electromagnetic sounding, *Geophys. J. Int., 146, 217-236*

ISO-3D Final Report

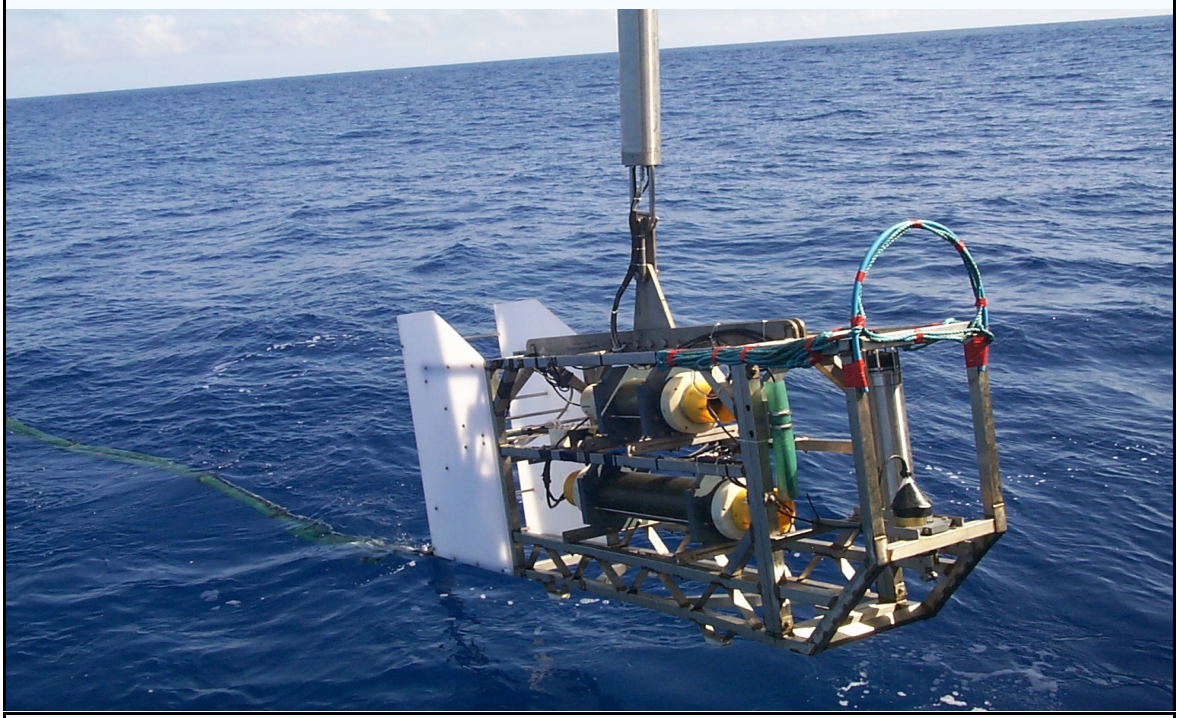

Part 5

Conclusions

Chapter 13

The Digital Archive

S.M.Dean[1] and the ISO-3D group[2]

1. School of Ocean and Earth Science, Southampton Oceanography Centre, Empress Dock, Southampton, SO14 3ZH, UK

2. Other members of the ISO-3D group: M.C. Sinha, J.M. Miranda, A. Junge, A.H.Flosadottir, L.M. MacGregor, F.M. Santos, J. Luis, N. Lourenço, A. Soares, N. Barker, Z. Cheng and S. Riches

13.1 Format and structure of the digital archive

The ISO-3D digital archive is distributed across 6 CD-ROM disks (figure 13.1). Each CD-ROM is written in an ISO-9660/JOLIET/HFS format compatible with Windows 3X/9X/NT, Macintosh and UNIX computers. To ease file identification on the majority of computer systems, long names (greater than 8 characters) have been used for many files and directories; for computer systems unable to read long files names (e.g., DOS based computers) each directory contains the text file named "TRANS.TBL" which maps all long names down to their 8 character length equivalent.

Disk 1 contains the final report, original project proposal, annual reports, technical annex, CSEM demonstration experiment cruise report, and all ISO-3D papers, abstracts and posters produced by the group to date. Disk 2 contains the entire natural source baseline dataset from the CAM1 submarine cable. The remaining archive space on Disk 2 is devoted to the results of the CSEM demonstration experiment, cruise CD120. Disk 2 contains the LEMUR clock check data, the DASI telemetry log and the underway data: GPS navigation, long base line navigation, magnetic, gravity and bathymetry data. The DASI Piggy-back logger data completes Disk 2. The remaining data from the DASI Piggy-back logger and the data from the five LEMUR instruments are distributed across Disks 3-6.

13.2 Overview of data formats

Where possible, data files have been converted into column formatted, space delineated, text files. This format is suitable for all the CAM-1 submarine cable data, underway, long base line, XBT and current meter data. DASI and LEMUR data is stored in the instruments original binary format. Details on the LEMUR data format is provided in Chapter 4. Although many of the data types are self-explanatory (e.g., the underway data and CAM1 cable data) a single header line at the top of each file provides a title for each column. In the case of the instrument clock checks, the current meter data and the DASI telemetry log, a text file is included with each data type to describe the format and, if necessary, any conversions that have been applied. The text description files are named using the file extension ".readme", e.g. "lemur_telemetry.readme", and have been placed in the directory with their corresponding data.

13.3 Accessing the electronic ISO-3D reports and documents

Electronic versions of this final report and all previous public domain ISO-3D documents and publications have been converted into Adobe Portable Document Format (PDF) documents and included in the digital archive. To read, Adobe Acrobat reader version 4 or above is required. Acrobat Reader installation files for Windows 95/98, NT and Macintosh are provided on Disk1:/acroread/. Each PDF document has been optimised to provide the highest quality paper copy, with many embedded PostScript figures, and are designed to reproduce on A4 format paper.

The digital archive contains the following PDF reports:

- Final Report
- ISO-3D Proposal (part 1)
- ISO-3D Proposal (part 2)
- 1998 Annual Report
- 1999 Annual Report
- Technical Annex (revised January 2001)
- CSEM Demonstration Experiment Cruise Report (CD120)

Papers:

- "Voltage measurements in the CAM-1 submarine cable between Madeira Island and Portugal mainland". Fernando A. Monteiro Santos, António Soares, Luís Trindade, Rita Nolasco, Helena Rodrigues and ISO-3D team.

Posters:

- "Investigation of crustal fluids at the Lucky Strike hydrothermal site using controlled source electromagnetic sounding". N D Barker , M C Sinha , L M MacGregor and members of the ISO-3D team. Presented at the 2001 meeting of the European Geological Society.
- "Fine scale magnetization in the Lucky Strike segment". J Freire Luis, J M Miranda, N Lourenço and M C Sinha. Presented at the 2000 meeting of the European Geological Society.
- "Induction Sources in the Ocean: The ISO-3D project". A H Flosadottir, A Greer, A Junge, J F Luis, L M MacGregor, J M Miranda, S Riches, F A M Santos, M C Sinha, A Soares and R H Tyler. Presented at the 1998 meeting of the IAGA.

Abstracts:

- "Investigation of crustal fluids at the Lucky Strike hydrothermal site using controlled Source Electromagnetic Sounding". N D Barker, L M MacGregor, M C Sinha, J Luis, N Lourenco, A H Flosadottir, A Soares, M Miranda and F Santos. For the 2001 meeting of the European Geological Society.
- "Long-period magnetotelluric studies in the Azores". A Junge and F Santos. For the 2000 meeting of the AZMT.
- "Preliminary electric field observations in the CAM-1 cable between Madeira and Lisbon". F Santos, A Soares, J M Miranda, M Victor and the ISO-3D group. For the 1999 meeting of the European Geological Society.
- "Induction sources in the ocean: a model code for oceanic and controlled sources". A H Flosadottir and L M MacGregor. For the 1999 Fall meeting of the American Geophysical Union.
- "Investigation of crustal fluids at the Lucky Strike hydrothermal site using controlled source electromagnetic sounding". L M MacGregor, M C Sinha, F Santos, M Miranda, A Soares, J Luis, N Lourenco and A H Flosadottir. For the 1999 Fall meeting of the American Geophysical Union.

PDF has been used for plots of data not otherwise included completely within this report. In particular, plots of the CAM-1 cable data have been converted into an interactive PDF file with navigation facilities to step through days or months worth of data, and a zoom facility to allow each day to be selected and viewed individually from the month view. The following data plots are available:

- CAM-1 MT cable data
- Current meter water conductivity (CD120)
- Current meter flow direction (CD120)
- Current meter flow speed (CD120)
- Current meter water temperature (CD120)
- XBT temperature profiles (CD120)

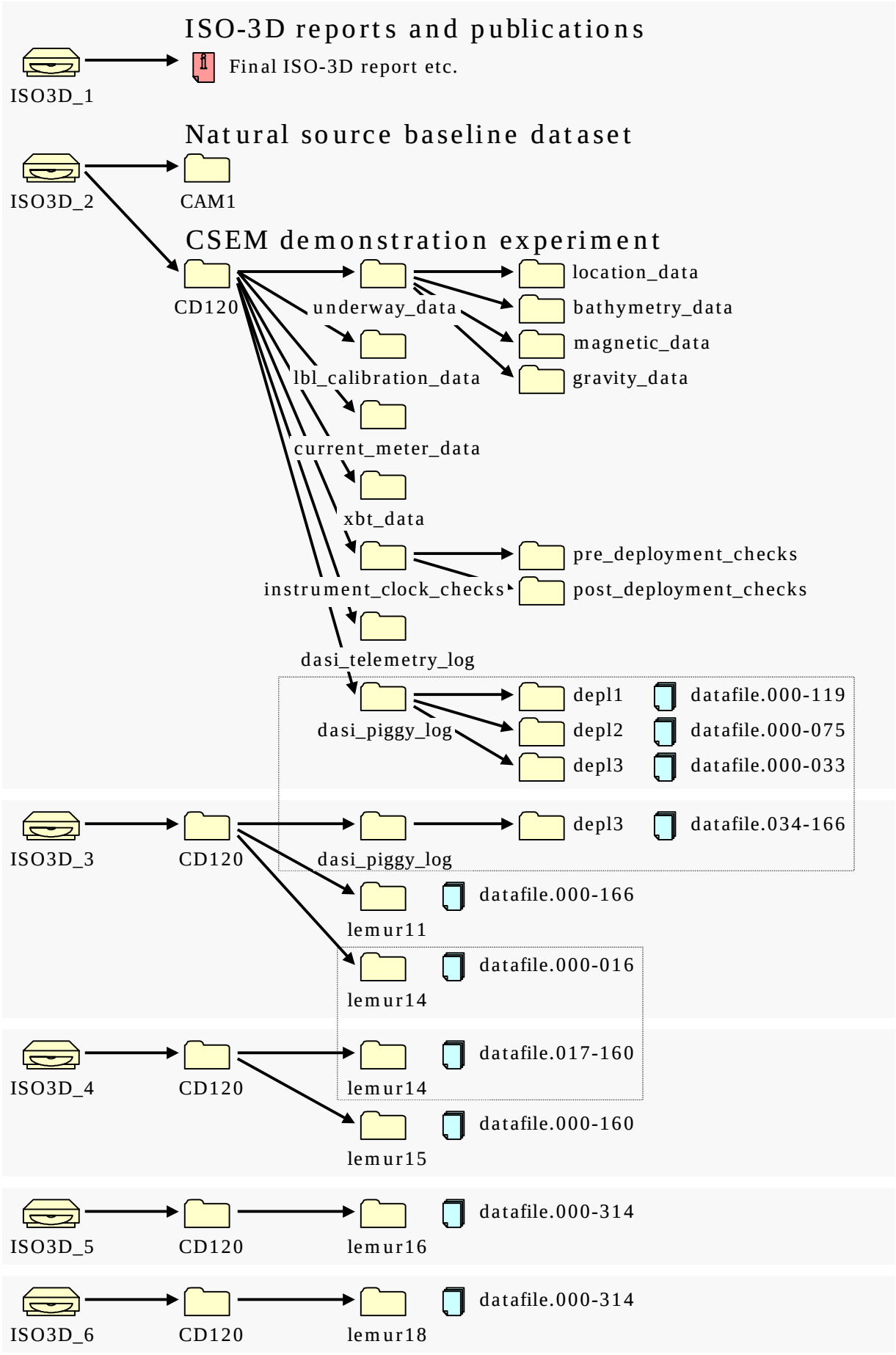

Figure 13.1. Structure of the ISO-3D digital archive.

Chapter 14

Applications of 3-Dimensional Electromagnetic Induction by Sources in the Ocean: Conclusions

M. C. Sinha[1] and the ISO-3D Working Group[2]

1. School of Ocean and Earth Science, Southampton Oceanography Centre, Empress Dock, Southampton, SO14 3ZH
2. Other members of the ISO-3D team: Other members of the ISO-3D group: J.M. Miranda, N. Lourenço, J. Luís, F. Santos, A. Flosadottir, A. Junge, L. MacGregor, A. Soares, S.Dean, N. Barker, S. Riches and Z. Cheng

14.1 Scientific and technological background

At the outset of this project, the development of new methods for measuring and exploiting electromagnetic fields at the ocean floor was being hampered by the absence of a tractable 3-dimensional forward modelling code. The requirement for such a code was that it should be capable of modelling induction throughout a structure in which resistivity could vary by several orders of magnitude in any spatial direction; that it should be capable of including the effects of isolated or distributed induction sources with 3-dimensional geometries embedded within the ocean; and that it should be able to run on reasonably powerful workstations, without inevitably requiring supercomputer facilities.

During the course of the project, the ISO-3D consortium has successfully developed, tested and documented an appropriate code, 'ISIS'. In parallel with this we have established long term monitoring of induced voltage in a trans-ocean submarine cable; improved and constructed seafloor instrumentation; collected and analysed natural field data on land; analysed land-based data for the effects of ocean tidal signals, and the cable data for the electrical structure of the underlying lithosphere; carried out a major research cruise to the Mid-Atlantic Ridge; and analysed the resulting magnetic and CSEM data from the Lucky Strike spreading segment and hydrothermal field.

Overall the project has made significant progress and produced substantial technical or scientific results in all major areas proposed for investigation. It has also drawn together a diverse group of European researchers, and fostered excellent collaborations and working relationships which we are confident will continue to bear fruit in the future. The project has generated data compilations, new data and new research tools that have enormous potential for future research in the field of marine electromagnetics and its application to studies of the ocean, the solid earth, and the interactions between them; and the collaborations established through ISO-3D will continue to be exploited as we pursue new goals.

14.2 Scientific and technical achievements of the project

We have developed the 'ISIS' (Induction by Sources In the Sea) numerical modelling code, based on a pre-existing 3-D electromagnetic solver; and rigorously tested it, including verifying its accuracy by comparison against other 1-D and 2-D numerical codes.

We have completed a technical development and construction programme for seafloor instruments for CSEM sounding. This has made substantial improvements in reliability and ease of operation to the DASI transmitter system and to the LEMUR seafloor receiver systems, and provided additional LEMUR instruments for Southampton and Lisbon Universities.

We have established a monitoring site for logging naturally induced electric fields generated along the abandoned CAM-1 telecommunications cable, which runs from the island of Madeira to the Portuguese mainland. We have analysed a 15 month time series of data from the cable, to assess its stability and to investigate water transport. We have estimated the lithospheric scale (i.e. to depth of at least 200 km) geoelectrical structure of the eastern Atlantic seafloor between Madeira and Lisbon, using data from the cable and the geomagnetic observatory on the Canary Islands. The result indicates that the seafloor sediment layer has an integrated conductance of order 10,000 S; and that this is underlain by a much more resistive crystalline lithosphere, and then by relatively conductive asthenosphere at depths greater than 100 km.

We have collected magneto-telluric sounding data from the Azores islands. A preliminary analysis of these suggests a highly conductive shallow structure, influenced by the surrounding ocean, as expected; but also a second highly conducting layer in the mantle, at a depth of approximately 50 km. The structure

here, above the Azores mantle hot spot and Mid-Atlantic Ridge, differs significantly from that beneath the mature lithosphere traversed by the CAM-1 cable.

We have analysed data from 6 land MT sites in northern Germany and 8 sites in Scotland, and shown the presence of a strong tidal component at the semidiurnal lunar period. The observed data are matched surprisingly well by simple models based on induction by tidal water movements in the North Sea.

We have carried out a major geophysical and oceanographic research expedition, MADRIGALS (RRS *Charles Darwin* cruise 120), to a segment of the Mid-Atlantic Ridge south of the Azores, during which we carried out a seafloor CSEM survey and simultaneously collected a wide range of supporting oceanographic and geophysical data. We have analysed total field magnetic anomaly data to show that the summit of the Lucky Strike axial volcano on the Mid-Atlantic Ridge is characterized by exceptionally weak seafloor magnetization. We attribute this to the effects of hydrothermal fluid circulation, leading to alteration and demagnetization of shallow crustal rocks in this area.

We have made a preliminary determination of the resistivity structure in the upper 2 km of the crust beneath the Lucky Strike segment, and compared it to that of other spreading ridges. Resistivity at Lucky Strike is less than 1 Ωm immediately beneath the seafloor, increasing to more than 10 Ωm at depths of 800 to 1000 m, and then increasing more slowly (in a logarithmic sense) to a few tens of Ωm at a depth of 1.5 to 2 km. These resistivity values are substantially higher than those beneath the back-arc, intermediate-spreading-rate Valu Fa Ridge; but similar to, or only slightly higher than, those beneath the Reykjanes Ridge to the north. The upper crust at Lucky Strike is significantly less resistive than that beneath the East Pacific Rise at 13ºN, even though both are axial sites of active high temperature hydrothermal venting. It is less resistive by more than an order of magnitude than mature lithosphere in the eastern Pacific. Superimposed on the vertical structure at Lucky Strike are systematic lateral variations in resistivity, with typical wavelengths of 2-3 km or longer. Data from LEMUR instruments deployed close to the summit of the seamount indicate relatively low resistivities in the uppermost crust; while resistivity over the same depth range appears to be higher along the eastern edge of the median valley.

We have created for distribution a digital archive of data collected during the project, and of model results and scientific conclusions to date. We have communicated the results of our work at national and international conferences, and prepared papers for submission to international peer-reviewed scientific journals.

14.3 Future research and opportunities

Future research by the ISO-3D working group immediately after the end of the formal project phase will be aimed at extending and better constraining our scientific results through further careful modelling of a range of data using the ISIS code. This work is expected to include:

- Application of detailed 3-D modelling to natural source EM data to investigate mantle structure beneath the Azores islands; the influence of tidal water movements on MT observations in northern Europe; and the correlations between basin scale ocean circulation between Madeira and Portugal, the structure of the underlying seafloor, and voltage signals induced in the CAM-1 cable.
- Further modelling of CSEM data from the Madrigals study, firstly to tackle the issue of topographic influences on the seafloor data, and secondly to produce a fully integrated interpretation of all data from this area, in order to better understand the links between sub-sea-floor structure, volcanic and tectonic processes related to seafloor spreading, and the venting of high temperature hydrothermal fluids.

The successful collaboration between the ISO-3D partners has already led to the submission of proposals for national funding for further work on the Mid-Atlantic Ridge by Portuguese and UK participants. The planned SEAHMA project (already funded in Portugal, proposal submitted early summer 2001 in the UK) includes a CSEM study of a highly contrasting hydrothermal site, Saldanha, also southwest of the Azores, but in a location where circulation of high temperature fluids appears to be related to tectonism within an ultramafic setting at a segment boundary, as opposed to a volcanic setting at a segment centre.

The continuing success of seafloor EM sounding techniques in providing geophysical information relating to the presence and properties of fluids in pore spaces beneath the sea floor has now generated renewed and tangible interest from the hydrocarbon industry. During the last year of the ISO-3D project, Southampton and Lisbon members of the ISO-3D working group played a leading role in an experimental sea floor survey in the South Atlantic ocean, funded by a European oil company and making use of instruments developed partly with ISO-3D funding. Further studies of this type are already scheduled for the Southampton group, using further industrial funding; and both the expertise and the instrumentation central to some of the ISO-3D project's objectives are now in strong demand from the industrial sector.

Lastly, an issue of major environmental importance both from the point of view of structural stability of continental margins, and the potential effect on the greenhouse properties of the atmosphere, is that of the distribution, properties and stability of gas hydrates. Modelling by groups outside ISO-3D has already revealed the utility of seafloor CSEM methods in the study of seafloor hydrates and of trapped free gas beneath them, and this is likely to be an area in which members of the ISO-3D working group will seek to make a contribution to environmental research in the near future.